Conversion Of Carbon Dioxide To Hydrocarbons Using Iron Nanoparticle-Carbon Nanotube Catalysts

Minett, Daniel

Award date:
2014

Awarding institution:
University of Bath

CONVERSION OF CARBON DIOXIDE TO HYDROCARBONS USING IRON NANOPARTICLE-CARBON NANOTUBE CATALYSTS

Daniel Minett

Supervisory team:
Dr Davide Mattia, Dr Matthew Jones, Dr Andrew Johnson, Dr David Smith,
Professor Bob Tooze

A thesis submitted for the degree of Doctor of Philosophy

University of Bath

Department of Chemical Engineering

October 2013

Abstract

Dealing with carbon dioxide waste is an on-going societal and technological challenge. One attractive proposition is to chemically convert waste carbon dioxide into useful chemical products. One possible route is to combine two well-known chemical processes, reverse water gas shift and Fischer-Tropsch synthesis, to make a catalyst capable of converting carbon dioxide directly into hydrocarbons.

Iron nanoparticles supported on carbon nanotubes (CNT) have shown promise in the Fischer-Tropsch process. In this thesis, iron nanoparticles supported on carbon nanotubes (Fe@CNT) are shown to be effective catalysts for the coupled reverse water gas shift and Fischer-Tropsch reactions. Controlled oxidation of synthesised CNT can remove the graphitic shell from residual iron nanoparticles, activating them for catalysis. This process removes the need for expensive purification of CNT prior to use.

Carbon nanotube powders generated in this way are difficult to handle, and could be difficult to scale-up. A method has been developed to grow long, aligned carbon nanotubes on a commercial cordierite monolith support, which has potential for scale up. The developed method does not require pre-treatment of the monolith prior to CNT synthesis. Using the same oxidation method these Fe@CNTs-monoliths have been demonstrated to act as catalysts for carbon dioxide conversion. The monolithic catalysts demonstrate improved mass transfer capabilities, leading to higher activities for the monolithic catalyst over a similar powder catalyst.

Acknowledgements

I would like to thank the many people who have helped me over the four years I have spent at Bath, which have led to this thesis. First and foremost I would like to thank my supervisors, and the various academics who have shown interest in this project. Especially Dr Davide Mattia and Dr Matthew Jones, without whose help, encouragement and endless patience this thesis would not exist today. I'm also appreciative of the help of Dr Andrew Johnson, Dr Pawel Plucinski, Dr Sofia Pascu, Dr David Smith, Professor Bob Tooze, Professor Stan Kolaczcowski and Dr Janet Scott, whose insights and comments on my work have been much appreciated.

Secondly, I'd like to thank those I have worked with along the way in this project, who have lent valuable technical support. Amongst others the chemical engineering technical support staff, the technical support staff at MAS, and the technicians at SASOL, without whose valuable technical expertise, training and help I would not have been able to complete this thesis. I would especially like to thank Dr John Mitchells, who constantly performs miracles to keep the microscopy equipment at the University alive, and whose expertise has been invaluable throughout my PhD.

I would also like to thank my labmates in the Mattia and Jones group without whose support, and help this PhD would have been lonely indeed. Hannah Leese, Kah Peng Lee, Anyela Ramirez Canon, David Miles, and Sofia Bekou, thank you for your support, and for putting up with me when I put the cricket on the radio all day. Special thanks to Dr Justin O'Byrne and Rhodri Owen, who worked alongside me on this project and has had a significant contribution to all the work in this thesis.

Finally I'd like to thanks my friends here in Bath, my family and all the members of the DTC. You've put up with me moaning about this and that for four years, without your support and help I'd never have been able to make it to the end. Special thanks to the lunch crew (you know who you are) for solving all my problems over a crossword, a sandwich and a drink.

To my family, thank you for everything, I couldn't have done it without you.

List of Publications, Presentations and Prizes

Journal Publications

Minett, D. R.; O'Byrne, J. P.; Jones, M. D.; Ting, V. P.; Mays, T. J.; Mattia, D., One-step production of monolith-supported long carbon nanotube arrays. *Carbon* **2013,** 51, (0), 327-334.

O'Byrne, JP, Owen, R E, Minett, DR, Pascu, S. I.; Plucinski, P. K.; Jones, M. D.; Mattia, D., High CO2 and CO conversion to hydrocarbons using bridged Fe nanoparticles on carbon nanotubes. *Catalysis Science & Technology* **2013,** *3*, 1202.

Minett, DR, O'Byrne, JP, Pascu, S. I.; Plucinski, P. K.; Jones, M. D.; Mattia, D., CO_2 conversion over monolithic carbon nanotubes catalysts, *Catalysis Science & Technology,* **in preparation**.

Conference Proceedings

Carbon Dioxide conversion to hydrocarbons with reactivated iron-carbon nanotube catalysts - Oral Presentation at International Conference of Carbon Dioxide Utilisation, June 2013, Washington D.C, USA, awarded £1000 bursary by the CO_2Chem network to attend

Carbon dioxide conversion to hydrocarbons using structured carbon nanotube supports–Poster presenter at SuBiCat I: Sustainable Catalytic Conversions of Renewable Substrates, March 2013, St Andrews, Scotland, awarded £200 bursary by the conference chair to attend

Catalysts for carbon dioxide conversion using carbon nanotube supports-Poster presenter at Advances in Carbon Dioxide Utilisation, December 2012, Imperial College London

Session chair and Poster presenter at Gordons Research Conference/Seminar in Green Chemistry, July 2012, Barga, Italy

Catalysts for carbon dioxide conversion using carbon nanotube supports- Poster presenter at CSCT Summer Showcase, July 2012 1st Prize – Best Poster (£50)

Novel approach for the production of monolith supported carbon nanotubes -Poster presenter at ChemonTubes conference, April 2012, Arcachon, France

Conversion of carbon dioxide into useful feedstocks using carbon nanotube supports - Poster presenter and speaker at Great Western Carbon Dioxide meeting, June 2011, Bath 1st Prize – Best Poster (£50)

Conversion of carbon dioxide into useful feedstocks using carbon nanotube supports - Poster presenter and speaker at CSCT summer showcase, July 2011

Synthesis of catalytic species for the conversion of hydrogen to useful feedstocks using carbon nanotubes as a support - Poster presenter at Chemical Science & Technology towards a Low-Carbon Economy, October 2010, Oxford 2nd Prize – Poster Prize (£50)

List of Public Engagement activities

Bristol Tobacco Factory Science Café (2012) – The Fuel of the Future, part of panel discussion on future fuel technologies

Bath Royal Literary and Scientific Institute (2011) - Chemistry on the Nanoscale: Small Things solving Big Problems, gave a lecture on my research area, and the potential impact of my research

Cheltenham Science Festival (2010-2012) – Part of centre for sustainable chemical technologies stand, involved in development of various CO2 reduction themed activities and discussed my research with members of the public

Table of Contents

List of Figures

Notation and Nomenclature

Notation	*Definition*
AACVD	Aerosol assisted chemical vapour deposition
Ar	Argon
atm	atmosphere
BET	Brunauer–Emmett–Teller
C_2H_2	Acetylene
C_2H_4	ethene
CCS	Carbon Capture and Storage
CCU	Carbon Capture and Utilisation
cCVD	continuous Chemical Vapour deposition
CNF	Graphitic Nano fibres
CNT	Carbon Nanotube
CO	Carbon monoxide
CO_2	Carbon dioxide
CVD	Chemical Vapour Deposition
EDX	Energy Dispersive X-ray spectroscopy
EOR	Enhanced Oil Recovery
EU	European Union
Fe	Iron
Fe@CNT	Iron supported on carbon nanotubes, prepared by oxidation method
FID	Flame Ionisation Detector
FT	Fischer Tropsch
GC	Gas Chromatograph
GC-MS	Combined Gas Chromatograph Mass Spectrometer
h	Hours
H_2	Hydrogen
I_D	Intensity of D band
I_G	Intensity of G band
$I_{G'}$	Intensity of G prime peak
I_{Si}	Intensity of Si peak
min	minutes
MWCNT	Multi Walled Carbon Nanotube
nm	nanometre
NPs	Nanoparticles
PXRD	Powder X-Ray Diffraction
RWGS	Reverse Water Gas Shift
sccm	Standard cubic centimetres per minute
SEM	Scanning electron Microscopy
SWCNT	Single Wall Carbon Nanotube
TCD	Thermal Conductivity Detector
TEM	Transmission electron Microscopy
TGA	Thermo-gravimetric analysis
TPO	Temperature programmed oxidation
wt.%	Weight percentage
X	Conversion
XPS	X-ray Photoelectron Spectroscopy
XRD	X-Ray Diffraction
α	Alpha value

1 Introduction

Over the last century there has been growing concern about the potential effects of uncontrolled release of carbon dioxide (CO_2) into the atmosphere. [1] The effect of atmospheric CO_2 on global temperatures was first outlined by Svante Arrhenius in 1896. [2] Arrhenius was the first to try and quantify the contribution of CO_2 to the 'greenhouse effect', and also speculated on how changes in CO_2 concentrations might have contributed to previous climate fluctuations.

The 'greenhouse effect' was first theorised by Joseph Fourier, [3] and then experimentally determined by John Tyndal in 1862, who showed that even small amounts of gases such as water, CO_2 and methane can be virtually impenetrable by infra-red heat radiation. [4] The presence of these gases in the atmosphere has a similar effect on the planets temperature, via the following mechanism. Direct solar radiation which is absorbed by the earth heats the planet; to balance this energy and prevent temperatures increasing continuously the earth must re-radiate the same amount of energy. Because the earth is much cooler than the sun, the energy is radiated at lower wavelengths, mostly in the infra-red region of the spectrum. If the earth's atmosphere did not contain greenhouse gases, this energy would radiate away and global temperature would be around -19 °C, significantly below freezing.[1] Naturally occurring amounts of greenhouse gases raise the global temperature by around 33 °C to around 14 °C.[1] Greenhouse gases have strong infra-red absorption bands and are excited by the infra-red radiation. When the molecule relaxes energy is re-radiated in all directions whilst also retaining some energy itself. The result of this is that the sun's energy is not all radiated away from the earth, causing the earth's atmosphere to warm, see Figure 1.1 for an illustration of this effect. Global temperature is also affected by a number of other factors including effects such as surface albedo (i.e. how reflective the earth is), solar cycles and atmospheric aerosols (such as clouds). [5]

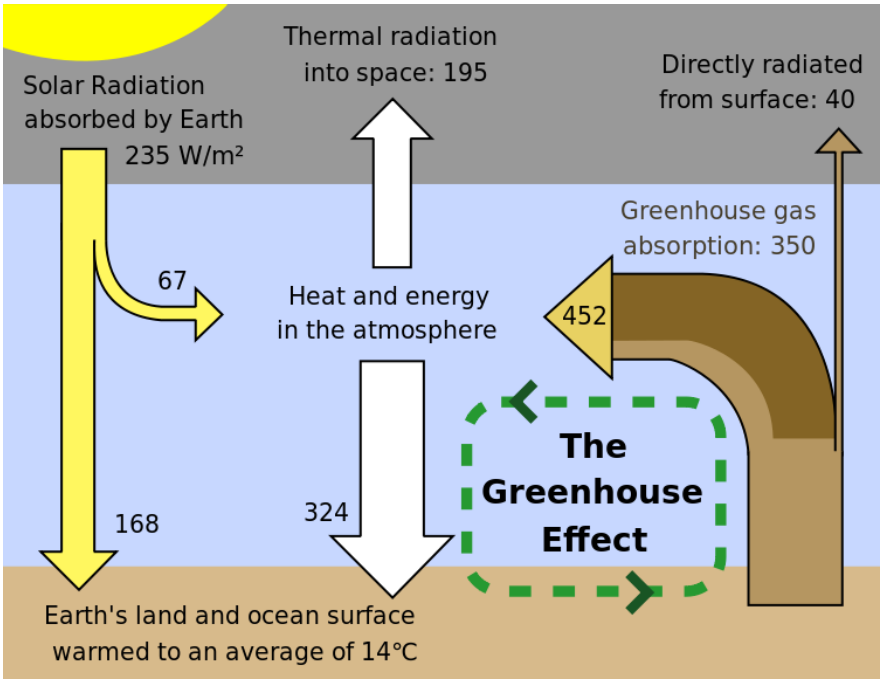

Figure 1.1 The global energy balance, illustrating the influence of greenhouse gases on the retention of energy in the atmosphere, energy is expressed in terms of Watts per square metre (W/m^2) [6]

Increasing the concentration of CO_2, or other greenhouse gases in the atmosphere, increases the degree of this effect though the full warming effect of this increase may not be felt at ground level immediately. Since detailed records began, it is clear that CO_2 levels in the atmosphere have been continuously rising (ignoring natural seasonal variations), as illustrated by records for the last 50 years from the Mauna Loa observatory, the longest continuous measurement of CO_2 level as shown in Figure 1.2. Evidence for historical CO_2 levels from ice-cores and tree rings indicate that current levels of carbon dioxide in the atmosphere are higher than they have been for a hundred thousand years. This year for the first time recorded levels of CO_2 at Mauna Loa breached the 400 ppm limit, a rise of more than 25% since the concentration was first recorded here in 1958. [7]

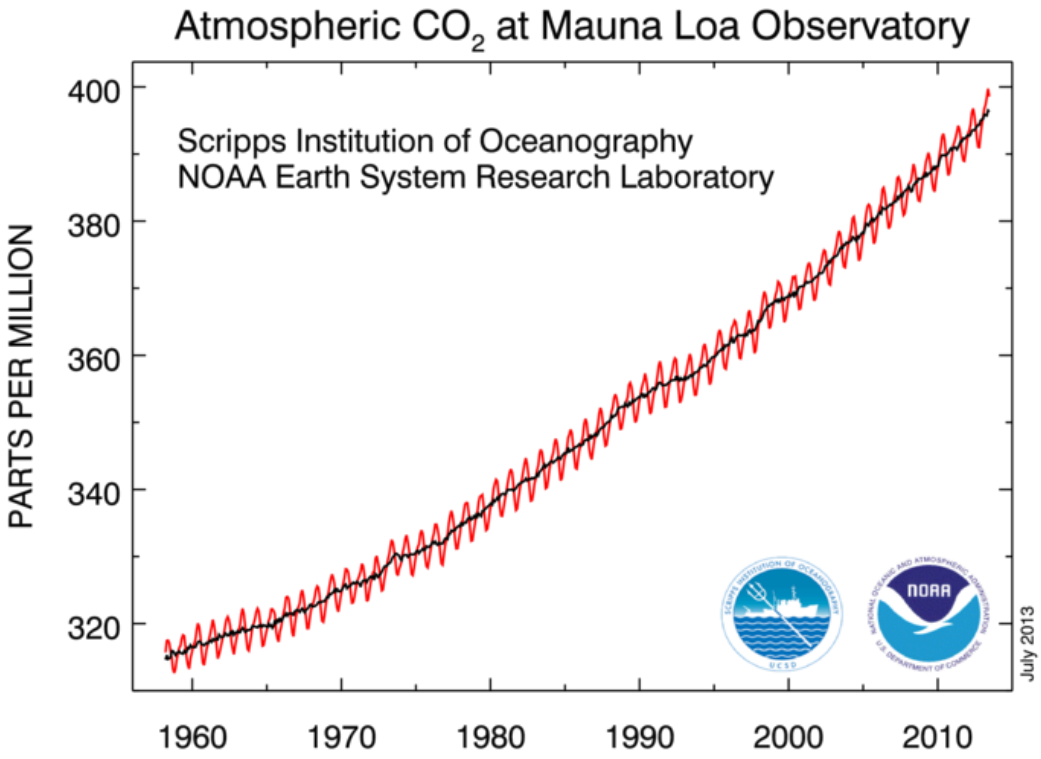

Figure 1.2 Atmospheric concentrations of CO_2 measured at the Mauna Loa observatory [7]

As a result of the continuing global increases in CO_2, it is inevitable that global temperature will increase. [1] Arrhenius estimated that temperature rises of the order of 4-6 °C could be expected if the concentration of atmospheric CO_2 doubled, though he expected this process to take 3000 years. [2] These calculations were of the right order of magnitude; however, he lacked sufficient information to correctly determine the rise in temperature. Nevertheless, he was the first to calculate the effect of changes in CO_2 levels to global temperature change.

Modern studies are still uncertain about the degree of temperature rise, and the time it will take to occur, but a number of different climate models have assayed predictions for global temperature rise. [8] All models predict significant temperature rises over the next 100 years. The Intergovernmental Panel on Climate Change (IPCC) currently believes that a doubling of CO_2 concentrations is likely to result in a temperature rise between 2 and 4.5 °C, depending on the scenario adopted (Figure 1.3). [1]

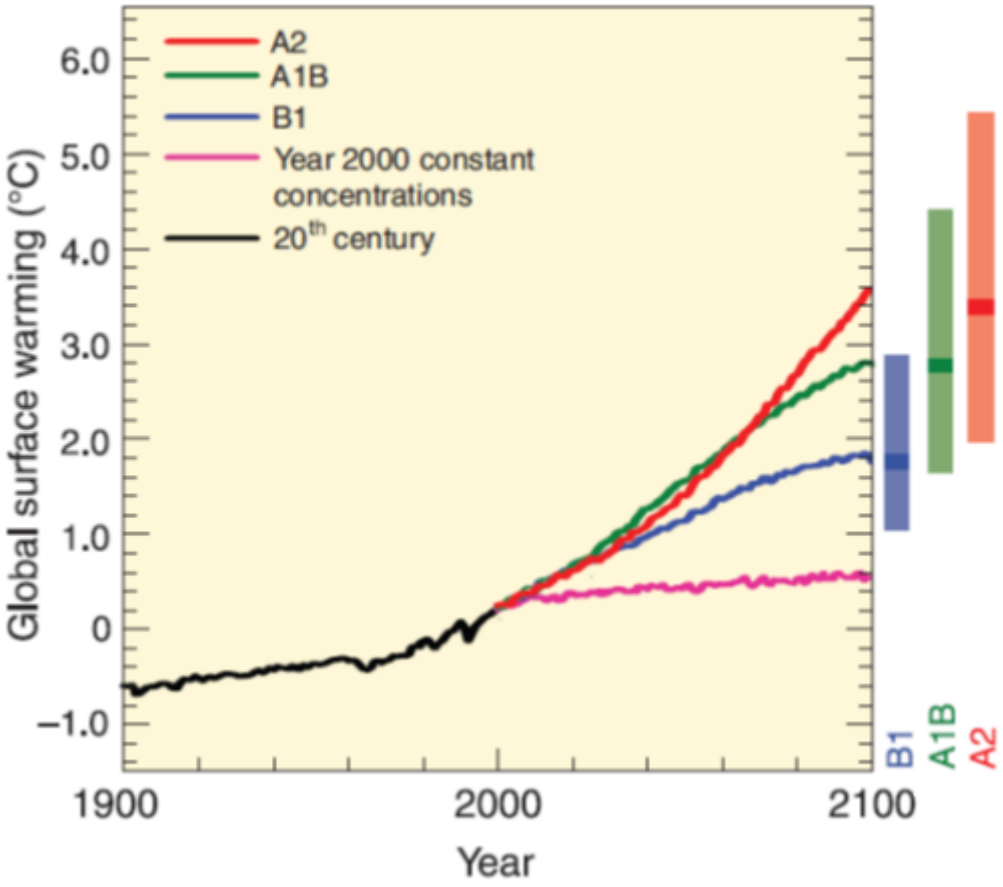

Figure 1.3 Multi-model means of surface warming (relative to 1980–1999) for the scenarios A2 (rapid population growth, with slow technological adaptation and economic change), A1B (strong economic growth with a balanced energy portfolio) and B1(similar population growth to A1 but a rapid transition to a service and information economy), shown as continuations of the 20th-century simulation. The bars in the figure represent the best estimate (solid line within each bar), and the likely range of values to be expected. [1]

In order to mitigate global temperature rise, it is important to limit further CO_2 emissions. The IPCC targets currently state that in order to limit the likelihood of temperatures rises of more than 2 degrees, total atmospheric carbon cannot increase to more than 450 ppm, necessitating a decrease in CO_2 emissions of 50% by 2050, and then further cuts after this. [1]

A number of efforts have been made to commit the world to global carbon dioxide reductions. The Kyoto protocol seeks to reduce the emissions of developed countries that have contributed the most to global warming, but does not place emissions reductions on developing countries such as China. The Kyoto protocol has not been ratified by the USA, and Canada withdrew in 2011. As such the Kyoto protocol affects less than half of the world's ten leading CO_2 emitters. Whilst the Kyoto protocol has had some success, particularly in the EU where carbon dioxide emissions have decreased, globally emissions of carbon dioxide continue to rise, with the small decreases in CO_2

production in developed countries, being offset by the export of these emissions to developing countries, as illustrated by Figure 1.4.

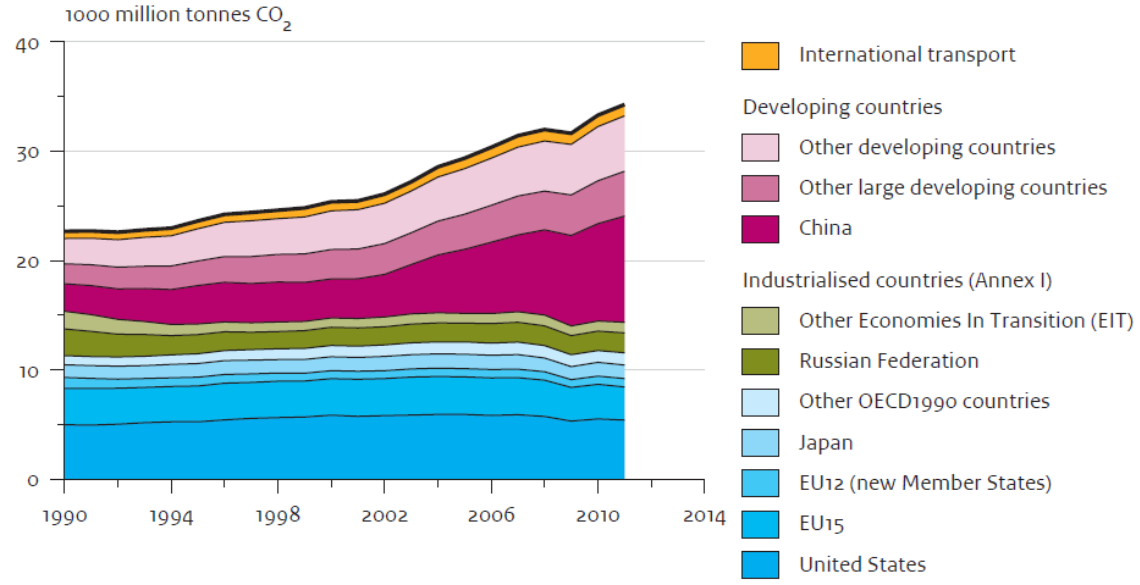

Figure 1.4 Global CO_2 emissions per region from fossil fuel use and cement production

Despite cautions on the perils of excess CO_2 production, coal is still the fastest growing energy source in the world. [9] In order for this energy expansion not to produce significantly more CO_2 than is acceptable under IPCC limits, we need to consider how CO_2 production can be mitigated.

Renewable power production may provide a long term answer to this problem with production of energy from wind, solar and water power on track to provide 20% of EU power by 2020. [10] However considering the continuing increase in CO_2 emissions, this may not be enough to keep temperature rises below 2 degrees. As such the global scientific community needs to find other ways to mitigate CO_2 production.

1.1 Carbon capture

An attractive method for dealing with waste CO_2 is carbon capture. This involves capturing the CO_2 as it is produced by power plants (or other large emitters), and not releasing it into the atmosphere. This process is unlikely to be applied to small scale emissions such as transportation, due to the diffuse nature of carbon dioxide production. Carbon capture systems have largely been designed to be implemented with large scale production of CO_2, as carbon dioxide is more concentrated. The carbon capture unit is attached to the plant outlet and seperates and captures the produced CO_2 from other gases released. Currently this process is rather expensive and energy intensive, estimates for the cost of carbon capture vary widely but it is expected that demonstration plants will

cost between 60 and 90 €/ton of CO_2 captured, whilst larger scale projects will have a cost between 30 and 45 €/ton of CO_2 captured. Increased investment and research in this area is beginning to lower these costs. [11,12] Some reports estimate that the cost of coal power with carbon capture will be less than cost of coal power today in 2025, if sufficient investment is made. [11]

A number of different technologies have been developed in order to capture CO_2. The most widely implemented technology currently in use, involves the use of monoethylamines which can reversibly react with CO_2. This technology is not ideal, as only 30% of the carbon capture absorbant is amines, with 70% of the mixture being unused water significantlty increasing the systems weight and volume. [13]

A number of other technologies are currently being explored at the R&D level including zeolites, [14,15] mesoporous carbons, [14,15] calcium oxide, [14] Metal Organic Frameworks (MOFs), [14,16] and ionic liquids [16] amongst others. Development of these techniques to industrial scale could dramatically reduce costs of carbon capture technologies, however many of these new materials are still some way from industrial application. [16]

1.1.1 Carbon Capture and Storage

Once the CO_2 is captured a new problem emerges, how to deal with the large quantities of CO_2 produced. Two main strategies are generally followed: to store it or to use it. These two processes are commonly called carbon capture and storage (CCS) and carbon capture and utilisation (CCU).

CCS refers to processes in which once captured the CO_2 is stored and locked away, ideally in stable geological stores for significant lengths of time. Processes must also minimise the amount of CO_2 which leaks into the atmosphere over time. Figure 1.5 shows some of the range of options available for storage of CO_2. [17] Currently enhanced oil recovery (EOR) or injection of CO_2 into depleted oil wells in order to force oil out of the well is one of the more popular methods, as more oil is produced as a byproduct (though the long term sustainability of this process must be questioned). [13]

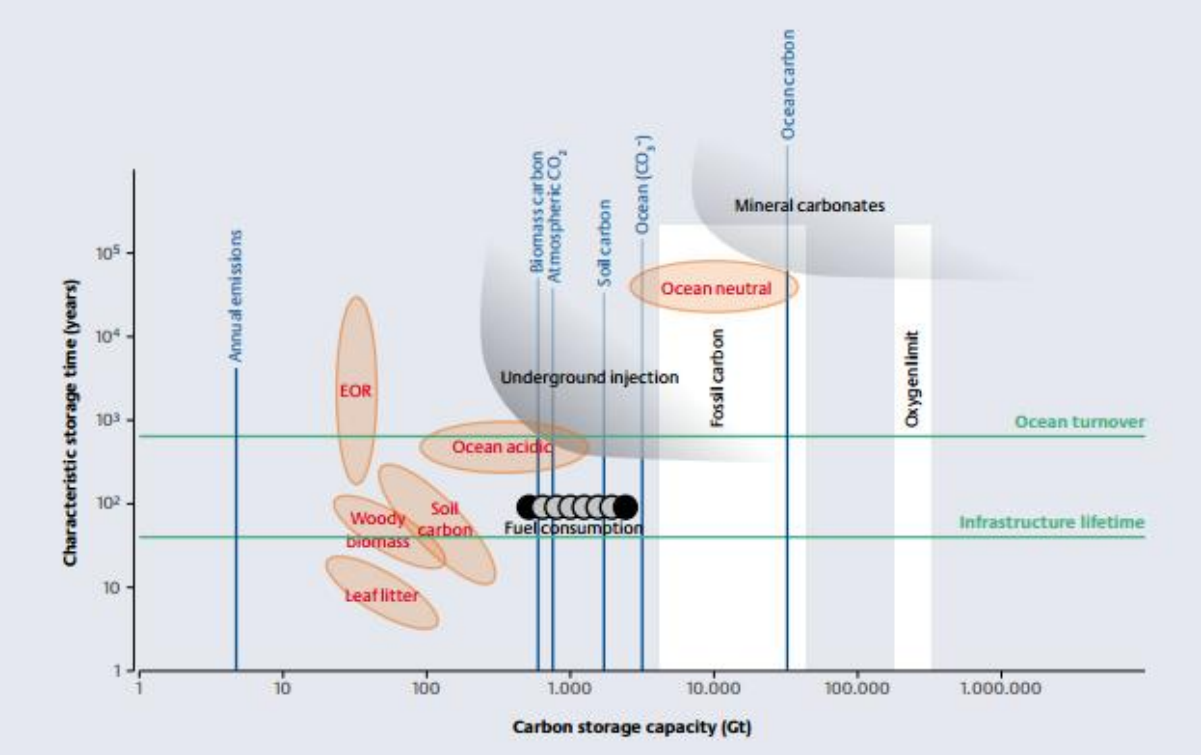

Figure 1.5. Estimated storage capacities and times for various sequestration methods. The "fossil carbon" range includes at its upper end methane hydrates from the ocean floor. The "oxygen limit" is the amount of fossil carbon that would use up all oxygen available in air for its combustion. Carbon consumption for the 21st century ranges from 600 Gt (current consumption held constant) to 2400 Gt. "Ocean acidic" and "ocean neutral" are the ocean's uptake capacities for carbonic acid and neutralized carbonic acid, respectively. The upper limits of capacity or lifetime for underground injection and mineral carbonates are not well constrained. EOR stands for enhanced oil recovery.[17]

Whilst the capacity for EOR is limited, though currently more economically favourable, other techniques such as underground injection and mineralisation are predicted to have very large storage capacities. [17] Injection of CO_2 into underground saline formations currently has two pilot scale processes operating in Norway, with no reported leaks. Locating other suitable underground formations could store significant amounts of CO_2. Costs of this process are not offset as in EOR however. [13]

Mineralisation, or the reaction of minerals with CO_2 to form carbonates is another potential large scale store of CO_2. This process is currently limited by the relatively slow reaction rate of mineral carbonates, high energy input and also the large quantities of mineral carbonate which will be produced. [13] Advances in 'energy neutral' mineralisation could potentially result in significant expansion in the storage market. Recent work has also found that useful byproducts such as iron can be produced, which could improve the economics of the process (though it is not yet clear if the quantity of product produced may be too large to be reliably consumed, or if the additional energy cost required to produce iron is worthwhile). [18]

1.1.2 Carbon Capture and Utilisation

An alternative to CCS is CCU, where CO_2 is used as a chemical precursor in order to make more valuable products, instead of storing it. This can be considered to be a complement to CCS serving similar goals, whilst potentially also providing economic benefits. CCU is a very broad field which covers the production of a wide range of different chemicals and products, as well as simply using pure CO_2 as a product in itself. Figure 1.6 shows some of the many products that are accessible via reactions of CO_2.

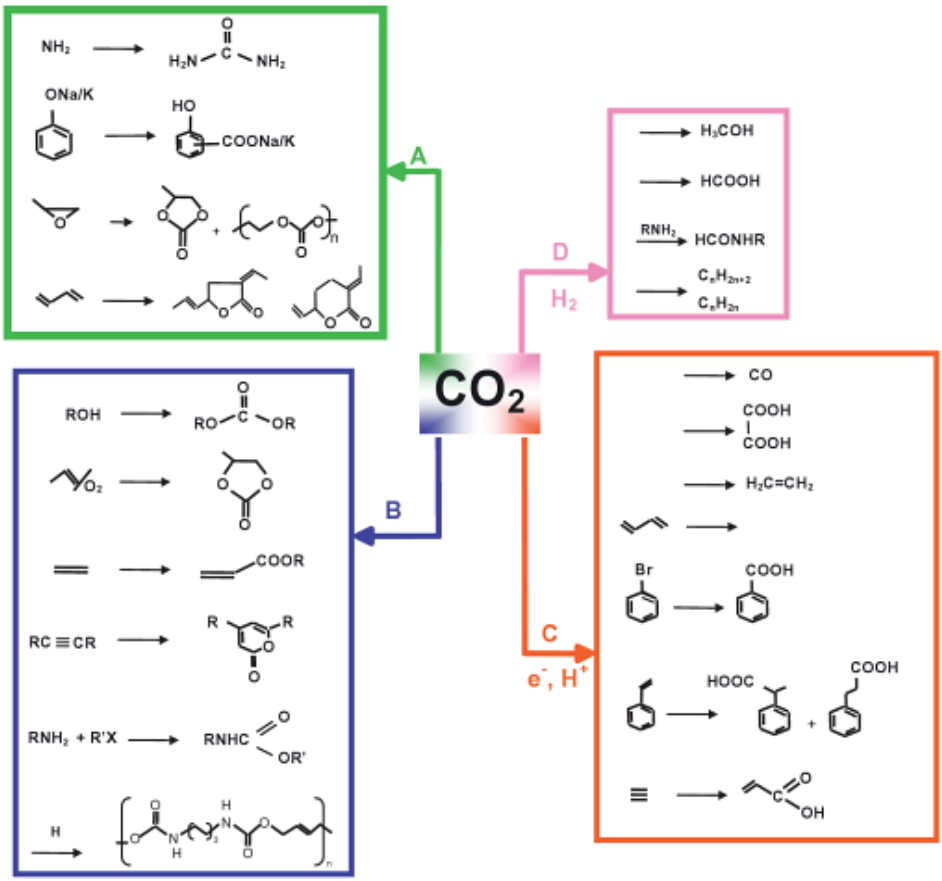

Figure 1.6 A selection of the chemical products that can be obtained from CO_2 via different routes A + B) via reaction with other chemicals, C) Electrochemically and D) via hydrogenation [19]

Utilisation of CO_2 on an industrial scale is seen today with the synthesis of urea (107 million tonnes per year), [20] the production of salicylic acid (30,000 tonnes per year), [20] the production of methanol (2 million tonnes per year) [20] and cyclic organic carbonates, [21] but large scale conversion of CO_2 into other products has not yet been developed to an industrial scale. Large quantities are also used as a supercritical solvent, and in the food industry.

Reacting CO_2 with organic molecules, as well as photochemical and electrochemical conversion of CO_2 are all active areas of research, with a wide variety of processes currently under-development. This thesis will focus on the products of CO_2 as a result of thermal combination with hydrogen.

1.1.3 Feasibility of large scale carbon capture and utilisation

Global production of CO_2 has been increasing steadily since the industrial revolution (Figure 1.4). Current global production of CO_2 is more than 30 gigatonnes annually. [22] To put this into context, this is more than 7 times the annual production of oil, the largest commodity chemical. Estimates of global chemical manufacture place the market at considerably less than 1 gigatonne a year.

As such, consumption of all CO_2 emissions produced by the chemical sector or even the energy sector is extremely unlikely. In all likelihood usage of CO_2 will consume only a fraction of the global supply. Current estimates suggest that at best 7% of the CO_2 produced could be utilised by the chemical industry, as the quantity of CO_2 produced is significantly more than the global chemical industry could utilise. [19] CO_2 use must, therefore, be seen as a contributor to the reduction of global CO_2 production, but not as the solution.

Products produced from CO_2 must be in relatively high demand (as large quantities will be produced) and high value in order to support the economic cost of capturing and converting the CO_2. Large scale carbon capture and utilisation at minimal cost will require several preliminary conditions to be met; To minimise purification costs, a clean source of CO_2 is required, To minimise energy costs, the electrolysis of water to produce hydrogen needs to be as efficient as possible, and the energy used to produce this hydrogen must be from renewable sources. [19] In the following sections the potential sources of CO_2 and hydrogen are discussed.

1.1.3.1 Sources of CO_2

Taking CO_2 produced from power plants and converting it adds a couple of extra complications. First, the CO_2 produced from these sources is not pure, and frequently contains contaminants and catalyst poisons, requiring the gas stream to be purified before it can be used.

CO_2 is produced in smaller, more manageable amounts than by power plants, by a number of different industrial processes as a by-product (Table 1.1). In general CO_2 produced by these processes is cleaner, and is produced in smaller quantities. [23] If CO_2 can be captured and utilised from these processes in an energy efficient manner, the global warming impact of many of these high economic value processes will be minimised.

Table 1.1 Industrial processes which produce CO_2 [23]

Industry	CO_2 produced (Mt/yr.)
Oil Refining	850-900
LNG Sweetening	20-25
Ammonia synthesis	160
Ethene synthesis	155
Ethylene oxide synthesis	10
Fermentation	200
Cement production	1000
Iron + Steel production	870

1.1.3.2 Production of Hydrogen

It is important to note that for the CO_2 reducing reactions detailed below to be sustainable, it is essential that the hydrogen used for the reaction comes from sustainable sources. At present hydrogen is largely obtained by steam reforming of methane, obtained from fossil fuel sources. If this hydrogen was used to convert CO_2, the net environmental impact on CO_2 produced would be positive, with more carbon produced than is used. In order for hydrogen to be a carbon neutral reactant it must come from sustainable sources. Currently a large amount of work is being performed on the concept of a 'hydrogen economy'. [24] In order for this to be successful advances must be made in the generation of hydrogen from sustainable sources. The most likely source of sustainable hydrogen is water, either through electrolysis, [25] or photo-catalytic routes. [26] Other possible sources of hydrogen include the gasification of various types of biomass. [27] Further development of these techniques in order to obtain a sufficient amount of renewable hydrogen would be required before large scale adoption of the techniques discussed here.

Current efforts to produce hydrogen sustainably involve the production of hydrogen via electrolysis using renewable power at periods of low demand. As renewable power is highly variable, large amounts of power can be produced at time when there is no demand for it. In these situations producing hydrogen, and using it to convert CO_2 into useful products can be economic. Combination of hydrogen and CO_2 creates a higher energy density product, which is much easier to store than

hydrogen. As such it is a much more appropriate fuel for many transport applications, and as an energy store. A process like this could be difficult to integrate into the current chemical industry as supply would be much more variable than current processes.

1.2 Products of CO_2 hydrogenation

The five major C1 products which are directly accessible from CO_2 by hydrogenation are methane, methanol, formaldehyde, formic acid and carbon monoxide; each of these products can be accessed through use of different catalysts and processes. Though CO_2 is often considered a stable product, in fact when combined with hydrogen a number of different products are thermodynamically favourable. By modifying the process operating conditions and introducing catalysts a number of different products can be obtained.

1.2.1 Methane

Methane is an important resource, with around 1.9 Gt produced annually. [28] The reaction of CO_2 with hydrogen to give methane (otherwise known as the Sabatier process) as shown in equation 1.1, is well known being one of the first catalytic reactions to be discovered. [29]

$$\mathbf{CO_2\,(g)\ +\ 4H_2\,(g)\ \leftrightharpoons\ CH_4\,(g)\ +\ 2H_2O\,(l)} \qquad (1.1)$$

ΔH_r^o = -251.1 kJmol^{-1}; ΔS_r^o = -410.5 J K^{-1} mol^{-1}; ΔG_r^o = -128.8 kJ mol^{-1}

The reaction traditionally takes place over nickel catalysts, though recent catalysts developed for this reaction include $PdMg/SiO_2$, [30] Ru/Al_2O_3, [31] Ru/TiO_2 [31] and Ni/ZrO_2. [32] The reaction typically proceeds at temperature between 300-500 ^oC, and there have been reports of conversions to methane as high as 99%. [30-33] Attempts have been made to convert CO_2 into methane at lower temperatures using homogeneous chemistry, but these processes all involve expensive high energy hydrides rather than hydrogen directly. [34-36] It is unlikely that production of methane via this route will ever be desired, especially as methane is abundant, and easily obtained from the decomposition of biomass. The shale gas revolution currently taking place in the US, is driving down the costs of methane, [37] making direct production of methane unlikely to ever be competitive.

Combination of hydrogen and CO_2 to give methane as an energy store during periods of low energy usage is currently being explored. The stored methane can then be burnt using traditional power plants in periods of low renewable energy output. It is believed that this technology could be more efficient than battery technology in terms of energy storage. [38] Another area where the Sabatier reaction could play an important part is in future missions to Mars, using the CO_2 in the atmosphere

to generate fuel and water (which can then be further electrolysed to give H_2 and O_2). [31] The key advance required in both these technologies is the production of methane with complete selectivity

1.2.2 Methanol

Methanol is another important industrial chemical, with a combined production of over 100 million tonnes, this is currently mostly manufactured using CO produced from CH_4. The fact that CO_2 can react with H_2 to give methanol is already used in some current industrial processes. CO_2 is used as an additive to consume the excess H_2 produced from the conversion of CH_4 to syn-gas, [39] as in equation 1.2.

$$\mathbf{CO_2\ (g)\ +\ 3H_2\ (g)\ \leftrightharpoons\ CH3OH\ (l)\ +\ H_2O\ (l)} \qquad (1.2)$$

ΔH_r^o = -129.3 kJmol^{-1}; ΔS_r^o = -408.7 J K^{-1} mol^{-1}; ΔG_r^o = -7.4 kJ mol^{-1}

Therefore many of the catalysts used for the conversion of CO to methanol are also active for the conversion of CO_2 to methanol. Typically the reaction takes place at 250 ^oC using $CuZnO_2/Al_2O_3$ with conversions of the order of 40%, significantly less than the conversion from carbon monoxide. This comparatively low conversion rate will always be lower than that for the conversion of CO to methanol, so will struggle to compete economically. [39] Methanol is the precursor for synthesis of dimethylether (DME) a product which has attracted a lot of interest as a potential fuel source. It has also been used by Mobil to produce gasoline. Air Fuel Synthesis have recently developed a combined process, producing methanol from CO_2, and then converting the methanol into gasoline. [40]

1.2.3 Formic acid

Formic acid is another chemical which can be produced from CO_2. Demand for formic acid currently stands at approximately 700,000 tonnes a year. [41] Production of formic acid from CO_2 is completely atom efficient as in equation 1.3 making this an attractive process.

$$\mathbf{CO_2\ (g)\ +\ H_2\ (g)\ \leftrightharpoons\ HCOOH\ (l)} \qquad (1.3)$$

ΔH_r^o= -31.1 kJmol^{-1} ΔS_r^o= -212.6 J K^{-1} mol^{-1} ΔG_r^o= 32.3 kJ mol^{-1}

A number of processes have been developed utilising homogeneous catalysts to produce formic acid, but these are not ideal for industrial production using expensive metals such as rhodium, [42,43] ruthenium, [44,45] and iridium [46] and having additional separation issues as well. An iron based homogeneous catalyst has also been developed, but turnover numbers (TONs) for this catalyst are low. [47] Heterogeneous catalysts that have been developed for this reaction include a Raney nickel catalyst, [48] and more recently a heterogeneous ruthenium hydroxide catalyst. [44] As the reaction is

thermodynamically unfavourable at STP all reactions which have successfully reported conversion to formic acid have typically been performed at high pressures, ranging from 5 to 50 bar, and at relatively low temperatures, ranging from 20 to 120 ^{o}C. [44,46,47]

1.2.4 Formaldehyde

Formaldehyde is another important industrial chemical, with around 9 million tonnes produced each year used as a precursor for many other chemicals, especially polymers. [49] Currently produced mainly from methanol, a route from CO_2 could potentially be economically competitive. [50] The hydrogenation of CO_2 to give formaldehyde is thermodynamically unfavourable as can be seen in equation 1.4.

$$\mathbf{CO_2\ (g)\ +\ 2H_2\ (g)\ \leftrightharpoons\ HCOH\ (g)\ +\ H_2O\ (l)} \qquad (1.4)$$

ΔH_r^o = -7.2 kJmol^{-1}; ΔS_r^o = -186.3 J K^{-1} mol^{-1}; ΔG_r^o = 48.3 kJ mol^{-1}

Currently there has been very little work on the conversion of CO_2 into formaldehyde. A number of studies have reported that formaldehyde and formates are formed as an absorbed intermediate in methanol formation, but there appears to be little evidence of this formaldehyde desorbing. [33,51] This reaction has been performed with methanol catalysts at lower temperatures (150 ^{o}C, 6 bar)[51] than typical for reactions to give methanol, so exploring methanol catalysts at lower temperatures may be a promising route to a viable formaldehyde catalyst. Since formaldehyde is currently produced by the oxidation (typically using an Fe_2O_3/Mo/V catalyst at 250-400 ^{o}C) or partial oxidation and dehydrogenation of methanol (typically using a silver catalyst and an excess of methanol at 680-720 ^{o}C), a catalyst which produced it directly from CO_2 would be of great interest. [49] This reaction is very difficult to achieve, being energetically unfavourable at all temperatures at atmospheric pressure. Indeed it has been noted that formaldehyde has a tendency to decompose to CO_2 and H_2 at temperatures above 150 ^{o}C. [49] Any probable reaction to give formaldehyde from CO_2 and H_2 would face challenges to achieve a good selectivity to formaldehyde over methanol, and would only be able to occur at relatively low temperatures and high pressures.

1.2.5 Carbon Monoxide

The final C1 product accessible from CO_2 is carbon monoxide (CO). The chemistry of carbon monoxide is well established with a number of important industrial processes using carbon monoxide as a feedstock.

$$\mathbf{CO_2\ (g)\ +\ H_2\ (g)\ \leftrightharpoons\ CO\ (g)\ +\ H_2O(l)} \qquad (1.5)$$

ΔH_r^o=-2.4 kJmol^{-1} ΔS_r^o= -76.9 J K^{-1} mol^{-1} ΔG_r^o= 20.6 kJ mol^{-1}

Generating CO from CO_2, would be advantageous as this carbon monoxide can then be used to directly generate a number of other important feedstocks, as a large number of hydrocarbons can be accessed through the FT process. The reaction of CO_2 and H_2 to give CO and H_2O can be seen to be the reverse of a common industrial process, the water gas shift (WGS) reaction. Widely used in industry, the reaction of H_2O and CO to give CO_2 and H_2 is used to adjust the CO/H_2 ratio in methanol synthesis and FT processes, as well as to generate the high purity H_2 necessary for ammonia synthesis. A number of metal species have been identified as having activity in the catalysis of the reverse water gas shift reaction, including a number of iron catalysts, Cu/ZnO/Al_2O_3 catalysts (also commonly used for methanol synthesis) and gold nanoparticles on a variety of supports. [52] The reaction to give CO from CO_2 is thermodynamically unfavourable, however when coupled with the FT reaction it becomes thermodynamically favourable. [53]

1.2.6 Hydrocarbons from CO_2

Production of hydrocarbons by hydrogenation of CO_2 could provide a number of different potential products.

$$\boldsymbol{x}\mathbf{CO_2}\ (\mathbf{g})\ +\ \mathbf{3}\boldsymbol{y}\mathbf{H_2}\ (\mathbf{g})\ \leftrightharpoons\ \boldsymbol{C_xH_y}\ (\mathbf{g})\ +\ \mathbf{H_2O}(\mathbf{l}) \qquad (1.6)$$

ΔH_r^o= varies kJmol^{-1} ΔS_r^o= varies J K^{-1} mol^{-1} ΔG_r^o= varies kJ mol^{-1}

Currently there are a number of different routes to higher and lower hydrocarbons being researched. Most approaches include the synthesis of hydrocarbons via carbon monoxide followed by Fischer Tropsch, whether long chain length hydrocarbons like diesel or gasoline, or shorter chain functionalised molecules such as olefins. An alternative is Air Fuel Synthesis process producing gasoline via methanol. [40]

The controlled synthesis of short chain olefins such as ethene, propene and butene would be of significant interest, since selective synthesis of these products is still a challenge. The synthesis of higher hydrocarbons, and specifically the synthesis of short chain olefins from CO_2 and CO is explored in greater depth in section 2.6 .

1.3 Motivation for this work

This motivation for this work is to explore novel catalyst support systems for the conversion of CO_2 into commercially viable products. The development of selective catalysts for the conversion of CO_2 into valuable products could provide an additional revenue stream to offset the cost of capture and storage of CO_2. Current government policy has set ambitious targets for the reduction of CO_2 emissions across the EU in order to limit the impact of climate change. The UK aims to reduce CO_2 emissions by 80% by 2050, in order to meet this challenge. [54] A number of different strategies are being pursued to meet these reduction strategies.

In this work carbon nanotubes are investigated to determine whether they show promise as catalyst supports for the conversion of CO_2. The synthesised CNT's are investigated for the first time as catalyst supports for the reaction combining the RWGS and the FT processes in order to produce valuable lower olefin products. In particular the use of iron nanoparticles supported on CNTs will be explored, and attempting to utilise the residual iron nanoparticles from CNT synthesis as catalysts. The use of residual iron nanoparticles from carbon nanotube synthesis could significantly reduce the number of synthesis steps, and provide an interesting route to these supported iron catalysts.

It has long been known that carbon nanotubes have beneficial properties as a catalytic support, but several factors have limited its uptake as a support material, including a high pressure drop in a packed bed configuration, and low density, and health and safety concerns due to powder handling. Here the synthesis of carbon nanotubes and their preparation on structured supports is explored, in order to create catalyst supports more suited to industrial use and scale up. This project specifically looks at the preparation of carbon nanotubes directly onto the common industrial catalytic support cordierite.

1.4 Structure of the Thesis

The layout of this thesis is as follows:

Chapter 2 – discusses the different methods for the synthesis of carbon nanotubes, including previous attempts to grow these catalysts on structured supports. It also includes an in-depth review on the conversion of CO_2 into hydrocarbons via the Fischer-Tropsch reaction, and the use of iron and carbon nanotube based catalysts for the Fischer Tropsch reaction, and the factors known to effect this reaction

Chapter 3 – describes the characterisation techniques used in this study for analysis of the synthesised materials

Chapter 4 – describes the different methods used for synthesising CNT powder, and development of the method for CNT synthesis, along with detailed characterisation of the resulting materials

Chapter 5 - Describes the synthesis of CNT onto a cordierite support, and detailed characterisation of the resulting substrates

Chapter 6 - describes the methods used to synthesise the catalysts used in this study, describing the design and construction of the reactors used to test CO_2 conversion

Chapter 7 – describes the activation of the carbon nanotubes for catalysis, and subsequent investigation into the behaviour of these catalysts

Chapter 8 – summarises the results and conclusions of the previous chapters, discussing the potential opportunities for exploring this topic further in future work.

Figure 1.7 is a summary of the links between the chapters described here.

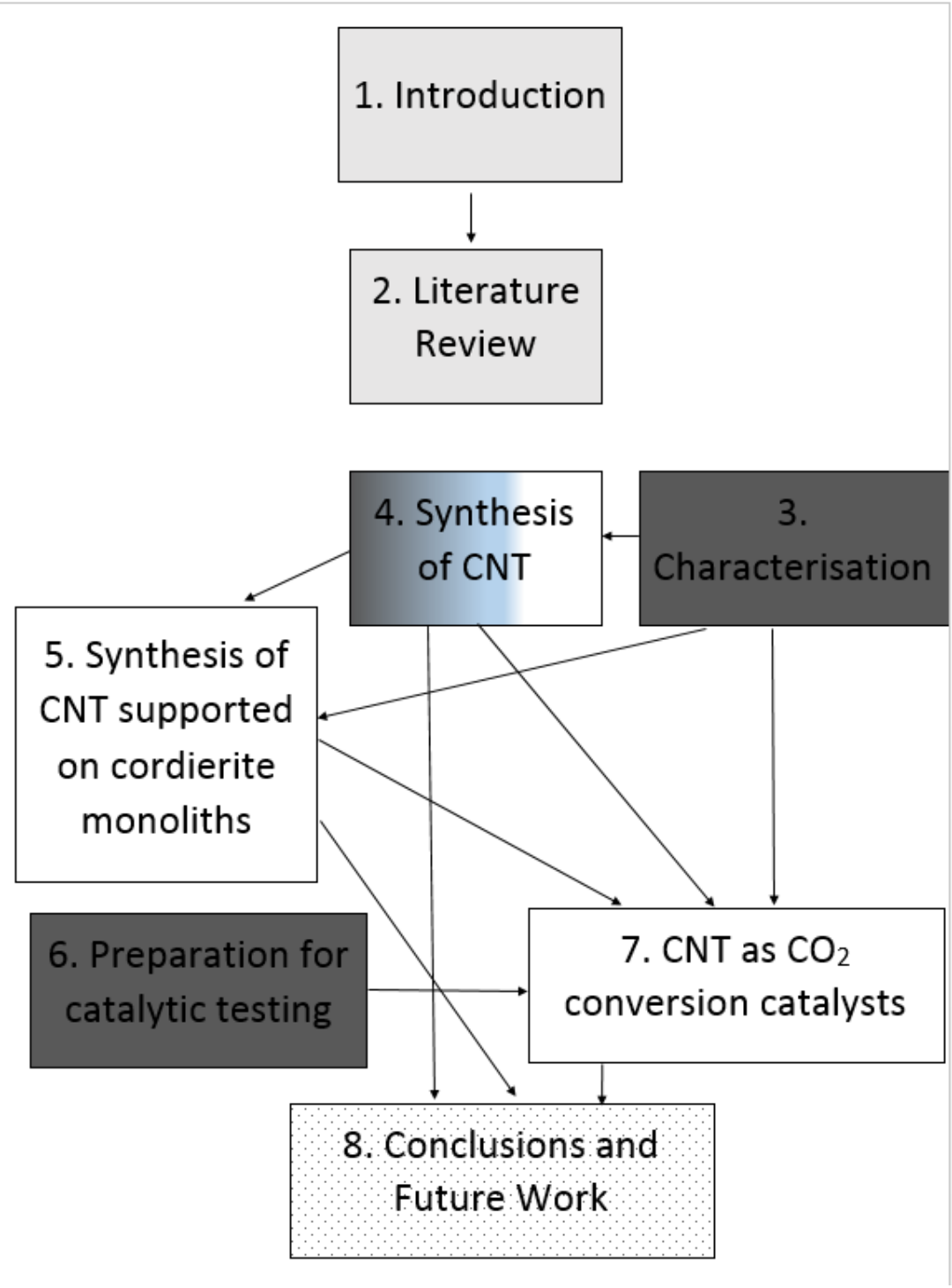

Figure 1.7 Diagram showing the links between the research activities performed in this thesis, and their associated chapters ( ) indicates assessment of the literature ( ) indicates experimental methods ( ) indicates results and discussion

2 Literature Review

In this literature review a number of key topics will be outlined which relate to the proposed research topic, the review will concentrate on two main topics, the growth of carbon nanostructures, particularly on the synthesis methods used, and attempts to grow structured CNT supports for use in catalysis. The second area looked at will be attempts to catalytically convert carbon dioxide into hydrocarbons, with a particular focus on the use of Fischer Tropsch catalysts. The review highlights some of the promising work performed using CNT supports in Fischer Tropsch catalysis.

2.1 Synthesis of Carbon Nanotubes and Nano-fibres

2.1.1 Carbon Nanotubes and Carbon Nano-fibres

Carbon fibres come in a number of different forms. These include the well-known single wall carbon nanotube (SWCNT), which is a single cylinder of graphitic carbon, and multi wall carbon nanotube (MWCNT), consisting of multiple cylinders of graphitic carbon wrapped around each other. Also found are carbon nanofibres (CNF), which are distinguished from nanotubes by the lack of a hollow core, these come in two main forms known as parallel or platelet, consisting of stacked graphitic plates, and herringbone or fishbone fibres, consisting of stacked angular plates of carbon. [55,56] In this review we will concentrate on the production of MWCNT, rather than other graphitic fibres, as these have shown to be particularly interesting for FT catalysis.[57]

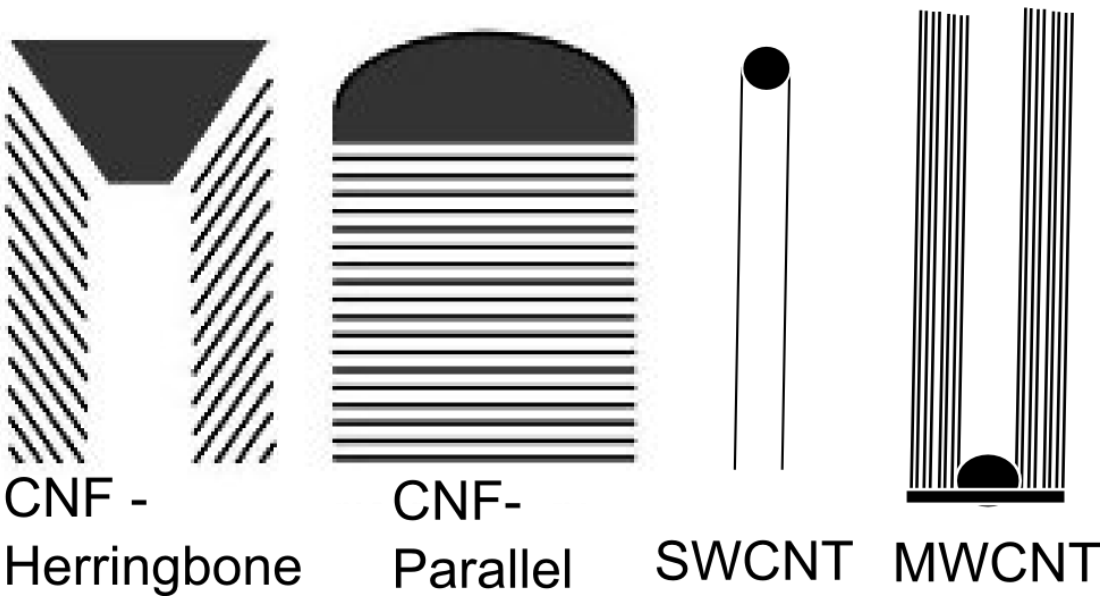

Figure 2.1 Different types of carbon nano structures [55]

Carbon nanotube (CNT) synthesis is a widely explored area. Since Iijima *et al.* published images of single wall carbon nanotubes, [58] and brought CNTs to popular attention a large body of research has been performed with over 222,000 papers found in a search for the term carbon nanotube on Web of Knowledge on 26/10/13. Carbon nanotubes have electrical, optical, magnetic, mechanical, thermal, electrochemical and biochemical properties, which make them interesting materials for a wide variety of applications. [59] A full exploration of the cause of these properties is beyond the scope of this thesis (the reader is referred to: Carbon nanotubes and related structures : New materials for the twenty-first century by Peter Harris [60] for a good introduction to the topic of carbon nanotubes). Potential applications range from bio-medical sensors, [61] composite reinforcements, [62] and as membrane materials. [63]

Many of the same characteristics that make CNTs attractive for the applications described above, such as the intrinsic porosity, resistance to acids and bases at room temperature, controllable synthesis and properties, and ease of metal recovery at end of lifetime, make them ideal candidates for catalyst supports. [55]

Carbon nanotubes can be synthesised by a number of methods. These include arc-discharge, [58] laser ablation, [64] and chemical vapour deposition methods. [65,66] Large scale synthesis of well defined, pure carbon nanotubes is still a challenge. Whilst arc-discharge and laser ablation have proved successful at the lab scale for synthesising carbon nanotubes with desired characteristics, the availability of raw materials and ability to scale up the process is limited. CVD is much easier to scale up to give a commercial processes, a number of processes already exist which produce CNTs on a large scale, but work still needs to be done in order to increase carbon yield and reduce variations in the CNT properties.[67] Global CNT production has been expanding significantly, with an expansion of more than 10 times between 2006 and 2011. Exact figures for CNT production capacity are hard to come by, but estimated production is estimated to be around 4.5 kilotons a year in 2011.[68] A number of processes capable of producing CNTs at the rate of kg/hr, have been developed. To date there seems to be an oversupply of CNTs as perhaps indicated by major player BASF (200 tonnes/year) exiting the CNT market in 2013.[69] Other major producers such as Showa Denko (200 tonnes/year) and Nanocyl (400 tonnes/year) remain in the market.[69,70] The costs of MWCNT and SWCNT vary dramatically, but MWCNT can be obtained for less than £75/g (Sigma Aldrich, 11/10/13), whilst SWCNT are about 10 times as expensive being obtainable for around £700/g (Sigma Aldrich, 11/10/13). The cost of CNT is highly dependent on the purity, with many of the large scale production processes requiring costly thermal annealing or chemical treatments to purify the produced nanotubes. [68]

Chemical vapour deposition methods are split into two general forms, catalytic and non-catalytic processes. Here the focus will be on the catalytic synthesis of carbon nanotubes. [67,71,72]

2.1.2 Chemical Vapour Deposition

Synthesis of carbon nanotubes by catalytic chemical vapour deposition can be performed in a number of ways, but follow two basic methods [73-75] : The first method involves pre-coating a substrate with a metal particle which will then catalyse the growth of carbon nanotubes, and then place it in a reactor where a reactant stream containing a mix of a carbon source and hydrogen is flowed over the substrate at high temperature in an oxygen-free atmosphere. Carbon nanotubes then grow on the prepared substrate. [76-78]

The alternative method avoids the pre-coating step by depositing the catalyst onto the substrate during the reaction, along with the carbon source. Typically a metallo-organic species such as ferrocene, cobaltocene or nickelocene is used as the catalyst. [79] This method has the advantage of avoiding the pre-preparation step, but with the corresponding disadvantages of having less control over where the catalyst species, will deposit, and the size of the resulting nanoparticles, which will affect the nanotube properties, as will be discussed later. [59]

This study will use a variation of the second approach, the floating catalyst continuous chemical vapour deposition (cCVD) method, in which a catalyst is flowed over the substrate in a tubular reactor, placed in a furnace. The catalyst precursor and feedstock are flowed through the reactor in an inert atmosphere, at temperatures ranging from 600 °C to 1200 °C. [80,81] As the catalyst precursor passes through the reactor it will decompose and deposit on the substrate, forming a nanoparticle which acts as a catalyst. Deposition of the carbon source onto the catalyst leads to the formation of carbon nanotubes. This method was first developed by the Dresselhaus group, [80] and has been widely improved on since. [59,82,83]

Many of these methods vary in the way the catalyst precursor and the carbon source are introduced into the reactor. In the method first developed by Dresselhaus *et al*. [80] the catalyst precursor, ferrocene, is sublimated, and then a gaseous carbon source is flowed over the substrate. This is conceptually similar to methods where the catalyst precursor is pre-deposited on a support before having a gaseous carbon source flowed over it. An example of a typical set-up for this synthesis method is shown in Figure 2.2 .

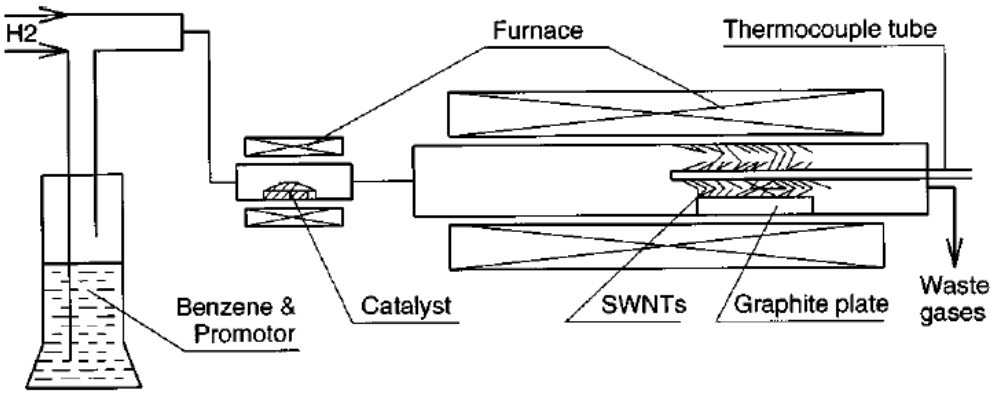

Figure 2.2 Example of floating CVD apparatus [80]

The main other methods involve the introduction of a mix of both the carbon source and the catalyst source at the same time. Two major methods to do this have been developed, the first, known as injection chemical vapour deposition, introduces the solution of catalyst precursor and carbon source into the reactor by injecting into the reactor using a syringe. This method was first developed by Andrews *et al.* [84]. An example of a typical injection CVD apparatus is shown in Figure 2.3 .

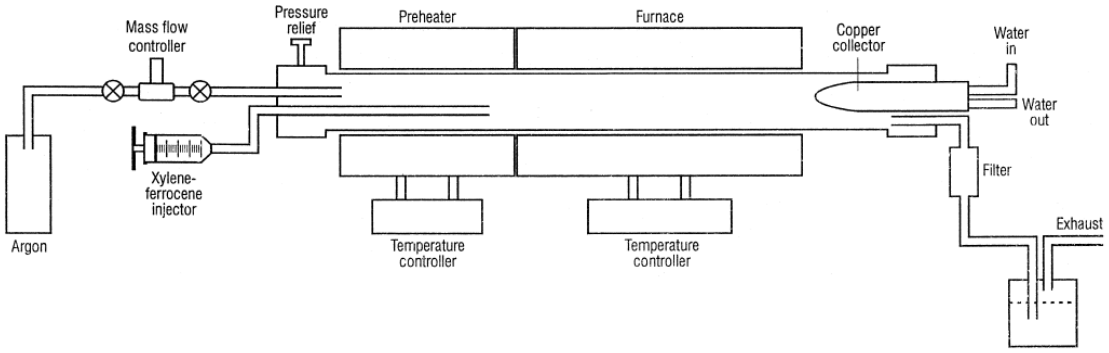

Figure 2.3 Example of Injection CVD apparatus [84]

The other major method is the aerosol assisted CVD method (AACVD), where the solution of catalyst precursor and carbon source is aerosolised before being introduced into the reactor. This method was first developed by Mayne *et al.* [85]. A typical example of the aerosol CVD apparatus is shown in Figure 2.4 .

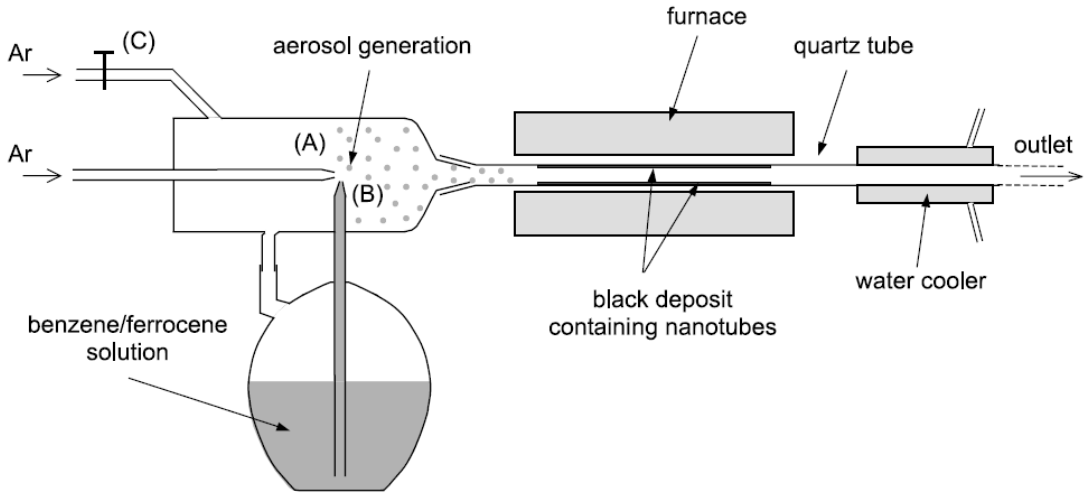

Figure 2.4 Example of aerosol formation apparatus [85]

These last two methods have the advantage of controlling the dosage of ferrocene and carbon/hydrogen feedstock into the reactor, compared to methods utilising a gas carbon source which vaporises the ferrocene in order to introduce it into the reactor system. [66] Since the vaporisation of ferrocene is difficult to control without a separate temperature controlled furnace, the aerosol and injection style reactors allow better control of ferrocene introduction to the reactor, without the need for an additional furnace.

cCVD has been performed with a wide variety of catalysts, carbon and hydrogen precursors, temperatures, and substrates. [66,79,80,82,83,85,86] Table 2.1 gives some indication of the wide range of synthesis conditions used in this process for the ferrocene catalyst. Together these studies have allowed the identification of key factors which play a role in the successful growth of CNT. These include the temperature, size of the catalyst nanoparticles, the carbon source, substrate, flow rate of gas and synthesis time. [87]

Temperature is an important factor in carbon nanotube synthesis, however the optimal temperature for synthesis will vary depending on the catalysts used, the support and the carbon source, as such there is no universal optimal temperature. [87] Singh *et al.* achieved optimal growth of CNT on a quartz substrate using toluene as a carbon source and ferrocene as a catalyst precursor at a temperature of 760 °C using an injection based method. [88] Pinault *et al.* however have reported better synthesis of CNT at temperatures of 850 °C using an aerosol based method using the same support, carbon source and substrate. [66] Optimal temperature conditions will vary dependant on the experimental method, carbon source and

Table 2.1 Variety of feedstocks and operating conditions reported for synthesis of CNT

Reference	Carbon Source	Amount of catalyst	Substrate	Flowrate	Type of Nanotubes	Temperature °C	Time
Liu, H [83]	Ethene	100 mg	SiO_2/Si	500 sccm Ar, 10 sccm ethene	MWCNT	850	5 min
Liu, H [83]	Ethene	100 mg	SiO_2/Al/Si	500 sccm Ar, 10 sccm ethene	MWCNT	850	5 min
Ci, L [81]	Ethyne	Unreported	Quartz tube wall	1200 sccm Ar, 8 sccm ethyne	Unreported	900-1200	Unreported
Lee, Y [82]	Ethyne	0.1 g	Quartz tube wall	500 sccm Ar 10 sccm ethyne	Unreported	1: 150 2:700-1000	5 min
Ionescu, M [59]	Ethene	100 mg	Silicon wafer	Ar 90% H_2 5% ethyne 5%	MWCNT	600-1000	10 min
Cheng, H [80]	Benzene	Unreported	Graphite plate/tube wall	70-90 and 150-225 sccm H_2	SWCNT	1100-1200	1-30 min
Zhang, Z [89]	Xylene	Unreported	SiO_2/Si	Unreported	Unreported	800	Unreported
Mayne, M [85]	Benzene	2.5-5wt%	Quartz tube wall	2000 sccm Ar	Unreported	800-950	15 min
Hou, H [86]	Anthracene	1 g 1:1-7 ratio to a	SiO_2/Si	300-400 sccm H_2	MWCNT	580-700	Unreported
Hou, H [86]	Dibromo-anthracene	0.5 g 1:1 ratio	SiO_2/Si	400 sccm Ar	MWCNT	1: 400 2:1000-1100	Unreported
Singh, C	Toluene	9.6 wt.%	Quartz	750 sccm 10% H_2 90%Ar	MWCNT	700-850	60 min
Pinault, M [66]	Toluene	5 wt.%	SiO_2/Si	400 sccm	MWCNT	800-850	15 min
McKee, G [90]	Benzene	4.7 g/litre	Varied	100 sccm	MWCNT	750	5-240 min
Meysami, S	Toluene	5 wt.%	Quartz	1000 sccm	Mwcnt	800	15 min

substrate which will inevitably change other factors such as size of catalyst nanoparticle and flow rate. [75]

The size of the catalyst nanoparticles formed plays a significant role in the formation and structure of CNTs. Correlation between the size of the outer-diameter of CNTs and the diameter of nanoparticle catalysts has been observed. [91,92] Though nanoparticle size may very over the course of a reaction, *in situ* TEM studies have shown that during synthesis a pear shaped nanoparticle is formed, with the bottom outer diameter corresponding to the outer diameter of the CNT, and the smaller top corresponding to the inner diameter. [93]

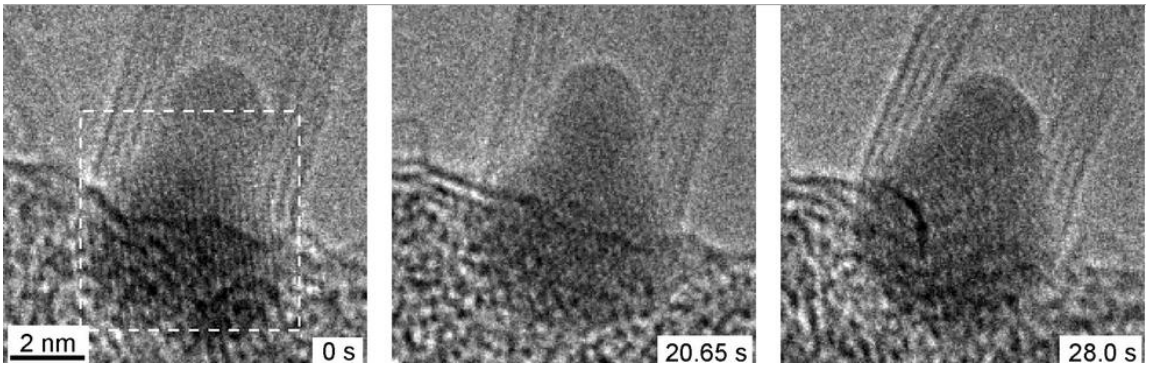

Figure 2.5 *In situ* ETEM microscopy of the growth of a catalyst from a fluctuating nanoparticle of $(Fe,Mo)_{23}C_6$ structure[93]

Smaller particles are more active for the growth of CNTs, and sintering of nanoparticles leading to large nanoparticles can stop nanotube growth. [56] Several modelling studies have also demonstrated that nanoparticle size will change over the length of the reactor, dependant on temperature, flow-rate and position in the reactor. [94,95]

A large number of metallic catalysts have been reported for the CNT synthesis, with many different transition metals and mixtures of transition metals shown to be active catalyst.[78] The most important factors which influence CNT growth are still debated,[78] however some key properties can be identified including the diffusion of carbon through the metal, and the affinity of the metal to carbon, and hence the strength of the bonding. For injection based CVD; ferrocene, nickelocene and cobaltocene have mainly been used, but any precursor containing an active metal which decomposes under CVD conditions could be used. Of these catalysts ferrocene is most used, due to its high activity and stability in air. Of the pure metal catalyst iron is generally the most active; however in some cases combined catalysts are more active than one metal alone. [96] Changing the substituent attached to the ferrocene ring also has some effect on the CNTs formed. Growth of nanotubes can be slowed or stopped by adding inhibitors such as

iodine, bromine and oxygen containing species. [97-99] The addition of substituent groups to ferrocene can lead to smaller nanoparticles, though the reason for this has not been determined, with a number of potential causes being investigated. [97]

A number of different liquid phase hydrocarbons have been used for synthesis of CNT, a majority of early studies in this area have used benzene[85] or xylene [65] as a carbon source. Many recent studies have used toluene as a precursor instead of benzene due to its similar effectiveness as a carbon source and significantly lower toxicity. [100-103] A systematic study of different carbon sources using the AACVD method, has found that the most effective carbon source in terms of carbon nanotubes produced was ethylbenzene with a precursor conversion yield of 38.2 ± 8.5%, compared to toluene with a precursor conversion yield of 21.2± 5.9% and benzene with a precursor conversion yield of 16.6± 2.4%. [104] The second most active carbon source was isopropylbenzene with a precursor conversion yield of 27.4 ± 6.6%, this was noted as being the cheapest of the carbon sources used, with high potential for cost effective CVD. [104] Other groups have used a number of naturally derived precursors such as camphor, [105] palm oil,[106] and turpentine[107] with some success.

A high flow rate is used for most CNT synthesis applications, with total flow rates of over 500 sccm being typical (Table 2.1). This high flow rate aids synthesis by diluting the concentration of the carbon source,[78] which reduces the number of walls formed on a catalyst. Hydrogen is sometimes used as a diluent in the gas stream (Table 2.1). When oxidic nanoparticles are used as a catalyst, hydrogen is used to reduce them to metallic iron which can catalyse the formation of carbon nanotubes. [108] It also inhibits the growth of other amorphous carbon structures. [109] Other gases which have been introduced into the gas stream include water,[110] and carbon dioxide[111] these both promote CNT growth, acting as weak oxidising agents to remove amorphous carbon upon formation.

Several different substrates have been used in the literature. The majority of substrates used by these papers are some variant of silicon, [59] silicon dioxide (quartz), [86] or silica [112] but the use of carbon, [80] zeolites, [77,113] alumina [114] and wash-coated cordierite monoliths [115,116] have also been reported as supports for CNT growth. As a key component in electronics, CNT grown on silicon are of great interest. Often however silicon can react with the catalyst and deactivate it, preventing nanotube growth. [117] As a result silicon wafers coated with thermal silicon dioxide, [86] or silicon wafers coated with silicon dioxide and alumina [83] are commonly used instead.

Interactions between the catalyst particle and the substrate can change the properties of the catalyst particles, and its resulting activity.[78] The interaction between a metal catalyst particle and a support, can affect the electronic interactions, atomic diffusion, and allow the formation of alloys.[78] In particular on the common nanotube growth support silicides which are much less active are commonly formed. Strong interactions between nanoparticle and support can also affect the melting point[78] and reducibility of the nanoparticle.[118]

The ability of the metal nanoparticle to act as a catalyst, can change with temperature. In particular, it has been reported that above 800 °C deposition occurred preferentially on silicon oxide rather than silicon. [89] Experiments using cyclohexene and ferrocene as carbon source and catalyst, respectively, showed that the substrate selectivity varies with temperature with selective growth only occurring in a small temperature range between 770 and 800 °C. [119] Simultaneous growth was obtained on all substrates (silicon, silicon/silicon dioxide wafers, and pure silicon dioxide) at temperatures between 700 and 770 °C, whereas growth occurred only on pure silicon dioxide at temperatures of 800 °C and above, with no growth below 700 °C.

This conflicts somewhat with other literature reports, in which CNT's have been grown on Si/SiO_2 wafers at temperatures of 850 °C [120]. This apparent discrepancy is likely due to the thickness of the silicon dioxide layer used. Xiang *et al.* [119] used a silicon dioxide layer only 50 nm thick, whereas Liu et al and others use much thicker silicon dioxide layers of 300 nm and above. [66,83,89] Xiang *et al.* [119] suggest that the inactivity of the iron catalyst above 800 °C is due to the catalyst diffusion through the silicon dioxide layer and reaction with silicon, forming inactive $FeSi_2$ or $FeSiO_4$. A thicker buffer layer will increase the length of time necessary for iron to diffuse through the silicon dioxide layer and so the substrate will remain active for longer.

It is important to note that the synthesis of CNT depends not only on parameters previously discussed, but also on the position in the reactor of the substrate, [121] though this is commonly neglected in reports of CNT growth[100,101,103]. Castro *et al.* highlight the importance of an isothermal zone for the synthesis of CNT, as would be expected, [102] but Meysami *et al.* highlight the changes in carbon nanotube properties and morphology observed across a reactor even with a uniform temperature gradient. [121] It was noted that these differences were mainly caused by the inhomogeneity of temperature and catalyst concentration in the reactor. As the catalyst is consumed, the concentration decreases along the reactor changing the properties of the carbon structure formed as a result.

2.1.3 CNT growth mechanism

The mechanism for nanotube growth is an area of much research. A number of growth mechanisms have been proposed. One mechanism popular in the literature is the vapour-liquid solid (VLS) mechanism (Figure 2.6 a-c), in which a carbon precursor breaks down on the surface of the catalyst particle, and then diffuses through the catalyst particle and precipitates to form the nanotube or nanofiber around the nanoparticles. [122] Other workers have suggested an alternative mechanism in which this diffusion only takes place on the surface of the nanoparticles, a vapour-solid-solid (VSS) mechanism, as diffusion through the bulk phase is improbable in a solid nanoparticle (Figure 2.6 d-e). [123] Both these mechanisms can either involve base-growth, where the nanoparticles remains embedded in the surface and the nanotube grows up from here, or tip growth in which the nanoparticles remains at the tip of the tube as it grows. [124] The state of the metal nanoparticle as liquid or solid is a matter of controversy, [78] in-situ TEM observations have shown that the iron nanoparticles formed although highly deformable are still crystalline during growth. [125] However the wide range of materials used suggests that some particles may be liquid, whilst others solid under standard growth conditions. [78]

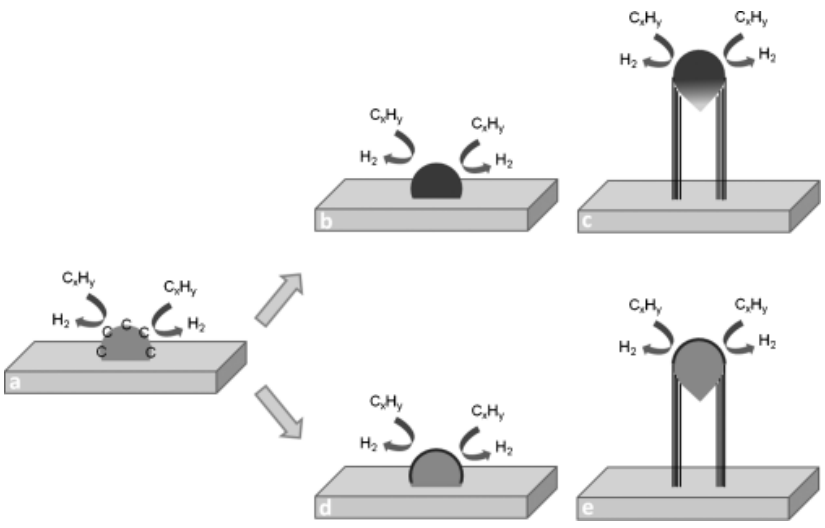

Figure 2.6 The three steps involved in the Vapour-Liquid-Solid (VLS) mechanism: a) decomposition of the carbon-containing precursor on the surface of the catalyst particle; b) diffusion of carbon atoms through the particle as a solid solution; and c) precipitation of carbon at the metal-support interface and formation of a nanofiber or a nanotube. In an alternative mechanism, carbon species diffuse only on the surface of the catalyst particle (d–e). [122]

It has long been noted that increasing the time for CNT synthesis, results in longer CNT over time. It has also been noted that this effect tends to decrease over time though the mechanism for

deactivation is a matter of debate. Initial work on this problem has favoured the suggestion that deactivation of the catalyst is due to the thickness of the carbon layer preventing diffusion of the carbon source through the CNT to the catalyst, and assuming a base growth mechanism was followed stopping growth. [126] Comparison between the square root diffusion law and the observed growth gave a good correlation supporting this theory. Other explanations for the catalyst deactivation in various synthesis methods include the deposition of amorphous carbon around the catalyst particles [127], a phase change in the iron catalyst [128], or migration of the catalyst into the substrate[129]. A more recent study has found that the activity of the catalyst can be recovered if injection of ferrocene is stopped, but the injection of toluene continues. [101] This suggests that the deactivation mechanism cannot involve the thicker catalyst bed inhibiting the diffusion of the carbon source to the catalyst. Two deactivation mechanisms are best supported by this study, one is that with continuous addition of iron to the mixture the iron catalyst particles continue to grow, eventually diffusion of the carbon through the iron nanoparticle slows the rate of reaction eventually leading to termination. [101] Another possible cause is the build-up of a layer of amorphous carbon at the base of the CNT, this eventually covers the catalyst particle, preventing the carbon source reach the catalyst and terminating the reaction. [101]

2.1.4 CO_2 as a feedstock for CNT production

Recently some developments have been made in the use of CO_2 as a carbon feedstock for the production of CNTs. [130] Xu *et al.*[131] report the successful growth of CNTs using CO_2 as a carbon feedstock, and a Fe/CaO catalyst. Attempts at using more common supports such as Al_2O_3, SiO_2 and MgO resulted in no nanotubes being produced. CNTs were generated in a narrow temperature range between 790 and 810 °C, and yields were low. The exact mechanism of this process is unknown. It is known that carbon monoxide can produce carbon nanotubes under pressure in the presence of an iron catalyst.[132] Since iron catalysts are capable of converting carbon dioxide into carbon monoxide (a known carbon source for CNT growth) via the reverse water gas shift reaction, this catalysis may play a role. A more successful attempt to grow carbon nanotubes from CO_2 was achieved recently through a two-step process. [133] In this work carbon dioxide was first converted to methane and water using a nickel methanation catalyst. Water was removed using a desiccant, in this case silica gel, the resulting methane was then used to synthesise CNT using the standard CVD process over a nickel catalyst. This led to yields of CNT from CO_2 of over 30%. [133] These results are significantly better than those achieved using a one-step process, likely due to the removal of water *in situ.* The formation of two moles of water for

each carbon atom liberated will inevitably be a significant barrier to the conversion of CO_2 to CNT in one-step, as the build-up of steam at high temperatures could decompose the formed nanotubes.[134] Further advances in this area could lead to the production of sustainable CNT from CO_2, economic calculations performed by Chu *et al.* [133] indicate that this process could conceivably offset most of the cost of CO_2 capture by sale of CNT, though the impact of increased quantities of CNT being produced have not been assessed.

2.2 Carbon nanotube health concerns

The potential health impacts of CNTs have long been a source of concern. The similarity of CNTs structure to asbestos has meant that CNTs have long been regarded as a potential cause of lung disease. [135] As a new nano-material the effect of release of CNTs into the environment must also be considered.

Reports on CNT toxicity in the literature have often been conflicting due to the relative difficulty in standardising the CNTs used. [136] The structure and functionality of the CNTs can have a profound effect on the resulting toxic behaviour. Long CNTs have been shown to cause asbestos like symptoms in animal models. [137] However recent studies have shown that by shortening or functionalising long CNTs, these toxic effects are not observed. [138,139] Further studies are needed to determine the long term impact of CNTs on human health, but it appears that provided the CNTs are treated correctly health impacts can be minimised. The use of long carbon nanotubes is still considered to be potentially hazardous and especially inhalation of nanotubes is to be avoided. [140] It is important to note that residual catalyst nanoparticles can contribute significantly to the toxicity of the nanotubes.[141] It is known that iron nanoparticles on carbon have significant inflammatory response, and can generate hydroxyl radicals.[142] Some studies however have shown that encapsulated CNT are non-toxic, with the iron remaining contained within the graphitic coating,[143] but others disagree.[141] These results suggest that residual catalyst can be a problem, but it depends on the biological system and the synthesis conditions of the CNT.

2.3 Advantages and disadvantages of catalysis using carbon nanotubes

2.3.1 Carbon nanotubes and nanofibers as catalyst supports

As previously mentioned carbon nanotubes and nanofibers have several properties that make them attractive as catalysts in a number of different applications. By controlling the synthesis of carbon nanostructures, it is possible to obtain high surface area supports, with a relatively uniform pore structure, and controllable surface chemistry of the CNTs.[55,56]

Carbon structures are also resistant to acids and bases, making them potential catalysts in reactions that involve acidic or basic conditions. [56] CNTs are combustible allowing there use as precious metal supports more viable, as the metal can be recovered once the catalyst deactivates or is no longer needed. [55]

Carbon nanotubes have a sp2 carbon structure, allowing them to act as efficient conductors (though this can be significantly affected by defects in the nanotube structure). Binding of metal nanoparticles to MWCNT can have significant electronic effects on the nanoparticle, dependant on the defect structure of the support, and the curvature of the support.[55] Computational studies have shown that nickel bound to a nanotube wall can demonstrate significant variations in magnetic moment and the charge transfer direction between nickel and carbon can be reversed.[144] The differences between a nanotubes outer surface and inner surface can have implications on the reducibility of catalysts, with very different behaviours inside a nanotube compared to outside.[145]

The mechanical and thermal properties of CNTs are also interesting, with high strength, thermal conductivity and thermal stability. Like graphite and diamonds, carbon nanotubes also display high thermal conductivity, with the thermal conductivity of SWNT at room temperature being 6600 W/m K. [55] Studies of the thermal stability of CNT show that they are fairly stable at high temperatures, though this stability depends both on the structure of the CNT, and the amount of remnant catalyst present in the structure (Table 2.2). Purified CNT have higher stability than activated carbons. This stability allows them to be used as catalyst supports even in high temperature reactions. [55]

Table 2.2 Approximate thermal stability of different forms of carbon in air[55]

Type of Carbon	Thermal resistance in air atmosphere (°C)
SWCNT	~800
MWCNT	~650
CNF	~600-900
Activated Carbon	~500-600
Graphite	~800

The physical, electronic, mechanical and thermal properties of CNTs make them very interesting materials for a wide variety of catalysis. There are however some issues in using carbon nanotubes as catalyst supports. Carbon nanotubes are still fairly expensive in comparison to traditional alternatives such as alumina, silica and activated carbon (though the price of CNTs is expected to continue to fall, as production increases). [67] Therefore carbon nanotubes must show significant improvements over cheaper supports in order to be viable for catalysis. Secondly, CNTs as produced require extensive pre-treatment before they can be used for catalysis, to remove residual catalyst particles.[67] Commonly the CNTs must are also pre-treated in order to deposit the catalyst particles. Finally CNT powders can be difficult to handle in traditional catalytic reactor designs, as the fine powder nature of the CNTs is difficult to incorporate without high pressure drop. Utilising CNT powder in reactors would also make it likely for clouds of CNT to be formed, which, due to the concerns relating to CNTs effect on long term health (see section 2.2) could prove a barrier for implementation in large scale catalysis.

2.3.2 Residual catalyst particles in carbon nanotubes

Synthesising CNTs commonly uses a metal catalyst. This metal catalyst will usually remain either at the tip of the carbon nanotube or the base of the carbon nanotube unless deliberately removed. Additionally many synthesis methods such as the injection and aerosol methods involve continuous injection of catalyst. These methods result in not only catalyst particles at the tip and base of the CNT, but also catalyst deposited in the core of the nanotube and on the surface of the carbon nanotube. In these cases the deposited particles are typically covered with a thin layer of graphitic carbon.[100,101]

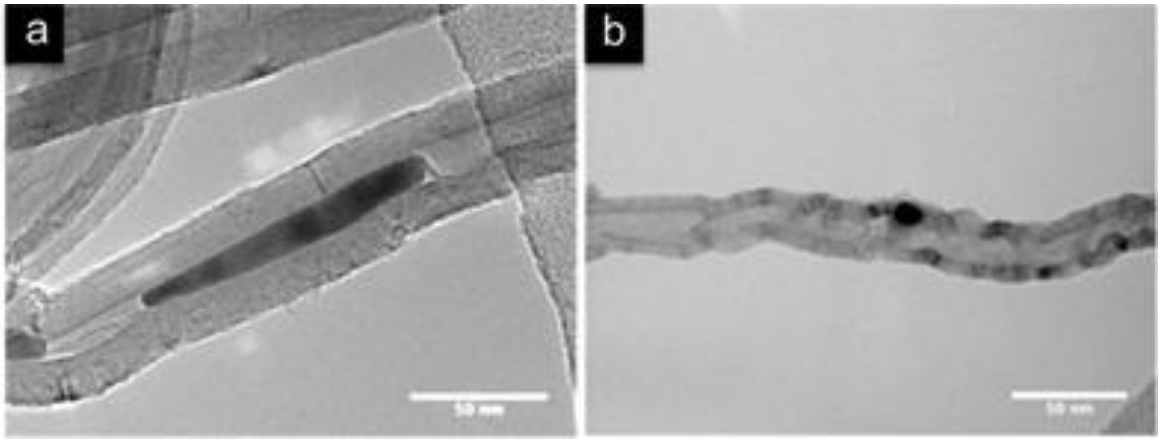

Figure 2.7 a) an iron catalyst particle that has been pulled into the tube during growth and b) a catalyst nanoparticle on the surface of the tube[101]

Residual nanoparticles have been noted in a wide variety of studies, and the presence of these nanoparticles has been used for a number of different purposes. Reduced iron nanoparticles embedded in the catalyst walls has been demonstrated to have ferromagnetic activity.[146] The magnetic nanoparticles have biomedical applications in drug delivery, biosensors and biological separation, as well as lithium ion batteries, data storage devices and catalysis. [147] The effects of residual metal is also acknowledged in electrochemistry, where ppm levels of residual nanoparticles are observed to dominate electro-chemical activity. [148]

Residual catalyst nanoparticles have been reported to have some catalytic activity. In most cases CNT are purified using an acidic treatment prior to use in catalysis (and indeed prior to sale), in order to eliminate the effect of residual nanoparticles on catalysis. This acidic treatment will not necessarily remove all iron nanoparticles as has previously been reported.[149]

Van de Vyver *et al.* have reported that residual nickel nanoparticles on carbon nanofibres have catalytic activity for the hydrogenation of cellulose, he also notes the presence of graphene layers which partially inhibit access to the metal nanoparticle. [150,151] Bahome also reports that residual nickel nanoparticles on carbon nanofibers had some activity in the Fischer Tropsch reaction, producing predominantly methane. [152] In the same study, residual iron nanoparticles are reported to be inactive for CO_2 conversion. Zhang *et al*, report the use of residual iron and cobalt particles in commercial CNTs as catalysts for NH_3 decomposition at temperatures over 700 °C, with no additional pre-treatment required. [153] In the cases of Bahome *et al*, the CNT have been acid treated, this could open the tubes and give limited access to nanoparticles within the tube explaining the activity. In the case of Zhang *et al,* the commercial catalysts will have been treated to remove impurities, coupled with the corrosive conditions of NH_3 decomposition this may remove the graphitic layer giving access to the catalytic species. In these studies no mention is made of the graphitic layer and its inhibiting effect on catalysis.

2.3.3 Depositing catalysts on a carbon nanotube support

Attaching a catalyst to a carbon nanotubes can be done in a number of ways, with methods published in the literature including simple impregnation,[55] ion-exchange,[55] deposition/precipitation, [154-156] and tethering the catalyst to a specifically created functional group linker. [157,158]

The surface of the carbon nanotubes is often modified in order to better control the deposition of the catalyst. This is done via two distinct routes, modifying the surface to create defects which metals can deposit in, or by tethering a homogeneous catalyst to a surface group on the carbon

nanotube. [159] In both cases the nanotubes are commonly oxidised using an oxidising agent at temperature (60-100 °C), for example nitric acid, to create surface groups such as carboxylic acid. [160] These groups can interact with a chemical tether, or form a defect site for nanoparticle growth on the nanotubes.[55]

Deposition of metal nanoparticles on the surface of carbon nanotubes has been achieved for a variety of metals, including cobalt, [161] copper, [155] gold, [154] iridium, [162] iron, [55] manganese, [163] palladium, [154] platinum, [154] rhodium, [164] ruthenium, [156] and silver, [154] among others, via impregnation of the carbon nanotube with an appropriate metallic salt. Reactions with metallic salts such as nitrates and chlorides have resulted in highly dispersed metal nanoparticles deposited on the surface of the CNT, improved size control of the deposited nanoparticles can be achieved by using functionalised nanotubes. [55]

2.3.4 Preparing structured carbon nanotube supports

As has been shown CNTs and CNFs have shown promise as catalyst supports with their structure yielding improved catalytic activity and selectivity. [55] However, these fine and light powders can be difficult to handle. In order to utilise these powders in industrial scale reactors, they must be compressed and extruded into a new structure in a multi-step process. [165] Preparing a structured support directly would be a significant improvement.

Structured catalyst supports such as monoliths have clear advantages over traditional powder catalysts when used in large-scale reactors, [166] including lower pressure drop and better control of heat and gas flow, giving uniform flow distributions and residence times, [167,168] along with the typical advantage of heterogeneous catalysts - no need to separate the catalyst from the products. [168] Monoliths are typically made of ceramics, metals or carbon and contain small diameter (0.5-4 mm), uniform channels. [168] Ceramic monoliths such as cordierite (a ceramic material consisting of magnesia, silica, and alumina in the ratio of 2:5:2), are commonly used in catalytic converters as the support material.[166] As well as catalytic converters, monolithic reactors have been used in a range of reactions, including NOx conversion with ammonia for large-scale applications, [169,170] the Fischer-Tropsch process, [171,172] synthesis of hydrogen from ammonia, [173] hydrogenation of unsaturated bonds in a number of species, [174] steam methane reforming [175] and biodiesel synthesis. [176]

A major limitation of non-porous monoliths as catalyst supports is their very low surface area, with a typical bare cordierite monolith having a surface area of around 0.7 m^2g^{-1}. [166] As such they cannot compete with supports with large surface areas such as alumina or zeolite powders. In

order to overcome this problem, monoliths are coated with a thin layer of a high surface area material to allow higher loadings of catalyst onto the support. Commonly, an alumina or silica slurry coating is applied onto the monolith, with the increase in surface area dependant on the thickness of the applied wash-coat, resulting in values of up to 15-30 m^2g^{-1} for 0.1-50 μm thick coatings. [115,177] Achieving a uniform wash-coat on a large scale can be challenging. [177] Other attempts to increase the surface area of monoliths have involved coating the monolith with activated carbons. [178,179]

To further increase the surface area of wash-coated cordierite, CNTs and CNFs have been grown. [115,180,181] Carbon layers grown in this way have been shown to double the surface area of the wash-coated monoliths. [115] Coating a monolith with CNTs/CNFs offers a safer and more practical solution to the issues affecting powder CNTs, providing a CNT support with lower pressure drop directly upon synthesis without the necessity of subsequent treatment whilst the adhesion between the monolith surface and the CNTs makes it unlikely that the CNTs will become airborne. [182]

Typically, CNTs/CNFs are grown on washcoated monoliths via catalytic chemical vapour deposition (cCVD). This process requires pre-treatment of the monolith (after wash-coating with alumina) consisting of the impregnation with a catalyst, usually iron-, cobalt- or nickel-based, to initiate growth of the carbon layer. [115,182,183] Other attempts have involved using a TiO_2 washcoat [184] and a Cu-Ni catalyst. [185] CNT synthesis is usually performed using the CVD method with ethane or methane as a carbon source. To the author's knowledge no growth of CNTs on monolith has been tried with the more advanced injection and aerosol based methods discussed previously.

The thickness of the alumina wash-coat layer was found to be an important factor in the growth of the CNF layer. If the alumina layer was less than 0.1 μm, the distribution of the alumina wash-coat was non-uniform, and growth of the carbon layer was similarly uneven. [115] When the alumina layer was thicker (~17 μm) the thickness of the CNF layer grown was smaller, suggesting that some of the CNFs were embedded within the porous alumina. [181] Further studies have shown that a thin wash-coat is considered desirable for the growth of the CNF layers, with a 0.1 μm thick alumina layer being reported as optimal. [115] Even under these optimal conditions, the CNF layers produced are thin and poorly aligned. [115,180] Other groups have reported being able to achieve growth using the low surface area bare cordierite without alumina coating using a cobalt catalyst, an a vacuum impregnation step. [182] When tested as catalytic supports, activity is reported as significantly higher with this activity increasing in relation to surface area. [173]

The use of acid treatments (e.g. 8h reflux under HNO_3) to functionalise and clean the nanotubes has been reported to enbrittle the monoliths, caused by leeching of Mg and Al present in the cordierite. Shorter refluxing times however yielded structurally stable monoliths with functionalised pure nanotubes. [186]

2.4 Reverse Water Gas Shift and Water Gas Shift catalysis

The water gas shift reaction, or the conversion of carbon monoxide and water (known as water gas) into hydrogen and carbon dioxide as in equation 2.1, has been used industrially to produce hydrogen for processes such as the Fischer Tropsch process and the Haber process for the last century.

$$CO + H_2O \rightleftharpoons CO_2 + H_2 \qquad (2.1)$$

There are three major types of water gas shift catalyst currently in use, iron-promoted catalysts (typically Fe_2O_3/Cr_2O_3) which operate at high temperatures (350 - 450 °C), copper-zinc oxide catalysts (typically $Cu/ZnO/Al_2O_3$) which operate at low temperatures (190 – 250 °C) and sulphur tolerant cobalt molybdenum sulphides, which can operate in gas streams containing sulphur.[187] In addition to this there a number of precious metal catalysts, including platinum and gold which have been explored as potential catalysts for fuel cell applications. Thermodynamic conversion is higher at lower temperatures; however iron catalysts are much less active at this temperature. For this reason, typical industrial water gas shift takes place in two stages, with first a high temperature shift reaction, followed by a second reactor at lower temperatures to shift the equilibrium further. [187]

The water gas shift reaction is a mature reaction, but its counterpart the reverse water gas shift reaction has received relatively little attention academically until recently, but the reverse water gas shift reaction is increasingly seen as a viable route for turning carbon dioxide into carbon monoxide for further use.[188]

Figure 2.8 illustrates the thermodynamics of the RWGS at 1 bar and a CO_2:H_2 ratio of 3:1. When performing the RWGS on its own, the reaction is favoured at higher temperatures (>700 °C) where methane formation is inhibited. However in order to be industrially viable the reaction temperature must be kept as low as possible to reduce costs.[188]

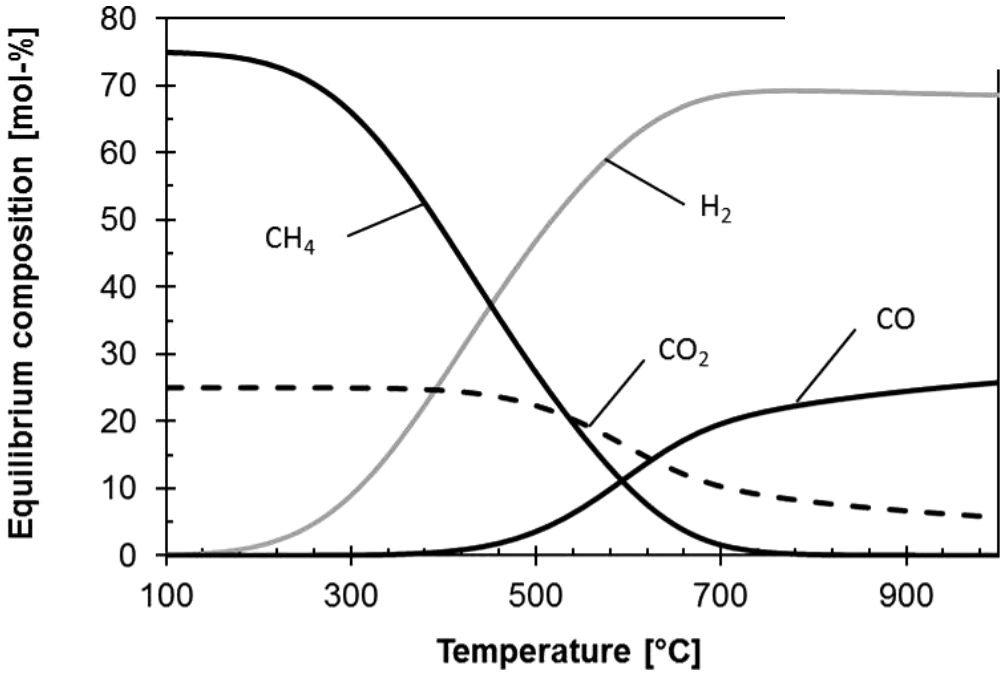

Figure 2.8 Thermodynamic equilibrium composition of the product gas of the RWGS reaction at 0.1MPa for a molar H_2/CO_2 inlet ratio of 3.[188]

The WGS and RWGS are known to take place over FT catalysts. In standard FT reactions this leads to the formation of CO_2, and increased H_2 concentrations. When CO_2 is used as a carbon source instead of CO, the reverse water gas shift reaction can occur producing CO which subsequently reacts to give hydrocarbons. [53]

2.5 Fischer Tropsch catalysis

Fischer Tropsch chemistry has been explored as an alternative route to liquid hydrocarbon fuels, to combat oil shortages or to reduce dependency on oil since its discovery. First discovered by Franz Fischer and Hans Tropsch in 1925, the process for the combination of carbon monoxide with hydrogen to give a variety of hydrocarbons. The process was first developed and commercialised during the Second World War, by chemists working in Germany in order to produce a supply of fuel from coal due to the shortage of oil available due to the war. The process was then abandoned due to being un-economic. A second period of sustained research took place in South Africa in the early 80's, as the apartheid government sought to find other sources of fuel, to counteract the shortage of hydrocarbons caused by international sanctions. Today this reaction is attracting increasing interest as a potential source of hydrocarbons not from traditional fossil fuel sources, but *via* the gasification of biomass into syn-gas, or by producing CO from CO_2 and using this for Fischer Tropsch. Current large scale uses of this process however produce hydrocarbons from coal and natural gas.[189]

Fischer Tropsch is generally accepted to proceed via a step-wise process, where CO is converted into a -CH_2- unit absorbed on the surface and water (Equation 2.2), followed by complete hydrogenation to methane (Equation 2.3) or step wise addition of CH_2 units to give the longer chain alkenes and alkanes, (Equations 2.4 to 2.5). The water gas shift reaction is an undesired side-reaction in this process (Equation 2.1, see section 2.4).

$$CO + 2H_2 \rightarrow -CH_2 - + H_2O \quad (2.2)$$

$$-CH_2 + H_2 \rightarrow CH_4 \quad (2.3)$$

$$\mathrm{x} - CH_2 \rightarrow C_xH_{2x} \quad (2.4)$$

$$C_xH_{2x} + H_2 \rightarrow C_xH_{2x+2} \quad (2.5)$$

$$CO + H_2O \rightleftharpoons CO_2 + H_2 \quad (2.1)$$

The kinetics of the FT catalysis are described by the Anderson-Schulz-Flory model.[189] This assumes the reaction to be a simple polymerisation, where the probability of chain growth can be described by the factor alpha, which determines the likelihood of the molecule forming adding to a pre-existing chain, forming a new chain, or terminating the reaction. This is expressed as:

$$\frac{\boldsymbol{W_n}}{\boldsymbol{n}} = (\mathbf{1} - \boldsymbol{\alpha})\boldsymbol{\alpha}^{(\boldsymbol{n}-\mathbf{1})} \quad (2.6)$$

Which can be rearranged to give:

$$\log \frac{\boldsymbol{W_n}}{\boldsymbol{n}} = \boldsymbol{n} \log \boldsymbol{\alpha} + \text{constant} \quad (2.7)$$

where n= the number of carbon atoms, W_n= the weight fraction of a hydrocarbon with carbon number n and α=the probability of chain growth

Using this equation the distributions of hydrocarbons obtained for different values of alpha, can be plotted (Figure 2.9). From this graph we can determine the values of α it would be desirable to obtain in order to preferentially produce each of the different products of the FT process can be determined. In order to produce a methanation catalyst, obviously an α of 0 is desirable, with no

chain growth. For the production of diesel and gasoline, alpha ≈ 0.9 would be desirable, and for the production of short chain olefins, alpha ≈ 0.4-0.5 is optimal.

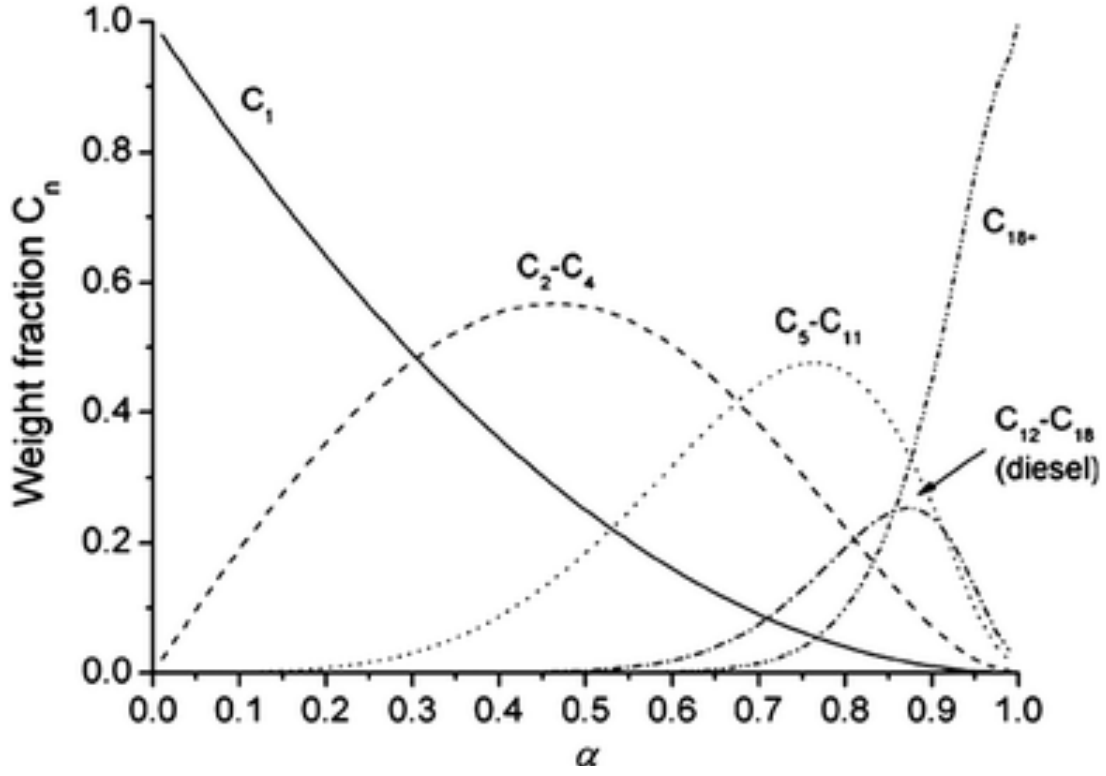

Figure 2.9 Anderson Schulz Flory Distribution [190]

2.5.1 Mechanism of the Fischer Tropsch reaction

The mechanism of Fischer Tropsch catalysis is a matter of significant debate in the literature, with a large variety of different mechanisms proposed these include the CO insertion mechanism, the carbide/alkyl mechanism, the alkenyl mechanism and the enolic mechanism, with a number of further elaborations based around these.[191]

As the Fischer Tropsch reaction is a polymerisation reaction, all mechanisms proposed will consist of the generation of an initiation intermediate, a chain growth or propagation step and a termination or desorption step. There is still significant debate in the literature over which of these mechanisms is correct, but it is generally acknowledged that more than one parallel pathway can take place on the catalyst surface. Here the major proposed mechanisms from the literature are outlined.

2.5.1.1 **CO insertion mechanism**

The CO insertion mechanism, also known as the Pichler-Schulz mechanism is shown in Figure 2.10 .[191,192] This mechanism is similar to that of the insertion of carbon monoxide in homogeneous coordination chemistry [193]. The mechanism proposes that the chain initiator is an absorbed CH_3 unit, which reacts with absorbed CO units before being reduced by hydrogen to return to a CH_2 unit. If termination of the reaction occurs before the oxygenate species is reduced, an alcohol or an aldehyde is produced. This mechanism is thought to be the main source of oxygenates in the Fischer Tropsch reaction. [191] Recent computational studies have suggested that chain growth via this mechanism is unlikely, however chains can be terminated by the insertion of a CO molecule, which will result in the formation of oxygenates. [194]

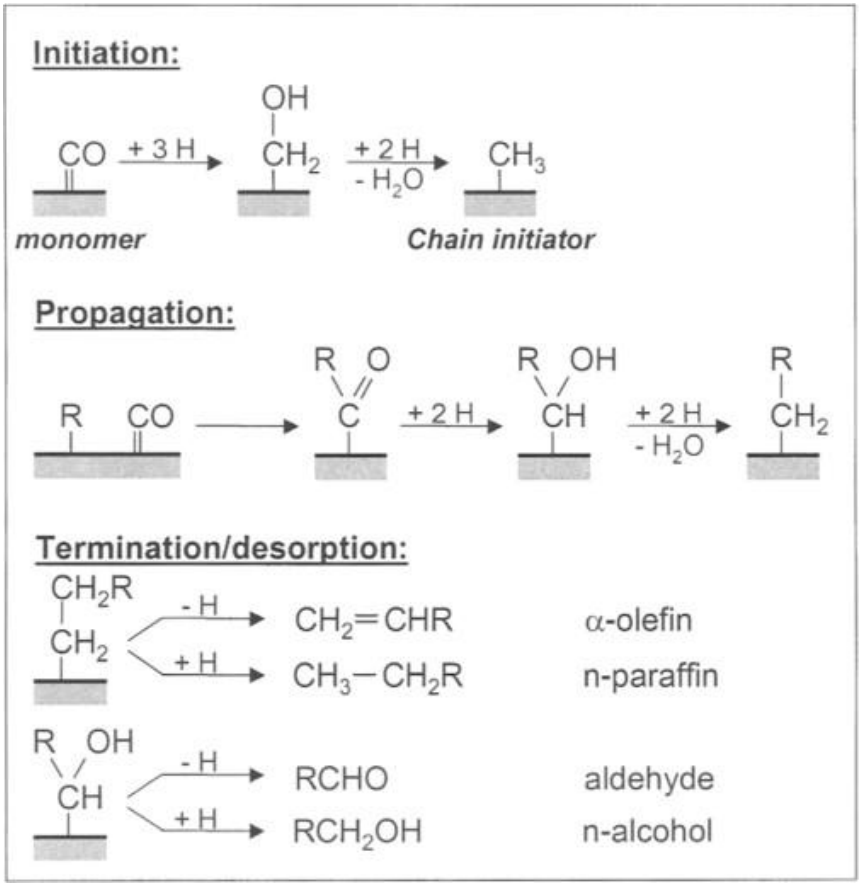

Figure 2.10 CO insertion mechanism (R= C_nH_{2n+1} with n≥0) [191]

2.5.1.2 **Alkenyl mechanism**

The alkenyl mechanism (Figure 2.11) proposes that the initiator species for this reaction are absorbed ethyl units[195,196], with chain growth achieved through reactions with absorbed CH_2 units. This process explains the production of olefinic species, as well as branched hydrocarbons via allyl isomerisation, however it cannot explain the formation of methane, paraffins or oxygenates. It is assumed that paraffins are formed by the subsequent hydrogenation of the olefinic species, and methane is formed via another mechanism. An alternative mechanism must also be invoked to explain the formation of oxygenates, as none of the probe ethyl units were found in the formed oxygenates. [195]

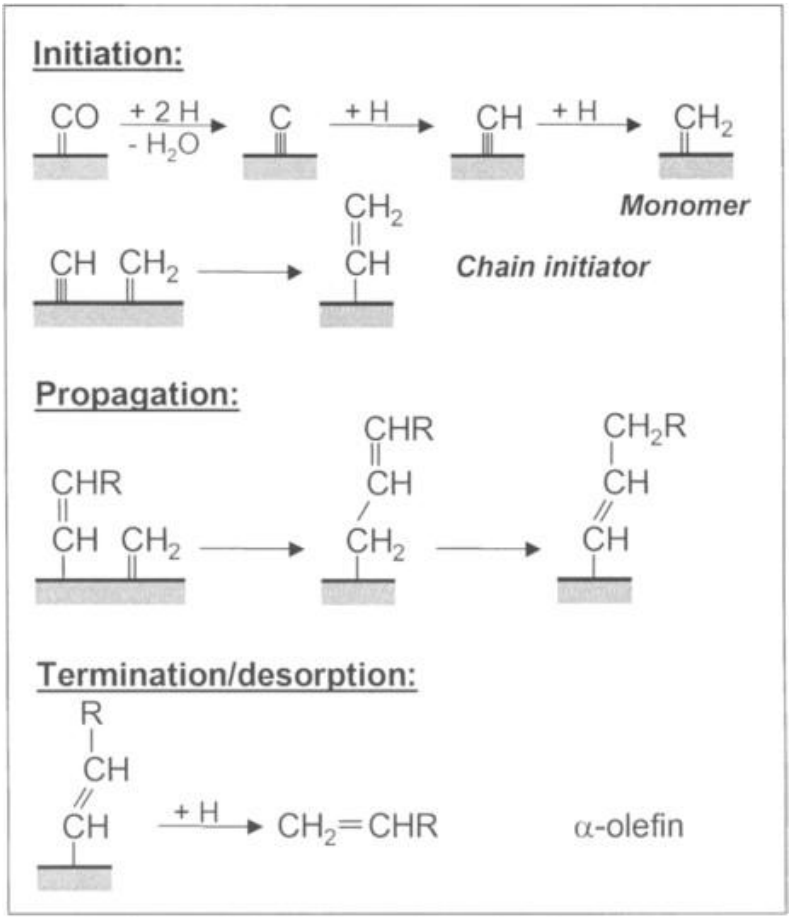

Figure 2.11 Alkenyl mechanism (R= C_nH_{2n+1} with $n \geq 0$) [191]

2.5.1.3 **Enol mechanism**

The Enol mechanism (Figure 2.12) proposes that CO is absorbed and reacts with hydrogen to form a surface enol species. These surface monomers then react together to form longer chains. Termination of the reaction forms oxygenates and α-olefins, and does not allow direct formation of alkanes. Alkanes must be formed by the further hydrogenation of alkenes. [191]

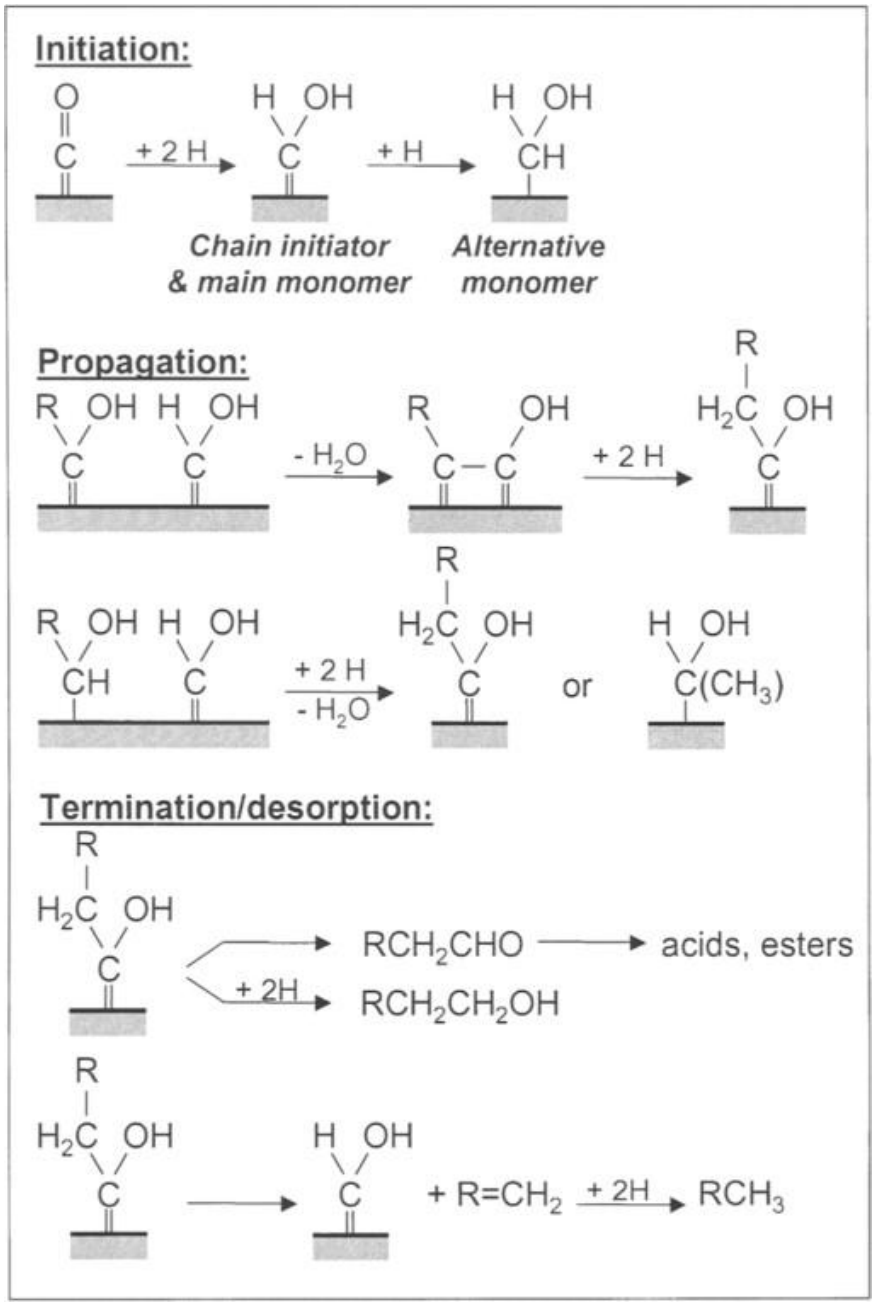

Figure 2.12 Enol mechanism (R= C_nH_{2n+1} with n≥0) [197] according to [191]

2.5.1.4 **Alkyl mechanism**

The alkyl mechanism (Figure 2.13) is the most generally accepted mechanism, for FT synthesis matching well with most observed evidence. CO is absorbed onto the surface of the catalyst, subsequent hydrogenation with absorbed hydrogen removes surface oxygen and produces water, and the absorbed carbon is hydrogenated stepwise to form a CH_3 unit. Propagation occurs by the incorporation of absorbed CH_2 units. This mechanism initially developed out of the carbide mechanism which proposed that the reaction proceeded via the formation of iron carbides, with the carbon in the resulting products coming directly from this carbide. [191] However experiments using C_{14} labelled carbides failed to show significant inclusion of C_{14} carbon in the resulting products so this route was discounted. [198]

A number of experiments have offered support for the CH_2 unit being a key part of the mechanism,[199] showing that when decomposing diazomethane on a catalytic surface with hydrogen a product distribution similar to that obtained via Fischer Tropsch is seen, suggesting a similar mechanism with the CH_2 unit key to the reactions activity. Further experiments using CH_xCl_{4-x} units appear to confirm the importance of the CH_x units, with CH_{1-2} allowing chain growth but CH_3 leading to methane formation. [200].

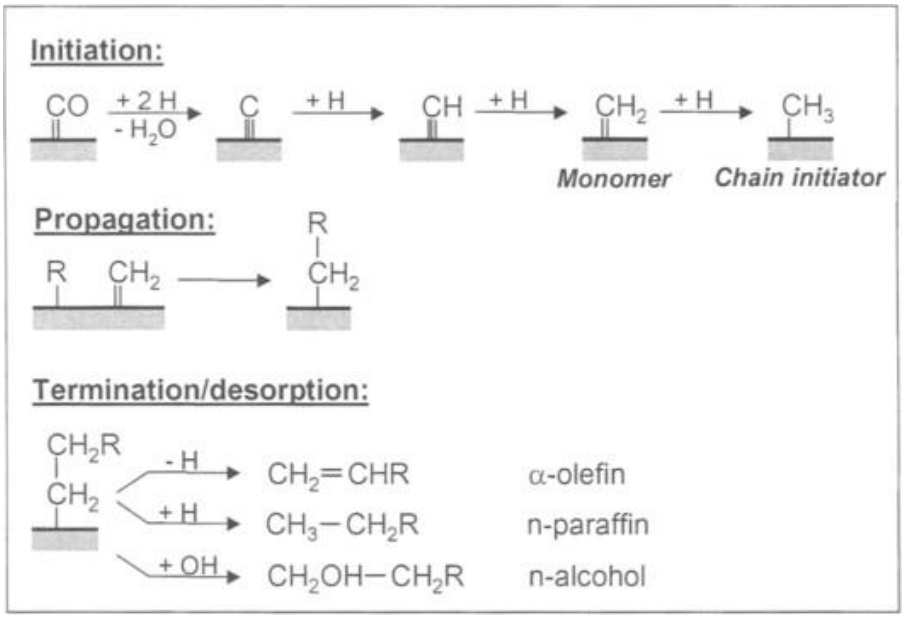

Figure 2.13 Alkyl mechanism (R= C_nH_{2n+1} with $n \geq 0$) [191]

This alkyl mechanism cannot easily explain the formation of oxygenates, though it has been proposed that oxygenates could be formed via reaction with surface hydroxyl group, leading to the formation of alcohols. There is no experimental evidence for this though and formation of

some species detected would be impossible. [194] A more likely explanation is that oxygenates are formed via CO insertion or an alternative mechanism. [194]

2.5.2 Metals active in Fischer Tropsch catalysis

A wide selection of FT catalysts have been developed, using a metals such as iron, cobalt, nickel and ruthenium. For industrial use iron and cobalt tend to be the more popular catalysts. Nickel is a highly effective catalyst for the Sabatier reaction, [32] and therefore tends to produce more methane than the other catalysts. Ruthenium is less used due to its high cost. [201] As cobalt is not very active in the WGS reaction cobalt FT catalysts are used where the ratio of CO to H_2 does not need to be adjusted. [190]

Iron is a much better WGS catalyst than cobalt, and so tends to be used for feedstock compositions where hydrogen levels are low, such as that produced from coal. The iron catalyst is able to simultaneously act as a water gas shift catalyst and a FT catalyst. [202] This is a simplification of the actual catalytic mechanism, as iron forms a number of different phases on the surface of the catalyst, which have different activities for the various reactions. Some of these phases such as the iron magnetite [202] or amorphous iron oxide [203] are active WGS catalysts, whilst others such as the iron carbide [204] species are active for the chain growth of hydrocarbons.

2.5.3 Nanoparticles as FT catalysts

Nanoparticles have been shown to be highly effective catalysts for Fischer Tropsch catalysis. A number of different nanoparticles have been used, but the majority of studies have used either iron or cobalt nanoparticles (often with additional dopants), supported on a variety of different supports.[205] The exact effect of the size and shape of different nanoparticles is still an active research area, and is not the same for different metals. In general it would be expected that nanoparticles would show increased activity at smaller sizes due to increased surface to volume ratio, and the presence of more defect sites which are commonly active for catalysis. It is important to note that with nanoparticle size effects, there are two measures of increased activity that should be considered turn over frequency (TOF), or the activity per active site, and the activity per gram of catalyst. It would be expected that increasing the surface area would increase the activity per gram of catalyst, as with a higher dispersion more active sites would be available. If the intrinsic activity of the catalyst is changing due to particle size effects the TOF would also increase.

For cobalt nanoparticles a systematic study performed by Bezemer *et al.* on a CNF support found that the TOF of cobalt nanoparticles was close to constant for nanoparticles as small as 6-8 nm;

below this size the TOF decreased rapidly, and also gave increased selectivity towards methane, rather than the preferred higher hydrocarbon products (Figure 2.14).[206] It was found that the increased selectivity to methane was due to increased coverage of hydrogen on the nanoparticle surface. It was also found that CO bonded irreversibly to the corner sites of the cobalt nanoparticle, these accounted for a higher percentage of the surface area of small nanoparticles, explaining the loss of activity. It appears that the surface terrace sites are the most active. [207]

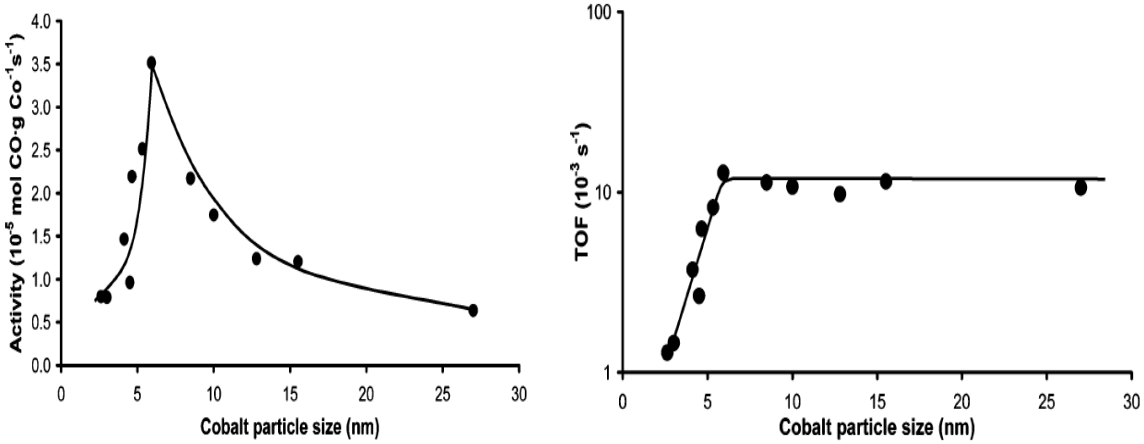

Figure 2.14 (left) activity against cobalt particle size (right) TOF against cobalt particle size[206]

For iron nanoparticles, TOF increases continuously with smaller particle sizes, down to average particle sizes as small as 2 nm. It is to be noted that much of this TOF relates to the iron nanoparticles abilities as a methanation catalyst, with TOF for C2+ hydrocarbons remaining relatively unchanged, but with significant increases in the TOF for methane. [208] This reported increase in TOF conflicts with earlier reports in the literature of smaller TOFs at lower particle sizes. [209,210] The reason for these differences has not been explained, but is possibly due to the difference in temperature regimes used in the two studies, with a higher temperature (350 - 370 °C) used in the recent study compared to lower temperature (270 - 280 °C) in the older studies.

2.5.4 Effect of catalyst support

The catalyst support is important in FT synthesis, with interactions between the support and the catalyst particle changing the behaviour of the catalyst particle. Strong interactions between the metal nanoparticle and the support will have two major effects, one the shape of the nanoparticle formed will be different with improved interactions to the support, and second because of these strong interactions the resulting nanoparticle will be harder to fully reduce, resulting in a mix of species present on the catalyst surface. [205] As a result, the effects of the support on the

Table 2.3 Performance of relevant Iron Fischer Tropsch catalysts under a variety of conditions. CO:H_2 ratio is 1:2 unless otherwise specified. Robs refers to the observed reaction rate per gram of catalysts, while FTY is the iron time yield, or observed activity per gram of iron. NR, or not reported, refers to data that was not available in the original reference

Paper	Catalyst	iron	GHSV	Temperature	Pressure	Conversion	R_{obs}	FTY	Selectivity				olefin
		wt%	$cm^3\ g_{cat}^{-1}\ h^{-1}$	°C	bar	%	$\mu mol\ g^{-1}\ s^{-1}$	$\mu mol\ g_{Fe}^{-1}\ s^{-1}$	CO_2	CH_4	C_2-C_4	C_5^+	ratio
Torres *et al.*[208]	Fe/CNF	10.0	NR	350	1	NR	0.14	1.41	NR	23.0	65.0	12.0	0.94
Torres *et al.*[208]	Fe/Al_2O_3	12.0	NR	350	1	NR	0.05	0.65	NR	22.0	65.0	13.0	0.94
Torres *et al.*[208]	Fe/SiC	10.0	NR	350	1	NR	0.65	6.52	NR	31.0	62.0	7.0	0.94
Torres *et al.*[208]	Fe/SiO_2	10.0	NR	350	1	NR	0.01	0.14	NR	38.0	61.0	1.0	0.92
Torres *et al.*[208]	Bulk Fe	30.0	NR	350	1	NR	0.008	0.08	NR	76.0	23.0	1.0	0.91
Torres *et al.*[208]	Fe/CNF	10.0	NR	340	20	88	2.98	29.8	30.7	9.5	46.7	13.1	0.81
Torres *et al.*[208]	Fe/Al_2O_3	12.0	NR	340	20	81	2.22	26.6	31.5	13.1	44.6	10.8	0.67
Torres *et al.*[208]	Fe/SiC	10.0	NR	340	20	77	6.38	63.8	36.5	9.6	50.4	3.5	0.33
Tavasoli *et al.*[161]	Fe0.5Co10/CNT	0.5	3600	220	20	54	1.84	N/A	2.1	9.4	3.5	85.1	0.49
Vannice *et al.*[211]	$K[HFe_3(CO)_{11}]/C$	4.38	NR	275	1	6.1	0.60	13.7	NR	41.0	58.0	3.0	0.63
Vannice *et al.*[211]	$K[MnFe_2(CO)_{13}]/C$	2.03	NR	275	1	1.7	0.29	14.3	NR	28.0	64.0	8.0	0.71
van Steen *et al.*[212]	Fe-Cu (IW)/CNT	8.3	1860	220	25	45.3	1.00	12.0	0.4	NR	NR	NR	NR
van Steen *et al.*[212]	Fe-Cu-K	25.8	1860	220	25	12.1	0.27	1.0	48.7	NR	NR	NR	NR
van Steen *et al.*[212]	Fe-Cu (DP)/CNT	8.1	1860	220	25	3.61	0.08	1.0	16	NR	NR	NR	NR
Bahome *et al.*[213]	Fe/CNT	12.1	2120	275	8	80	3.75	45.1	6.4	13.7	39.5	40.4	0.11
Bahome *et al.*[213]	Fe-K/CNT	9.3	2120	275	8	84.9	6.33	58.9	11.2	9.8	26.3	52.6	0.72

Paper	Catalyst	iron	GHSV	Temperature	Pressure	Conversion	Robs	FTY	Selectivity				olefin
		wt%	$cm^3\ g_{cat}^{-1}\ h^{-1}$	°C	bar	%	$\mu mol\ g^{-1}\ s^{-1}$	$\mu mol\ g_{Fe}^{-1}\ s^{-1}$	CO_2	CH_4	C_2-C_4	C_5^+	ratio
Chen *et al.*[57]	Fe-in/CNT	NR	NR	270	51	40	122	NR	18.0	12.0	41.0	29.0	NR
Chen *et al.*[57]	Fe-out/CNT	NR	NR	270	51	29	58.3	NR	12.0	15.0	54.0	19.0	NR
Chen *et al.*[57]	Fe-AC	NR	NR	270	51	17	16.9	NR	5.0	15.0	71.0	9.0	NR
Abbaslou *et al.*[214]	Fe-np/CNT	20	6480	275	20	25	1.53	7.67	16.3	12.1	31.0	40.6	NR
Abbaslou *et al.*[214]	Fe-wp/CNT	20	6480	275	20	10	0.61	3.07	12.6	34.3	39.3	10.0	NR
Schulte et al.[215]	Fe/O-CNT	20	996	340	25	48.3	0.57	2.8	22.5	NR	NR	NR	0.41
Schulte et al.[215]	Fe/N-CNT	20	996	340	25	26.5	0.31	1.6	11.5	NR	NR	NR	0.47
Motchelaho *et al.*[216]	Fe/CNT	10	2400	275	8	20	0.18	1.8	NR	48	35.7	17	NR
Motchelaho *et al.*[216]	Fe/treated CNT	10	2400	275	8	59	0.54	5.4	NR	19	22.9	58	NR

catalyst activity can be difficult to separate from effects of different nanoparticle shape and size, and reduced or improved reducibility.

Table 2.3 shows a number of different iron catalysts on a variety of supports in the FT reaction at various conditions. Recent studies clearly show that iron behaves very differently depending on the strength of the interaction with the support. Using Iron time yield (FTY), or the rate of reaction per gram of iron in the support (used as an approximation for TOF, as the number of active sites cannot necessarily be determined) typical oxidic supports, such as SiO_2 and Al_2O_3, which have strong interactions with the iron gave relatively low activities, with a FTY of <0.65 μmol CO g_{Fe}^{-1} s^{-1}. However weakly interacting supports such as GNF and SiC had FTY of 1.41 μmol CO g_{Fe}^{-1} s^{-1} and 6.52 μmol CO g_{Fe}^{-1} s^{-1} respectively. This effect holds for a variety of operating conditions.

2.5.5 FT catalysts using carbon supports

A number of studies explore FT catalysis on carbon supports. [217] These catalysts are claimed to have higher activity per unit volume than other FT catalysts due to better dispersions, as well as giving higher selectivity to olefins. [212]

A series of papers by Vannice *et al.* [211,218-224] explores the use of iron-manganese nanoparticles, produced from carbonyl species on an activated carbon support, for FT catalysis. The group produced a series of FeMn carbonyls, sometimes with the addition of a potassium salt. [219] These air sensitive compounds were characterised on and off the supports using a number of techniques including IR spectroscopy, [222] Mossbauer spectroscopy, [218] TEM/EDX, [218] and chemisorption studies. [220] The work demonstrated that the Fe catalyst when doped with Mn and K was especially selective towards low weight olefins, in the C_2-C_4 range, with selectivities as high as 85-90%. A Fe:Mn ratio of 2, with the presence of a K promoter was suggested to give the best balance between activity and selectivity, with a selectivity to olefins of 71%. [211] The highly dispersed catalyst report high FTY of >10 μmol CO g_{Fe}^{-1} s^{-1}, however overall conversions achieved were relatively low (1-10%). The reactor was operated at atmospheric pressure and relatively low temperature, so higher conversions could be achieved at higher temperatures and pressures (though this may correspondingly reduce selectivity) and larger amounts of catalyst. [220,223]

The use of CNTs as catalytic supports is an area of increasing interest, [55] and a number of catalysts supported on nanotubes have demonstrated activity for the FT reaction of syn-gas.

[57,161,205,208,212-214,225,226] To the author's knowledge there are no reports of the combined RWGS and FT process using CO_2 as a feedstock with a catalyst supported on CNTs.

The catalysts deposited on CNTs explored so far for the FT reaction have tended to be either solely iron nanoparticles deposited on the nanotubes, [57,212-214] or bimetallic catalysts with another metal as a promoter - copper, cobalt and ruthenium have been explored previously. [161,213,225]

The preparation method of the catalyst is believed to be important in the resulting activity. Van Steen *et al.* [212] report that three iron catalysts prepared by incipient wetness and two different deposition-precipitation methods had different catalytic behaviours. The incipient wetness catalyst was the most active giving initial FTY of 12 µmol CO g_{Fe}^{-1} s^{-1} after 24 hours, but the catalytic activity decayed rapidly over time with only 4 µmol CO g_{Fe}^{-1} s^{-1} after 48 hours. The deposition catalysts had lower activities with around 1 µmol CO g_{Fe}^{-1} s^{-1}, but did not demonstrate as significant a deactivation profile. This activity difference is thought to be due to differences in the iron crystallite structure and dispersion and hence differences in the iron phases present on the surface.

An important factor in the activity of nanoparticles supported on CNTs is whether they are supported on the inside or outside of the CNT, with confinement within the CNT drastically changing nanoparticle activity. [145,227] This effect also applies in FT synthesis as Chen *et al.* [57] report on the dramatic effect of confinement in nanotubes on the activity of iron nanoparticles. With NPs confined in CNTs, the CO activity is 122 µmol CO g^{-1} s^{-1} and gives a much higher yield of higher hydrocarbons, whilst outside the CNT the yield is 58 µmol CO g^{-1} s^{-1}, and is only 16.9 µmol CO g^{-1} s^{-1} on activated carbon, whilst also increasing the selectivity to higher hydrocarbons. This effect is attributed to the known change in the redox chemistry of iron oxides trapped in nanotubes. [228,229] This makes it easier for the catalyst to be reduced and form more FT active iron carbides. This finding is elaborated on by Abbaslou *et al.* [214] who found that iron nanoparticles confined in narrow carbon nanotubes (inner diameter 12 nm or less) gave higher activities, whilst those confined in wider carbon nanotubes (inner diameters 12-50 nm) did not exhibit this effect. It is to be noted that unlike Chen *et al.,* where nanoparticle sizes compared inside and outside of the tube were very similar, Abbaslou *et al.*[214] reports nanoparticles of differing sizes inside the two types of nanotubes. This raises the question whether effects observed related to confinement or to the nanotube size. It is to be noted that comparisons between catalysts performed by different authors are difficult due to the variety of different temperatures and pressures used, and the structure sensitivity of the

reaction. Since most papers do not report dispersion, a true TOF cannot easily be calculated for comparison purposes.

The effects of varying the composition of the CNT, by incorporating oxygen and nitrogen into the nanotube structure, on the behaviour of CNTs as a catalyst material has been explored. [215] Doped materials, showed comparable initial activity, with oxygen containing CNT being more active (9.1 µmol CO g_{Fe}^{-1} s^{-1} N-CNT vs 10.1 µmol CO g_{Fe}^{-1} s^{-1} O-CNT) but after 50 h on stream the activity of the oxygen doped CNT had decayed significantly, whereas the nitrogen doped CNT maintained a higher activity (2.8 µmol CO g_{Fe}^{-1} s^{-1} N-CNT vs 1.6 µmol CO g_{Fe}^{-1} s^{-1} O-CNT). It is surprising to note that both these catalysts showed relatively high water gas shift activities, though the major detected iron phase was an iron carbide, with no magnetite detected. This activity was attributed to very small un-reduced iron magnetite particles that could not be detected by XRD. Similar, but slightly lower activities for Fe/CNT (1.8 µmol CO g_{Fe}^{-1} s^{-1})were obtained by Motchelaho [216], and though relatively stable still showed a slow decrease in activity over 120 hours. Increased activity (5.8 µmol CO g_{Fe}^{-1} s^{-1}) was observed if the support was treated with nitric acid, suggesting that the increased activity may be due to improved dispersion of nanoparticles on the support.

Mixed metal nanoparticles on carbon nanotubes reveal a more complex behaviour; cobalt-iron nanoparticles on nanotubes give good (~25 %) selectivity to alcohols, and good activity (1.8 µmol CO g^{-1} s^{-1}). [161] Varying the Co-Fe ratio varies the activity, with low values of Fe giving higher conversions. High values of Fe gave lower activity, but were more active as water gas shift catalysts. Fe-Ru nanoparticles supported on carbon nanotubes were reported to be stable for a long period of time with little decay unlike Fe-Ru catalysts supported on other supports. This was attributed to interactions with the carbon nanotube support which do not interfere with the reduction of the iron species, but are strong enough to prevent sintering. The Fe-Ru catalyst shows typical behaviour when promoted with K and when the Fe-Ru ratios are varied. [230]

Recently a carbon material that has attracted a lot of interest is graphene [231]. Though currently produced in very low quantities, the similarity of graphene to carbon nanotubes makes it a support of potential interest. Two recent studies have attempted to perform Fischer Tropsch catalysis using graphene oxide. [232,233] It was demonstrated that graphene oxide is an effective support for Fischer Tropsch synthesis, with both studies showing significantly improved conversions using a graphene oxide support compared to an activated carbon support. Both

studies reported significant differences in catalytic behaviour dependant on the treatment the catalyst received. [232,233]

2.6 Carbon Dioxide conversion

2.6.1 FT catalysts used for CO_2 conversion

A number of catalysts have been used for CO_2 conversion, for the production of alkane, or alkene species, catalysts have been based off FT-style iron catalysts, though other methods have been used including electrolysis and conversion through a methanol route. [234-236] Direct hydrocarbon synthesis has been achieved using modified iron or cobalt FT catalysts to produce hydrocarbons with CO as an intermediate, [190,235,237] as well as by using hybrids of copper-based methanol catalysts and zeolites to produce hydrocarbons using methanol as an intermediate. [236]

Standard FT catalysts used for the conversion of natural gas to hydrocarbons may not be as effective as catalysts for conversion of CO_2. As previously discussed the water-gas shift reaction is an undesired side reaction in FT. Many FT catalysts try to minimise this side reaction to increase yield, especially in hydrogen rich systems, such as those obtained from methane. FT catalysts used for systems in which there is not enough H_2 present in the original feedstock (such as coal) utilise this reaction to produce the necessary hydrogen producing CO_2 as a by-product. [201] The reverse WGS is an essential step in the conversion of CO_2 to hydrocarbons, so catalysts optimised to remove this step will not be effective.

2.6.2 Iron catalysts for CO_2 conversion

Some of the most successful catalysts for conversion of CO_2 into higher hydrocarbons have been iron based catalysts.[238] A number of groups have explored the effectiveness of iron catalysts using a number of different supports, synthesis methods and promoter metals in order to increase CO_2 conversion. When undergoing a FT-style reaction these products are typically CO, CH_4, and higher hydrocarbons, though methanol and higher alcohols can also be formed. [190,239] Conversion of CO_2 into CH_4 is easily achieved, as it is the thermodynamically favoured product of CO_2 and H_2, but it is the least valuable product of the reaction. A preferred situation is to reduce the amount of CH_4 formed, and produce more of the higher hydrocarbons.

Iron catalysts that have been successfully used for the conversion of CO_2 include, unsupported iron-manganese catalysts doped with rhodium and lanthanide [235], $Fe_3(CO)_{12}$ supported on ZSM-5, [240] Fe-Mn-K/SiO_2, [241] Fe-Mn-K/Al_2O_3, [242-244] Fe-Ru-K/Al_2O_3, [230] and Fe-Mn-Ce/Al_2O_3, [245] as

Table 2.4 Performance of relevant catalysts for the conversion of CO_2 into hydrocarbons. CO_2:H_2 ratio is 3:1 unless otherwise specified. Robs refers to the observed reaction rate per gram of catalysts, while FTY is the iron time yield, or observed activity per gram of iron. NR, or not reported, refers to data that was not available in the original reference

Paper	Catalyst	iron wt%	dopant wt%	GHSV $cm^3\ g^{-1}\ h^{-1}$	Temperature °C	Pressure bar	Conversion %	Robs µmol $g^{-1}\ s^{-1}$	FTY µmol $g_{Fe}^{-1}\ s^{-1}$	Selectivity CO (%)	CH_4 (%)	C_2-C_4 (%)	C_5^+ (%)	Olefin Ratio
Sai Prasad *et al.*[237]	Fe	100	0.00	1900	300	1	16.21	0.01	0.01	36.4	31.6	22.5	2.8	0.05
Sai Prasad *et al.*[237]	Fe-V	90	10.00	1900	300	1	11.17	0.01	0.01	27.3	28.9	38.3	5.5	0.14
Sai Prasad *et al.*[237]	Fe-Cr	90	10.00	1900	300	1	25.70	0.02	0.03	21.5	50.8	25.9	1.8	0.22
Sai Prasad *et al.*[237]	Fe-Mn	90	10.00	1900	300	1	23.15	0.02	0.02	8.1	35.0	50.0	6.9	0.26
Sai Prasad *et al.*[237]	Fe-Zn	90	10.00	1900	300	1	26.54	0.02	0.03	4.4	23.2	55.6	16.5	0.70
Sai Prasad *et al.*[237]	Fe/Al_2O_3	NR	NR	1800	400	20	48.90	0.83	NR	12.4	42.4	41.0	4.1	0.06
Sai Prasad *et al.*[237]	Fe-K/Al2O3	ratio 0.2	NR	1800	400	20	67.30	1.15	NR	6.0	17.2	45.5	26.5	0.73
Sai Prasad *et al.*[237]	$Fe\text{-}K/Al_2O_3$	ratio 0.5	NR	1800	400	20	69.60	1.19	NR	2.7	16.0	46.5	31.5	0.86
Sai Prasad *et al.*[237]	$Fe\text{-}K/Al_2O_3$	ratio 1:1	NR	1800	400	20	68.40	1.17	NR	3.1	17.4	46.2	31.8	0.91
Sai Prasad *et al.*[237]	Fe/SiO_2	NR	-	1896	300	10.1	6.90	0.06	NR	71.0	23.4	5.7	0.1	0.01
Sai Prasad *et al.*[237]	Fe/TiO_2	NR	-	1896	300	10.1	11.50	0.10	NR	35.7	33.3	26.7	4.4	0.03
Sai Prasad *et al.*[237]	Fe/Al_2O_3	NR	-	1896	300	10.1	22.80	0.21	NR	11.4	38.3	42.6	7.8	0.01
Sai Prasad *et al.*[237]	$Fe\text{-}K/Al_2O_3$	NR	-	1896	300	10.1	30.40	0.28	NR	40.5	7.6	28.3	23.5	0.91
Sai Prasad *et al.*[237]	Fe/HY	17	0	1896	300	10.1	10.10	0.09	0.54	33.0	48.7	17.3	1.0	0.00
Sai Prasad *et al.*	Fe/NaY	17	0	1896	300	10.1	20.80	0.19	1.11	29.3	10.3	29.8	28.2	0.71
Sai Prasad *et al.*	Fe-KY	17	0	1896	300	10.1	17.90	0.16	0.95	31.3	8.6	29.2	30.6	0.76
Dorner *et al.*[244]	Fe/Al_2O_3 (9%)	9	0	5400	290	13.8	18.20	0.64	7.13	10.1	55.1	34.9	0.2	0.17
Dorner *et al.*[244]	Fe/Al_2O_3 (17%)	17	0	5400	290	13.8	29.20	1.03	6.06	10	54.9	35.1		0.17
Dorner *et al.*[244]	Fe/Al_2O_3 (25%)	25	0	5400	290	13.8	32.10	1.13	4.53	10	54.9	35.1		0.17
Dorner *et al.*[244]	$FeMn/Al_2O_3$ (17 % 4%)	17	4	5400	290	13.8	34.40	1.21	7.14	11.5	42	46.5		0.41
Dorner *et al.*[244]	$FeMn/Al_2O_3$ (17 % 12%)	17	12	5400	290	13.8	37.70	1.33	7.82	10.7	34	55.3		0.55

Paper	Catalyst	iron wt%	dopant wt%	GHSV $cm^3 g^{-1} h^{-1}$	Temperature °C	Pressure bar	Conversion %	Robs µmol $g^{-1} s^{-1}$	FTY µmol $g_{Fe}^{-1} s^{-1}$	Selectivity CO	CH_4	C_2-C_4	C_5^+	Olefin Ratio
Dorner *et al.*[244]	FeMn/ Al_2O_3 (17 % 20%)	17	20	5400	290	13.8	25.90	0.91	5.37	15.8	40.7	43.4		0.47
Dorner *et al.*[244]	FeMnK/ Al_2O_3 (17% 12% 2%)	17	14	5400	290	13.8	39.50	1.39	8.20	10.5	29.4	60.1		0.79
Dorner *et al.*[244]	FeMnK/ Al_2O_3 (17% 12% 8%)	17	20	5400	290	13.8	41.40	1.46	8.59	11.5	26	62.4		0.81
Dorner *et al.*[245]	FeMnCe/Al_2O_3 (17% 12% 2%)	17		5400	290	13.8	38.60	1.36	8.01	11.5	31.5	57.1		0.53
Dorner *et al.*[246]	FeMnKCe/Al_2O_3 ()	17		5400	290	13.8	50.4	1.78	10.46	14.8	22.9	62.3		0.81
Lee *et al.*[230]	Fe-Ru-K	NR	NR	2000	300	10	42.00	0.40	NR	NR	7	23.7	69.3	0.90
Huang *et al.*[240]	Fe/ZSM-5	NR	NR	1000	260	1	18.50	0.0007	NR	0	7.3	92.7	0	1
Hu *et al.*[247]	FeMnK	10.5	89.5	3360	260	13.7	45.00	0.78	93.39	19.2	12.1	68.7		0.74

well as iron catalysts doped with a number of other metals including V, Cr, Zn and supported on a variety of supports including titania and different zeolites. [237] Table 2.4 shows some of the iron catalysts used in this reaction.

The majority of catalytic studies have been performed using iron based catalysts doped with potassium, manganese or both which have been reported to give good activities ranging from 0.01 to 8 µmol g_{Fe}^{-1} s^{-1} depending on catalyst composition and reaction conditions. [237,244]

Using K or other alkali metals has been shown to be a very successful method of promoting activity, with increases in activity of up to 40 % reported. [237] Sai Prasad *et al.* [237] show that carbon dioxide absorption increases with the increasing basicity of the metal anion used on a zeolite support, as well as selectivity to higher hydrocarbons. It is believed that this is due to higher absorption of CO_2 by the basic alkali ions, increasing surface coverage of carbon dioxide on the catalyst surface, and hence increasing the chance of a coupling reaction. This effect is also observed in standard FT chemistry.[220]

The type of support used has an effect on CO_2 conversion and selectivity. Al_2O_3 is the most effective support to be reported for the Fe-K catalyst. Dorner *et al* [244] theorise that this is due to the formation of potassium alanate, a known reversible hydrogen absorber in the operating temperature region. It is suggested that this potassium alanate pulls hydrogen away from the iron particles (allowing the iron to absorb more CO), whilst also activating hydrogen allowing it to react more readily to give hydrocarbons. Alanate formation has been detected, but no studies have proven the relationship of alanate presence with improved catalytic performance. Sai Prasad *et al*. [237] attribute alumina's effectiveness as a catalytic support to increased dispersion of the iron particles on alumina compared to silica.

A wide range of selectivities and conversions has been reported for the various iron based catalysts seen in the literature. Huang *et al.* [240] report that $Fe_3(CO)_{12}$ complexes when deposited onto a ZSM-5 support via a multiple reflux and impregnation method gives a catalyst with a selectivity above 90 % to ethene, with a low activity of 0.0007 µmol g^{-1} s^{-1}, when run at 260 ^{o}C at 1 atm in a microflow reactor, with a H_2 to CO_2 ratio of 2. This selectivity was highly dependent on temperature with higher temperatures yielding higher activity, but with a corresponding decrease in selectivity as more methane and propene are produced, whilst at lower temperatures giving neglible conversions. Changing the ratio of H_2 to CO_2 also changed conversion and selectivity, with more H_2 leading to higher conversion rates and lower selectivity to ethene. The iron carbonyl catalyst was reduced at 200 ^{o}C under hydrogen, and it

is likely to have formed nanoparticles, though no attempt was made to determine the size of the nanoparticles formed, or of the resulting iron crystallites.

Dorner *et al.* [244] report their highest activities using high wt. %'s of Fe, K and Mn deposited on an alumina substrate, using catalysts prepared by co-incipient wetness impregnation at a variety of Fe, K and Mn ratios. It was found that increasing the wt.% of Fe led to an increase in conversion, but a decrease in activity per gram of iron. The increase in conversion reached a maximum at around 17 wt.% Fe, after which no further increases in conversion were observed. The addition of Mn to the Fe catalyst also resulted in an increase in conversion and activity, as well as an increase in selectivity to olefins, alkene containing species. This effect reached a maximum at around 12 wt.%, after which activity, conversion of carbon dioxide and selectivity to hydrocarbons decreased, though more CO was observed to have formed. Addition of K to the catalyst resulted in slightly higher conversions, and an increase in selectivity to olefin species. A conversion of 8.59 µmol g_{Fe}^{-1} s^{-1} was achieved in a continuous stirred tank reactor (CSTR) at 290 ^{o}C, 13.6 atm with a H_2:CO_2 ratio of 3. Attempts to increase the conversion of this catalyst involved incorporating a reverse water gas shift catalyst, ceria into the catalyst. Initial attempts at this showed negligible improvements in activity, [245] with 2 wt.% ceria increasing activity from 5.37 µmol g_{Fe}^{-1} s^{-1} to 8.01 µmol g_{Fe}^{-1} s^{-1} for a FeMn/Al_2O_3 catalyst, without the presence of potassium, and larger amounts of ceria decreasing activity to 7.43 µmol g_{Fe}^{-1} s^{-1}. This was attributed to the ceria impregnated at the same time as Fe and Mn, depositing on top of the nanoparticles and thus blocking the active sites. Efforts using a two-step incipient wetness method, where first ceria was deposited on the catalyst, followed by the FeMnK catalyst proved more successful, with conversion increasing from 8.59 µmol g_{Fe}^{-1} s^{-1} to 10.46 µmol g_{Fe}^{-1} s^{-1}. [246] Surprisingly the larger ceria particles formed were more active than the smaller ones, despite smaller ceria particles being shown to give higher RWGS activity. This was attributed to more of the smaller ceria particles being blocked by deposited FeMnK particles. [246]

Sai Prasad *et al.* [237] explored a large number of variables in the hydrogenation of carbon dioxide, looking at a variety of conditions and catalysts. It was found that the K content of the catalyst was an important factor in conversion of CO_2, decreasing the selectivity to methane, and increasing selectivity to C_2-C_4 hydrocarbons. The K species seemed to increase chain growth probability and improve carburisation. This effect is well known in FT catalysis, and is thought to be due to a combination of the basicity of the K and the K dopants effects on crystallite formation. The catalyst was doped with V, Cr, Mn and Zn. V reduced the rate of CO_2

conversion, Cr, Mn and Zn increased CO_2 conversion, with Zn being the most effective promoter at 300 ^oC, 1 atm with a H_2:CO_2 ratio of 3. This was believed to be due to the high basicity of Zn increasing the absorbance of carbon dioxide on the catalyst surface. The Zn promoted catalyst produced the highest activity of 0.0265 µmol g_{Fe}^{-1} s^{-1}, while Cr gave a slightly lower conversion of 0.0257 µmol g_{Fe}^{-1} s^{-1}, but with lower selectivity with a large percentage of CO and methane produced. Mn gave a lower conversion of 0.0231 µmol g_{Fe}^{-1} s^{-1}, but resulted in more methane being produced. Alumina, titania and silica were tested as catalytic supports, with alumina being the most active (especially with a K promoter), and silica being unfavourable. This supports results achieved by Dorner *et al.* [244] but no attempt is made to explain the surprisingly low activity of silica supported catalysts.

Attempts to improve iron conversion and selectivity have involved the use of iron supported on manganese molecular sieves. [247] Specifically nanofibres of $KMn^{3+}Mn_7^{4+}O_{16}$ were formed, these nanofibres contain two of the better promoters for this reaction. Result achieved were promising, when the catalyst was reduced under CO, very high activity of 93.4 µmol g_{Fe}^{-1} s^{-1} was achieved, with 45% olefinic selectivity. When reduced under H_2, lower but still high activities of 54.3 µmol g_{Fe}^{-1} s^{-1} were achieved. Modification of the reduction conditions was also reported to affect the products obtained, with catalysts reduced at low temperature (350 °C) producing predominantly C_2-C_6 carboxylic acids and high temperature reduced catalysts (450 °C) producing predominantly olefins, with higher activity.

Lee *et al.* [230], report that the addition of a Ru component to an iron catalyst increases the chain growth potential of the catalyst to give increased production of higher hydrocarbons with not insignificant production of hydrocarbons with chain lengths >10. Conversion of CO_2 for the Ru and K promoted Fe catalyst is slightly higher, than for the iron catalyst promoted solely with potassium, with conversions of around 0.4 µmol g^{-1} s^{-1} at 300 ^oC, 10 atm and H_2:CO_2 ratio of 3. This level of activity was only reached after 20 hours, after which the activity level did not appear to change.

You *et al.* report on the use of an unsupported iron catalyst. [248] They observed similar trends for the unsupported iron, compared to iron supported on alumina. Addition of K increased selectivity to light olefins, though high wt.% of potassium had less effect. It was also observed that addition of boron supressed formation of C5+ hydrocarbons, leading to increased selectivity towards the C_2-C_4 olefin fraction.[248]

2.6.3 Importance of reactor type

It is important to note that observed conversions can vary dramatically with reactor type. Results in section 2.6.3 are mostly obtained with a variety of fixed, or packed bed reactors, however some results obtained by Dorner *et al.,* use a CSTR. This group later reported that results obtained transferring the same catalyst into a fixed bed reactor were dramatically different, to achieve similar conversions GHSV had to be reduced from 5400 ml g^{-1} h^{-1} to 100 ml g^{-1} h^{-1}.[249] The precise reasons for the much lower activity observed in fixed bed reactors has not been explained, but the most likely reason is improved mass transfer in the CSTR reactors.

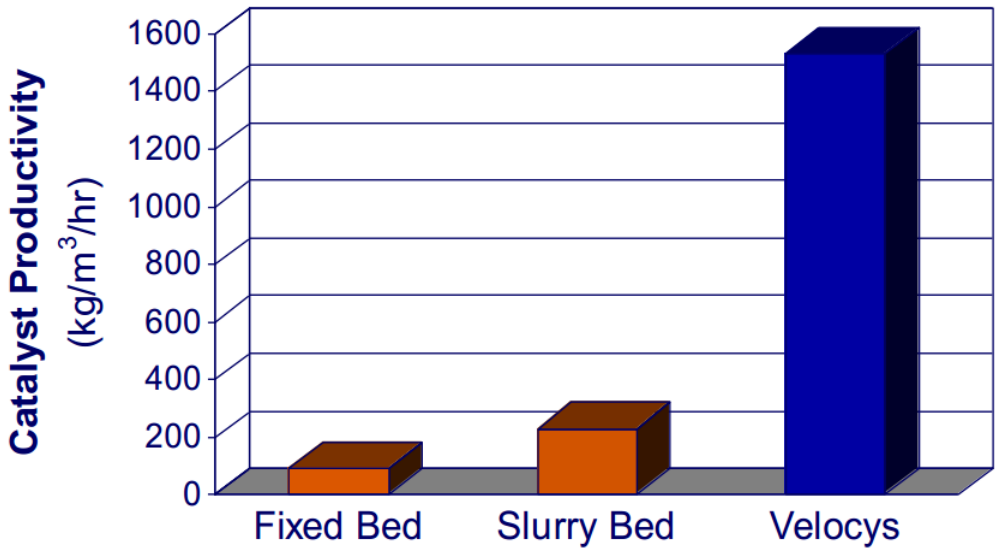

Figure 2.15 Catalyst productivity of catalyst in fixed bed, slurry bed and microchannel velocys reactor[250]

Work by Velocys in developing a micro channel reactor shows the dramatic influence reactor type can have on catalyst productivity, with their FT catalyst showing an order of magnitude improvement compared to a fixed bed reactor, obtained through improved control of temperature, and contact time with the catalyst (Figure 2.15). [250] The micro channel technology is viable on much smaller scales than traditional FT reactors, utilisation of similar technologies for CO_2 conversion may significantly increase the economic viability.

2.7 **Motivation**

This review of the literature has revealed a number of gaps that this work will attempt to address. The synthesis and mechanism of MWCNT formation is now relatively well understood, and large quantities of CNT are synthesised annually. [68, 69] CNT have shown promise as catalyst supports for a number of different reactions, in particular the FT process.[55] A number of questions remain however about the use of CNT as a heterogeneous catalyst support, as the nature of powder CNT make them difficult and potentially hazardous to handle. Synthesis of CNT on a formed substrate, such as SiO_2, quartz or cordierite monoliths can help address these issues.[115] Synthesis of CNT directly onto cordierite monoliths is however still a fairly intensive, multi-step process which can result in disintegration of the monoliths. The main challenge for CNT synthesis on a support appears to be the dispersion of iron nanoparticles onto the low surface area cordierite support in order to grow nanoparticles, in most cases the introduction of an alumina wash-coat is used to get around this.[115] Some CNT synthesis techniques introduce catalyst and carbon source at the same time, utilising techniques like this may help avoid these issues.[66]

A large amount of work has been done using CNT as supports for the FT reaction. It has been demonstrated that CNT supports have many advantages over traditional supports, including increased stability over many oxidic supports, improved activity over oxidic supports and activated carbons, and increased selectivity to olefins. [205] Likewise there has been extensive work performed using iron based catalysts for the reduction of carbon dioxide in the combined RWGS and FT process, in order to produce lower olefins.[244] Despite the improved selectivity to olefins reported over CNT catalysts, no exploration has yet been made of the activity of iron supported on CNT for CO_2 hydrogenation. In this work attempts will be made to utilise iron supported on CNT for the reduction of CO_2.

3 Characterisation Techniques

The focus on development of novel catalysts and supports has required using a number of different characterisation techniques. In this chapter the experimental procedure used for each technique is described, along with a short description of the theory behind each technique, the type of information that can be obtained and analysis of the inherent errors.

3.1 Raman Characterisation

Raman spectra of samples were recorded using different Raman spectrophotometers. Raman spectra were initially recorded from 1000-3000 cm^{-1} using a BW-TEK i-Raman system equipped with a 785 nm laser, however this machine was difficult to use with problems encountered in excluding light and focusing on a surface.

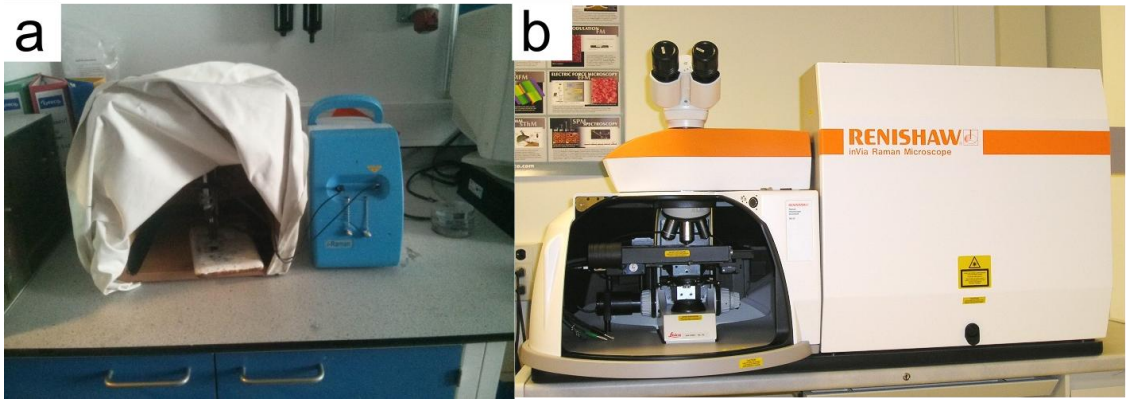

Figure 3.1 The Raman systems used in this work a) BW-TEK i-Raman system b) Renishaw Invia system

Later access to a Renishaw Invia system equipped with both a 532 nm and 785 nm laser, was obtained, this system being integrated with an optical microscope, allowing the laser to be focused directly onto the point of interest. The majority of spectra are recorded with the green 532 nm laser using the Renishaw Invia system unless otherwise specified.

In order to avoid altering the CNTs, the laser power was set to 5% to prevent the laser burning or damaging the CNTs. Raman spectra were taken of either CNT powders dispersed in ethanol and dropped onto a silicon slide, or directly on the substrate by focusing the Raman laser onto the surface.

In order to reduce error, each spectra was measured at least 3 times at different points and the resulting spectra were averaged. A sample of silicon was used to calibrate the laser position at 520nm at the start of each analysis session.

3.1.1 Theory of Raman Spectroscopy

Raman spectroscopy is a powerful spectroscopic technique for determining information about the vibrational modes of a material. A mono-chromatic laser source is shone on the material, interaction between the photon and the molecule's electron cloud excites the molecule to a higher energy level, upon relaxation a photon is emitted, at the same energy level, at a higher energy level or at a lower energy level. Those photons at the same energy are elastically scattered or Rayleigh scattered, whereas those that change energy are in-elastically or Raman scattered. This shift can only occur if vibration of the molecule deforms the electron cloud, and the degree of this shift in energy yields information about the vibrational modes of the molecule. [251]

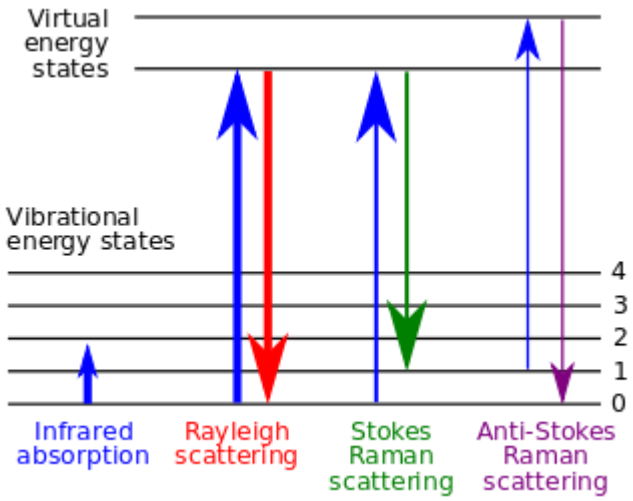

Figure 3.2 Energy level diagram showing the states involved in Raman signal. The line thickness is roughly proportional to the signal strength from the different transitions. [252]

Raman spectroscopy of carbon nanotubes can yield a significant amount of information about the structure of the carbon nanotube, with multiple characteristic vibrations. Characteristic vibrations of CNT include the Radial Breathing Mode (RBM) (~200 cm^{-1}), the D band (~1340 cm^{-1}), the G band (~1580 cm^{-1}) and the G' band (~2600 cm^{-1}), though the position of these bands will shift depending on the frequency of the laser used. [253,254]

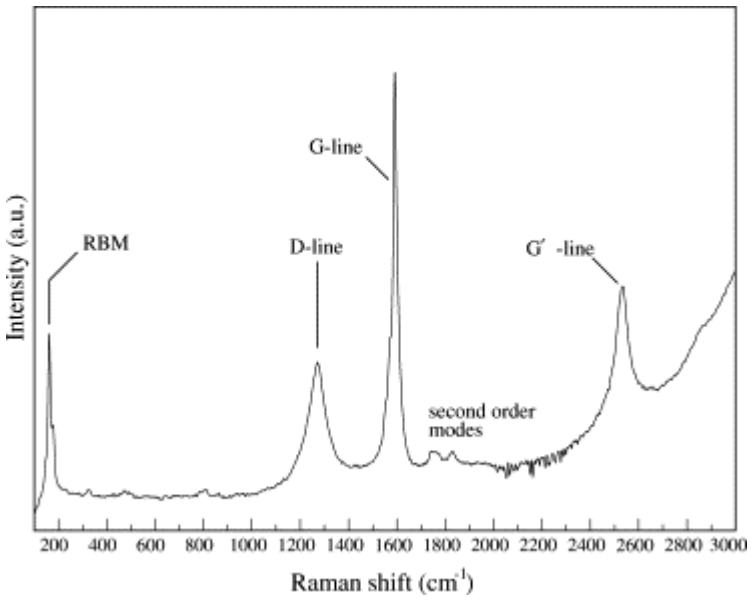

Figure 3.3 Example raman spectra of a CNT showing its characteristic features[254]

The RBM is characteristic of small diameter CNT (<2 nm), and occurs around 200 cm^{-1}. Whilst this band can typically be seen for SWNT, it can also be seen in MWCNT if the inner diameter of the tube is less than 2 nm. In most cases however this band is not visible in the Raman spectra of MWCNT. [255]

The D band, a group of peaks around 1340 cm^{-1}, are typically assigned to defects in the graphitic layer with the intensity of the D band related to the disorder of the sample. The G band, a group of peaks in the 1550-1600 cm^{-1} region, corresponds to the tangential vibration of the carbon atoms, and its intensity is a good measure of the graphitisation of a material. This band is a single peak at 1582 cm^{-1} for graphite, and is considerably less intense in MWCNT than SWCNT. The ratio of the D and G bands is commonly used as a measure of the purity of MWCNT. [255]

The G' signal typically occurs at around 2600 cm^{-1}, is an overtone of second order harmonic of the D-band. The presence of this band indicates that there is long range order in the sample, and can be used as a good measure of the purity of the sample, as it is sensitive to the presence of defects. [256] In addition to these signals there are a number of other second order signals between 1600 and 1800 cm^{-1}, these signals have low intensity and have not been the subject of much study. [255]

3.2 Thermo-gravimetric Analysis

Temperature programmed oxidation (TPO) experiments were carried out in a thermo-gravimetric analyser (TGAQ500, TA-instruments). Samples of carbon coated cordierite were ground into a fine powder and thoroughly mixed using a pestle and mortar, before weighing 20 mg into a crucible for testing. Powder samples were tested as produced. The temperature was ramped at a rate of 5 °C/min from room temperature to 900 °C in 100 ml/min of air for simple oxidation studies.

In order to ensure the sample taken for TGA was representative, the samples were well mixed before sampling. Due to insufficient time available on the TGA machine, it was not possible to perform repeats on all samples. Several samples were repeated and gave results which were the same ±10%. 10% was taken as the error in the TGA measurements.

3.2.1 Theory of Thermo-gravimetric analysis

Thermo-gravimetric analysis is a useful test to determine the purity and stability of CNTs.[255] Important features of a TGA curve are the initiation temperature (the temperature at which the sample starts to decompose), the oxidation temperature (typically defined as the point of maximum oxidation, determined from the highest point of the derivative of weight loss), the complete oxidation temperature (the point at which the sample does not lose further weight). The residual mass is also important, as the ash species remaining (typically metal oxides) can give an estimation of the percentage metal composition of the sample.

The presence of more than one peak in the derivative weight-loss is indicative of impurities, whilst the width of the peak can also indicate the purity of the material, with a narrower peak indicating a purer material. Oxidation temperatures of the different carbon materials are not very well defined, but it is generally accepted that amorphous carbon materials will decompose first at approximately 200-300 °C, followed by SWCNT at 350-500 °C and finally MWCNT at 400-650 °C. [255] The stability of the CNT can be influenced by the number of walls in the CNT, the length of the CNT, the presence of impurities such as residual catalyst particles and defects and the degree of crystallisation of the CNT.

3.3 X-Ray Diffraction

Powder X-ray diffraction (PXRD) patterns were recorded with Co $K\alpha_{1,2}$ radiation (1.79 nm) from 20° to 90° (2ϑ), typically at a scan rate of 1.34°/min, at ambient temperature using a Panalytical X'Pert Pro X-ray diffractometer. Experiments were performed in flat-plate mode.

In situ PXRD experiments were carried out using an Anton Paar XRK900 reaction chamber under flow conditions. Experiments were performed in flat-plate mode. Typically, the scan range was 25° to 65° (2ϑ), and the rate 1.34°/min. The system was flushed with helium, at a flow of 30 ml/min. Oxidation was carried out under a flow of 30 ml/min of air. Hydrogenation was carried out under a flow of 30 ml/min hydrogen. Reactions were performed under 30 ml/min H_2 and 10 ml/min CO_2.

XRD spectra were taken of a thin layer of sample, weighing approximately 8 mg for CNT samples. To ensure the sample was representative, the sample was well mixed before taking a small amount for XRD.

Thanks to Dr Phillip Landon and SASOL for providing access to XRD facilities and running the measurements.

3.3.1 Theory of X-Ray Diffraction

X-ray diffraction is a non-destructive technique to determine the structure of crystalline materials, by analysing the patterns of diffracted X-ray beams after being passed over the material. Different crystal structures will give different diffraction patterns dependant on the position of the atoms in the crystal. This can be simply described using Bragg's law. Diffraction patterns for the compounds detected were obtained from a database of example patterns.

The size of particles detected can be determined using the Scherrer equation, this relates the broadening of a peak, to the size of the particles detected. The Scherrer equation only applies to crystals less than 0.1 µm in size. For very small particles (*circa* 4 nm), peak broadening may be so significant that the equation cannot be applied.

$$\tau = \frac{K\lambda}{\beta \cos\theta} \tag{3.1}$$

Where: τ is the mean size of the ordered (crystalline) domains, K is a dimensionless **shape factor.** The shape factor has a typical value of about 0.9, but varies with the actual shape of the crystallite, λ is the X-ray wavelength; β is the line broadening at half the maximum intensity (FWHM), after subtracting the instrumental line broadening, in radians, ϑ is the Bragg angle

3.4 Surface Area determination

Brunauer–Emmett–Teller (BET) specific surface areas (N_2, 77 K) were obtained from low pressure (up to 1 bar) nitrogen sorption measurements at 77 K using a Micrometrics ASAP 2020 volumetric gas sorption analysis system. The specific surface area was calculated according to the British Standard guidelines for the BET method from regression analysis of data in the relative pressure range from 0.05 to 0.3.[257] Samples were degassed at 200 °C under dynamic vacuum for 12 hours prior to analysis. As the samples analysed were generally low density, and had low surface are, the sample tubes were filled with as much sample as possible, weighed then analysed.

Thanks to Dr Valeska Ting, Dr Tim Mays at the University of Bath, and Mrs Carol Reed at Sasol for providing BET facilities

3.4.1 BET Theory

BET theory provides a simplified model for the adsorption of gas molecules onto a surface, and is used to calculate the surface area of materials. Based off the Langmuir equation (3.2), which relates the coverage of the surface to the gas pressure assuming that all gas layers are absorbed on one layer.

$$\theta = \frac{KP}{1 + KP} \tag{3.2}$$

Where θ = fractional coverage of the surface P = gas pressure K= k_a/k_d where k_a= the rate of absorption onto the surface and k_d = the rate of desorption from the surface

The BET equation (3.3) extends this model to a multi-layer system. The BET equation makes 3 assumptions, that gas molecules can physically absorb to a solid surface in layer infinitely, that there is no interaction between the layers and that the Langmuir theory can be applied to each layer.

$$\frac{V}{V_{mon}} = \frac{cz}{(1-z)(1-(1-c)z)} \tag{3.3}$$

Where V= the absorbed gas quantity V_{mon} = the monolayer absorbed gas quantity c = BET constant and where $z = p/p_0$ where p= equilibrium pressure and p_0= saturation pressure

From this, the surface area of the sample can be determined from the absorption cross section of the absorbing species, in most cases nitrogen, using the following equation (3.4).

$$S_{BET} = \frac{v_m N s}{V a} \quad (3.4)$$

Where V= the absorbed gas quantity V_{mon} = the monolayer absorbed gas quantity N = the Avogadro number s=the absorption cross sections of the absorbing species and a = the mass of sample

3.5 Scanning Electron Microscopy

Scanning electron microscopy (SEM) was normally carried out using a JEOL SEM 6480LV operating at 5 - 20 kV acceleration voltage. Higher resolution SEM was carried out using a JEOL FESEM 6301F operating at 5-20 kV acceleration voltage. Monolith samples were mounted on a stainless steel disc using double sided sticky carbon tape. Images were typically taken in secondary electron image (SEI) mode.

The resulting micrographs were analysed using Image J, a public software used for image analysis. The thickness of the carbon layer was measured from the monolith wall to the tips of the nanotubes, to ensure reproducibility at least two samples were imaged, and the layer thickness was measured at 100 points across the sample before being averaged to give the layer thickness. The standard deviation of the measured points was used to determine error. It is noted that in a number of places on the sample the carbon layer at the edge of the sample can be damaged whilst handling, leading to occasional points where carbon was not present, for obviously damaged parts of the layer, thickness was not measured. It is also to be noted that the exact position of the monolith wall could not always be observed due to carbon growth in the direction of the electron beam

Thanks to Dr John Mitchells and the Microscopy and Analysis Suite at Bath for technical support and training whilst using the microscopy facilities at Bath.

3.5.1 Theory of Scanning Electron Microscopy

Scanning Electron Microscopy scans an object with a beam of electrons, in order to gain information about the object surface topography and composition. [251] There a number of different modes which can be used, but typically SEI mode is used. This mode detects the secondary electrons emitted by atoms excited by the electron beam. The number of electrons emitted is a function of the angle between the electron beam and the surface and so the SEI signal provides primarily information on the topography of the sample. [258]

3.6 Transmission Electron Microscopy

CNTs were characterised using a transmission electron microscope (TEM, JEOL 1200) operated at 200 kV. High resolution TEM images were obtained using a CM200 operated at 200kV. Samples for TEM analysis were mechanically detached from the monolith, dispersed in ethanol and deposited onto Cu or Ni grids. Samples were analysed in bright field mode. Energy dispersive X-ray (EDX) spectroscopy was performed using an Oxford Instruments X-max 80 mm^2 SDD EDX detector running Aztec software.

Thanks to Dr Zabeada Aslam and the Leeds EPSRC Nanoscience and Nanotechnology Facility, for providing access to higher resolution TEM coupled with EDX analysis. Thanks to Dr John Mitchells and the Microscopy and Analysis Suite at Bath for technical support and training whilst using the microscopy facilities at Bath.

3.6.1 Theory of Transmission Electron Microscopy

TEM is another electron microscopy technique, but this time the beam of electrons is passed through an ultra-thin sample, interacting with it as it passes through. TEM is capable of imaging samples at very high resolutions, up to the sub-nanometre scale. The most common method of analysis is bright field analysis, where absorption of the electrons passing through the sample results in an image of various intensities. Areas of the image with high atomic density or thickness will appear darker, whereas areas with low atomic density will be bright.

Energy dispersive X-ray (EDX) spectroscopy is an analytical technique for the elemental analysis of a sample, which can easily be coupled with TEM. Upon excitation of the sample with a high energy beam of electrons, an electron can be excited from the inner shell to the outer shell. On relaxation of an outer shell electron to fill the resulting electron hole, an X-ray is emitted with the energy equivalent to the gap between the two shells. The energy of the resulting X-ray beams is characteristic for each of the different elements, allowing us to identify the elements present.

3.7 Gas Chromatography – Mass Spectroscopy

After sampling the reaction products in a 50 ml SGE gas tight syringe with luer-lock fittings, the sample was then injected into an Agilent GC-MS equipped with a HP-Plot Q column, as well as an FID (Flame Ionisation Detector), TCD (Thermal Conductivity Detector), and MS (Mass spectrometer) for analysis. The HP-Plot Q column, is a polystyrene-divinylbenzene based column, which is designed to separate polar and a-polar compounds. It is designed to separate hydrocarbons (in the C_1-C_3 range), CO_2, air, water and polar solvents. Though not

specifically designed for this purpose it is capable of separating hydrocarbons in the C_1-C_7 range. It is not capable, though, of separating nitrogen, oxygen, carbon monoxide or argon which all have very similar retention times.

The temperature program used to heat the column is shown in Figure 3.4 with typical retention times marked.

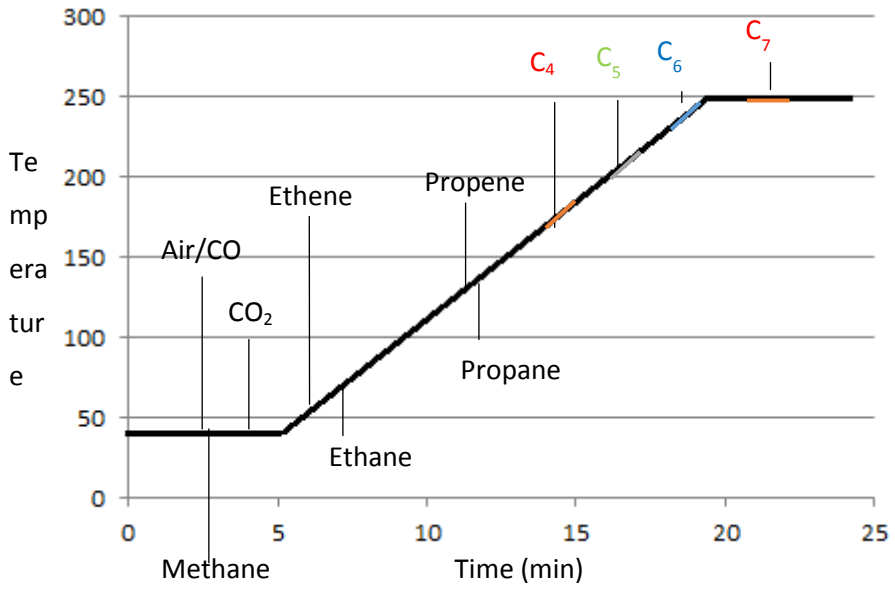

Figure 3.4 Temperature program of GC run with typical retention times marked

The GC-MS was calibrated with a BOC special gas with 1 % v/v of CH_4, C_2H_6, C_3H_6, C_3H_8, n-C_4H_{10}, CO, CO_2, and N_2 makeup gas (see Figure 3.5 for typical GC traces for the calibration gas on the three different detectors, see Table 3.1 for typical response and retention times).

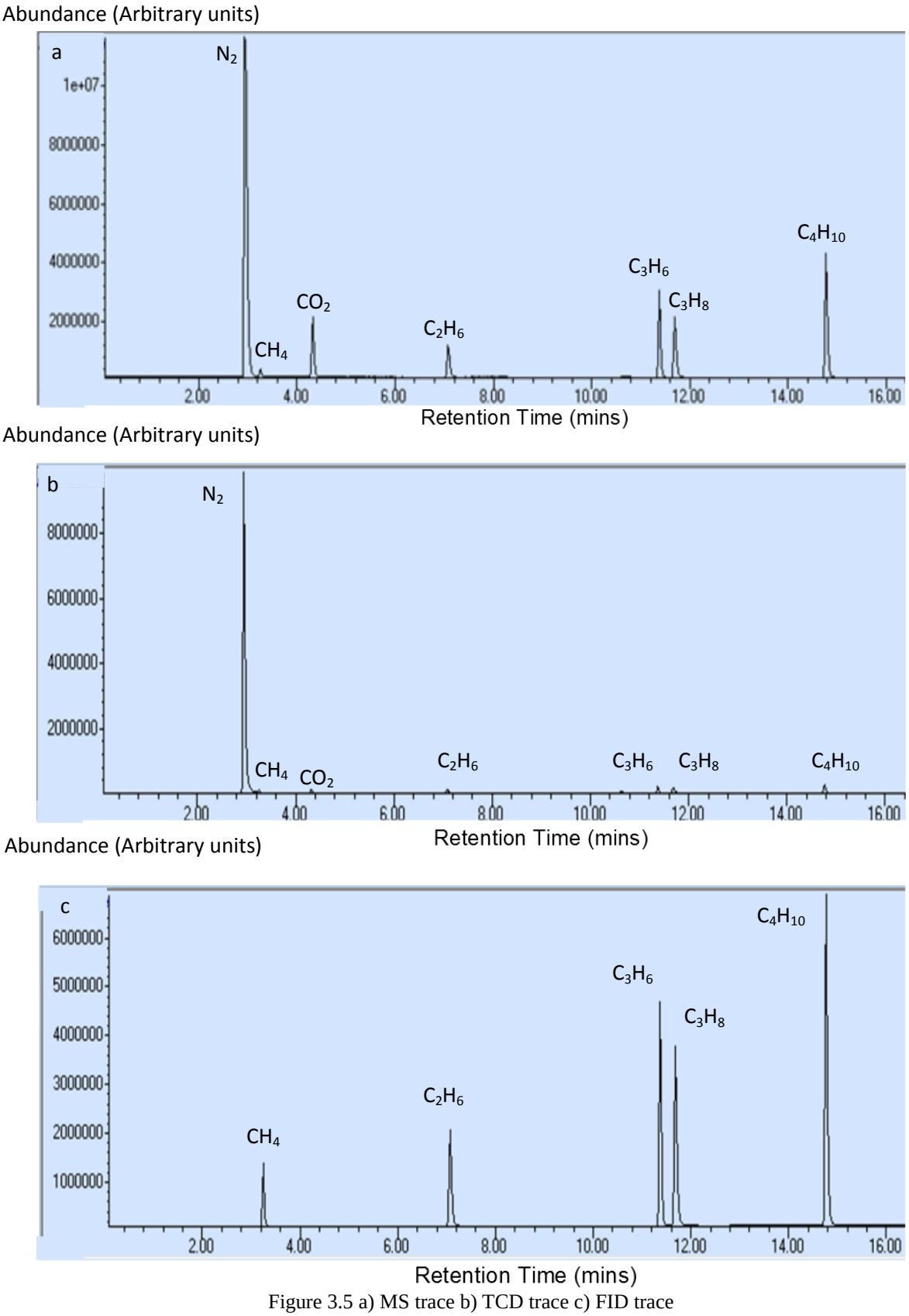

Figure 3.5 a) MS trace b) TCD trace c) FID trace

Table 3.1 Typical Retention times and responses for calibration gases

Gas	Retention Time / min	MS Response/ Arbitrary Units	FID Response/ Arbitrary Units
CH_4	3.25	7.10×10^6	3.22×10^7
CO_2	4.32	6.43×10^{7i}	N/A
C_2H_6	7.08	4.16×10^7	7.21×10^7
C_3H_6	11.37	8.76×10^7	1.32×10^8
C_3H_8	11.69	7.78×10^7	1.36×10^8
$n\text{-}C_4H_{10}$	14.77	5.33×10^7	2.19×10^8

Response factors for each of the hydrocarbons were calculated from the peak areas for both the MS and FID. The response factors for C4+ hydrocarbons for which no calibration sample existed were estimated: The FID signal response is roughly equivalent to the number of carbon atoms in the molecule; therefore plotting the C1-C4 hydrocarbon response factors gives a linear trend (see Figure 3.6) This trend was extrapolated to higher hydrocarbon numbers, using the Microsoft Excel TREND function, to give estimated response factors for larger hydrocarbons. It is noted that different hydrocarbon isomers will give slightly different responses but this difference is negligible (as can be seen by the very similar response FID factors for propene and propane in Table 3.1).

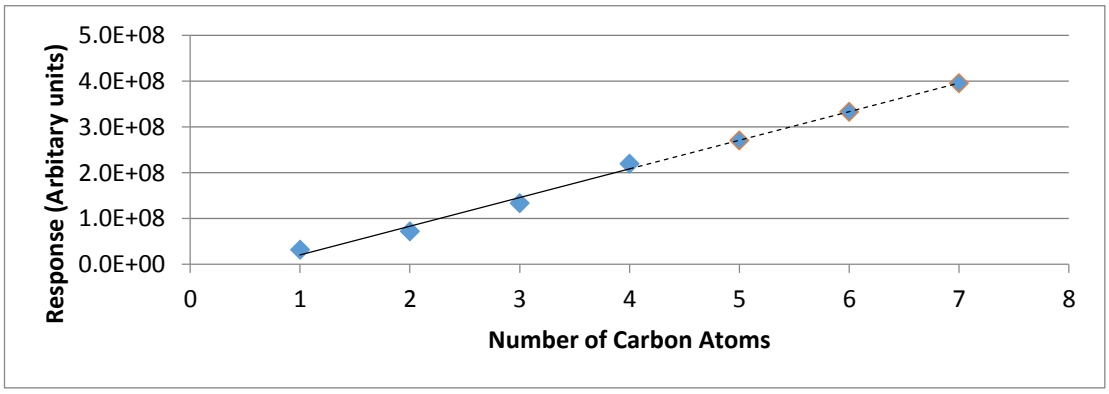

Figure 3.6 Response factor of FID detector to 1 mol% of hydrocarbons, in relation to carbon number

The response factor for CO_2 was calculated from the peak area in the MS. Although CO could not be separated from the N_2 makeup gas, tests with 50:50 mixtures of CO_2 and CO showed that both had similar response factors. As a consequence the response factor for CO_2 was used to calculate the amount of CO produced.

Calibration was repeated before each reaction to ensure accuracy, and guard against detector drift. The identity of each of the calibrant gas peaks was confirmed by analysis of the mass fragments detected by the mass spectrometer to determine the most likely compound. Products which appeared in analysis of real gas samples were also identified from mass fragments, and an appropriate response factor assigned.

Conversion of carbon dioxide was determined with reference to the external standards. Whilst a method using an internal standard would have been preferred, the difficulties encountered separating the typical internal standard gases nitrogen and argon from carbon monoxide, meant an internal stand method would have been impractical for a one column analysis. No columns were available which were capable of separating both the inert gases such as nitrogen, argon, carbon dioxide and carbon monoxide and the higher hydrocarbons.

Ideally a two column system would have been used, with gases such as argon, air and carbon monoxide separated using one column, and higher hydrocarbons separated using a second column. However as the GC-MS system was utilised by other users, and no other GC were available a more general column was required to separate all molecules in one analysis. Therefore the decision was made to do the analysis without an internal standard, and use external calibration.

Determination of the CO_2 conversion inherently contains some error, as it requires using extrapolated calibration factors. Though this procedure is common, some error will be introduced as a result. The absence of an internal standard, can also lead to some variation in the detected carbon balance. Repeating experiments showed that conversion remained the same within ±10%, this error was used as standard for those which were not repeated.

The amount of each compound detected was determined, using the response factors indicated above, to calculate the molar percentage of each compound present using equation (3.5).

$$\frac{A_a}{RF_a} = n_a \, mol\% \tag{3.5}$$

Where A= Peak area RF= Response Factor a = compound of interest and n= mole fraction

Where more than one carbon atom was present in a molecule, the amount of CO_2 converted to give this molecule was determined, as in equation (3.6).

$$mol\ \%\ HC_{(x)} * \ x = X_{CO_2} \tag{3.6}$$

Where HC=hydrocarbon; x= number of carbon atoms in hydrocarbon and X_{CO2}= mol fraction of CO_2 converted to give hydrocarbon

The total conversion of CO_2 was determined using equation (3.7).

$$\frac{\sum X_{CO_2}}{n_{CO_2} + \sum X_{CO_2}} = C_{CO_2} \tag{3.7}$$

Where X_{CO_2}= mol fraction of CO_2 converted to give products nCO_2 = mol fraction of CO_2 detected C_{CO_2}= CO_2 conversion

Selectivity was determined with respect to moles of carbon incorporated into the final product, using equation (3.8)

$$\frac{M_{product}}{M_{CO_2}} = \ S_{CO_2} \tag{3.8}$$

Where $M_{product}$ = mol of carbon in product M_{CO_2} = mol of CO_2 converted S_{CO_2} = Selectivity with respect to CO_2

Hydrocarbon selectivity or the selectivity to a particular hydrocarbon from all the hydrocarbons formed was determined using equation 3.9.

$$\frac{M_{product}}{M_{HC}} = \ S_{HC} \tag{3.9}$$

Where $M_{product}$ = mol of carbon in product M_{HC}= mol of CO_2 converted to HC and S_{HC} = Selectivity with respect to total hydrocarbons

Olefin to paraffin ratio was determined as a fraction of carbon containing units with more than one carbon, using equation

$$\text{Olefin fraction} = \frac{m_{x_{2=}}}{m_{x_{2=}} + m_{x_2}} \quad (3.10)$$

Where $m_{x_2=}$ = mass of olefin containing 2 or more carbon units and $m_{x_{2=}} + m_{x_2}$ = total mass of carbon units with 2 or more carbon units

Observed rate of reaction was determined using equation

$$R_{obs} = \frac{X_{CO_2} * n}{g_{CNT}}$$

Where R_{obs}= observed rate of reaction g_{CNT}= grams of CNT catalyst n = moles of CO_2 per second X_{CO2}=conversion of CO_2

3.8 Mass balance

Determining the mass balance of the reaction is important, as this confirms that all products produced are detected. Limitations of the characterisation equipment used, mean that obtaining a full mass balance of the reactants and products is not possible. The limitations of the experimental method, and the efforts made to ensure that the mass balance is as accurate as possible are discussed here.

In order to obtain a full mass balance, the consumption of hydrogen, and the production of water must be monitored. The use of helium as a carrier gas does not allow the detection of hydrogen gas, as hydrogen and helium have very similar thermal conductivities preventing the TCD from being used to determine hydrogen content. The use of a nitrogen carrier gas would allow the detection of hydrogen, but would reduce the effectiveness of the GC-MS detection (and also increased difficulty in detecting carbon monoxide).

Water produced in the reaction is always detected in the GC-MS trace. This peak has not been calibrated, as the GC-MS detector is sensitive to water, calibration of the peak would require the introduction of significant amounts of water into the GC-MS which could potentially damage the detector. Coupled with the inability to detect hydrogen, it was determined that the risk to the GC-MS detector was too great to allow the calibration of the water peak. These limitations mean that obtaining a full hydrogen balance, and hence a full mass balance for the reaction is not possible.

The carbon balance for the reaction can be obtained more easily, as known carbon products can be detected. The major detected products are CO_2, CO, CH_4 and C2-C8 hydrocarbons, of various degrees of saturation and branching. Other possible products that could be formed in the reaction are the higher hydrocarbons C9+, these hydrocarbons would not elute in a typical 25 run, but would be expected to come off at a later time during subsequent runs. Analysis of GC traces has not revealed the presence of any of these unexpected peaks.

C8+ hydrocarbons can also condense to form liquids, and with very high chain length hydrocarbons forming solid waxes. If these are formed they would not be detected by the gas phase analysis technique. In order to rule out the formation of these hydrocarbons, the gas was flowed through a cold trap consisting of ethanol cooled to 0 °C, hydrocarbons formed would dissolve in this liquid. This trap was installed into the reactor system and various reactions were run over a week (25+ hours of operation), the ethanol in the trap was then analysed via GC-MS to determine whether any higher hydrocarbon products were detected. No hydrocarbon products were detected, suggesting that any products formed are produced in insignificant amounts which will not impact on the carbon balance.

Oxygenates, such as alcohols, aldehydes, ketones and carboxylic acids have been observed to form in some reductions of CO_2 with hydrogen. These oxygenates would also be detected by the GC-MS column under the conditions used. Using oxidic catalysts not mentioned in this thesis, some oxygenates have been detected and identified by mass fragment analysis, but no oxygenates were detected for the Fe/CNT catalysts.

One final product of the CO_2 reaction which could form is coke, or amorphous carbon deposits onto the iron catalyst. This is very difficult to detect on CNT catalysts, as the formation of a layer of coke cannot be determined by traditional analysis techniques, as there is already a large amount of carbon present. For this study the absence of coke formation has been assumed, as transmission electron microscopy images of the catalyst after reaction do not reveal the presence of an amorphous layer of carbon, suggesting coking is minimal.

The carbon balance was determined using equation (3.11).

$$\frac{n_{CO_2} + \sum X_{CO_2}}{M_{CO_2}} = D_{CO_2} \tag{3.11}$$

Where X_{CO_2}= mol fraction of CO_2 converted to give products n_{CO_2} = mol fraction of CO_2 detected M_{CO_2}= mol % CO_2 in reactor stream and D_{CO_2}=% carbon detected

The carbon balances were closed to within 10%, carbon balances obtained were between 90 and 110%. Errors in the carbon balance can be the result of inaccuracies in the response factors obtained, and the introduction of small amounts of air, which will result in disproportionate amounts of CO detected. As there is no internal standard it is difficult to fully close the mass balance, but all gases detected balance. It is possible that if some of the assumptions made above are incorrect, carbon would not be detected by the system resulting in further error in the carbon balances obtained.

3.9 Mechanical properties

Axial crushing strength was determined using an Instron 3369. A square monolith piece (0.6 cm × 0.6 cm) was placed under a 1 kN load and the pressure was slowly increased until the wall crumpled. The measurement was repeated five times to ensure accuracy. Crushing strength was only measured along the x axis, compression along the y or z axis resulted in almost instantaneous collapse of the monolith structure (Figure 3.7).

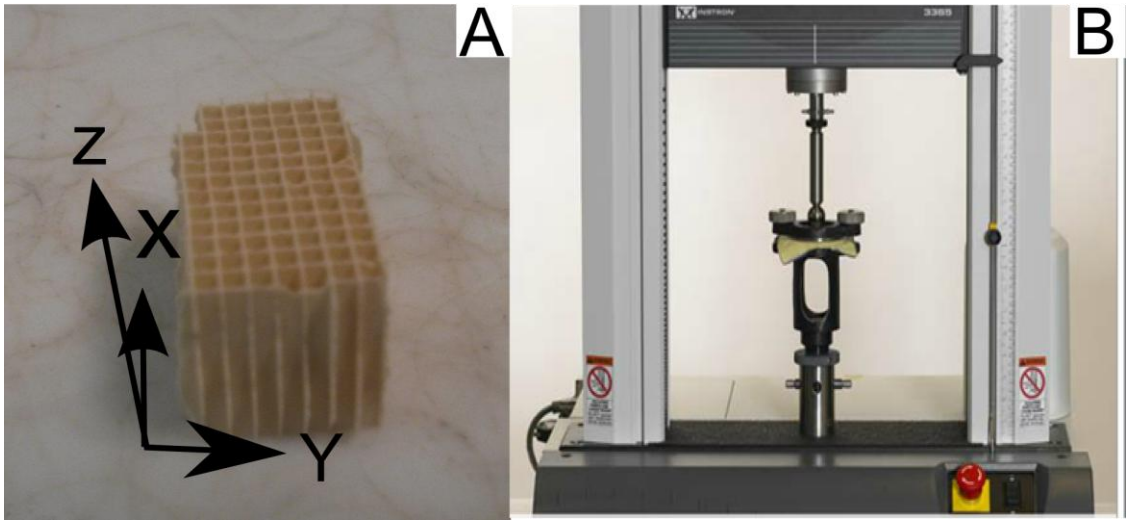

Figure 3.7 a) Cordierite monolith with x, y z axis b) Instrom 3369

3.10 Pressure Drop measurements

Pressure drop was determined via two methods. First during the reaction a pressure transducer was placed at the entrance of the reactor, whereas the backpressure transducer also measured the pressure. For specific pressure drop measurements a system was set up (Figure 3.8) consisting of two pressure transducers on either side of the metal reactor. A flow of air was passed through this reactor using a mass flow meter to determine the flow-rate. Pressure was recorded for both pressure transducers, with the difference between the two recorded as the pressure drop. The pressure transducers and mass flow controllers were calibrated to minimise error.

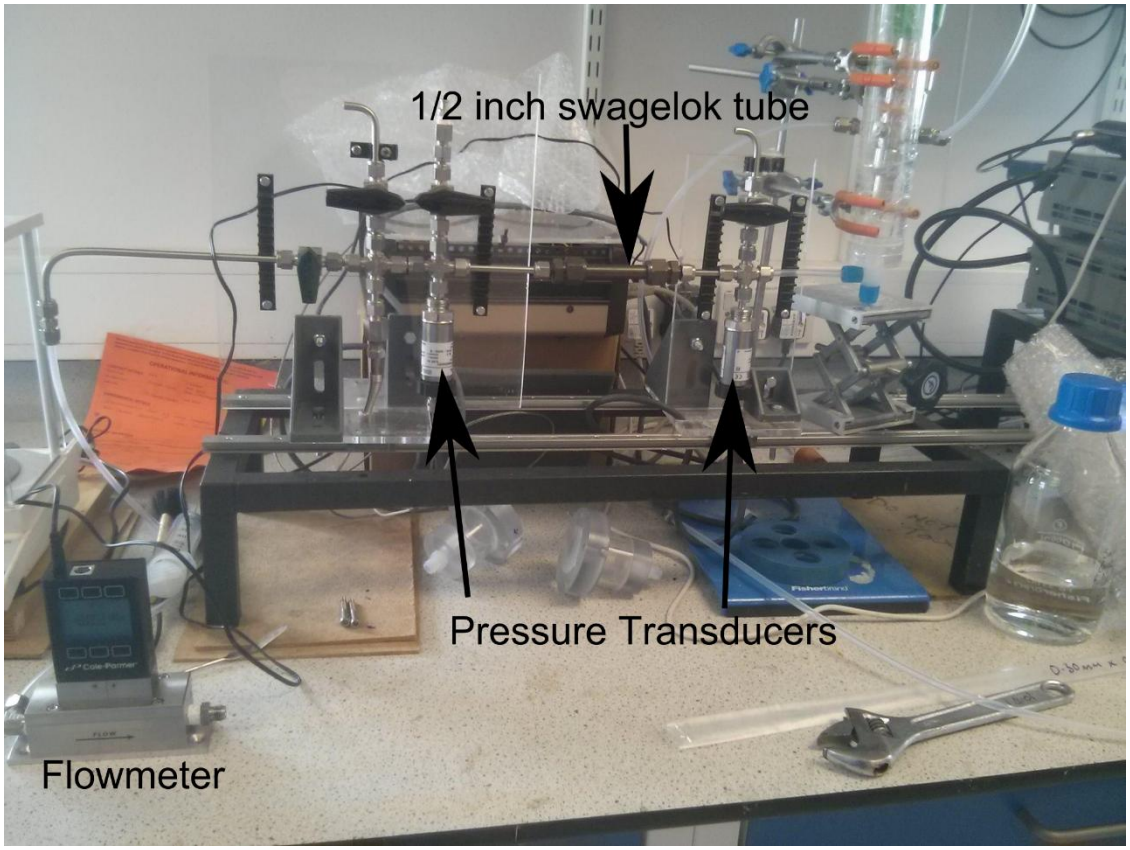

Figure 3.8 System for measuring pressure drop

4 Synthesis of Carbon Nanotubes

The synthesis of multi-walled carbon nanotubes can be performed via a number of different methods, using a variety of different manufacturing techniques. The most common methods and techniques used in the literature are discussed in detail in section 2.1 . The two synthesis methods used in this work are discussed in this chapter with a description of the experimental set-ups constructed, a discussion of the merits of the different techniques, and observations on efforts to achieve uniform MWCNT synthesis in sufficient quantities for catalysis.

4.1 Safety whilst handling and disposing of carbon nanotubes

Section 2.2 discusses the potential dangers associated with MWCNT and specifically highlights the concerns associated with the inhalation of high aspect ratio MWCNTs. In order to ensure safety, whilst handling CNTs, a N95 particulate respirator was worn as recommended by the National Institute of Occupational Safety and Health (NIOSH) for working with MWCNT, to reduce the risk of inhaling carbon nanoparticulates. [259]

When disposing of CNTs, nanotube waste was typically incinerated at 730 °C in air for 3 hours under extraction to ensure complete decomposition of the CNT waste. The quartz tube in which CNTs were grown was cleaned in acid, and washed in water. CNTs at greater than 0.1% w/w in water are recommended to be treated as hazardous waste, according to the latest guidelines. [140] When washing several litres of water are passed through the quartz tube, with a fraction of CNTs coming off in the water. Total CNTs produced are significantly less than a gram, so the concentration of CNT in water remains below this level.

4.2 Carbon Nanotube synthesis via floating CVD

Previous work in the lab [260] on the synthesis of CNT used the floating catalyst cCVD method, based on work performed by Liu *et al*. [83] A horizontal quartz tube (1 m × 2.54 cm outer diameter tube) was passed through the furnace, and heating rate, gas flow rate and growth times were controlled. Ferrocene ($Fe(C_5H_5)_2$, 98%, from Aldrich, 100 mg) was used as the catalyst and was placed at the entrance of the furnace in the quartz tube on a silicon wafer. Argon was used as the inert carrier gas, and ethene as the carbon source. Nanotubes were grown on 500 nm Silicon Oxide/Silicon wafer P/N type wafers, of varying sizes (1.5cm x 5-10 cm). These were placed at measured intervals along the furnace; a schematic of the system used is shown in Figure 4.1.

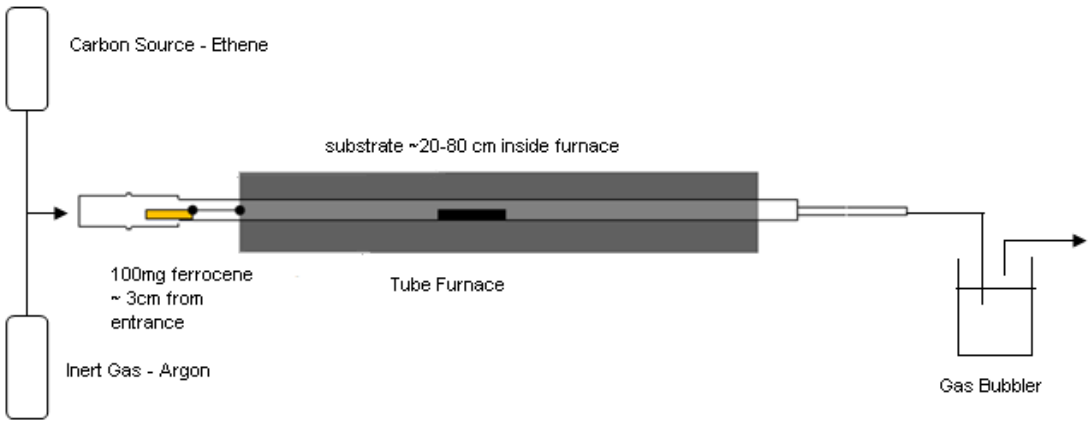

Figure 4.1 Schematic of the floating CVD reactor, the ferrocene catalyst was placed in a hot zone at the entrance to the reactor

The silicon/silicon oxide substrate was sonicated in acetone before use to ensure a clean surface. The resulting substrate was placed in the quartz reactor which was then inserted into the furnace. Before the furnace was turned on, argon (99.999% in purity) was introduced into the heating system at a flow rate of 300 standard cubic centimetres per minute (sccm) for 1 hour to eliminate the air in the tube, and ensure the substrate was fully dried. Then the system was heated at a rate of 60 °C min^{-1}. At the same time ethene gas was introduced into the system at a flow rate of 10 sccm with a constant argon flow rate of 300 sccm. Argon and ethene flow rates were controlled by mass flow controllers. Once the target temperature was reached the ferrocene catalyst was pushed all the way into the furnace to ensure complete sublimation. The ferrocene vapour was carried by the gas flow into the high temperature region where the pyrolysis of ferrocene and synthesis of the MWCNTs occurred at reaction temperature (between 750 and 1000 °C). The whole system was kept at the target temperature for 15 min, then the ethene gas was turned off and the system cooled down to room temperature in the flowing Ar gas. A graphical representation of the reactor program is shown in Figure 4.2.

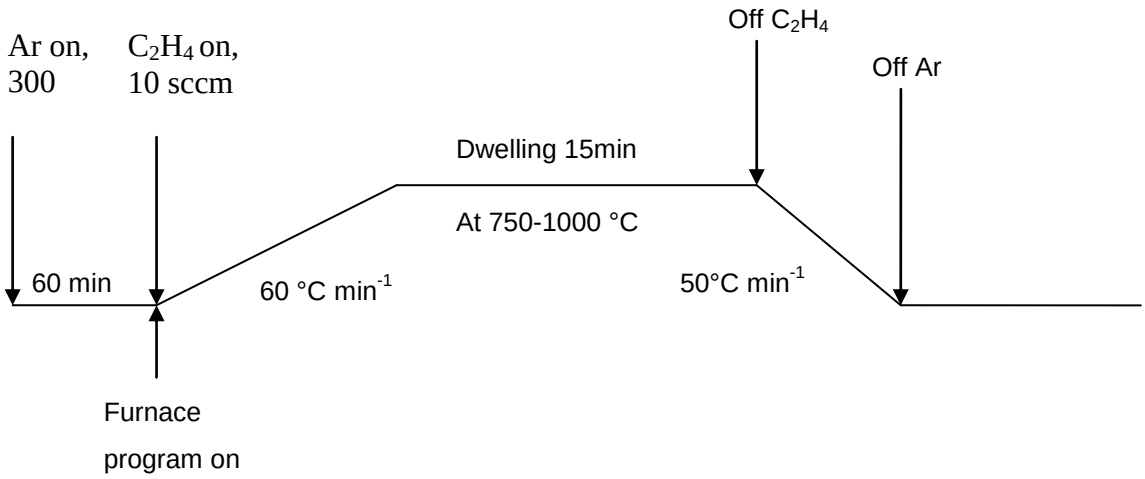

Figure 4.2 Graphical representation of the reaction program, showing the gas flow rate and temperature conditions used during a typical CNT synthesis

After reaction, the substrates were removed and analysed, first visually to determine whether a uniform layer of CNTs was formed, and then by Raman spectroscopy to confirm the production and quality of the CNTs. The quartz reactor was cleaned, first by oxidation of the remaining carbon deposit at 730 °C, and then cleaning with water and acetone.

An important safety consideration for this reaction is the use of a flammable gas (ethene) and an asphyxiant (argon). As ethene is present in the reactor at high temperatures, it is important to ensure that no oxygen is present in the system to prevent ignition. The system is flushed with argon for an hour before ethene is introduced, so no oxygen should be present at temperature. In case ignition does occur, a flashback arrestor is attached to the gas cylinder, to prevent ignition of the gas in it.

The entire system is vented through a gas bubbler (containing silicon oil) directly into the ventilation system, this prevents air entering the reactor from the exhaust, and also ensures that argon does not build up in the room and potentially hazardous carbon decomposition products are not released. The synthesis is performed in a well-ventilated room equipped with an oxygen depletion alarm in the event of a ventilation system failure.

4.3 Achieving consistent CNT synthesis

A number of problems were encountered using this initial synthesis method. Whilst synthesising a uniform carbon nanotube layer on the surface of the silicon dioxide could

occasionally be achieved, this process was not repeatable with the same conditions used often giving very different performance. This could easily be observed visually, as in Figure 4.3, where two silicon wafers are shown produced under the same conditions with one showing uneven growth across the silicon wafer, and the other showing relatively uniform growth. Other wafers showed no evidence of growth after introduction to the reactor under the same conditions.

Figure 4.3 Silicon wafers after growth at 850 °C for 15 minutes (left) demonstrating uneven growth across the wafer and (right) demonstrating uniform growth

A number of different factors were determined to potentially influence the synthesis process. Firstly, control of the ferrocene sublimation *via* this method is difficult, typically this synthesis method is performed using a 2-stage furnace, or even two different furnaces, with one furnace to sublimate ferrocene once reaction temperature has been reached (at 200 °C) and the second to bring the reactor to the synthesis temperature (over 700 °C). [80,83] Using only a single zone furnace, as in this work, such control is not as easily achieved, as such ferrocene would sometimes sublimate before the reactor reached the synthesis temperature, and slight changes in insulation and reactor position could result in premature ferrocene sublimation. In order to better control the ferrocene sublimation a Carbolite Wire Wound Three Zone Tube was purchased, this allowed greater control of the ferrocene sublimation, and reduced premature sublimation. The improved control of the ferrocene sublimation showed no improvement in the repeatability of MWCNT growth.

The second factor noted as a possible cause of poor growth was the choice of substrate. Silicon is known to cause a number of problems as a substrate in the synthesis of CNT, including poisoning the iron catalyst.[117] It was noted that even when no or poor growth was observed on the silicon wafer, growth was still seen on the walls of the quartz reactor. Using a quartz slide instead of a silicon wafer however resulted in no growth of CNT.

It was also observed that the quartz reactor slowly changed colour over prolonged use, developing an orange staining, as can be seen in Figure 4.4. This build-up of this orange colour was attributed to iron, from the residual iron catalyst left in the reactor from the CVD synthesis remaining after the carbon is burnt off.

Figure 4.4 Quartz reactor with heavy orange staining, this is attributed to residual iron

The build-up of iron on the quartz tube, over time led to preferential growth of CNT on the quartz walls over the silicon substrate. Repeating the synthesis using a new quartz tube without this iron staining resulted in the successful growth of a thin (~10 µm) CNT layer on the silicon/silicon dioxide wafers, as can be seen in Figure 4.5.

Figure 4.5 SEM micrograph of CNT layer produced via floating catalyst CVD method

To prevent this build-up a new cleaning procedure was implemented, to treat the quartz tubes using an acid bath after use. Firstly, repeated washing and brushing were used to remove as many of the deposited carbon nanotubes on the quartz tube as possible. Secondly the quartz tube was placed in a 1m by 32mm PVC-U tube, and then 500 ml of 28 % nitric acid was added. This was left for at least 24 hours in a fume cupboard, in the setup shown in Figure 4.6. Then after being extracted and washed thoroughly with water, and brushed to remove nanotubes, the quartz tube is then incinerated at 730 °C for 3 hours to remove any residual CNTs, before being washed and brushed again to remove residual iron. The removal of a quantity of CNT before incineration removes much of the iron before it is incinerated. The acid treatment helps remove residual iron on the nanotubes, and iron incorporated into the quartz tube wall. This procedure helps reduce the build-up of iron on the quartz tubes over time.

Figure 4.6 Experimental set up for soaking quartz reactors in acid to reduce iron build up, consisting of a polypropylene tube clamped upright in a fume-hood, the tube was filled with 28% nitric acid

To the best of the author's knowledge, the influence on iron staining on CNT synthesis has not been previously discussed in the literature. Ensuring that the quartz tube is sufficiently cleaned to limit build of iron incorporated into the walls of the quartz tube would seem to be an important factor in ensuring consistent CVD synthesis.

4.4 Characterisation of MWCNT produced by floating CVD method

Despite these improvements to the system, growth of carbon nanotubes was still problematic; the quantity of carbon nanotubes produced was very small with less than 10 mg formed on a 1 x 5 cm silicon/silicon dioxide wafer. Though a larger amount of carbon was deposited on the quartz wall of the reactor, TEM analysis of the carbon from the quartz walls indicated that a significant amount of soot-like particles, and carbon "onions" (metal nanoparticles surrounded by graphitic layers) were present in these samples with few CNT (Figure 4.7).

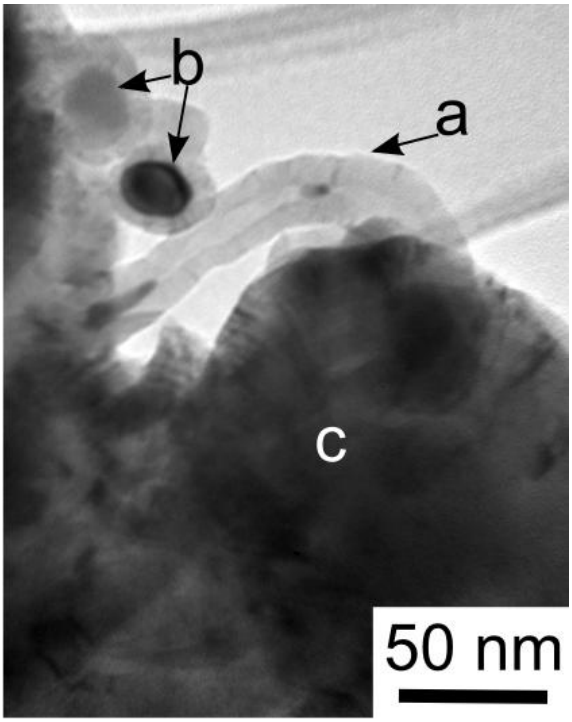

Figure 4.7 Representative TEM micrograph of carbon produced showing a) CNT b) carbon onions and c) amorphous carbon

Raman analysis of the carbon layer produced on the silicon wafers by this method, showed significant variance across the sample. Spectra taken at random intervals across the samples produced show significant differences (Figure 4.8). In some spectra, the silicon peak at 520nm is strongly visible, being the dominant peak, whereas at other positions the silicon peak can barely be detected, indicating a much thicker carbon layer in these positions. The intensity of the silicon peak with respect to the MWCNT peaks varies in intensity across the sample, confirming the non-uniform nature of the carbon layer synthesised.

The I_D/I_G ratio, and the $I_{G'}/I_D$ ratio also varies across the sample. The I_D/I_G ratio remains consistently high, with the ratio varying significantly from 0.75-0.95. This high I_D/I_G indicates

that the carbon produced incorporate a significant amount of amorphous material, as shown in the TEM micrographs previously. Despite that, in nearly all spectra the G' peak can be detected, confirming that some long range order exists and MWCNT have also been produced at most points along the silicon. The $I_{G'}/I_D$ ratio also varies significantly, from 0.43 to 1.08, suggesting that the CNT produced vary significantly in purity.

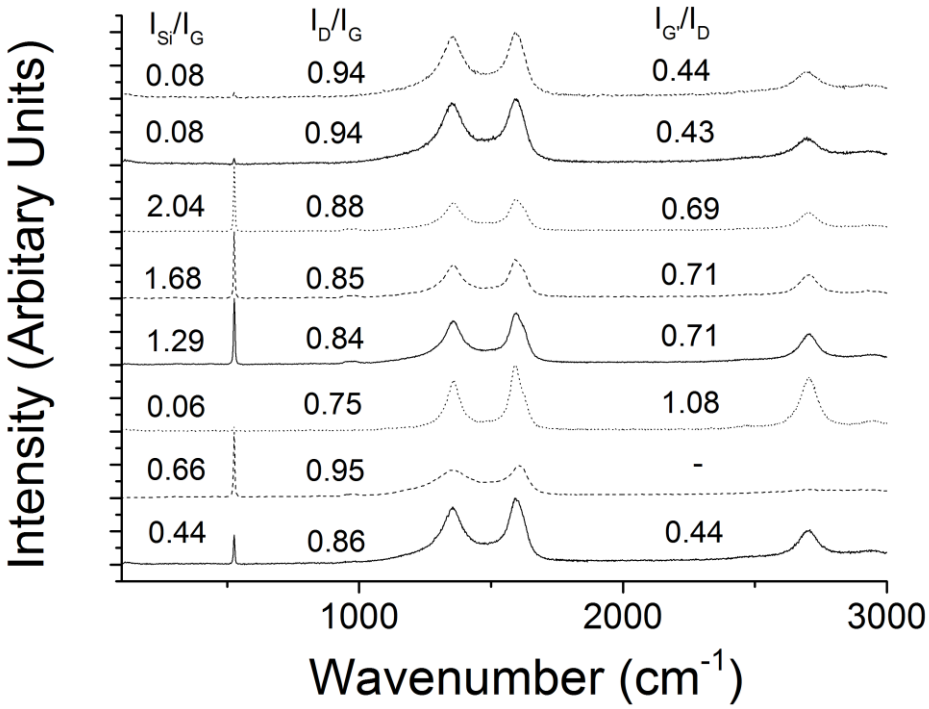

Figure 4.8 Raman spectra of CNT produced by floating CVD method on silicon taken at random intervals along the silicon substrate

Despite extensive optimisation of the floating CVD system, the total quantity of MWCNT produced was very low (<0.2 mg/cm^2 was produced in a typical reaction). The quality of the resulting MWCNT was also low, with significant quantities of amorphous carbon being produced. The reason for this uneven growth is unclear. One possible explanation is that the sublimation of the ferrocene catalyst does not result in a uniform distribution of ferrocene in the resulting gas stream. This means that the catalyst will not deposit uniformly across the silicon wafer, and so the resulting growth of the forest will be uneven. This effect may be even more pronounced when there is a layer of iron oxide on the quartz tube, which preferentially catalyses the ethane carbon source over the sparse amount of iron catalyst on the silicon wafer.

In order to perform catalytic tests, significantly greater quantities of higher quality MWCNT would need to be produced, with CNT production on the order of hundreds of milligrams being required. Production at the level provided by this process would have required weeks of CVD growth in order to provide enough catalyst for a single reaction. It was decided to explore other options in an attempt to increase MWCNT yield and purity. Exploration of the techniques available in the literature (Chapter 2.1) suggested that injection based floating cCVD was known to work well, so this option was chosen to be further explored. [67,84]

4.5 Carbon Nanotube Synthesis via Injection CVD

The injection based CVD method is based off work performed by Singh *et al.* [88] This method continuously injects the catalyst into the reactor, along with a suitable carbon source. This has several advantages including the ability to directly control when the catalyst is introduced into the reactor, and to continuously introduce fresh catalyst to the system.

The injection based system also used a Carbolite Wire Wound Three Zone Tube. A horizontal quartz tube (1 m × 2 cm outer diameter tube) was again used and heating rate, gas flow rate and growth times were controlled.

Ferrocene ($Fe(C_5H_5)_2$, 98%, from Aldrich, was again used as the catalyst. The carbon source was replaced with a benzene based derivative, which is known to be highly active for CNT growth. [104] A number of different benzene based derivatives have been previously used, such as xylene, toluene, ethyl benzene and iso-propylbenzene. [84,85,104] Ethyl benzene and iso propyl benzene have been reported to be among the most active carbon sources, but toluene was chosen as the carbon precursor as it is nearly as active, easily available, and relatively safe. [100,104] Typically 0.2 g of ferrocene was dissolved in 10ml toluene. This solution was injected into the reaction from a glass syringe, using an automated syringe pump, through a stainless steel needle. Argon was used as the inert carrier gas. The MFC were controlled using a custom Labview program, allowing gas flow rates to change automatically at set points, minimising error due to human factors. Nanotubes were grown on a substrate placed at measured intervals along the furnace; a schematic of the system used is shown in Figure 4.9, A Piping and Instrumentation diagram (P&ID) for this system is shown in Figure 4.10.

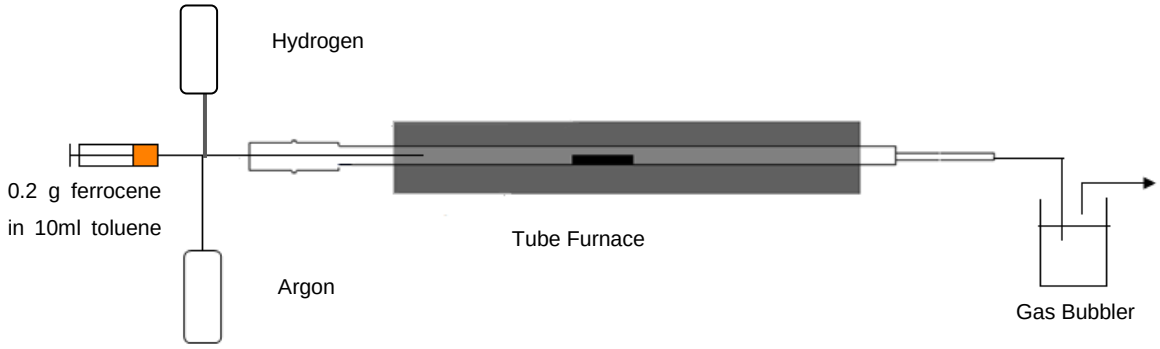

Figure 4.9 Schematic of injection reactor

A flow of argon (99.999% in purity) was introduced into the reactor at a flow rate of 50 sccm and the central zone was heated at a rate of 5 °C min^{-1}, ensuring complete elimination of oxygen and a uniform temperature gradient. After three hours, the target temperature had been achieved and stabilised. The flow of argon was then automatically increased to 450 sccm, and 50 sccm of H_2 were also introduced into the system. Hydrogen was used in accordance with the literature [100] in order to ensure the iron catalyst was reduced [108] and to inhibit growth of other amorphous carbon structures. [109]

The ferrocene/toluene mix was then injected into the reactor using an automated syringe pump to control the rate of injection in a zone typically at around 300 °C, the gas flow carrying the mixture into the heated zone where the pyrolysis of ferrocene and synthesis of the MWCNTs occurred at 790 °C. The system was kept at the target temperature for 1 hour, whilst the catalyst/toluene solution was continually injected at the rate of 10 ml/hour. After 1 hour the injection of catalyst was stopped, H_2 flow was stopped and argon flow was reduced to 50 sccm. This process was automated, with the gas flow timings controlled by a custom Labview program, the furnace was pre-programmed to follow the program shown below, and the syringe pump was also pre-programmed to inject at the appropriate time. The system was turned off and cooled down to room temperature under argon. The reactor program is shown in Figure 4.11.

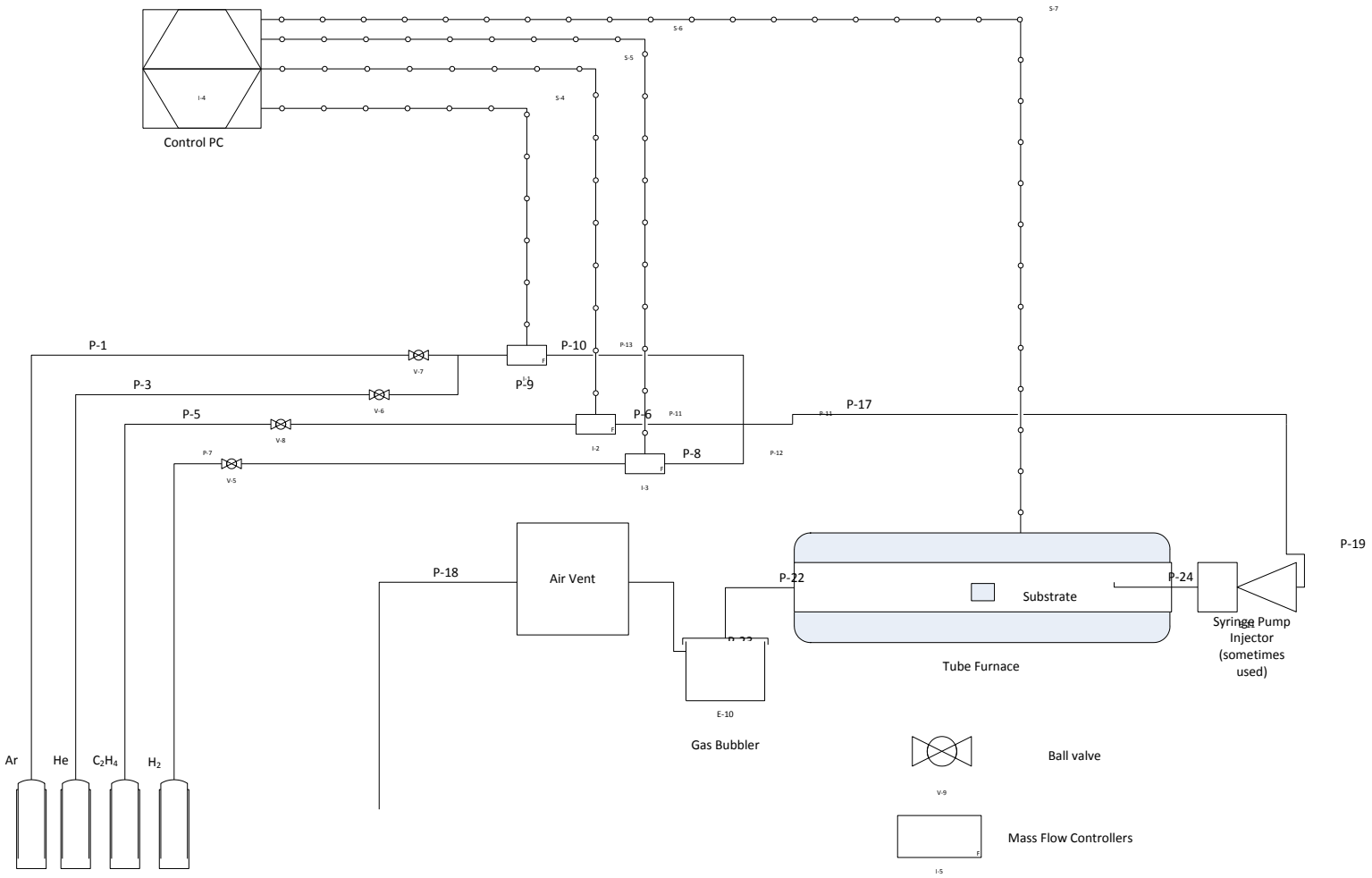

Figure 4.10 P&ID diagram of Injection CVD reactor

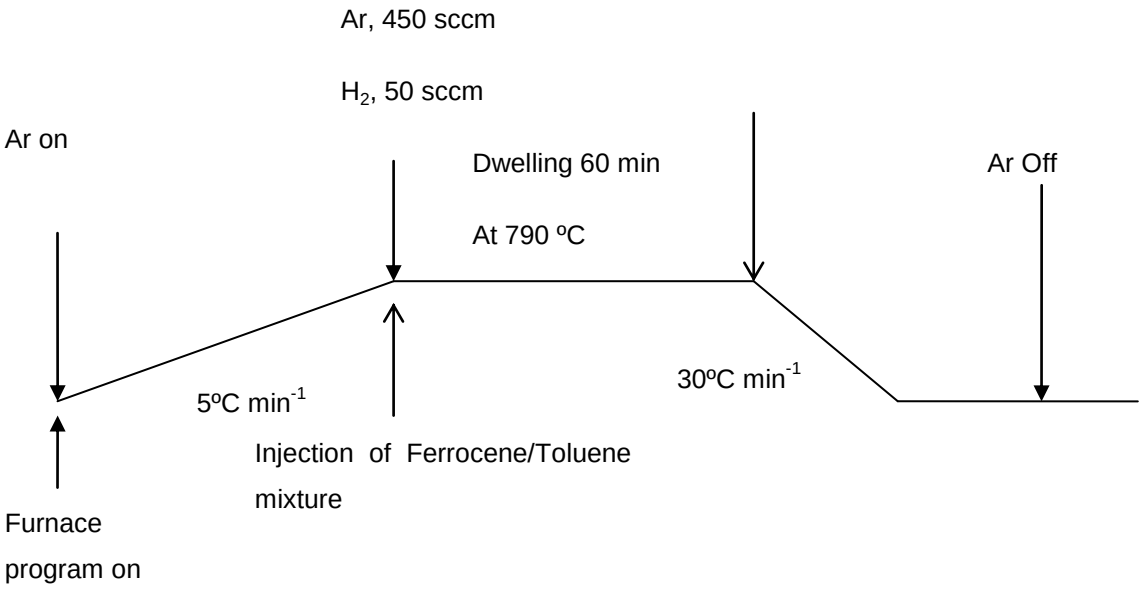

Figure 4.11 Graphical representation of the reaction program, showing the gas flow rate and temperature conditions used during a typical CNT synthesis

Safety aspects for this system are very similar to the previous one, with the use of an asphyxiant (argon) and a flammable gas (in this case hydrogen), so similar precautions are taken with the synthesis taking place in the absence of oxygen, and the whole system being ventilated. In addition to these hazards, the presence of the carbon source can cause some problems. Much of the work performed with similar CVD systems uses benzene as the carbon source, whereas toluene was used here as it is significantly less toxic and carcinogenic. Care is taken to avoid inhaling toluene vapours, and it was ensured that all materials exposed to toluene were resistant to its effects as a solvent, using glass, quartz and metal fittings rather than plastic where possible.

4.6 **Improved CNT synthesis**

Synthesis of carbon nanotubes using the injection based CVD technique, was more successful, with a thick aligned layer of CNT consistently being obtained on the silicon substrate, even when using iron stained quartz tubes (Figure 4.12). SEM micrographs clearly show the presence of a thick layer (~350 µm) of aligned CNT on the surface of the silicon wafer. This layer of CNT was uniform across the length of the typical 1 x 5 cm silicon pieces used as substrates. Repeated runs all demonstrated the presence of this layer of CNT. High-resolution SEM micrographs confirm that the CNT produced are highly aligned (Figure 4.12 b).

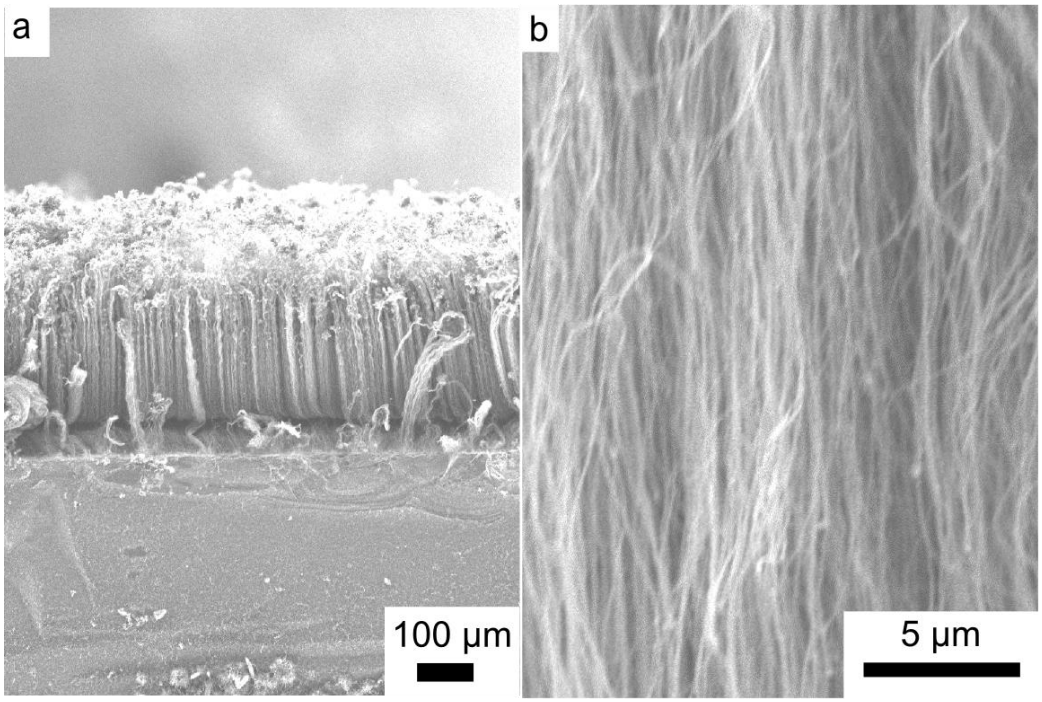

Figure 4.12 Figure SEM image of CNT growth on silicon for injection CVD method a) low magnification b) high magnification

The injection based CVD method introduces fresh catalyst continuously; this seems to counteract the effects of limited iron staining, with growth occurring on the silicon substrates despite iron staining. This may be due to the presence of a larger amount of iron in the system (200mg over 100mg), introduced in a controlled manner, meaning iron deposition is more controlled and uniform, reducing the effect of residual iron. The use of toluene, a more active carbon source than ethene may also play a role.

In order to ensure that the entire reactor was at the correct temperature, and the reactor inlet temperature was over 249 °C before injection (to ensure complete sublimation of ferrocene), the reactor was heated at 5 °C/min to 790 °C, and then kept at temperature for 30 minutes before injection, to ensure the reactor temperature had equilibrated. The length of reaction was also considerably longer, as with continuous injection of a fresh catalyst source, catalyst deactivation leading to inhibition of growth is much slower. As a result, the injection based CVD technique produced significantly more CNT, with 100 mg being produced on a 1 x 5 cm silicon piece after 60 minutes, compared to 10mg produced the floating catalyst CVD method.

4.7 Characterisation of CNT produced by Injection CVD method

Raman characterisation of the CNT produced by the injection CVD method (Figure 4.13) demonstrates the presence of relatively pure, uniform CNT, with a low I_D/I_G ratio of 0.32,

indicating the presence of relatively little graphitic impurities and a high $I_{G'}/I_D$ ratio of 2.41, confirming the presence of long range order. The silicon peak observed in the samples produced by the floating catalyst CVD method is not present, confirming the presence of a thick layer of MWCNT which the Raman laser cannot penetrate.

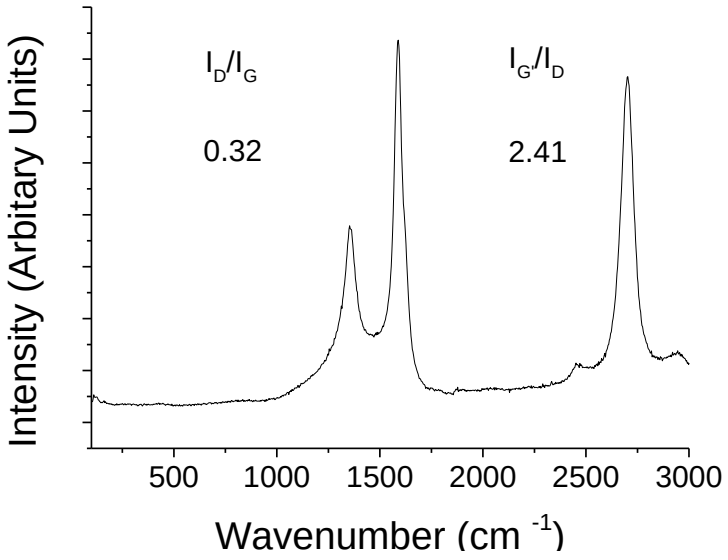

Figure 4.13 Raman spectra of typical MWCNT powder produced by the injection CVD method

Scraping off the black powder produced and analysing the resulting product using a TEM microscope also confirms the presence of MWCNT. The micrographs show the formation of straight nanotubes (Figure 4.14 a), unlike the branched [115] and disordered structures [173] observed by previous authors. TEM micrographs show the presence of darker spots, both inside the nanotube (Figure 4.14 b), and deposited on the outside of the nanotubes (Figure 4.14 c), these darker spots are attributed to the iron catalyst. The incorporation of iron nanoparticles in the bore and on the outside of the nanotube is well known, and provides supporting evidence of a base-growth mechanism. [100,101] The injection based CVD method continuously introduces fresh iron catalyst into the reactor, some of this excess is drawn up into the growing MWCNT and is thought to aid growth. This may counteract the difficulties encountered in the previous method where iron may have deposited non-uniformly on the substrate. By continuously injecting and dispersing ferrocene solution relatively uniform catalyst deposition is ensured. The remaining excess iron can deposit onto the outer surface of the nanoparticle, or increase the size of the catalytic nanoparticle. Too great an increase in the size of the resulting nanoparticle is thought to result in termination of growth. [101] The

nanoparticles deposited on the surface of the nanotube appear to be coated in a graphitic layer.

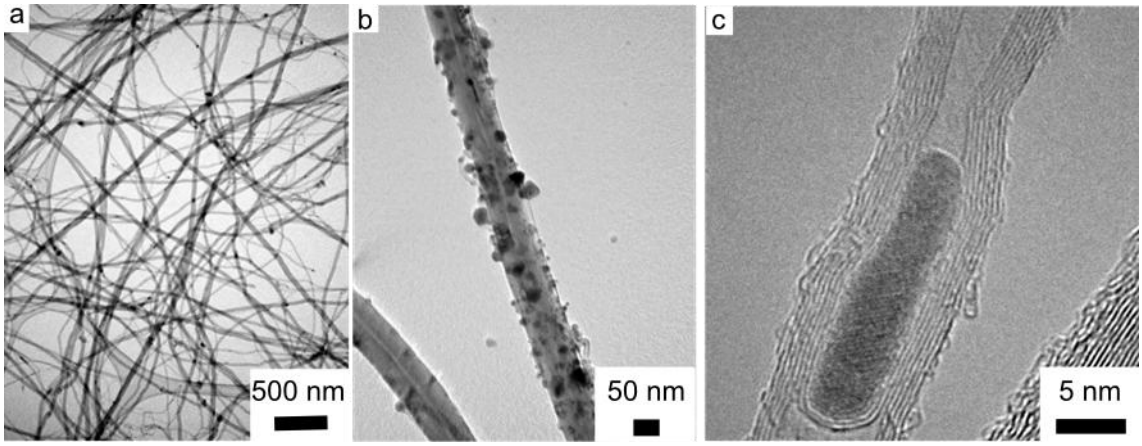

Figure 4.14 Representative TEM micrographs of MWCNT produced by injection CVD method a) low magnification b) micrograph showing nanoparticles enclosed in the nanotube and the nanotube walls c) micrograph showing nanoparticles deposited on the outside of the nanotube

The size of the MWCNT varied significantly, with an average diameter of 35 nm, and MWCNT as thin as 10 nm and as large as 65 nm recorded (Figure 4.15). The average length of CNT could not be obtained, as CNT produced were very long and entangled, meaning determination of the length of the CNT was impossible. Measurement of the CNT layer thickness on the silicon slide indicates that CNT length will be in excess of 100 µm in length.

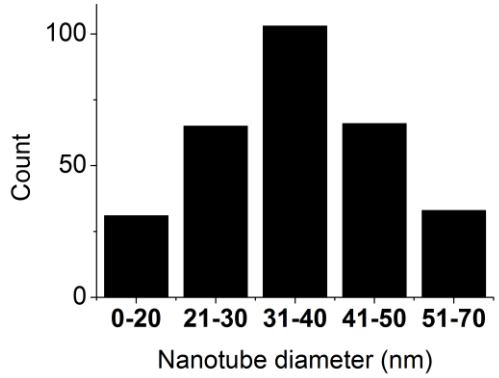

Figure 4.15 Distribution of MWCNT diameters produced by injection CVD method as determined by TEM micrograph analysis

The presence of iron in the MWCNT produced by this method was confirmed by XRD analysis of a typical sample of CNT powder (Figure 4.16). The XRD spectra includes several characteristic peaks centred around 56°, which would appear to suggest the presence of cementite, an iron carbide with the chemical structure Fe_3C, as well as a peak at 57° which may indicate the presence of metallic iron (though this is difficult to determine exactly as it is partially masked by the cementite peak). It also shows the presence of CNT, with a characteristic peak at 35°. [254]

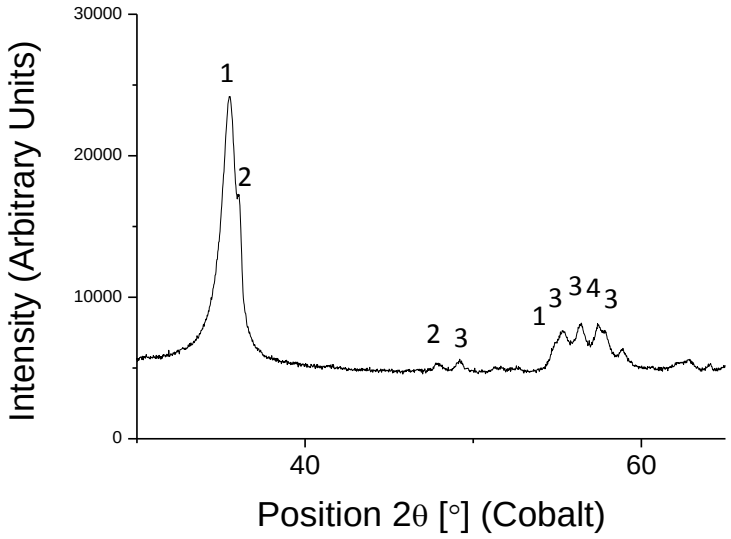

Figure 4.16 XRD spectra of MWCNT at 370 °C produced by injection based CVD 1)CNT 2) SiO_2 3) Fe_3C (cementite) 4) Fe (Iron metal)

Temperature programmed oxidation (TPO) confirms that a significant wt.% of the MWCNT is not consumed by oxidation up to 700 °C (Figure 4.17). Since carbon based species would be expected to have completely combusted by this temperature, this suggests that residual iron is responsible for the remaining wt.%., after combustion 31.3 wt.% of the initial mass of MWCNT. The phases of these iron oxide remains could not be easily determined and will consist of a mixture of Fe_3O_4 and Fe_2O_3, which are respectively 70 % and 72 % iron. This suggests that between 21.9% and 22.7% of the original MWCNT mass is iron, assuming a roughly equal mixture, this gives a value of 22.3% iron. This % mass of residual iron is higher than is normally reported for powder MWCNT, which is typically less than 10% for unpurified MWCNT, and around 3% for purified MWCNT, though these values can vary. [55]

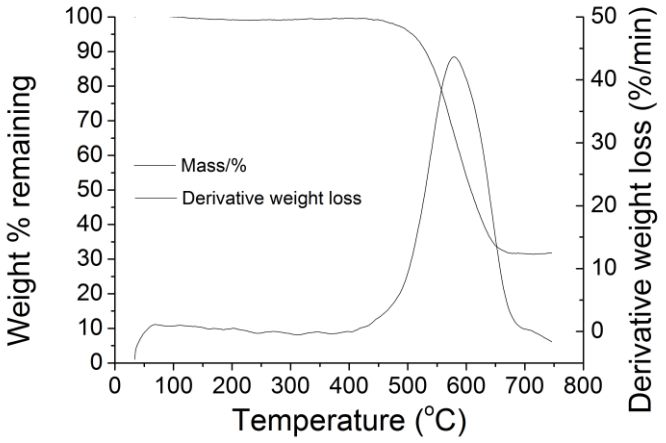

Figure 4.17 TPO of CNT powder sample, showing % weight loss of MWCNT with temperature, and the derivative weight loss

The combination of TGA, TEM and Raman characterisation indicates that the CNT sample is relatively pure, no amorphous carbon, carbon onions or other common CNT impurities can be detected by TEM for the CNT synthesised. Likewise the TGA peak does not show the presence of any other decomposition peaks other than that for CNT. Raman analysis confirms that the peaks are pure with a high $I_D/I_{G'}$ ratio. The broadness of the TGA peak however indicates that there is a range of sizes of CNT produced, as confirmed by TEM which shows a normal distribution of CNT diameters, with an average diameter of 35 nm (Figure 4.15).

The CNT powder produced by this method has a relatively low surface area (~35 m^2g^{-1}) due to the relatively large diameters of the CNTs produced. Surface areas for CNT can vary significantly depending on their diameter and orientation with respect to each other. Reported carbon fibre surface areas vary from 10 to 400 m^2g^{-1}. The synthesis method used here results in capped CNTs with a significant amount of iron in their core. Removal of iron from CNTs *via* hydrochloric acid treatment (24h reflux in conc. HCl) effectively doubled the CNTs surface area from 35 m^2g^{-1} to 62 m^2g^{-1}, by opening the nanotubes and removing some of this iron. However treatment and filtration of CNT in acid results in the agglomeration of CNT into a mat-like structure.

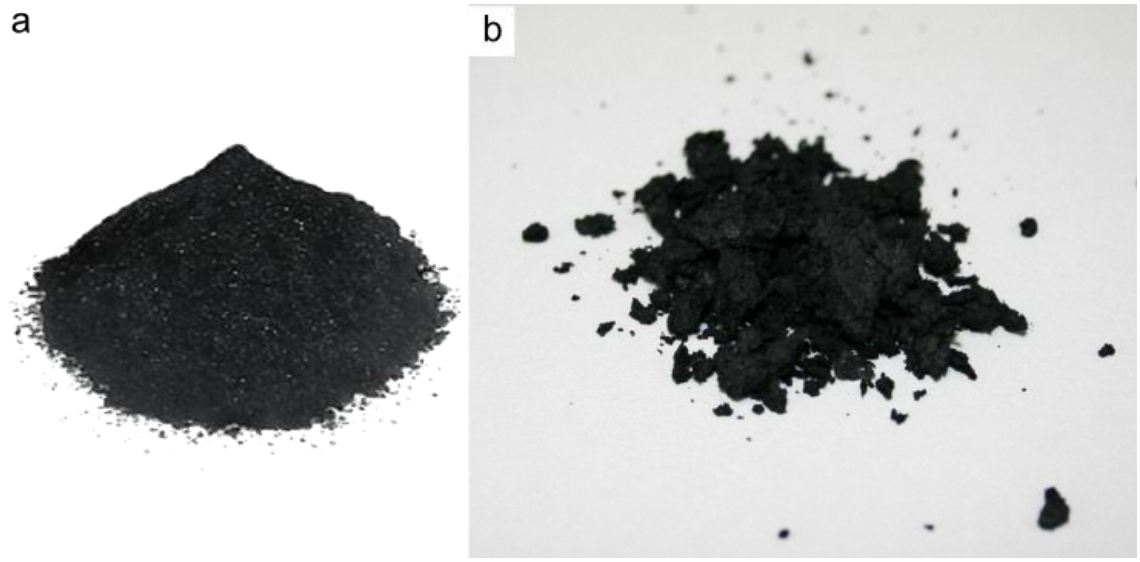

Figure 4.18 Picture of as produced power (left) vs. agglomerated powder after acid treatment (right)

4.8 **Conclusions**

Two methods were used for the synthesis of MWCNT, a floating catalyst synthesis method, and an injection based synthesis method. Synthesis of sufficient quantities of MWCNT using the floating catalyst CVD method was problematic. Good control of the sublimation of the ferrocene catalyst is necessary in order to produce MWCNT, but the resulting MWCNT form a non-uniform layer, with significant defects in the structure. The amount of CNT produced using this method is very low with 2 mg/cm^2 being produced. This technique is very sensitive to iron residue from previous reactions incorporating into the quartz tube. When the residual iron staining builds up CNT growth will occur preferentially on the quartz tube, rather than on the silicon substrate. The variety of problems encountered with the floating catalyst CVD method led us to determine that is was unsuitable for our purposes.

Injection based CVD proved to be a much more robust technique, being capable of growth even in the presence of iron-stained quartz. This method produces significantly greater quantities of CNT, thanks to a number of improvements. The process uses toluene (one of the more active carbon sources measured), continually injects larger amounts of iron catalyst, constantly refreshing the iron catalyst. This allows the reaction to continue for a longer time period, taking the standard synthesis time from 15 minutes to 60 minutes and as a result producing significantly more CNT with 20 mg/cm^2 being produced. MWCNT produced by this method appear to be less defective than MWCNT produced by the other method. TEM, XRD and TGA confirm the presence of a significant amount of iron residue on the MWCNT catalyst.

This iron residue has been reported in a number of previous studies, though the level of iron present is higher than normal. The surface area of the resulting MWCNT is relatively low, being only 35 m^2/g, this surface area can be increased if the MWCNT is treated with acid in order to remove amorphous carbon, open the tubes, and remove residual iron.

In order to produce sufficient amounts of MWCNT to perform catalytic tests, a procedure which produces as much CNT at possible is necessary. Therefore it was decided to continue future MWCNT synthesis using the injection based CVD method as it was both more robust and had a higher production capacity. This method was used for the preparation of structured CNT supports, as discussed in chapter 5. Catalytic tests were performed using the CNT produced by this method, the results of which are discussed in chapter 7.

5 Synthesis of CNT supported on cordierite monoliths

Initial work on this project focused on the production of carbon nanotube powders, chapter 4 focuses on the successful synthesis of these CNT powders. CNT have useful properties for a heterogeneous catalyst, however as chapter 2 discusses, the very fine powders produced by CNT synthesis are not ideal as heterogeneous catalyst supports. Here the synthesis of structured supports is outlined, this work was the basis for a paper published in the journal *Carbon*.[261]

One of the major concerns with CNTs is the safety aspects associated with inhaling the fine powder produced, which may have long term health effects (see Chapter 2.1.3). Anchoring the CNTs to a structured support could help alleviate these effects, by reducing their ability to become airborne. CNTs can be grown anchored to a support, or as a fine powder, but are typically sold in powder form.

Powdered catalysts are not ideal for use in large scale catalysis, where mass transfer and heat transfer effects are more significant. [262] Traditionally catalysts used for industrial reaction are made into ordered structures to reduce pressure drop, which can significantly increase costs for industrial scale processes. [263] Carbon nanotube powder will inevitably have a high pressure drop as there is little free space between the fine particles. Production of CNTs directly as a structured support, rather than as a powder would help address this problem.

As produced CNT can be formed as a forest of carbon nanotubes on the growth substrate, this layer of CNT can be used as a catalyst support. [173,186] The result will be an anchored layer of carbon nanotubes, and if grown on a suitably shaped substrate, a support with much lower pressure drop. While there are a number of potential different substrates used for CNT growth, in this work the main substrates explored have been silicon, quartz and cordierite monoliths (Figure 5.1). As can be clearly seen silicon and quartz (Figure 5.1 a + b), the typical substrates for CNT growth are not ideally shaped for introduction into standard fixed bed reactors.

Figure 5.1 a) Silicon, b) quartz and c) cordierite substrates

Cordierite, a natural mineral, is frequently manufactured into monoliths, shaped structures with high geometric surface area (Figure 5.1 c). [166] This is frequently used in the automotive industry as a support in catalytic convertors. [166] The high geometric surface area of cordierite monoliths make them perfectly suited for use as a substrate for CNT growth to produce a shaped CNT support. Though silicon and quartz, could be shaped in a similar manner they are already more expensive than cordierite (Table 5.1), and processing them into the correct form would further increase the cost.

Table 5.1 Price per kg of raw material as a powder, prices obtained from a web-search on ali-baba 19/08/2013, it should be noted that this price is for the raw powder, prices will increase on being formed into shapes, with quartz and silicon pricing increasing more sharply due to more difficult processing

Material	**Price per kg**
Silicon	£ 0.92-1.53
Quartz	£ 0.49-0.55
Cordierite	£ 0.28-0.31

Growth of carbon structures on monoliths has been performed by a number of previous authors,[115,116,173,180-183] with varying success, often requiring significant pre-treatment beforehand. In this chapter efforts to successfully grow MWCNT on cordierite in one step are explored, with full characterisation of the resulting carbon coated monoliths. The suitability of the monoliths is assessed for scale up to a level where they could be used as industrial heterogeneous catalysts.

5.1 Effect of alumina-washcoat on CNT Growth

Cordierite monoliths have very low volumetric surface areas (typically less than 0.7 m^2g^{-1}) and are typically coated with a high surface area material in order to increase the surface area, before being used as a catalyst support. [166] This 'washcoat' increases the low surface area of the cordierite monolith, and allows highly dispersed metal particles to be introduced on the surface. The washcoat can be any high surface area material, typically alumina is used, but silica and carbon are among some of the other coatings reported. [166]

In these experiments bare and washcoated cordierite were used, the bare monolith was produced by Corning and then washcoated by Johnson Matthey (both were kindly provided by Professor Stan Kolackzcowski, University of Bath). The bare cordierite was beige, whilst the

alumina coated cordierite had a white tinge. The alumina washcoated monolith had a thick alumina layer of 80 µm, with the layer being significantly thicker in the corners (Figure 5.2d). Example micrographs of typical samples can be observed in Figure 5.2. Experiments in this work have concentrated on using the pre-washcoated, bare cordierite, rather than preparing cordierite of defined alumina washcoat thickness in an attempt to avoid the complexity of preparing defined size, uniform, alumina washcoated monoliths.

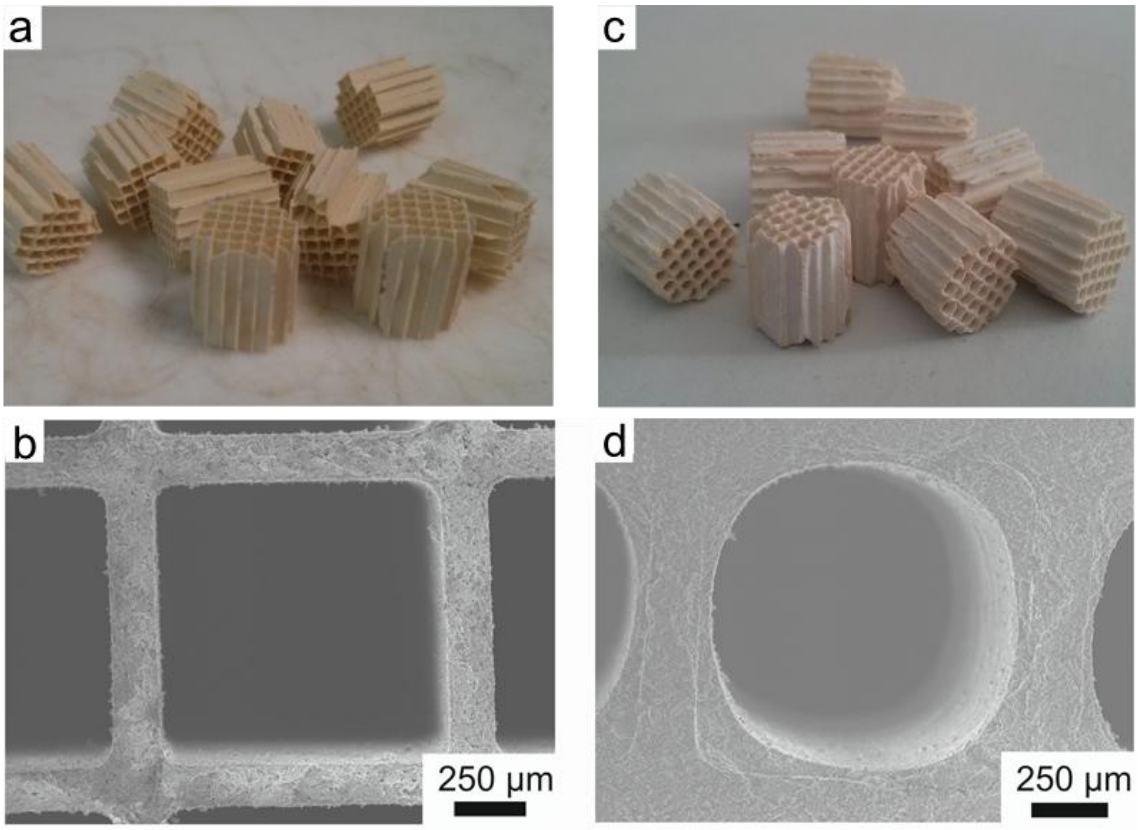

Figure 5.2 Bare cordierite vs. washcoated cordierite a) bare cordierite monolith b) SEM of bare cordierite monolith c) alumina washcoated monolith d) SEM of alumina washcoated monolith

Previous attempts to grow carbon nanotubes onto a cordierite monolith to create a carbon layer, have required complex pre-treatment steps of the monolith. [115] The carbon nanotube catalyst must first be finely dispersed onto the substrate before carbon nanotubes can grow. [115] Other authors have typically used an alumina washcoat in order to increase the surface area of the cordierite to allow dispersion of sufficient quantities of CNT catalyst onto the cordierite. [115,181] This requires first an alumina washcoat to be introduced (with reliably producing a uniform alumina washcoat being a non-trivial task, see the work of Moulijn *et al.* [168]), and then the introduction of the catalyst precursor.

Previous authors have noted that whilst an alumina washcoat can greatly aid the growth of the carbon nanotube layer, if the alumina layer is not thick enough (less than 6 wt.%) uneven growth can result. [115] Equally when thicker alumina coatings are used, the majority of CNT growth occurs within the pores of the alumina causing it to fragment. [181] It was reported that an optimal alumina loading appeared to be 6 wt.%, resulting in an even coating of alumina (approximately 0.1 μm thick) which allowed the growth of an accessible layer of CNF. [115]

Gong *et al* [173] have reported the growth of CNT on bare cordierite monoliths, using iron or cobalt catalysts, but required the use of high vacuum in order to impregnate the cordierite monoliths. In this study the injection CVD method outlined in chapter 4 was used. The major advantage of using this method is that it avoids the necessity of a pre-impregnating the catalyst, or adding a washcoat and then pre-impregnating the catalyst. By introducing catalyst and carbon source at the same time to deposit over the monolith, the need for a high surface area surface or an expensive pre-impregnation step is avoided.

The injection CVD method has resulted in cordierite monoliths with very different properties and behaviour to those previously reported. Experiments have also shown a significant difference in the behaviour of CNT growth between the 'bare' cordierite and the alumina washcoated cordierite (in terms of length and alignment), as can be observed in Figure 5.3.

Aligned CNT arrays over 100 μm in length can be observed to have grown from the bare cordierite (Figure 5.3a, c, e, g), without the presence of an alumina washcoat. This aligned growth has not previously been reported for CNT growth on cordierite. Figure 5.3c and e clearly show the presence of a micrometre range substructure, with the carbon layer consisting of larger tube like structure, significantly bigger than CNT. Higher resolution microscopy images (Figure 5.4) confirm that these tube like structures, are due to the formation of bundles of CNTs, which upon growth have become inter-twined with each other. This results in the tubular structures observed at lower magnifications. The mutual support of the nanotubes growing from the surface together, results in a relatively uniform aligned layer.

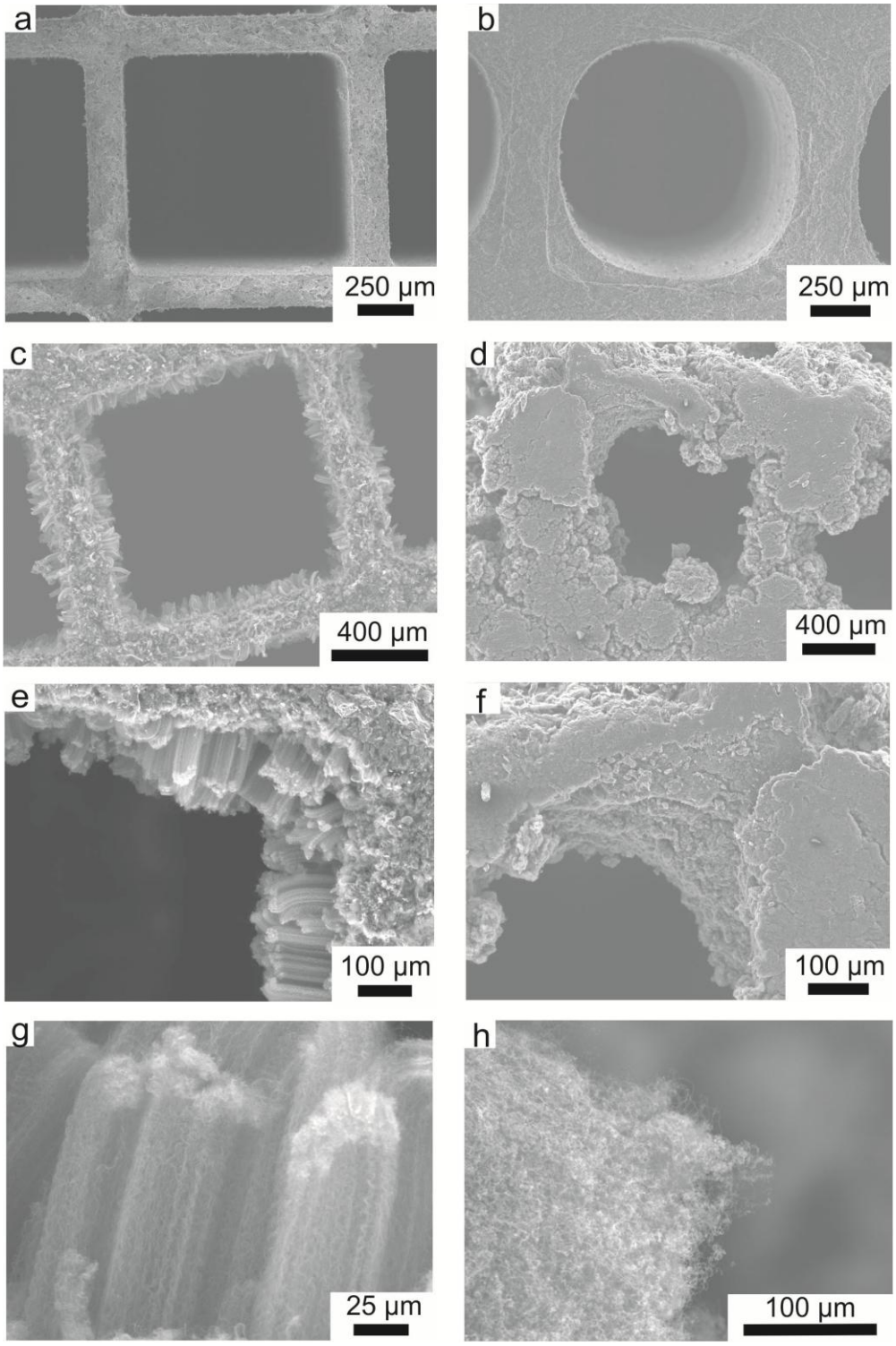

Figure 5.3 SEM micrographs of a) bare cordierite monolith and b) alumina washcoated cordierite monolith before coating with carbon. The differences in growth observed on bare and washcoated monoliths is shown, with c) e) and g) showing ordered uniform growth on bare cordierite at different magnifications, whilst d) f) and h) show disordered growth on alumina washcoated cordierite at increasing magnification.

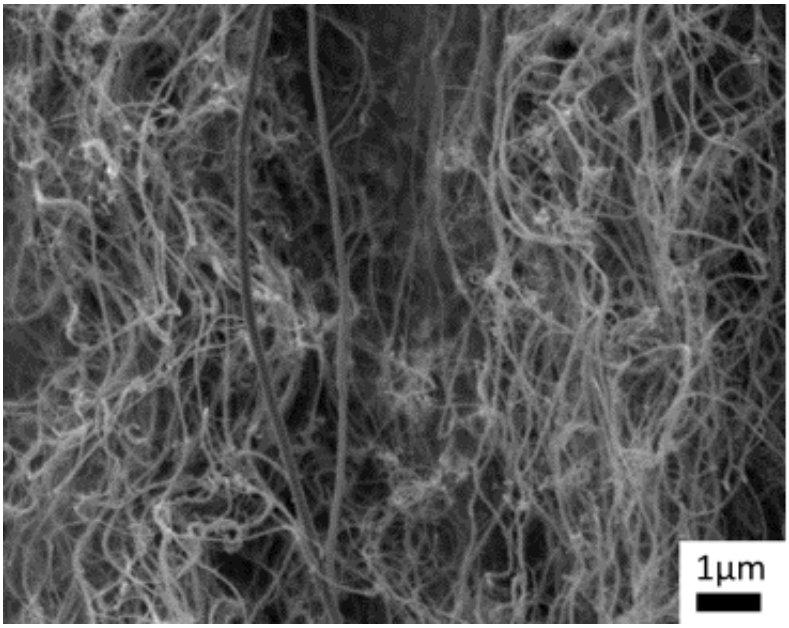

Figure 5.4 High resolution micrograph of CNT bundles on the cordierite monolith surface

On the other hand, for the same growth conditions on the alumina washcoated cordierite, growth is very disordered, with growth in random orientations, resulting in a highly uneven layer of carbon across the alumina washcoat (Figure 5.3d and f). At higher resolution images confirm the presence of a thick layer of intertwined CNT on the alumina washcoat (Figure 5.3h). This random orientation of CNT is in agreement with literature results for other attempts at CNT growth (Figure 5.5), with disordered growth previously being observed. [115,173,181]

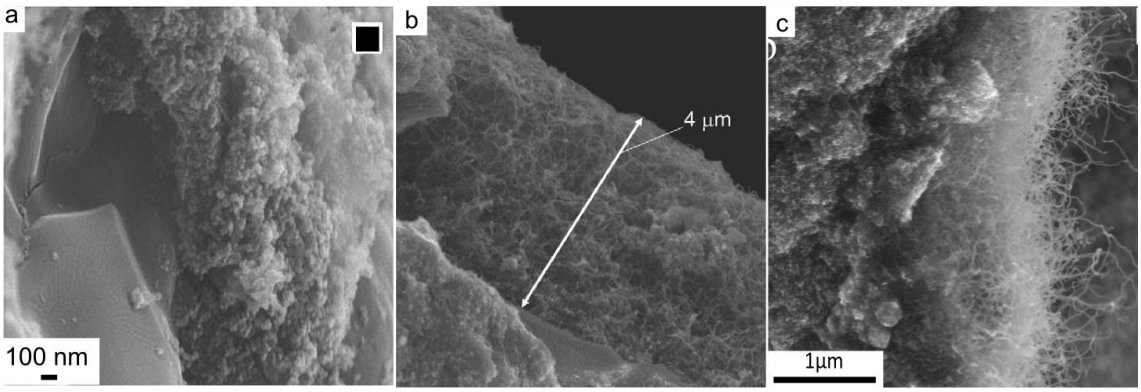

Figure 5.5 SEM micrographs of CNT growth observed in previous studies by a) Gong *et al.* [173] b) Bordeje *et al.* [115] and c) Jarrah *et al.* [181]

Growth on both bare cordierite and alumina washcoated cordierite has resulted in a significantly thicker layer of CNT than has previously been reported. This significant

improvement over published results is attributed to the particular growth method used in this work. As discussed earlier, this is based on an injection based CVD process where the ferrocene catalyst and the toluene carbon source are introduced into the reactor simultaneously. [66,85] This method allows the uniform deposition of iron nanoparticles onto the bare monoliths which have a more uniform surface with lower surface area [66] compared to the washcoated monoliths. The injection based method does not rely on the higher surface area provided by an alumina washcoat to achieve sufficient dispersion to produce nanoparticles, as is the case for the incipient wetness techniques used previously in the literature [66,115]. For the highly porous (0.42 mL g^{-1} [166]), high surface area (~190 m^2 g^{-1} [166]) washcoated alumina system, catalyst particles were deposited within the porous material. As a result, CNT growth occurs in all directions normal to the porous surface, resulting in the disordered layer of CNTs observed, as in previous studies (Figure 5.3h, Figure 5.5).

For the bare cordierite, with a low porosity (0.19 mL g^{-1} [166]) and low surface area (<4 m^2 g^{-1} [166]), nanoparticles deposit on the walls of the monolith, rather than in the monolith pores. The densely packed CNTs that result grow normal from the monolith wall, intertwining with each other to produce the relatively ordered layers of CNT produced.

Raman analysis of the CNT grown on washcoated and bare cordierite shows that growth for 60 minutes at 790 °C produces relatively pure CNT on both substrates. CNT growth on Al_2O_3 seems to result in slightly purer MWCNT with a low I_D/I_G ratio of 0.39, indicating the presence of low amounts of graphitic impurities and a high $I_{G'}/I_D$ ratio of 2.67 indicating significant long range order in the sample, and hence relatively pure crystalline CNT.

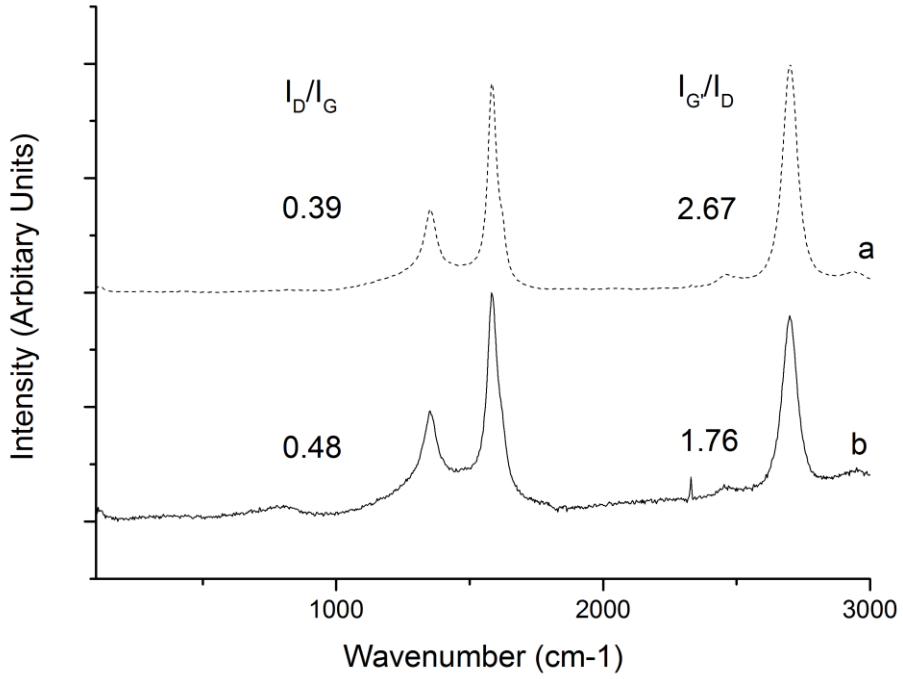

Figure 5.6 Raman spectra of a) MWCNT on Al_2O_3 washcoated cordierite b) MWCNT on bare cordierite

5.2 **Repeatability**

In order to ensure that the coating method used was repeatable, the synthesis procedure was repeated a number of times, and the thickness of the resulting carbon layer was measured each time. Representative SEM micrographs for these samples are shown in Figure 5.7. The reported carbon layer thickness, obtained by measurement of the thickness of the carbon layer from the monolith wall is given in Figure 5.7. The exact position of the monolith wall can be obscured in individual micrographs at higher magnifications (330x) as a result of carbon growth in the direction of the electron beam, however from lower magnification micrographs (60x) the monolith wall position can be more easily determined. There is some variation in the thickness of the carbon layer, but the average values reported all fall within the range of one standard deviation of the layer thicknesses measured. This is an acceptable level of error especially considering the errors inherent in determining the exact position of the monolith wall. On an individual monolith the standard deviation of carbon layer thickness is around 10 µm, indicating that though the carbon layer is relatively uniform there are some variations. Part of this variation comes from damage to the edges of the carbon layer when handling and error in determining the position of the monolith wall.

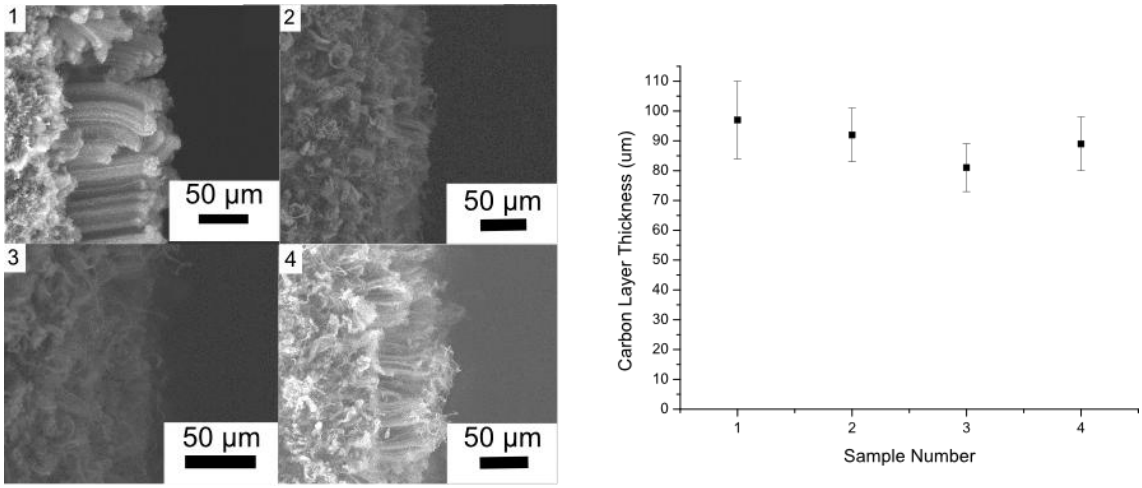

Figure 5.7 (left) SEM micrographs of carbon layer taken from 4 different runs (right) thickness of the carbon layer as determined from each experimental run at 790 °C for 60 min, error bars represent 1 standard deviation

5.3 **Mapping the Reactor**

In order to determine the position in the quartz reactor which was optimal for MWCNT growth, the temperature gradient across the reactor was measured Figure 5.8. It was determined that the temperature was uniform from a position 30 cm into the reactor, and maintained uniform temperature until around 60 cm. In order to determine the region where uniform growth occurred, cordierite pieces were placed at 10 cm intervals within the reactor from 30 to 80 cm (no pieces were places from 10-20 cm as the needle projects up to 10 cm inside the reactor, blocking the needle output could inhibit the introduction of catalyst to the reactor). It was demonstrated that cordierite pieces from 40 cm to 60 cm demonstrated uniform coating. After 60 cm growth begins to decrease as the uniform temperature zone is exited. Meysami *et al.* [121] report similar trends in their own map of a CVD reactor using a slightly different method. The 40-50 cm region was chosen as the optimal position for CNT growth, and all syntheses were performed in this region unless otherwise noted.

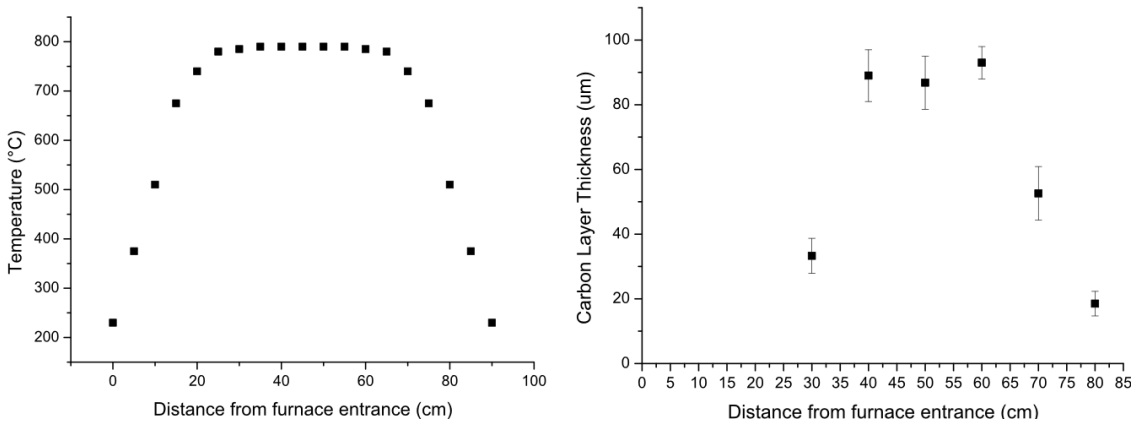

Figure 5.8 (left) Map of temperature against distance from the furnace entrance (right) variation in carbon layer distance in relation to distance from the furnace entrance

5.4 Effect of time and growth temperature on thickness of the carbon layer

The synthesis time and growth temperature were varied in order to understand the effect of changing synthesis conditions on the resulting support. Analysis of SEM micrographs taken of the coated monoliths at different synthesis times (Figure 5.9), shows similar aligned CNT growth for each of the synthesis times, with thicker layers observed with longer synthesis times .

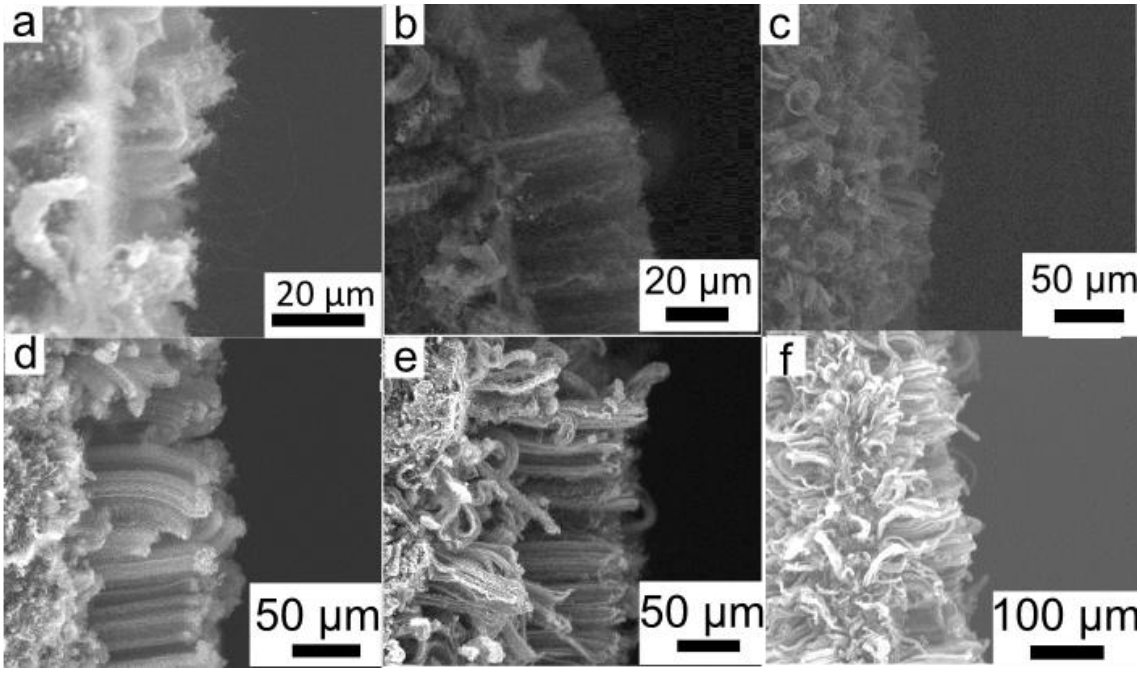

Figure 5.9 SEM gallery of CNT layer produced at different synthesis times a) 15 minutes b) 30 minutes c) 45 minutes d) 60 minutes e) 90 minutes f) 120 minutes

Raman spectra (Figure 5.10) of the samples synthesised at different times all clearly show the presence of carbon nanotubes, with characteristic Raman peaks at 1355 cm^{-1}, 1586 cm^{-1} and 2702 cm^{-1}. For shorter synthesis times (Figure 5.10 a-c) there is an underlying fluorescence peak beyond 2000 cm^{-1}, which is characteristic of cordierite samples, this suggest that for shorter synthesis times, the Raman laser can penetrate sufficiently to fluoresce the underlying cordierite, whilst after 60 minutes the laser can no longer penetrate and fluoresce the cordierite, as would be expected with the increasingly thick CNT layer.

The nature of the sample can be estimated from the ratio of the $I_{G'}$ peak to the I_D peak. With increasing time the ratio of $I_{G'}$ to I_D increases to a maximum of 1.76 after 60 minutes, before falling to 1.03. As the G' peak is highly dependent on long range order, this suggests that the purity increases over time, reaching a maximum before falling. Sample purity is still relatively low, as $I_{G'}$:I_D values of over 2 have been reported for high purity MWCNT.

The I_D:I_G shows no clear trend, with the lowest value of I_D:I_G after 60 minutes of 0.48, suggesting the presence of MWCNT nanotubes which are relatively defect free, in agreement with the $I_{G'}$:I_D ratio. The presence of other graphitic species including iron nanoparticles coated with a graphitic layer, which would result in overlapping peaks, can interfere with the I_D:I_G ratio, which may explain the lack of a clear trend. The data suggests that defects are mainly formed during the initial synthesis, and after synthesis for a long time, with more defects present at shorter synthesis times, and after longer synthesis times. This might be expected as this means impurities form during the initial stages of the reaction, before the CNT growth regime is established. Later CNT growth is generally pure, before finally when the catalyst begins to lose effectiveness, again more amorphous carbon is produced.

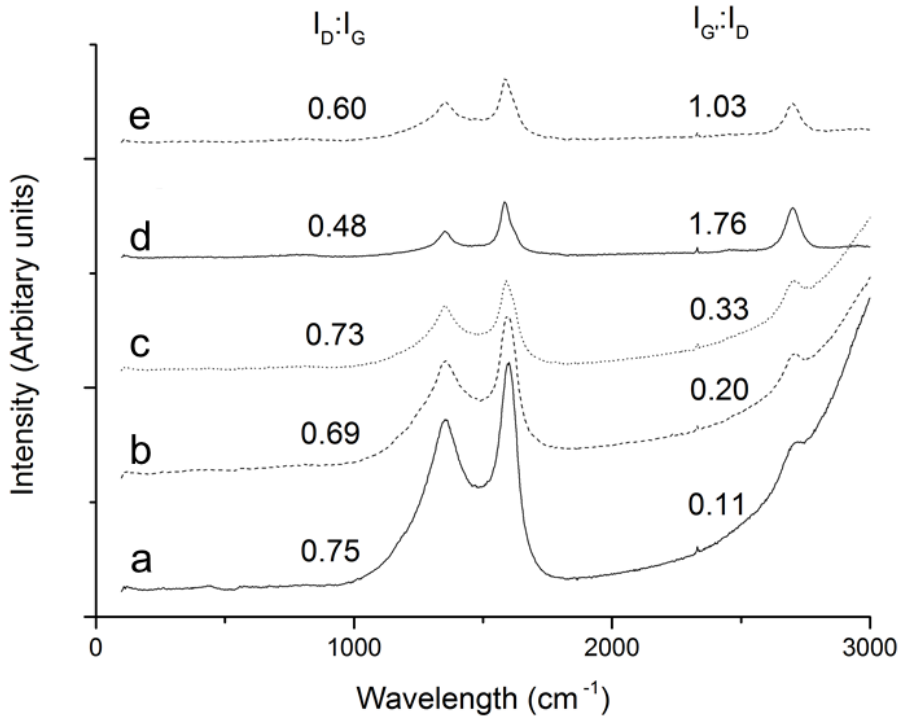

Figure 5.10 Raman spectra of CNT grown at 790 °C for a) 15 minutes b) 30 minutes c) 45 minutes d) 60 minutes e) 120 minutes

Changing the synthesis temperature has a significant effect on the resulting CNT growth. In this study four synthesis temperatures, were explored 730, 790, 850 and 910 °C. Micrographs of samples synthesised over different times at 730 °C (Figure 5.11a-c) and 850 °C (Figure 5.11d-f), also show aligned CNT layers with increasing thickness over time, though this effect is less pronounced.

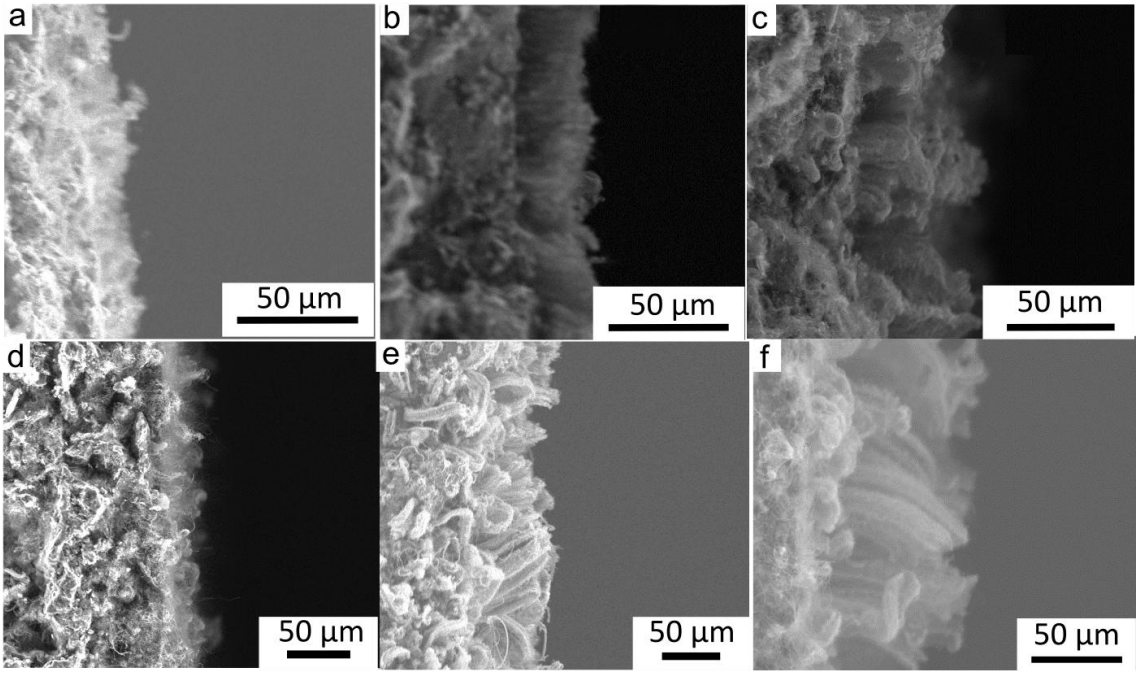

Figure 5.11 CNT layer after synthesis at 730 °C for a) 15 minutes b) 60 minutes and c) 120 minutes and those synthesised at 850 C for d) 15 minutes e) 60 minutes and f) 120 minutes

Raman spectra of the CNT synthesised at different temperatures (Figure 5.12) demonstrates the significant effect temperature has on the MWCNT produced. At 730 °C the pronounced cordierite fluorescence from 2000 to 3000 cm^{-1} can be seen, similar to that seen for MWCNT grown for less than 60 minutes, suggesting this layer is also thin enough for the laser to fluoresce the cordierite. There are also significant differences in the $I_{G'}/I_D$ and I_D/I_G ratios between the different samples. MWCNT synthesised at 790 °C are significantly purer than those synthesised at 730 or 850 °C, with much higher $I_{G'}/I_D$ and much lower I_D/I_G. This suggests that 790 °C is the optimum temperature for synthesising MWCNT.

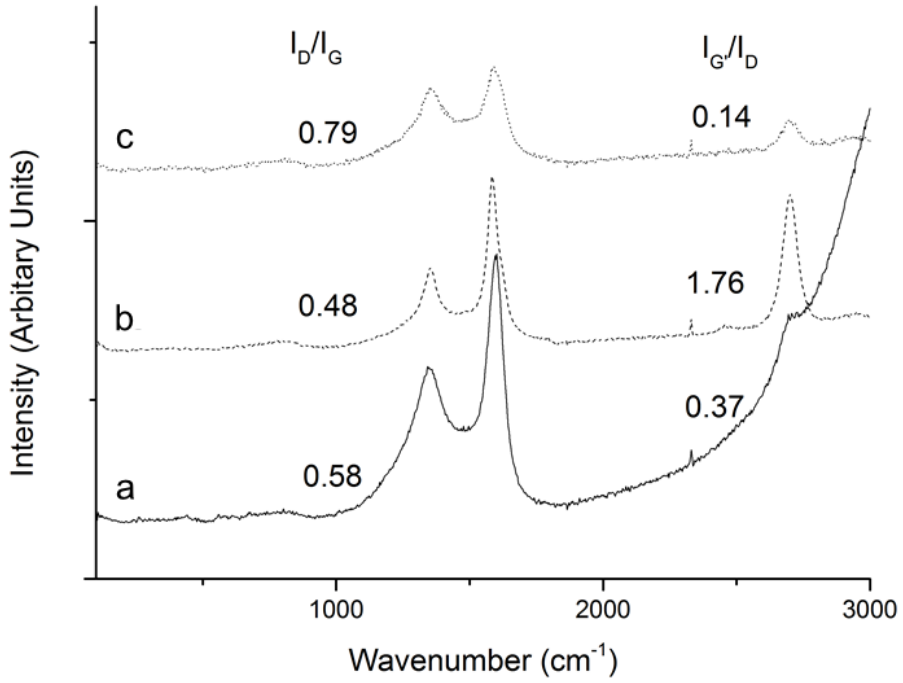

Figure 5.12 Raman spectra of MWCNT synthesised for 60 minutes at a) 730 °C b) 790 °C and c) 850 °C

When synthesis was carried out at the higher temperature of 900 °C, a markedly different carbon deposition was observed (Figure 5.13). For samples grown at lower temperatures the cordierite monolith was consistently coated with a dark black substance, the CNT layer being clearly visible to the naked eye. At 900 °C, instead a light grey layer was observed. SEM micrographs show very uneven growth, rather than the aligned layers previously observed. Though some nanotubes can be observed, the majority of the growth consists of larger structures which appear to be coated with deposited iron nanoparticles and amorphous carbon. Raman analysis indicates that this coating has a very high I_D/I_G ratio indicating the presence of amorphous carbon. The $I_{G'}/I_D$ ratio is also low indicating a fairly impure samples, however the presence of the $I_{G'}$ peak confirms the presence of CNT. No further attempts were made to synthesise CNT at higher temperatures than this.

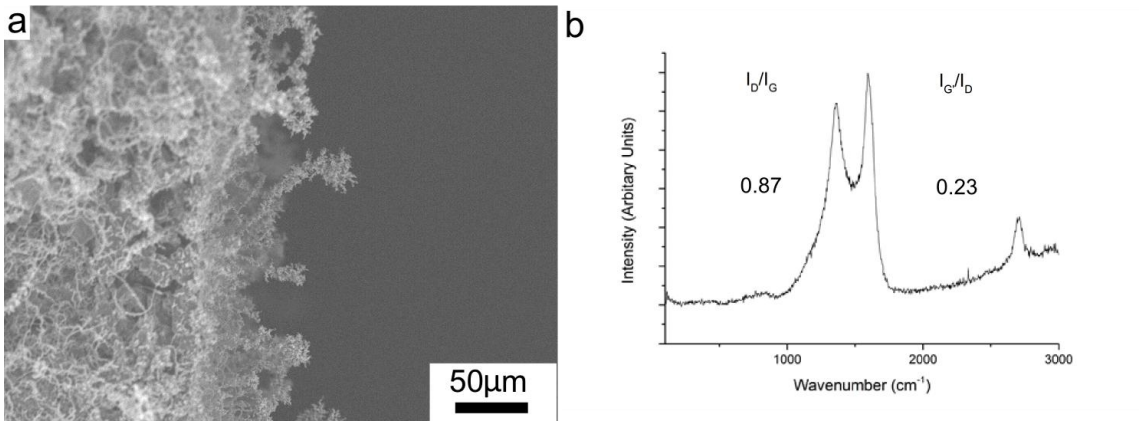

Figure 5.13 a) SEM micrograph of CNTs grown at 900 °C b) raman spectra of CNT grown at 900 °C

Temperature programmed oxidation (TPO) experiments provides supporting evidence that samples synthesised at 850 °C are less pure than those synthesised at lower temperatures. MWCNT synthesised at all temperatures have roughly the same initial oxidation temperature at around 440 °C, suggesting that the initial decomposition step is triggered similarly in all samples. The point of maximum oxidation (i.e. the point where most of the MWCNT decompose) is different for each sample, with MWCNT synthesised at 850 °C reaching this maximum first at 588 °C, followed by those synthesised at 730 °C at 599 °C, and finally those at 790 °C at 612°C. This supports the Raman data, with the most stable being those synthesised at 790, whilst those synthesised at other temperatures have more defects and so decompose earlier. Interestingly whilst MWCNT synthesised at 730 °C and 790 °C have similar final oxidation points, MWCNT synthesised at 850 °C gives a slightly narrower distribution suggesting that the MWCNT produced are more similar, if easier to decompose.

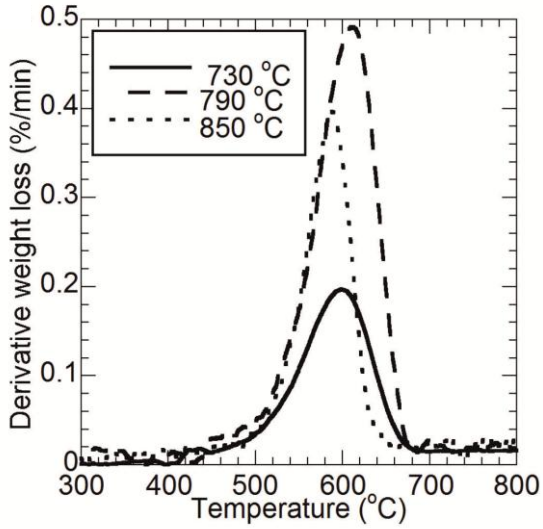

Figure 5.14 Derivative of the weight loss in temperature programmed oxidation experiments of the CNT composites after 60 minutes growth at different temperatures.

Interestingly the wt.% of MWCNT produced determined from the TGA data is lower than the amounts reported to have been produced in other studies, with only 4.3 wt.% CNT typically being produced after 60 minutes at 790 °C. This is despite the fact that the CNT layer is visibly observed to be much larger than those obtained by previous studies.

Table 5.2 Reported literature carbon wt.% and growth conditions

Author	*Synthesis Temperature*	*Synthesis Time*	*CNT wt.% per monolith*
***Bordeje* et al.** [115]	650	210 min	16
***Gong* et al.**[173]	700	20 min	11
***Jarrah* et al.** [181]	700	180min	15.4

Taking the reported masses of CNT, and comparing it to the CNT layer thickness measured raises some questions about the previously reported CNT wt.%. The thickness of the CNT layer is reported to be very thin, the thickest layer reported being 4 µm and therefore occupies a much lower volume than the cordierite, with each wall being approximately 200 µm in thickness and 1.1 mm in length. This implies that despite the CNT occupying only 2 % of the

volume of the cordierite, it accounts for 15% of the mass, implying that the CNT are much denser than cordierite. Given that the average density of cordierite is 2.65 g cm^{-3}, the density of the CNT layer can be calculated, by working out the volume occupied by CNT from the micrographs and using the following equations:

$$V_{cordierite} \times \rho_{cordierite} = M_{cordierite} \quad (5.1)$$

$$\frac{M_{CNT}}{M_{CNT} + M_{cordierite}} = wt\%\ CNT \quad (5.2)$$

$$\frac{M_{CNT}}{V_{CNT}} = \rho_{CNT} \quad (5.3)$$

Where M= mass V= volume and ρ=density

Solving these equations to find the density of the carbon layer, implies that the density of MWCNT would need to be 29.2 g cm^{-3} in the case of Gong et al. [173] This is clearly not correct, as the maximum theoretical density for MWCNT, though varying with size is reported to be less than 2.5 g cm^{-3}. [264] Determining the density of CNT grown in our own study for 60 minutes at 790 °C gives a much more reasonable value of 0.15 g cm^{-3}, which is comparable to reported bulk densities of MWCNT.[265] The difference between the absolute density and the bulk density is due to voidage with gaps between the CNT. None of the previous studies report the method used to determine CNT wt.%, but the method used may have included a source of error, perhaps incorporating the mass of the much denser catalyst particles in the calculation. In this study the mass of CNT was determined by measuring the weight loss on oxidation of the CNT, and as such only accounts for the carbon species present. Some of the difference may also be explained by incorporation of nanotubes inside the cordierite or alumina pore structure.

Analysis of the micrographs of all samples synthesised to determine the average thickness of the carbon layer for each sample reveals that the maximum thickness of the carbon layer observed is at 790 °C after 90 minutes, with a thickness of 160 µm. This is significantly greater than that of those grown at higher and lower temperatures, 730 and 850 °C, which result in maximum carbon layer thicknesses of 47 and 89 µm, respectively. 790 °C seems to be the optimum temperature range for CNT growth on this substrate.

Examining the micrographs it appears that further growth of the carbon layer is hindered or significantly slowed after 90 minutes, as after 2 hours the thickness of the carbon layer has not increased further. This slow-down effect has been observed in a number of previous experiments, and is thought to be due to a build-up of amorphous carbon preventing access to the catalyst particle. [100,101,127-129] This termination is not as pronounced for the thinner layers (if at all present) for those produced at 850 and 730 °C.

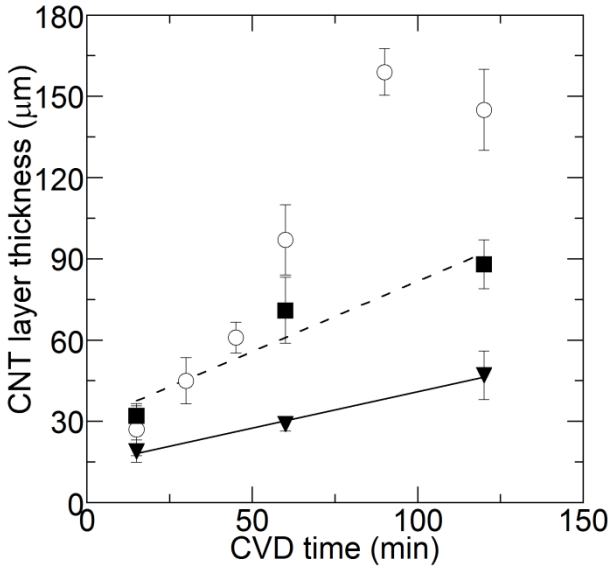

Figure 5.15 CNT layer thickness as a function of CVD growth time at (▼, —) 730 °C, (○) 790 °C. and (■, ---) 850 °C. The CNT layer thickness was determined from image analysis of SEM micrographs of the CNT layers at 10 μm intervals; error bars represent one standard deviation.

TPO analysis shows similar trends with carbon wt.% increasing with time, and 790 °C being the optimum growth temperature (Figure 5.16). It is to be noted that no slowdown is observed in the carbon wt.% change data, suggesting that beyond 90 minutes carbon is still deposited, but does not further increase the thickness of the CNT layer.

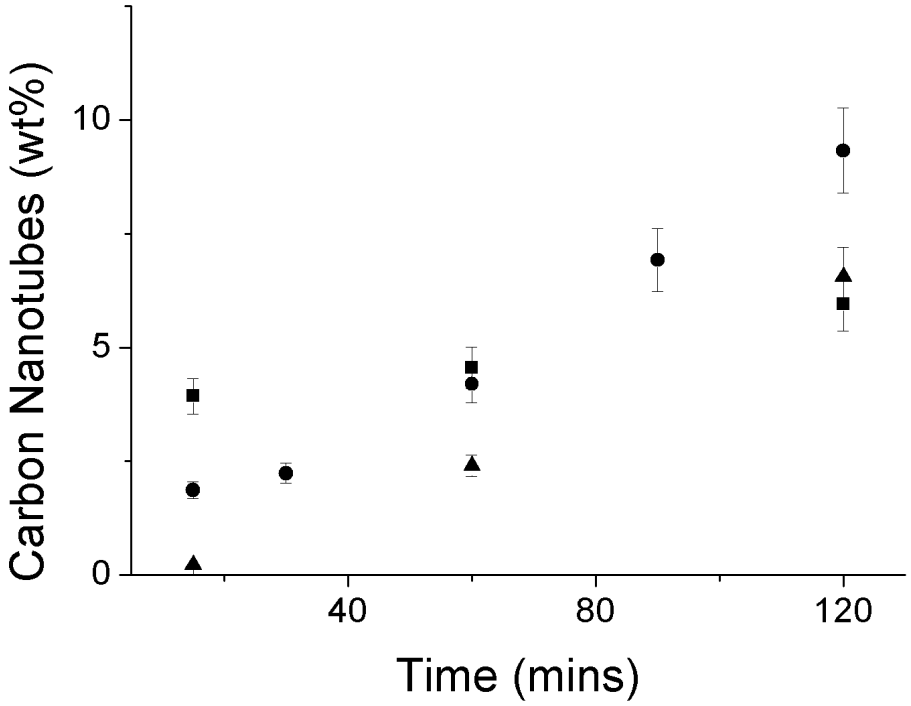

Figure 5.16 CNT wt.% as a function of CVD growth time at (▼) 730 °C, (○) 790 °C. and (■) 850 °C. The wt.% of CNT was determined by TPO of the cordierite monoliths, and observation of the total weight loss after complete combustion

The carbon layer thickness is significantly greater than those reported previously on this same support using a nickel (4 µm thickness after 220 minutes at 650 °C) or cobalt (0.6 µm thickness after 20 minutes at 730 °C) catalyst. [115] Even at 730 °C, where growth is significantly less than at higher temperatures, the carbon layer thickness of 19 µm after 15 minutes, and 47 µm after 120 minutes is still an order of magnitude greater than those previously reported. The use of a ferrocene/toluene mix, which continually provides fresh catalyst precursors into the system, has been suggested as a possible reason for the high growth rates observed in similar methods. [103] Synthesis at higher temperature and for longer synthesis time enabled by the use of iron catalyst with this method enables much thicker carbon layers to be obtained.

5.5 Surface area of the CNT layer

The surface area of the 790 °C CNT/cordierite monolith after 60 minutes growth is about 4 m^2g^{-1}. Heating in air at 550 °C for 20 minutes removes any remaining amorphous carbon and opens the ends of the CNTs, leading to a doubling of the surface area to about 8 m^2g^{-1}, without significant damage to the CNTs. This corresponds to an order of magnitude increase from the 0.7 m^2g^{-1} value of the bare cordierite. It is nonetheless significantly lower than values

previously reported of 30 m^2g^{-1} and 63 m^2g^{-1} for CNT/CNF layers grown on alumina washcoated monoliths. [115,116,173] This difference can be attributed to several factors: First, the alumina washcoat accounts for a significant percentage of the surface area of the CNT/CNF-washcoated monolith with approximately 50% of the surface area coming from the washcoat at 30m^2g^{-1}, and over 70% at 63 m^2g^{-1}. Secondly, the mass of CNT supported on the monoliths are relatively low, at only 4.2 wt.% carbon, and only 4.8 wt.% total catalyst mass. From the mass of CNT, we can estimate a surface area for the layer of CNT as 73 m^2 g^{-1}, this value is higher than the CNT powder obtained under the same conditions from quartz of 35 m^2 g^{-1}. This relatively low surface area is due to the large diameter (~35 nm), and capped nature of the CNTs produced.

As discussed previously, oxidation at 550 °C in air opens the caps, increasing the surface area. Removal of iron from oxidized CNTs (produced using the same method but on a quartz substrate) *via* hydrochloric acid treatment (24h reflux in conc. HCl) effectively doubled the CNTs surface area from 35 m^2g^{-1} to 62 m^2g^{-1}. Unfortunately, the same process applied to the CNT/cordierite results in the deterioration of the cordierite support.

Changing the synthesis temperature has a small effect on the CNT surface area, surface area is highest at 730 °C, and decreases slowly with increasing synthesis temperature (Figure 5.17). This is surprising as this increase in surface area is inversely proportional to the volume of the CNT produced.

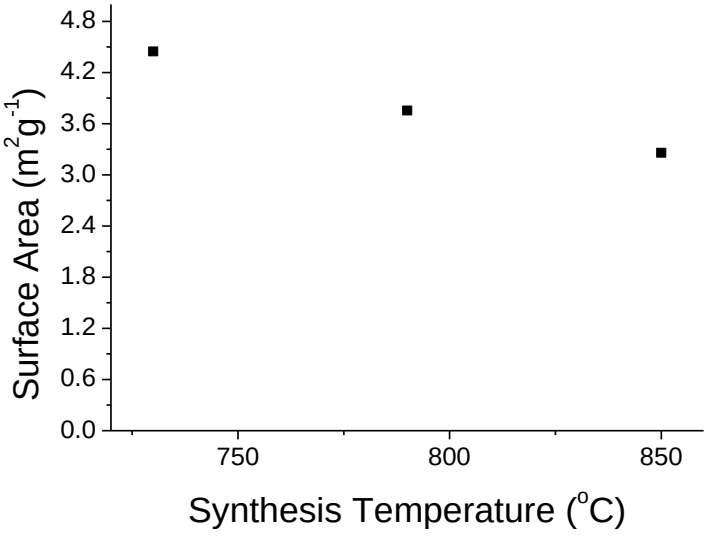

Figure 5.17 BET surface area of CNT-monolith composites grown for 60 minutes at various temperatures

Changing the synthesis time also affects the surface area of the resulting composites. Surface area increases with increased synthesis time (Figure 5.18). This corresponds to the increased volume of the CNT layer. Gong et al [173] report that after 20 minutes CVD growth no further increases in CNT surface area are observed, due to deposition of amorphous carbon. In our case this does not appear to happen with surface area increasing continuously.

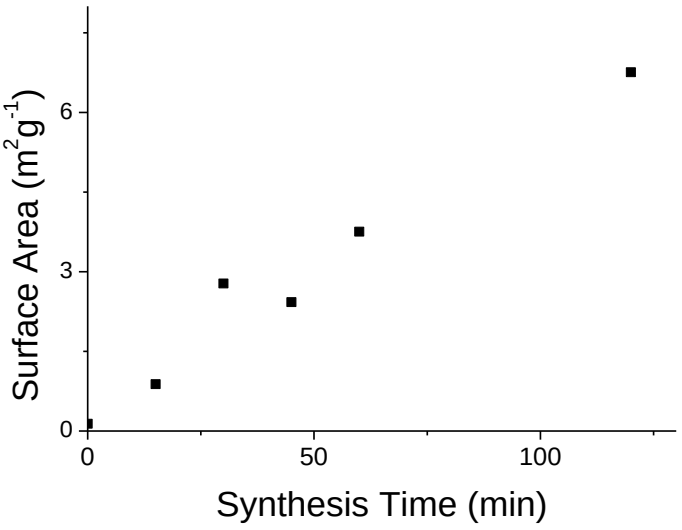

Figure 5.18 BET surface area of CNT-monolith composites grown at 790 °C for varying synthesis times

The errors inherent in these surface area measurements will be quite large, though determining the degree of error is difficult. The ASAP machines are typically designed to measure surface areas of greater than 20 m^2 g^{-1}, but the surface areas measured in this study are significantly below that. This is mainly due to the fact that cordierite itself has a very low surface area, and makes up a majority of the sample by mass. The high surface area CNT are a low percentage of the mass in the sample, so the overall surface area is low. The similarity between surface areas of similar substrates suggests that this error is relatively repeatable. More accurate determination of the surface areas at these low levels could be perhaps obtained using another probe gas such as krypton, but these facilities were not accessible during this work.

5.6 **Potential for scale up**

In order for this process to be successfully scaled up, the suitability of the monolith composite must be determined. To be useful as industrial heterogeneous catalysts supports the CNT composites must be structurally robust, have a lower pressure drop than the powdered form

of this catalyst, and be capable of uniform synthesis on a large scale. Here a preliminary investigation into the suitability of these catalysts for industrial use was carried out.

5.6.1 Mechanical stability

Previous authors have tested the mechanical strength of the CNT/monolith composites, reporting an increase in strength over the bare cordierite monolith, with this effect diminishing with increased carbon deposition at higher temperatures (eventually leading to the total collapse of the monoliths). [115] Mechanical testing of the composite monoliths formed in this study indicated that the monolith strength has been retained, with the axial crushing strength equal or slightly higher after CNT growth (Table 5.3). The composite strength does not appear to have increased significantly over that of the bare cordierite (though there is some increase). Changing the synthesis temperature and increasing the amount of carbon deposited does not appear to greatly affect the monolith strength, neither significantly weakening nor strengthening the composite (Table 5.3).

Table 5.3 Characterization of CNT coating of the composite monoliths at different temperatures after 60 minutes

Growth Temperature (°C)	CNT weight per monolith (%)	Average coating thickness (µm)	Axial Crushing Strength (MPa)*
730	2.4	29±3	54±4
790	4.5	97±13	55±4
850	4.4	71±12	58±8

* Bare monolith gave axial crushing strength of 49±6 MPa

Previous authors have also observed total collapse of monoliths [115,181] under conditions where growth is extremely fast, and high quantities of CNT are deposited. Generally this behaviour is not observed in our samples. Collapse of samples grown at 790°C or higher for longer than an hour, has been observed on rare occasions, but generally only 1 monolith in a batch of 10 will collapse. The precise reasons for this occasional collapse have not been determined, but is thought to be due to monoliths which have been structurally weakened whilst being cut from the cordierite. In the literature, this collapse is attributed to growth of CNTs within the macroporous structure of the monolith and damaging it. [181] In this case, though, few nanoparticles deposit within the macropores using this method, therefore this collapse is

rarely observed. No cracks in the monolith wall as observed by Jarrah *et al.* [181] have been seen in any micrographs of the bare or washcoated monoliths.

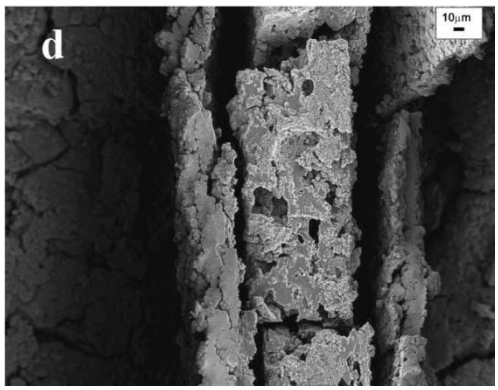

Figure 5.19 SEM micrograph of cracked monolith wall observed by Jarrah *et al.* [181] This effect is not observed for the samples produced in this work

The adhesion of the CNTs to the monolith was evaluated in two ways. First following literature procedure [116,173,180], the CNT/cordierite composites were subjected to extended maltreatment via sonication in ethanol at 37 KHz, for 30, 60, 120 and 180 minutes. The resulting samples were analysed via TPO. CNT composition decreases from 4.5 wt. % to 3.6 wt. % in the first 30 min after which no further loss of CNTs was observed (Figure 5.20). This weight loss is similar in absolute terms to previous studies, with 0.9 wt.% lost, compared to 0.6 wt.% loss [173,180] in previous studies, however the % weight loss is much higher with 20% weight lost in our study, but only 3 - 4 % loss in previous studies. [173,180] Some of this difference may be due to the unusually high carbon wt.% reported by previous author as discussed in section 5.4 . Previous authors have suggested that growth of CNF into the macroscopic structure of the cordierite from the alumina washcoat is the reason for this strong attachment. [180]

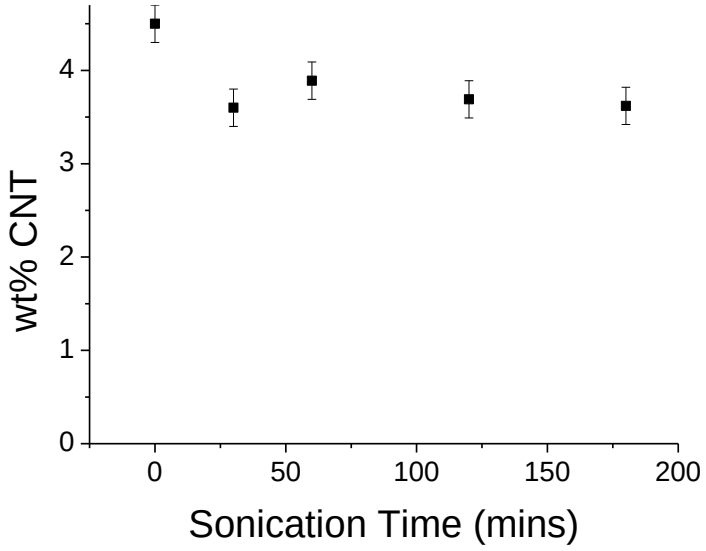

Figure 5.20 wt.% carbon on composite after ultra-sonication for varying lengths of time

In this case, this effect would be unlikely to occur, it is theorised that the attachment of the CNT to the substrate is through a nanoparticle at the base of the CNT, anchored to the cordierite. Additionally the entangled bundles of CNT could be expected to support each other, increasing attachment. A second method, closer to actual experimental conditions, was to place, the CNT/cordierite monolith in a reactor under a flow of gas, similar to that used in a FT reaction (100 sccm for 32 hours). No loss of CNT was observed after the first hour when loose debris was dislodged, much lower than the sonication case. In both cases the monolith has maintained its structural integrity.

The monolith composites seem to be physically robust, being slightly stronger than traditional cordierite, and are able to retain the carbon layer even in the face of very robust methods such as sonication. It is unlikely that as much abrasive force will be applied to the catalyst in typically operation, suggesting that after the initial loose catalyst is removed, the material should retain the majority of the carbon layer successfully.

5.6.2 Pressure drop

A key advantage of monoliths compared to packed bed reactors is a low pressure drop, which can be important in large scale reactions. In Figure 5.21 a comparison between 10 cm long × 1 cm diameter bare cordierite monoliths, washcoated alumina monoliths, CNT coated monoliths and an equivalent amount of CNT in a packed bed configuration (0.1 g, roughly equivalent to the weight of CNT grown on the coated monoliths) is shown. It can be clearly seen that the

equivalent amount of CNT has a very high pressure drop in comparison to all monoliths, as would be expected due to the low voidage or open space for gas to flow through. Theoretical values of pressure drop for the powder catalyst, using the Ergun equation (5.4) could not be obtained.

$$\Delta p = \frac{150\mu(1-\epsilon)^2 V_s L}{\epsilon^3 D_p^2} + \frac{1.75(1-\epsilon)\rho V_s^2 L}{\epsilon^3 D_p} \qquad (5.4)$$

where: Δp = the pressure drop across the bed, L = the length of the bed, D_p = the equivalent spherical diameter of the packing, ρ = the density of fluid, μ = the dynamic viscosity of the fluid, V_s = the superficial velocity and $\acute{\epsilon}$ = the void fraction of the bed

Due to insufficient information about the particle size, and geometry of the non-uniform CNT and the porosity of the resulting packed bed, D_p and $\acute{\epsilon}$ are unknown. This experiment clearly demonstrates the very high pressure drop of the CNT powder in comparison to the monolith.

Theoretical pressure drop values obtained for the empty tube using the Hagen-Poiseuille equation,[251] and for the monolith containing tube using a modified form of the Hagen-Poiseuille equation[166] indicate that a pressure drop of the order of 0.0001 bar would be expected for the empty tube, and 0.01 bar for the monolith containing tube. The experimental results suggest that there is an inherent pressure drop in the measuring equipment of ~0.03bar, when this is discounted, it can be observed that the pressure drop difference between the empty tube, and the monolith is around 0.01 bar, of the order of pressure drop expected. It is to be noted that the CNT coated monolith, despite having an apparently thinner internal channel does not have a notably different pressure drop to the bare cordierite monolith. The washcoated monolith however has approximately double the pressure drop of the CNT-coated monolith for similar free cross-sectional area (0.65 mm^2 and 0.64 mm^2, respectively). This higher pressure drop for the wash-coated monolith may indicate interaction between the flowing gas and the wash-coat causing some pressure drop, whereas this effect is not observed for the CNT coated monolith, suggesting that no pressure drop is caused by flow of gas through the CNT layer. This suggests a preferential flow of gas through the centre of the channel, rather than the dense CNT forest. This may impact mass transfer of the reactants to the catalyst, as gas preferentially prefers to pass through the monolith without significant

interaction with the CNT forest. No significant difference was observed between a single 10 cm long monolith and 10 × 1 cm long monoliths occupying the same reactor section.

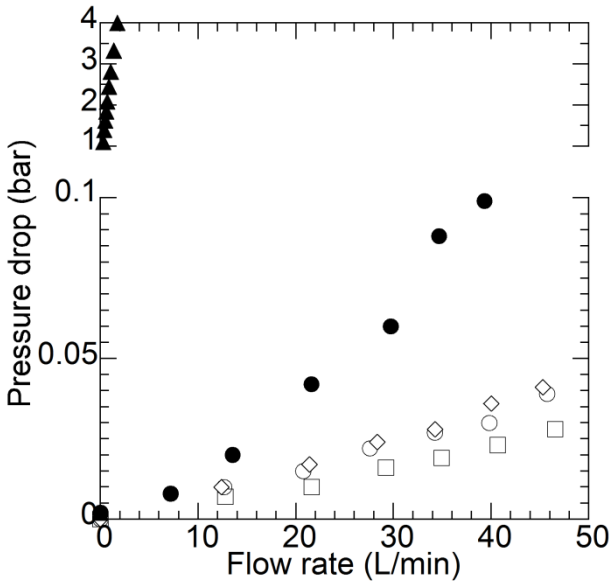

Figure 5.21 Pressure drop over a 10 cm × ½ inch Swagelok™ tube filled with: (○) 10 × 1 cm bare cordierite monolith; (◊) 10 × 1 cm CNT coated cordierite monolith; (●) 10 × 1 cm alumina washcoat cordierite monolith; (□) empty reactor tube; and (▲) equivalent mass of CNT powder in packed bed configuration.

This suggests that the monolith reactors would remove the issues associated with the extreme pressure drop observed for the powder catalyst. The pressure drop profile is similar to that of the Al_2O_3 washcoated cordierite monolith which has traditionally been used in a number of catalytic applications.

5.6.3 Uniform synthesis

Growth of CNTs has been successfully achieved on monolith pieces 1 cm length, and 1 cm in diameter. For a potential scale up of this process to industrial level it is necessary to determine whether growth of CNTs across longer monolith pieces is possible. An optical micrograph of a typical 9 x 1 cm CNT/cordierite monolith piece with SEM and Raman measurements taken along this monolith demonstrate the presence of CNTs across the longer monolith piece with uniform length and morphology consistent with results for the shorter samples is shown in Figure 5.22. This confirms that growth can be achieved on longer monolith pieces, and that

this process could potentially produce the CNT-monolith composites on the larger scale necessary for industrial catalysis.

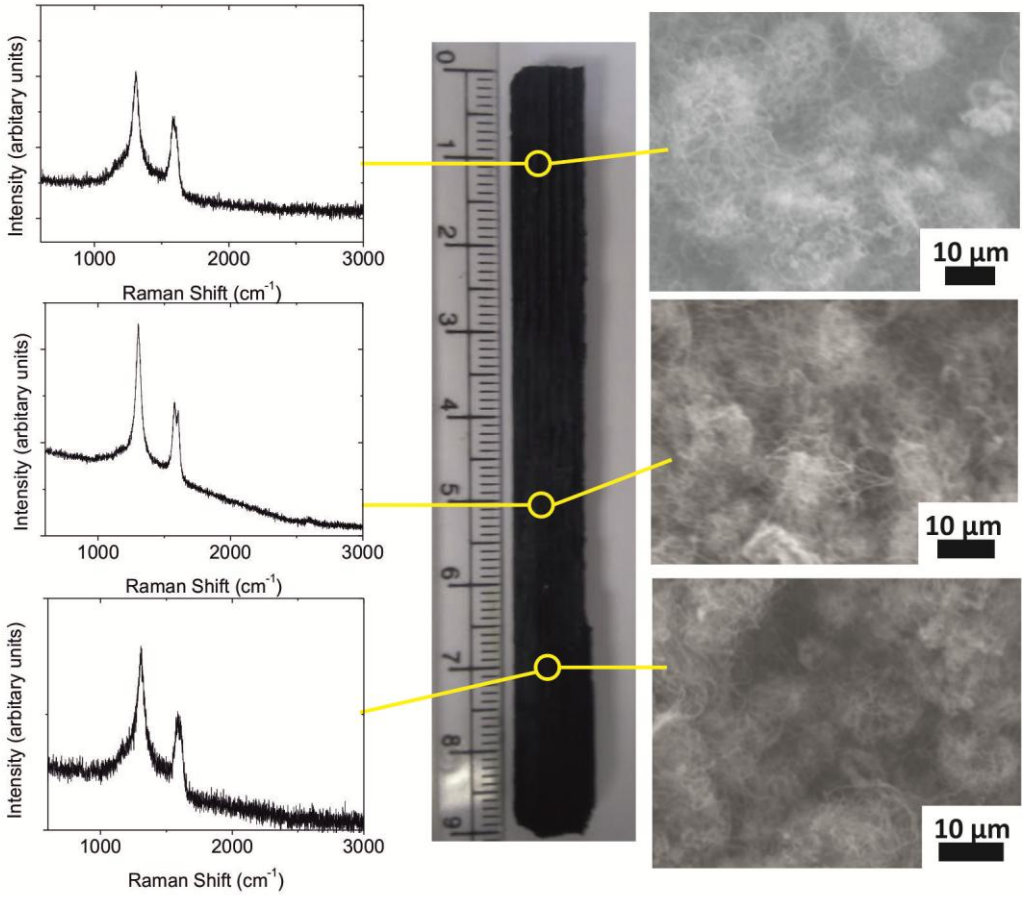

Figure 5.22 Optical micrograph of cross-sectioned 9 x 1 cm CNT coated cordierite monolith with SEM micrographs and Raman spectra showing uniform coverage by CNTs

5.7 Conclusions

In this chapter the growth of CNT has been demonstrated on bare cordierite monoliths, using an injection based CVD method. The use of the injection based CVD method allows the deposition of MWCNT directly onto the bare cordierite without the need for pre-preparation steps such as an alumina washcoat or an intensive catalyst impregnation step.

Growth of MWCNT using this method on bare cordierite shows marked differences to that grown on the alumina washcoated cordierite and those produced via other methods. The

resulting MWCNT produce a thick aligned layer on the monolith surface, the resulting carbon layer is significantly thicker than those reported by other studies, though the total carbon wt.% is lower. This may be due to an error in reporting of carbon wt.% in previous studies, as the values they obtain would suggest the produced carbon layer is much denser than the maximum density of MWCNT.

The MWCNT layer can be controlled by varying the synthesis time and temperature, increasing the synthesis time increases the growth rate, though growth of the carbon layer appears to halt after 90 minutes. 790 °C was the optimum temperature for MWCNT synthesis based on those used, higher and lower temperatures both led to a decrease in carbon layer thickness and carbon deposition.

The surface areas reported for these composites are much lower than those reported in the literature for similar materials. This may be due to the fact that MWCNT produced by the injection CVD method have relatively low surface areas, due to having relatively large diameters and being closed. Treatment of the MWCNT to remove amorphous carbon, and open the MWCNT ends has increased the surface area, by opening the MWCNT ends.

The MWCNT composites would seem to have the potential to be scaled up for large scale heterogeneous catalysis. The MWCNT composites have similar mechanical strength to cordierite, and have demonstrated the same ability as previous carbon composites to retain carbon after being subjected to extended maltreatment, losing only 20% of the CNT deposited after 2 hours of sonication in ethanol. This strong anchoring of the CNT to the support helps address the problem of the potential health hazards of MWCNT, since they are strongly anchored to the support, they are unlikely to become airborne and thus become a health hazard.

The MWCNT composites demonstrate low pressure drop, similar to that of the bare cordierite, and less than that of the wash coated cordierite. The pressure drop of the composite is two orders of magnitude less than the high pressure drop observed for the MWCNT powder. This addresses another of the potential concerns for the use of MWCNT on an industrial scale. A possible concern is that almost no increase in pressure drop is observed on addition of the CNT layer, suggesting that interaction between the gas flow and the CNT forest is not large.

The MWCNT composite has been slightly scaled up from the 1 cm x 1 cm pieces initially synthesised, to a 1 x 9 cm piece, confirming that growth can occur on longer pieces. Scale up beyond this level was limited by the CVD rig used.

After synthesis and characterisation of these composites the next goal of the project was to use these composites as supports in the catalysis of carbon dioxide, the following chapters discuss the preparation of an experimental rig to test carbon dioxide conversion chapter 6 and the use of these supports as catalyst supports chapter 7.

6 Preparation for Catalytic Testing

This chapter discusses the construction of two reactors for testing of catalysts, and the preparation of the catalysts used in these systems. Chapter's 4 and 5 discuss the synthesis of the carbon nanotube supports used in more detail, this chapter outlines the preparation of these supports as catalysts. Chapter 7 will discuss the catalytic results obtained.

6.1 Catalyst Preparation

6.1.1 Preparation of Cordierite Monolith

Cordierite Monolith (Dow Corning, 1.1 mm square channels, 62 cells/cm^2) was obtained from the group of Professor Stan Kolaczcowski. Cordierite monolith is an extruded, honeycomb ceramic, consisting of anisotropic cordierite (2MgO.2Al2O3.5SiO2) crystallites.[266] The resulting structure has very low thermal expansion properties. The cordierite monolith was obtained as 10 x 12cm cylinder. This cylinder was sliced into a number of 1 cm diameter cylinders using a band saw, then sanded down to ensure uniform thickness. The monolith slices were cut to an appropriate size to fit into the ½ inch Swagelok reactor using a punch set, a 9mm diameter punch was used to punch cylinders out of the disc. The resulting monoliths were 9 x 9 x10 mm cylinders. Fragments which did not match this size were discarded.

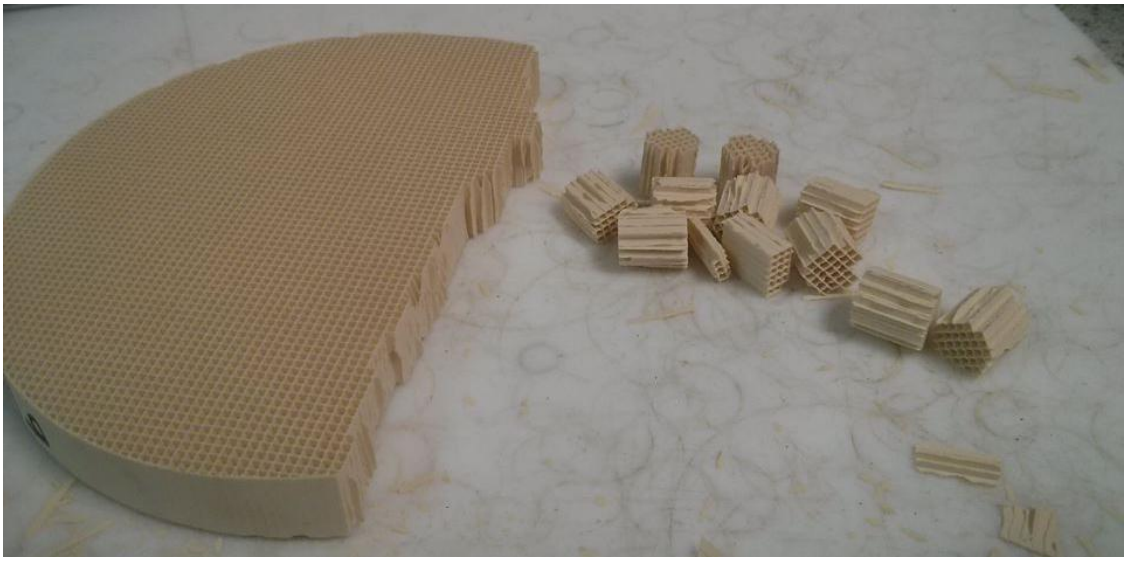

Figure 6.1 Cordierite monolith slice and resulting monolith pieces

Additionally when longer monolith pieces were required, the 10 x 10 x 12 cm cylinder was sliced to give 1.3 x 1.3 x 12 cm pieces, the outer layers were slowly cut using a Stanley knife typically to give a 9 x 9 x 120 mm cylinder. This was then cut to the desired length.

My thanks to Professor Stan Kolaczcowski and his group for providing the cordierite monoliths, and Mr Paul Frith and Dr Daniel Lou Hing for slicing the monoliths.

6.1.2 Purification of MWCNT by acid treatment

In order to remove residual iron nanoparticles and amorphous carbon, the MWCNT were refluxed under hydrochloric acid. 1.00 g of CNT were placed in 250ml of conc. HCL. The resulting solution was refluxed at 100 °C for 24 hours. After this treatment the resulting solution was filtered using a Whatman PTFE filter. After filtration the resulting nanotube powder was washed with de-ionised water, washing repeatedly until the resulting filtrate was ph neutral. After through washing, the remaining CNT were dried at 120 °C for 4 hours.

6.1.3 Incipient Wetness impregnation of carbon nanotube catalyst

Catalysts were prepared by the wet impregnation of metal solutions on the supports, using the incipient wetness method. Metal salts of $Fe(NO_3)_3.9H_2O$ were dissolved in a minimum amount of ethanol and added to the support. The mixture was left to dry at room temperature for 24 hours, before being crushed and dried for 12 hours at 100 °C, then finally being calcined at 370 °C for 4 hours.

6.1.4 Oxidation of Fe@CNT

In order to activate the Fe@CNT powder they were oxidised in a crucible under air. The sample was heated to 570 °C at 20 °C min^{-1} and held at temperature for 30 minutes, before cooling.

6.1.5 Oxidation of Fe@CNT Monolith

In order to activate the Fe@CNT Monolith for they were oxidised in a Carbolite Wire Wound Three Zone Tube Furnace. The monoliths were placed in ½ inch stainless steel Swagelok reactor and heated to oxidation temperature under 50 sccm of argon, after stabilisation at the oxidation temperature (usually 470 °C), argon was switched off and a flow of 50 sccm of air was passed over the catalyst for the length of the oxidation (usually 10 minutes). After the oxidation the reactor was flushed with 100 sccm of argon for 5 minutes, before being left to cool under 30 sccm argon.

6.2 Catalytic Testing

6.2.1 Atmospheric pressure testing of CO_2 conversion

In a typical hydrogenation experiment, a reactor 10 cm long, made of either ¼ or ½ inch stainless steel, was filled with catalyst. The catalyst was typically reduced under a H_2 flow of 50 sccm for 2 hours. CO_2 was then introduced into the reactor, with a typical ratio of H_2:CO_2 of 3:1. Typically flow rates of 6 sccm of H_2 and 2 sccm of CO_2 were used. The flow of gases was controlled by a number of mass flow controllers, controlled by a Labview program. Tests were performed at atmospheric pressure, in a temperature range from 250-400 °C. GHSV was typically 3200 $cm^3\ g_{cat}^{-1}\ h^{-1}$ for the monolithic catalysts or 1200 $cm^3\ g_{cat}^{-1}\ h^{-1}$ for the powder catalyst. Residence time over both catalyst types was the same at 1.58 minutes. A reactor was set up according to the schematic in Figure 6.2 using a 1m length single zone carbolite furnace, as shown in Figure 6.3 . A three way valve at the exhaust of the system allowed sampling of the reaction products when desired. The reaction products were sampled using a SGE 50 ml gas tight syringe. When sampling the three way valve was switched to connect solely to the gas tight syringe, through an air-tight luer-lock connection. The syringe was allowed to slowly fill with the exhaust gas; after 10 ml had been sampled, the three way valve was switched to connect the syringe to the ventilation system and the syringe was vented to remove any residual air. After this the syringe was reconnected to the reactor exhaust, and a sample was slowly taken. Typically around 40 ml of sample was taken over 5 minutes. The gas sample was analysed using a GC-MS (see section 3.7).

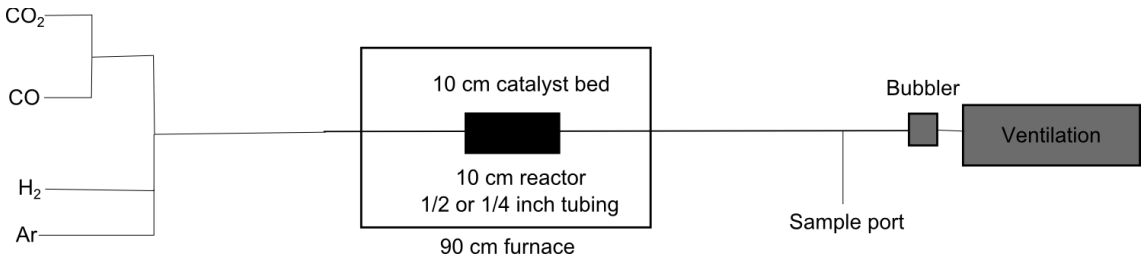

Figure 6.2 Schematic of low pressure reactor design

Figure 6.3 Picture of CO_2 testing setup

6.2.2 High pressure testing of CO_2 conversion

In order to test catalysts at higher pressures, a bespoke high-pressure catalyst testing rig was constructed (see Figure 6.5). This rig was capable of testing catalysts at pressures up to 30 bar, hydrogenating carbon dioxide and carbon monoxide with hydrogen. The entire system was placed in a walk-in fume-hood to minimise risk in case of a catastrophic failure.

The system utilised two MFCs for each gas, one for high flow rates (0-200 sccm, Omega), and one low flow rates (0-20 sccm, Bronkhurst). MFCs were controlled using a mixture of a custom Labview program, and Bronkhurst's flow DDE system. Typically the high flow rate MFCs were used to ramp the pressure quickly, whilst the low flow rate MFCs were then used to maintain lower flow rates at high pressure during the catalytic reaction. Switching between the high and low flow MFCs was controlled using a 3-way valve. Pressure was controlled using a fifth mass flow controller which allowed gas to flow once the correct pressure had been reached and maintained the set pressure. This system was limited to a maximum flow rate of 40 sccm. A pressure sensor was installed at the inlet of the reactor, which could be used to measure the inlet pressure, and hence the pressure drop across the system.

A 30 cm tube furnace was used for the heating of the reactor. In order to minimise the heating of joints under pressure, the reactor was designed so that no Swagelok connections were inside this furnace. A 35 cm long, ½ inch diameter, stainless steel reactor was used. The catalyst was typically placed in a 10 cm region at the centre of the reactor, held in position using quartz wool.

Upon installation of the new reactor, the system was pressure tested under a flow of carbon dioxide; once pressure was reached a low flow of CO_2 was introduced whilst the system was leak tested using snoop solution. If a leak was found the system was depressurised, the leaking joint tightened, and then the whole system was repressurised.

Experimental parameters for temperature and flow rate were comparable to those of the ambient pressure experiments, with reactions typically being run at 370 °C, and a $CO_{2;}H_2$ flow rate ratio of 1:3. Pressure was varied from 0 to 15 bar. Total flow rate was typically 8 sccm. GHSV was typically 3200 $cm^3\ g_{cat}^{-1}\ h^{-1}$ for the monolithic catalysts or 1200 $cm^3\ g_{cat}^{-1}\ h^{-1}$ for the powder catalyst. Residence time ranged from 1.58 to 3.94 minutes depending on pressure, and was 2.76 minutes at the standard test condition of 7.5 bar. Samples were taken through a three way valve in a gas tight syringe, using the same method as for the atmospheric pressure reactor.

To depressurise the reactor, the pressure regulator was set to zero and pressure was slowly released. An emergency relief valve was also installed which could be loosened to release pressure. A pressure relief burst disc was also installed, and set at 40 bar, which would release gas into the fume hood in the event of pressure build up.

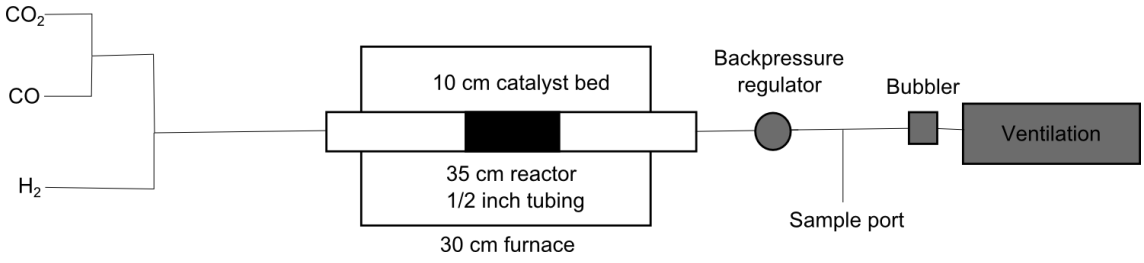

Figure 6.4- Schematic of high pressure reactor design

Figure 6.5 – High pressure reactor

6.3 Catalytic Testing Rig Safety

A number of different safety concerns needed to be considered for the catalytic testing rigs. Firstly flammable and asphyxiant gases are used for catalytic testing. In order to prevent ignition of the flammable hydrogen, the reactor is flushed at room temperature in order to remove oxygen, additionally a flashback arrestor was installed on the hydrogen cylinder to prevent any fire igniting the cylinder. A gas bubbler is also installed to prevent air being sucked back into the reactor via the exhaust stream.

To prevent build-up of asphyxiant gases, the reactors were set up in well ventilated areas, with the exhaust going directly into the ventilation system. In addition an oxygen sensor was installed in the lab set to alarm in the event of dangerously low oxygen levels. As the reaction produces carbon monoxide, there is some risk of leakage of carbon monoxide leading to

dangerous levels of this highly toxic gas, though ventilation should prevent this, a carbon monoxide sensor is present in case of a significant leak.

7 Carbon Nanotubes as CO_2 conversion catalysts

Carbon nanotubes have been successfully synthesised in powder form (chapter 4) and as a structured support (chapter 5). In chapter 6, the design and commissioning of a reactor for the testing of these catalysts for CO_2 conversion was discussed, and heterogeneous catalysts were prepared. In this chapter carbon nanotubes will be used as supports for carbon dioxide conversion catalysts, and the effectiveness of these catalysts will be discussed. The work in this chapter was performed in collaboration with Dr Justin O'Byrne of the University of Bath, who performed some of the experiments on the powder based catalyst included in this chapter for comparison purposes. Initial work on the development of the activation procedure for the powder catalyst (section 7.2.1) was published in the journal *Catalysis Science and Technology*. The *in-situ* XRD work, and some of the analysis of these catalysts was performed at Sasol Technologies UK, with the aid of Dr Phillip Landon. HR-TEM was performed at the University of Leeds, thanks to Dr Zabeada Aslam.

CNTs have been previously investigated as a support for Fischer Tropsch synthesis using a variety of promoted iron catalysts. [57,212-214] The MWCNT demonstrated some promising behaviours including improved selectivity to olefins, [205] better stability over time [213] and different behaviour for iron nanoparticles confined within the nanotube pore and those on the surface. [57,214] These results would suggest that CNTs could be a promising support for CO_2 conversion. To the best of the author's knowledge, iron nanoparticles supported on MWCNTs have not been previously reported in the literature for the conversion of CO_2.

MWCNTs are promising supports, but the powder catalysts have some problems associated with them, as discussed in chapter 5. Testing of the structured MWCNT supports, and comparison to the powder catalyst will also be performed.

7.1 Impregnated CNT Catalysts

To determine whether MWCNT could be an effective catalyst support, initial tests were performed using iron impregnated similar to those present in the literature, to use as a baseline comparison and determine whether CO_2 conversion was achieved.

In chapter 4, characterisation of the as produced MWCNT (MWCNT-AP) showed the presence of significant amounts of iron, with over 20 wt. % of the catalyst being iron. In order to ensure that this iron was not interfering with the catalysis, the MWCNT-AP was tested before and after impregnation with 10 wt.% iron (10 wt.% Fe/MWCNT-AP). The nanotubes were also treated using a standard acid wash to purify the nanotubes and impregnated with 10 wt.% iron

(10 wt.% Fe/MWCNT-AT). A 10 wt.% iron on activated carbon support (10wt.% Fe/C) was also prepared as a comparison. The resulting conversions are shown in Table 7.1. The catalyst preparation steps are described in more detail in chapter 6.

Table 7.1 Experimental results of CO_2 conversion, the reaction was performed at atmospheric pressure, using 0.1g of catalyst, at 370 °C. If the 10 cm catalyst bed was not filled by this weight of catalyst, the sample was diluted with silicon carbide. Total flow rate was 8 sccm using a CO_2 to H_2 ratio of 1:3. GHSV 4800 $cm^3\ g_{cat}^{-1}\ h^{-1}$

Catalyst	Alpha	Olefin Selectivity	X_{CO2} %	R_{obs} µmol $g^{-1}\ s^{-1}$	CO %	CH_4 %	C_2-C_4 %	$C5^+$ %
MWCNT-AP	n/a	n/a	0.15	0.02	93.3	6.7	n/a	n/a
10 wt.% Fe/MWCNT-AP	0.33	0.14	18.6	0.63	43.0	49.0	8.1	n/a
10 wt.% Fe/MWCNT-AT	0.30	0.18	18.9	0.64	38.1	49.6	12.3	n/a
10 wt.% Fe/C	0.40	0.23	5.2	0.18	99.2	0.4	0.4	n/a

It can clearly be seen that the MWCNT-AP has almost no activity for CO_2 conversion, confirming that residual iron from the MWCNT synthesis is not catalytically active. Impregnating the MWCNT with iron significantly increases the activity of the catalyst, with both impregnated catalysts (10 wt.% MWCNT-AP/MWCNT-AT) showing significant conversion of CO_2. Both MWCNT catalysts have significantly higher activity than the Fe/C support prepared by incipient wetness.

Comparing activity directly to literature catalysts is challenging due to the wide range of temperatures and pressures utilised in the literature. Comparing R_{obs} to Fe catalysts in the literature used for the FT reaction reveals similar activities under comparable conditions, with Fe/CNF catalyst used by Torres *et al.*[205] at 350 °C and 1 bar having an R_{obs} of 0.14, whilst a 20 wt% Fe/O-CNT catalyst used by Shulte *et al.*[215] at 340 °C and 20 bar had an R_{obs} of 0.57. Meanwhile the CO_2 reduction reaction, a Fe/Al_2O_3 catalyst used by Sai Prasad *et al*[237]. at 400 °C and 20 bar had an R_{obs} of 0.83. This suggests the catalyst has similar performance to reported literature catalysts. Olefin selectivity is lower than that reported for FT catalysis alone, with olefin selectivity of less than 0.2, CNT catalysts in the literature have olefin selectivities of 0.41 reported by Schulte *et al.*,[215] and 0.94 reported by Torres *et al.*[205] Olefin selectivity is higher than that reported by Sai Prasad *et al.*[237] for the CO_2 reduction reaction of 0.06. The improved selectivity of Torres *et al.* in particular is due to the presence of trace amounts of K and S

dopants, but there does seem to be an increase in olefin selectivity due to support on weakly interacting supports as reported by Torres *et al.*[205]

It is important to note that both the impregnation step and the acid purification step dramatically change the morphology of the catalyst support. As noted previously in chapter 4, the washing and filtration of the fine nanotube powder produced by CVD results in a mat of agglomerated CNT, which must be broken up before they are introduced into the reactor. The acid treatment also changes the nanotubes, removing impurities (as shown by the increased $I_{G'}/_{D}$ ratio, Figure 7.1), and has been reported to introduce surface functionality onto the surface of the CNT. [267]

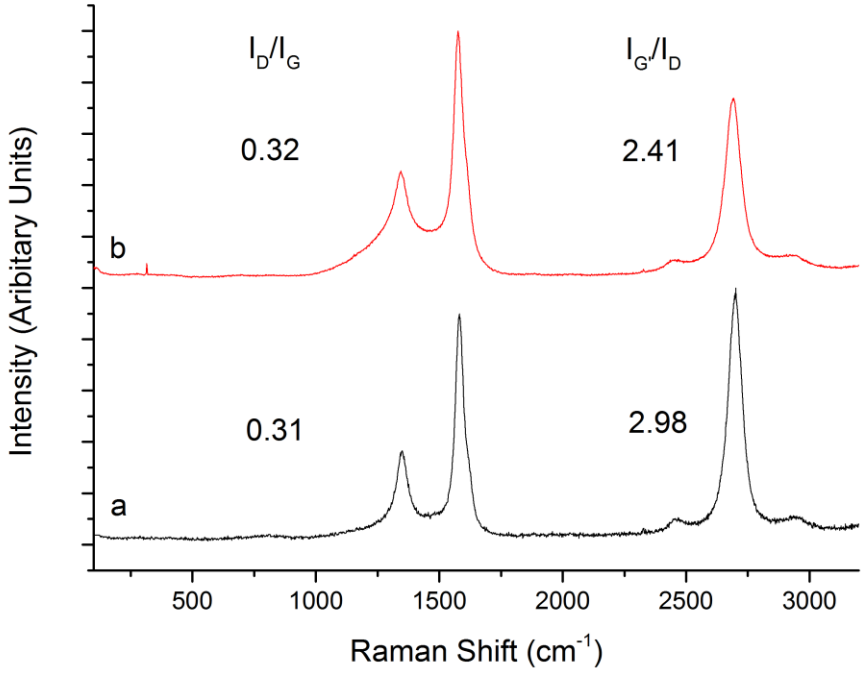

Figure 7.1 Raman spectra of a) acid treated CNT and b) as produced CNT

The results of these initial tests show that MWCNT can act as effective supports for iron catalysts, achieving higher conversions than an activated carbon catalyst.

7.2 Activation of un-purified CNT

The as produced MWCNT contain significant amounts of iron as described in chapter 5, with over 20 wt. % of the catalyst mass being iron. As demonstrated in section 7.1 , impregnated iron carbon nanotube catalysts are effective for CO_2 conversion, however the preparation process involves multiple steps. The presence of residual catalyst nanoparticles after MWCNT

synthesis is widely known, however most efforts have focused on the removal of this residue, rather than attempting to utilise them. [55] A number of studies have shown that some residual iron nanoparticles can remain even after strong acid treatment, as they are covered by a graphitic shell which prevents access. [149] Oxidation treatments have been shown to remove this layer, with research focussing on controlled oxidation in order to remove this graphitic layer without damaging the tube. [268-271] Despite this most authors in the catalytic literature report the use of strong acid washes in order to remove residual impurities. [161,212-214] These acid washes can significantly alter the catalyst, with nitric acid washes being reported to introduce functionality onto the nanotube surface.[272]

A few authors have reported on the effects of residual nanoparticles in CNT. Zhang *et al*, report the use of residual iron and cobalt particles in commercial CNTs as catalysts for NH_3 decomposition at temperatures over 700 °C, with no additional pre-treatment required. [153] Bahome has reported on the effects of residual iron and nickel nanoparticles on Fischer Tropsch synthesis, with iron having no influence on activity, whilst nickel showed slight activity as a methanation catalyst. [152] Van de Vyver *et al* reported that residual nickel nanoparticles on the tips of CNT are active for the conversion of cellulose, also noting the presence of graphene layers which partially inhibit access to the metal nanoparticles. The effect of residual metal is also acknowledged in electrochemistry, where ppm levels of residual nanoparticles are observed to dominate electro-chemical activity. [148]

Testing MWCNT-AP as CO_2 reduction catalysts demonstrated no catalytic activity, with only an insignificant quantity of methane being formed, in line with reports of Bahome *et al* for purified MWCNT (Table 7.1). [152] This is surprising as the iron content of the nanotubes has previously been calculated to be over 20 wt. % in the MWCNT-AP, significantly higher than that the wt. % used in preliminary catalytic activity explorations. Previous authors have demonstrated that increasing iron wt. % up to 25 wt. % results in increased conversions on other supports. [244]

An understanding of the CVD process, and TEM micrographs of the catalyst provide an answer to this. As has been previously reported, during MWCNT synthesis some metal nanoparticles are coated with carbon, rather than forming the seed for MWCNT growth (the exact reason for this occasional deactivation is unknown, though it is thought to be due to excess carbon, and differing nanoparticle sizes). [78] Metal nanoparticles can also be drawn up into the tube structure during synthesis. [100,101] The resulting nanoparticles are enclosed within the nanotube and cannot be accessed by the passing gases, and so are inactive for catalysis. This can be

easily confirmed by TEM analysis of the un-purified CNT, which shows that the iron nanoparticles present are either enclosed in graphitic shells on the surface of the nanotube, or confined within the nanotube itself (Figure 7.2). Though not reported by Zhang *et al.*, the reported activity of commercial CNT catalysts for ammonia decomposition is likely due to the removal of this graphitic layer at the high temperatures (700 °C) and corrosive conditions (NH_3 atmosphere), allowing access to the residual nanoparticles.

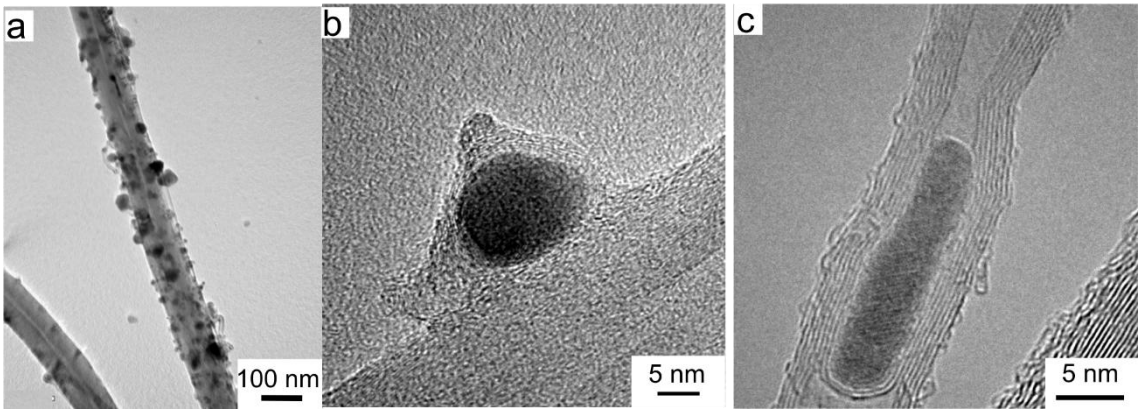

Figure 7.2 TEM micrographs of MWCNT-AP showing nanoparticles a) on the surface and at higher magnifications showing b) nanoparticle covered with a graphitic layer or c) confined within the CNT bore

7.2.1 Activation of powder catalyst

In order to activate the MWCNT-AP the graphitic layer surrounding the nanoparticles must be removed. This will allow the reactive gases to reach the catalytic particle. Opening the ends of the MWCNT should provide additional catalytic access for those NPs contained within the tube. Traditional cleaning methods such as refluxing and washing the MWCNT with strong acids can open nanotubes, and sometimes remove this graphitic layer.[273] However this process will also remove the majority of the residual nanoparticles.

An alternative method for removal of the graphitic layers is controlled oxidation of the MWCNT in air. [271,274,275] The graphitic layers covering the iron nanoparticle are less stable than the MWCNT themselves, so can be removed without damage to the MWCNT. [268] The exposure of metal nanoparticles at the tip of the MWCNT can also remove the graphitic 'caps' on the nanotube, perhaps allowing access to the metal particles contained within the tube. Initial studies for the activation of MWCNT were performed, [276] and it was found that if MWCNT were oxidised at 570 °C for 40 minutes under air, the graphitic layer was removed and the iron nanoparticles were exposed (Figure 7.3).

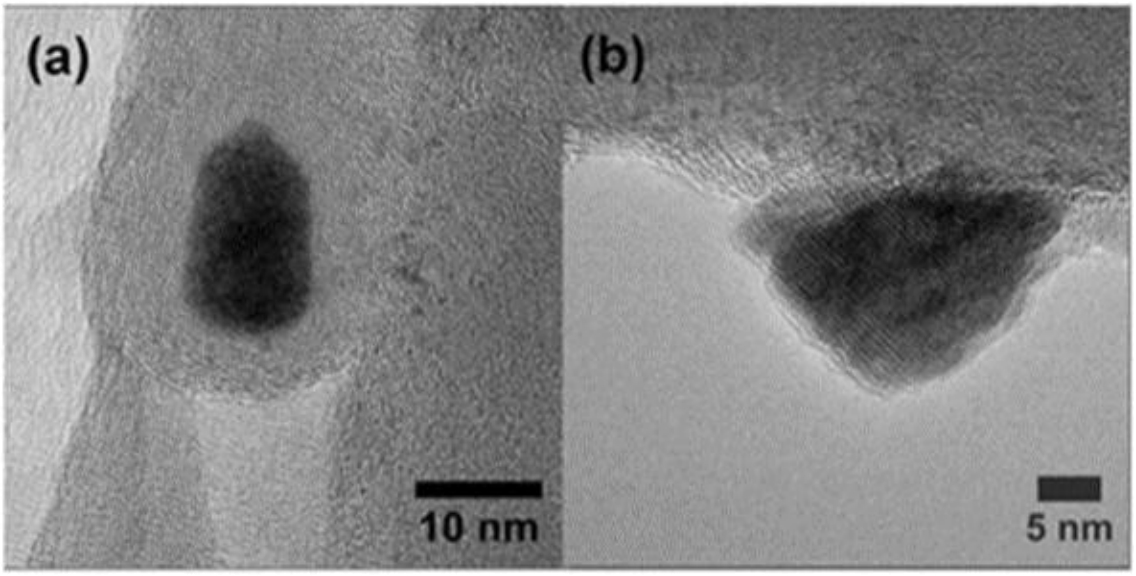

Figure 7.3 TEM micrographs of iron nanoparticle on the MWCNT a) as prepared, coated in a graphitic layer and b) after oxidation in air at 570 °C for 30 minutes, with the graphitic layer removed [276]

After exposing the iron oxide nanoparticle, the catalyst was reduced at 370 °C for 2 hours under hydrogen in order to activate the particle for catalysis. Examining the catalyst using *in-situ* XPS it was shown that the iron catalyst went through 3 distinct phases: Initially the iron is present in the zero valent form, or as iron metal, and coated with a graphitic layer, as shown by the Fe(0) peak which appears at 707.5 eV as seen in Figure 7.4 a, this peak is not very intense as it is masked by the graphitic carbon layer. Upon oxidation, the nanoparticle is exposed, and forms an intense Fe(III) peak at 711.5 eV and 724.5, as well as a satellite peak at 719 eV, as seen in Figure 7.4 b. These peaks are characteristic of Fe_2O_3.[277] Reduction of the catalyst results in formation of mixed metal Fe(II)Fe(III) oxide, as indicated by the appearance of a characteristic shoulder at 710 eV visible in Figure 7.4 c. [277] The Fe(III) ions are most prevalent, with 84% of iron detected being Fe(III) ions, and 16% of iron detected being Fe (II) ions suggesting the presence of a mix of Fe_2O_3 and Fe_3O_4 on the CNT surface, with the concentrations detected suggesting that Fe_3O_4 accounts for 32% of the surface iron. The iron concentration on the surface increases from 0.2 atom% to ~1 atom% during the treatment. This can be attributed to the iron signal being partially attenuated by the graphitic carbon layer. The iron loading observed is much lower than would be expected given that the CNT are ~21wt% iron, this can be attributed to the tubular nature of the CNT with the majority of the iron contained within the CNT bore.

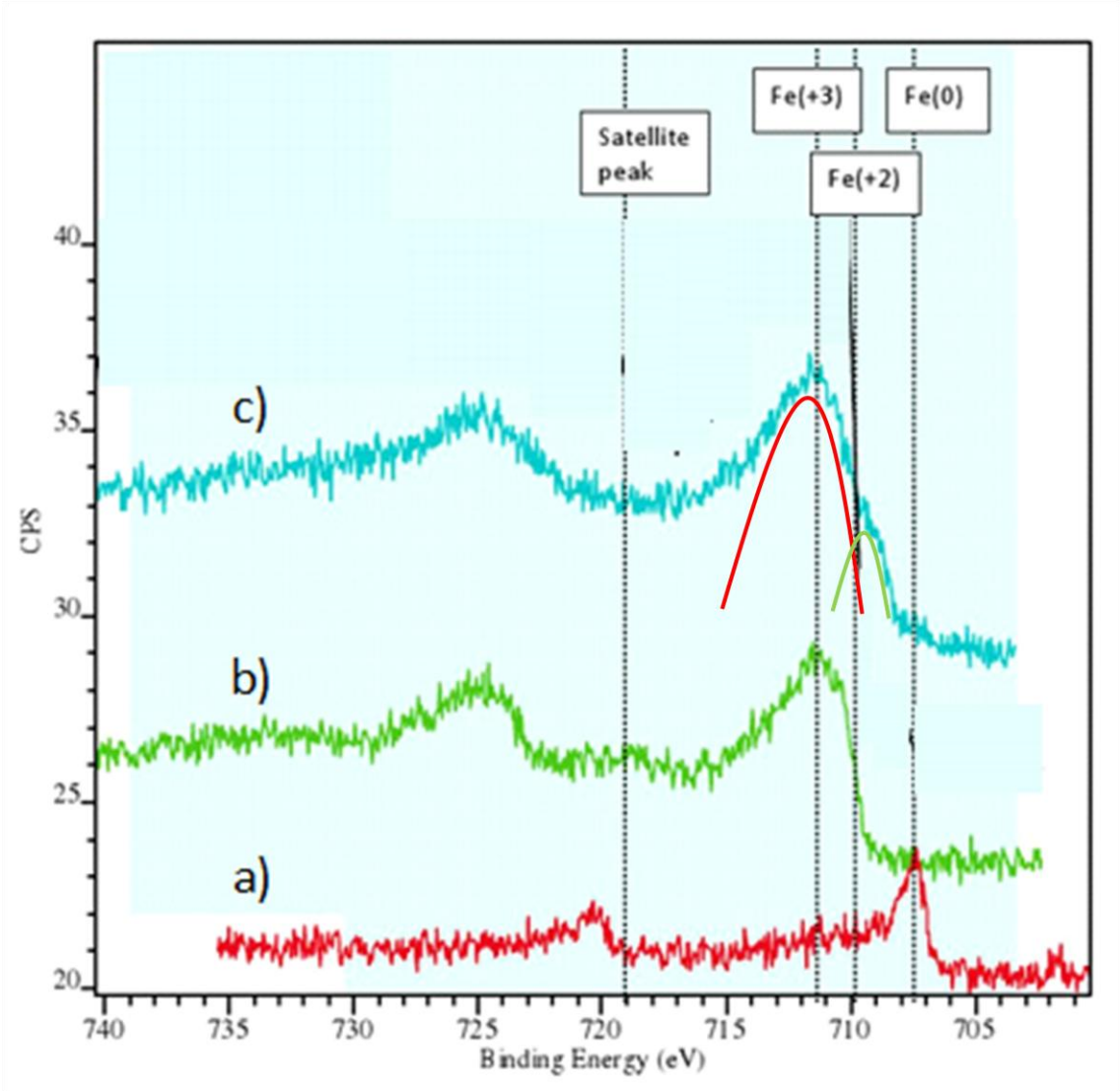

Figure 7.4 XPS (2p region $2p_{3/2}$ ~ 710 and $2p_{1/2}$ ~725 eV) Analysis of the oxidation states of iron particles on the surface of the Fe@CNT catalysts a) untreated as grown b) 40 min at 570 °C oxidised in air c) reduced in 50 sccm H_2 for 280 min

The process is illustrated in Figure 7.5.[276] From this point the activated MWCNT catalyst will be referred to as Fe@CNT powder.

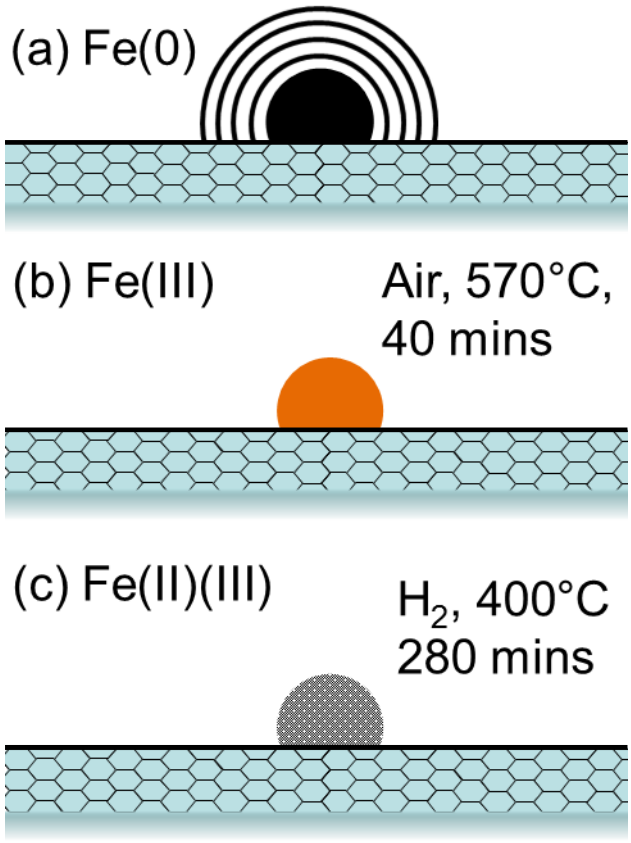

Figure 7.5 Oxidation states of a) untreated iron nanoparticle covered in a graphitic layer (not to scale) b) thermally oxidised nanoparticle with carbon layers removed and c) reduced particle treated with H_2 [276]

This process activates the as-produced powdered CNT support as a catalyst. The powdered catalyst demonstrated higher activities per gram of surface iron, than a reference Fe/MWCNT catalyst formed by incipient wetness impregnation.[276]

7.2.2 Activation of monolithic catalyst

Although powdered MWCNT produced via injection CVD have been activated for catalysis by a simple oxidation process, replicating this process with the monolithic catalysts was not a simple task. Oxidation of MWCNT grown on cordierite monoliths at 570 °C for 40 minutes led to an almost complete decomposition of the CNT layer, resulting in a rust coloured layer on the surface of the monolith, which can be attributed to residual iron (Figure 7.6).

Figure 7.6 a) CNT coated monolith b) after 30 minutes under air at 570 °C c) after 10 minutes under air at 570 °C

The CNT layer on 10, 1 cm by 0.9 cm diameter monoliths weighs approximately 150 mg. TPO of the powder shows that at 570 °C only 20% of the sample would be expected to oxidise (Figure 7.7). TPO of the cordierite/CNT powder show similar behaviour. Despite this when held at 570 °C for 40 minutes all CNT seem to have been removed. This is surprising as though the CNT powder appears to be slightly more stable than the cordierite/CNT, behaviour of the two samples are very similar up to 570 °C. One possible explanation for this behaviour is that the monolith structure provides increased surface area accessible to air, as well as increased diffusion of oxidation products, and improved heat transfer. These effects would not be observed in the TPO as the sample is ground down in order to be measured. This increased access may increase the rate of graphitic layer removal, allowing the exposed iron nanoparticles to catalyse the decomposition of the nanotubes. The packed nature of the CNTs on the surface of the monolith will mean exposed nanoparticles are in close proximity to neighbouring CNTs, possibly catalysing the decomposition of these nanotubes.

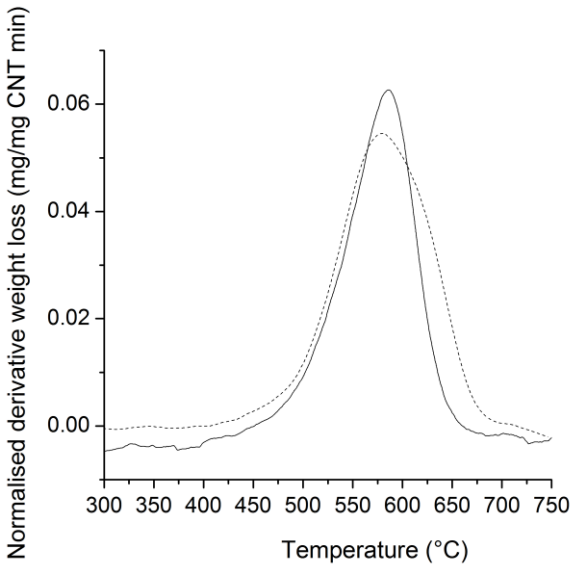

Figure 7.7 TPO profiles for CNT on cordierite (-) and CNT powder (---), normalised by weight of CNT

Previous work has shown that dynamic oxidation systems (i.e. those that heat the sample under the oxidising gas to higher temperatures) can oxidise the sample much quicker than those which use a static oxidation method (taking the sample to temperature before exposing it to the oxidising gas). [274] In order to have better control of the oxidation process, the monoliths were heated under a flow of 50 sccm argon until the desired temperature was reached, the oxidation gas air was then introduced into the system at 50 sccm, for a period of time. After this the monoliths were again cooled under argon.

In order to determine the ideal oxidation conditions for the process, a series of different oxidation temperatures (370 – 570 °C at 50 °C intervals) were tested. The monoliths were oxidised for 10 minutes as oxidising for longer periods result in the decomposition of all nanotubes. The activated catalyst was then tested at 370 °C at atmospheric pressure to determine which oxidation conditions resulted in the best performance.

Oxidation at 470 °C resulted in the best performance, however all tested catalysts demonstrated very similar activity. An odd trend was noted for this series of experiments, with conversion of over 3% and an Robs approaching 1 for all catalysts regardless of the oxidation treatment conditions. This was most notable when the monolith catalyst was oxidised at 370 °C, which is below the temperature at which oxidation of the MWCNT was first detected via TGA. It was thought to be unlikely that the graphitic layer would be removed under these conditions. This suggested that in this case the oxidation process, and the removal of the graphitic layer were having little effect on the catalytic activity.

The regularly performed blank test demonstrated the reason for this behaviour. Previous blanks had shown no activity for the empty stainless steel reactor, but after repeated oxidations, the stainless steel reactor demonstrated similar activity to those containing catalysts (conversion between 3.5 and 5 % for temperatures between 370 °C and 570 °C). Further tests with a fresh stainless steel reactor again showed no activity, but after oxidation for 10 and 30 minutes, the reactor showed increasing activity (Figure 7.8). It appears that repeated oxidations of stainless steel can result in a reactor capable of performing CO_2 conversion. Oxidised stainless steel has been reported as an effective methanation catalyst for CO_2 conversion, but appreciable activity was only observed above 425 °C. [278] Other authors should be careful to ensure that the reactor they used is not activated in a similar manner.

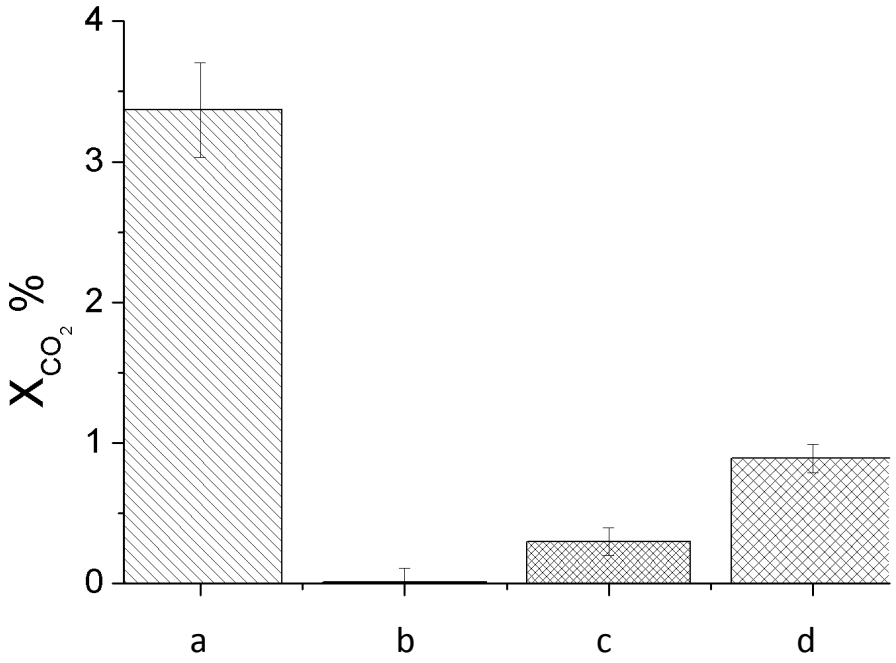

Figure 7.8 Conversion of CO_2 at atmospheric pressure without catalyst using different stainless steel reactors at 370 °C. Total flow rate was 8 sccm using a CO_2 to H_2 ratio of 1:3. a) repeatedly oxidised stainless steel reactor (at various conditions) b) unoxidised stainless steel reactor c) stainless steel reactor oxidised for 10 minutes at 570 °C d) stainless steel reactor oxidised for 30 minutes at 570 °C

Once the oxidation of the stainless steel reactor was identified as the likely cause for activation of the tube, the oxidation experiments were repeated, this time performing oxidation and reaction in separate stainless steel reactors (Figure 7.9). These experiments confirmed that the highest activity was observed for catalysts activated at 470 °C, with CNT/cordierite composites oxidised at lower temperatures showing little activity, presumably due to less of the iron nanoparticles being exposed. Oxidising the catalyst at higher temperatures, also showed less activity. This may be due to decomposition of the CNT support, and as a result the formation of larger iron particle agglomerates. The activated monolith catalyst will be referred to as Fe@CNT monolith from this point.

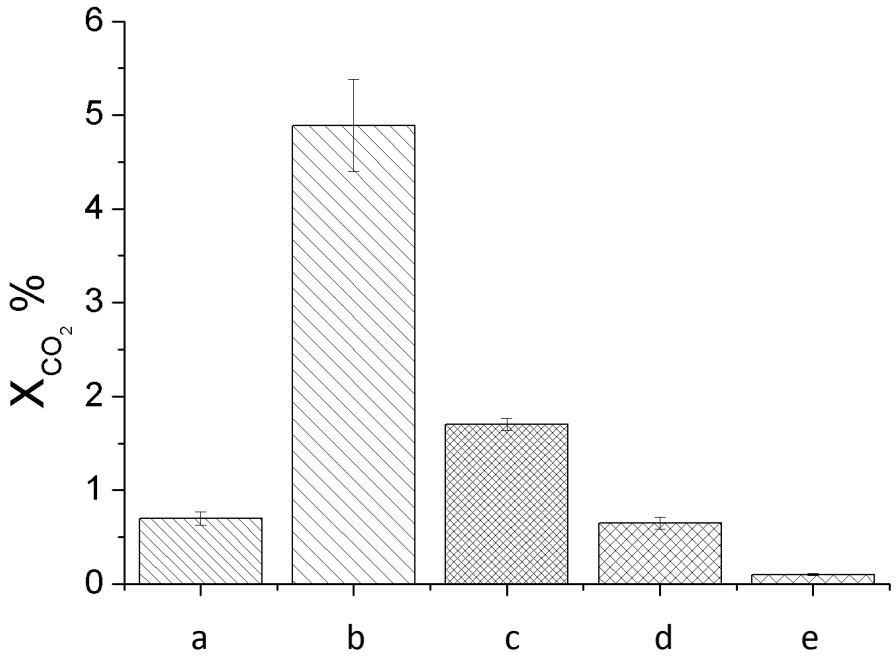

Figure 7.9 Conversion of CO_2 at atmospheric pressure over a 10 cm bed of Fe@CNT/monolith (synthesised at 790 °C for 60 minutes, approximately 0.15g of Fe@CNT), at 370 °C. Total flow rate was 8 sccm using a CO_2 to H_2 ratio of 1:3. The Fe@CNT bed was oxidised for 10 minutes at a) 420 °C b) 470 °C c) 520 °C d) 570 °C e) blank before being transferred to an un-activated steel reactor

7.3 Catalyst Characterisation

In order to gain a better understanding of the catalyst behaviour, the catalyst was characterised using a number of different techniques at each stage of the process. The oxidation process at 470 °C had no apparent effect on the surface area of the support, with monoliths tested before oxidation, after oxidation and after reaction giving surface areas which were the same within the significant error present for these very low surface areas (Table 7.2). Surface area of the monolith samples are relatively low with total surface area of the combined composites being less than 4 $m^2 g^{-1}$. However, considering that the MWCNT consists of less than 5% by weight of the monolith, the surface area of the active CNT layer itself is approximately 73 $m^2 g^{-1}$. It is to be noted that a large inherent error is present for these samples due to the very low surface areas, as discussed in the experimental section.

Table 7.2 BET surface area of Fe@CNT/Monolith catalysts after each stage of the process

Sample	Surface Area ($m^2 g^{-1}$)
As synthesised	3.57
After oxidation	3.69
After reaction	3.75

Comparing the Raman spectra of Fe@CNT monolith samples before and after oxidation, and after reaction show distinct differences between the samples (Figure 7.10). Samples before oxidation and after reaction have similar defect levels, with those after reaction being slightly more defective. After oxidation the level of defects detected shifts upwards, suggesting that the oxidation process as well as removing the graphitic layer introduces some oxidic defects into the tube structure. These defects seem to disappear after reaction, with I_D/I_G ratio and $I_{G'}/I_D$ ratio returning to previous levels. This suggests that the hydrogenation or reaction regime removes these defective sites.

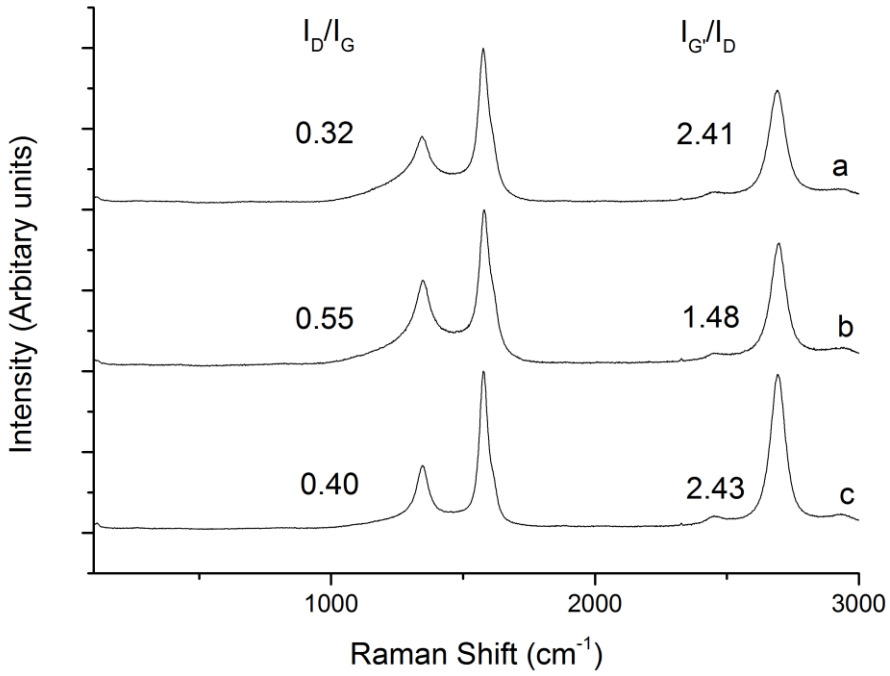

Figure 7.10 Raman spectra of FE@CNT monolith after a) preperation b) oxidation for 10 minutes at 470 °C and c) reaction for 8 hours at 370 °C

Attempts to analyse the Fe@CNT monolith via XRD proved futile, as CNT powder scraped off the monoliths surface resulted in an XRD pattern which was dominated by fragments of highly crystalline cordierite amongst the MWCNT powder (Figure 7.11).

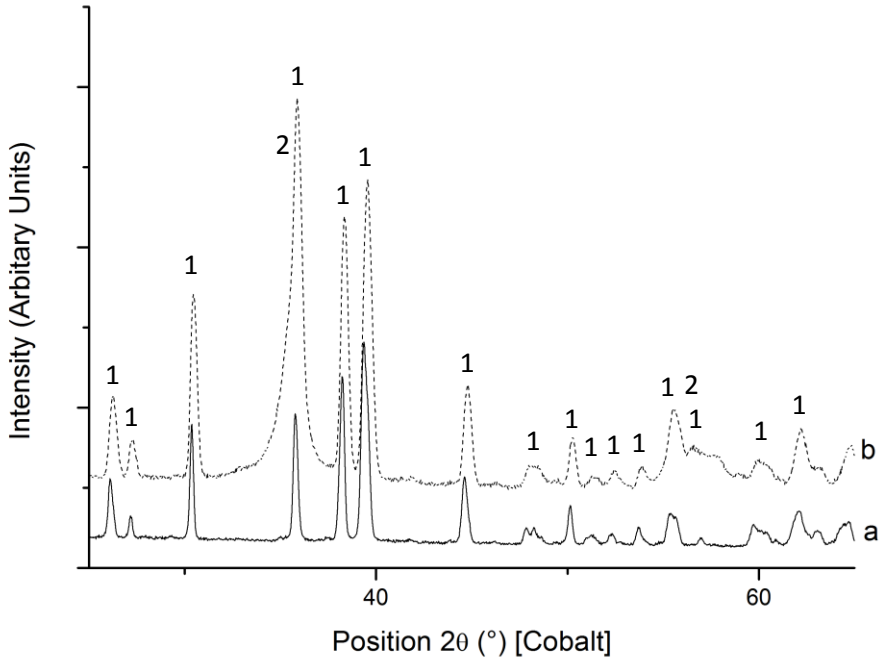

Figure 7.11 XRD spectra of a) cordierite and b) CNT scraped from cordierite monolith 1 cordierite peaks (attributed to mixture of oxides) 2 CNT peaks. Peaks belonging to the CNT catalyst are masked by highly crystaline cordierite

The oxidation, reduction and reaction process of the Fe@CNT powder were followed instead by *in-situ* XRD to determine the species formed. High resolution TEM images and EDX analysis were performed on the catalyst after preparation, after oxidation and after reaction in order to observe changes in the graphitic layer. The *in-situ* XRD showed clear changes in the species present on the catalyst at each stage of the reaction (Figure 7.12). Here the changes in the catalyst will be investigated in detail, along with discussion on the impact of these changes on the catalytic process.

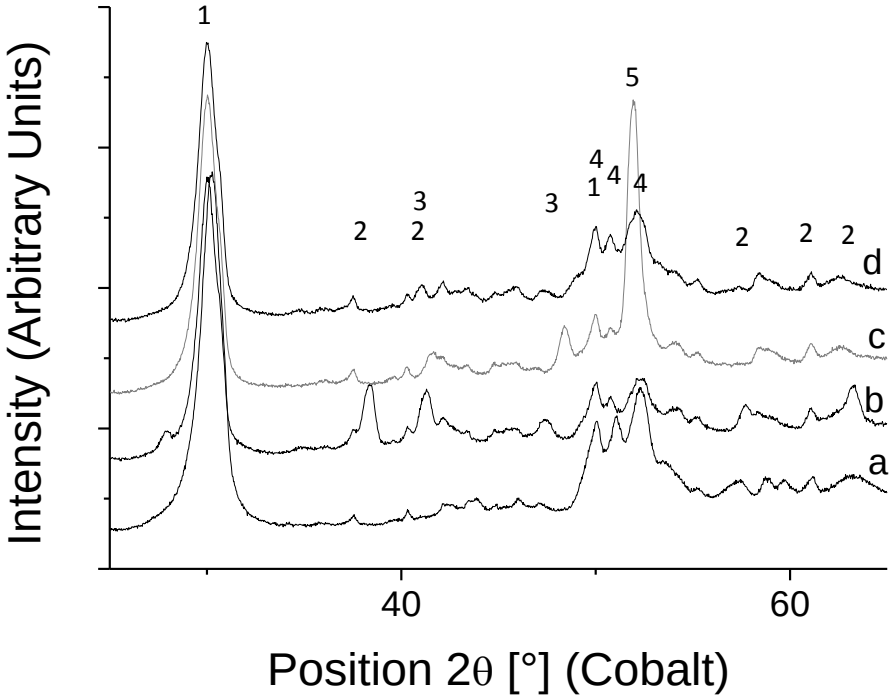

Figure 7.12 XRD spectra of Fe/CNT powder after a) synthesis at 790 °C for 60 minutes b) oxidation at 470 °C c) hydrogenation at 370 °C for 2 hours d) reaction at 370 °C for 4 hours 1) CNT 2) Fe_2O_3 haematite 3) Fe_3O_4 magnetite 4) Fe_3C cementite 5) Fe(0) iron metal

After synthesis, before any treatment of the MWCNT, the XRD spectra (Figure 7.12a) shows peaks corresponding to MWCNT, metallic iron, and an iron carbide species, which is a good match for the cementite species Fe_3C (this assignation must be treated with some caution as diffraction patterns for iron carbide species can have very similar peaks). TEM micrographs of CNT after synthesis on the monolith (Figure 7.13) clearly show the presence of iron in two distinct environments, on the surface of the nanotube, coated with a graphitic layer and inside the nanotube. EDX analysis cannot readily determine whether one is purely metallic iron and the other carbide, as the background carbon signal from the CNT is difficult to distinguish from the carbide. There is clearly however no oxygen present confirming the absence of an oxide species. Previous *in-situ* studies have observed the presence of both metallic iron and Fe_3C in the growth phases of CNT. [125,279] These species have also been previously detected after growth. [67]

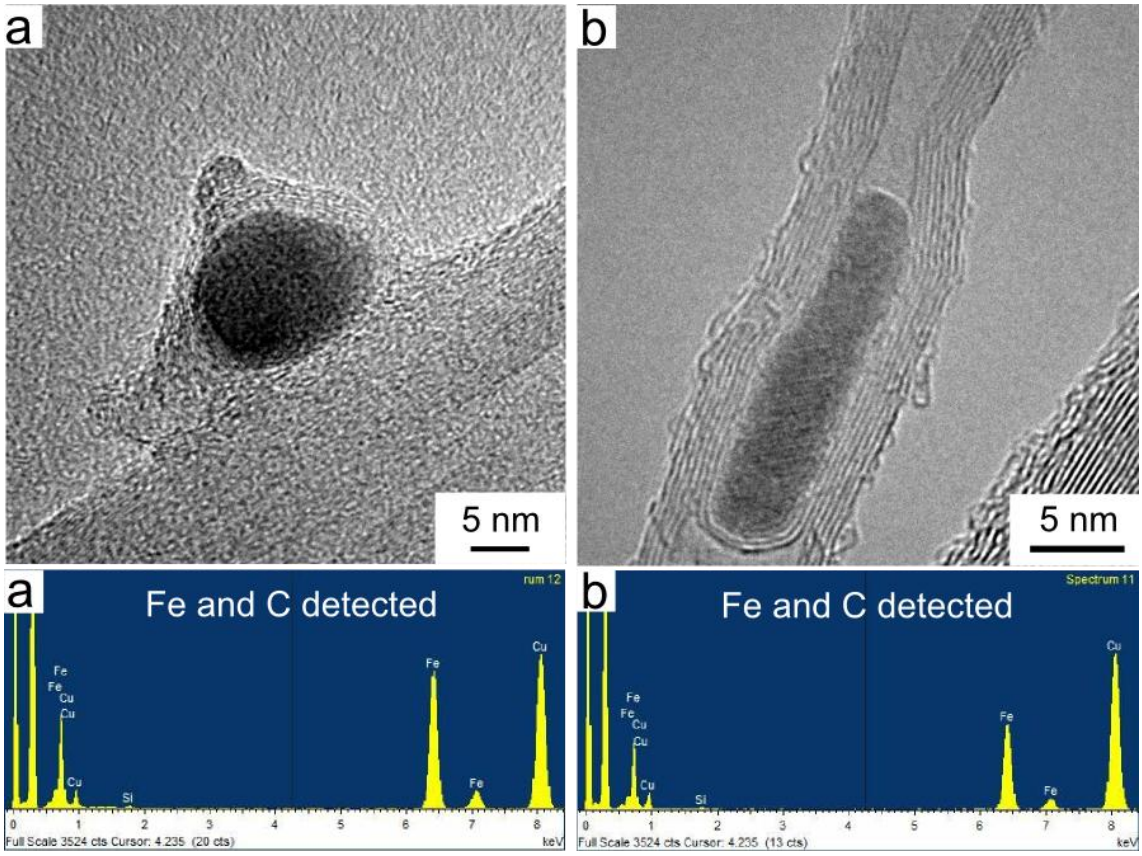

Figure 7.13 TEM micrographs of the two iron environments and elemental analysis a) outside of the tube, coated in a graphitic layer and b) inside the tube

As previously mentioned, the graphitic layer prevents access to the iron nanoparticles. Oxidation of the samples can remove this graphitic layer, but will also oxidise the nanoparticles formed. This can be clearly seen in the XRD spectra (Figure 7.14), which on oxidation shows clear changes. Firstly two major peaks can immediately be detected, belonging to the iron oxide haematite (Fe_2O_3), the most stable form of iron oxide at 36° and 42°. Also detected are a number of peaks belonging to magnetite (Fe_3O_4), which largely overlap with the minor Fe_2O_3 peak at 42°. As the oxide peaks increase, the iron and cementite peaks centred around 52° decrease in intensity. This is to be expected suggesting that the iron and cementite are being oxidised to more stable oxide forms such as haematite and magnetite. As the oxidation progresses, the CNT peak at 31° also begins to decrease. This is due to the exposed iron oxide nanoparticles begin to catalyse the decomposition of the CNT, leading to the carbon peak decreasing. It is important to note that the timings for this *in-situ* oxidation cannot be directly related to reaction conditions, as the *in-situ* XRD has a considerable amount of dead volume, whose size was not determined and, as such, the exact percentage of oxygen in the oxidation atmosphere is not well defined. These results do however support the experimental finding that oxidation for an extended period can result in decomposition of the CNT. This

decomposition begins before all iron particles in the sample are exposed and oxidised, as many are buried deep within the CNT core. As such is it not beneficial to continue the oxidation until all iron nanoparticles are oxidised.

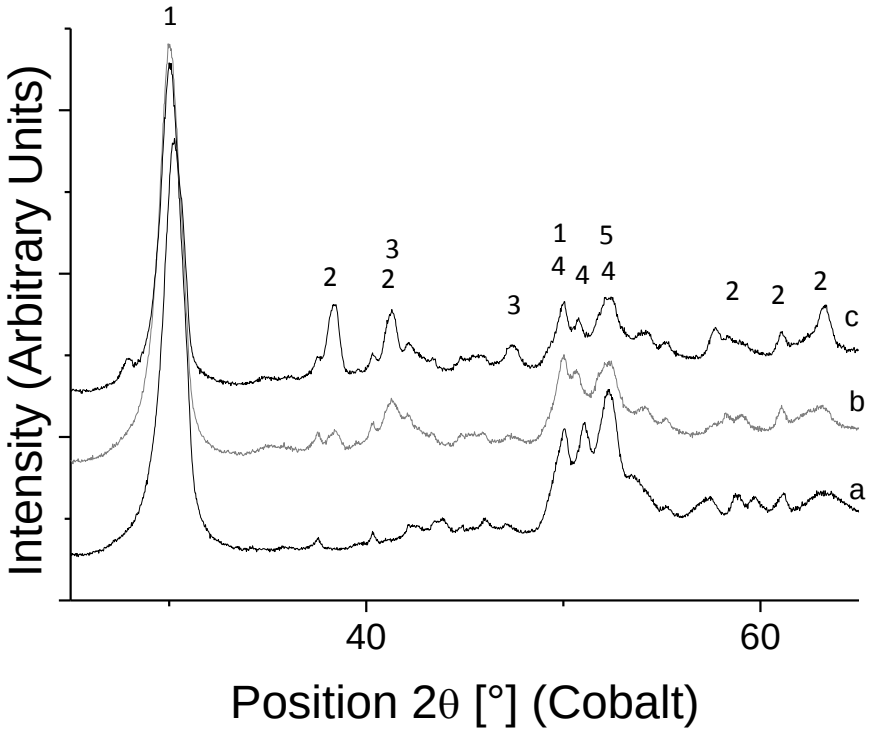

Figure 7.14 XRD spectra of Fe/CNT powder after a) synthesis b) oxidation in air for 10 minutes c) oxidation in air for 45 minutes 1) CNT 2) Fe_2O_3 haematite 3) Fe_3O_4 magnetite 4) Fe_3C cementite 5) Fe(0) iron metal

Performing several faster scans focusing in on the iron oxide peaks, showed that the peak at 42° stays constant, whereas the peak at 36° increases overtime (Figure 7.15). This suggests that the magnetite is acting as intermediate in the formation of haematite. This is supported by studies in the literature of cementite oxidation and iron oxidation. Oxidation of cementite is shown to produce both haematite and magnetite, [278] whilst oxidation of pure iron is shown to produce wursite ($Fe_{0.95}O$) and magnetite initially, before forming haematite at high temperatures. [280] The expected pathway of the oxidation of cementite sees the formation of magnetite followed by further oxidation to haematite. [278]

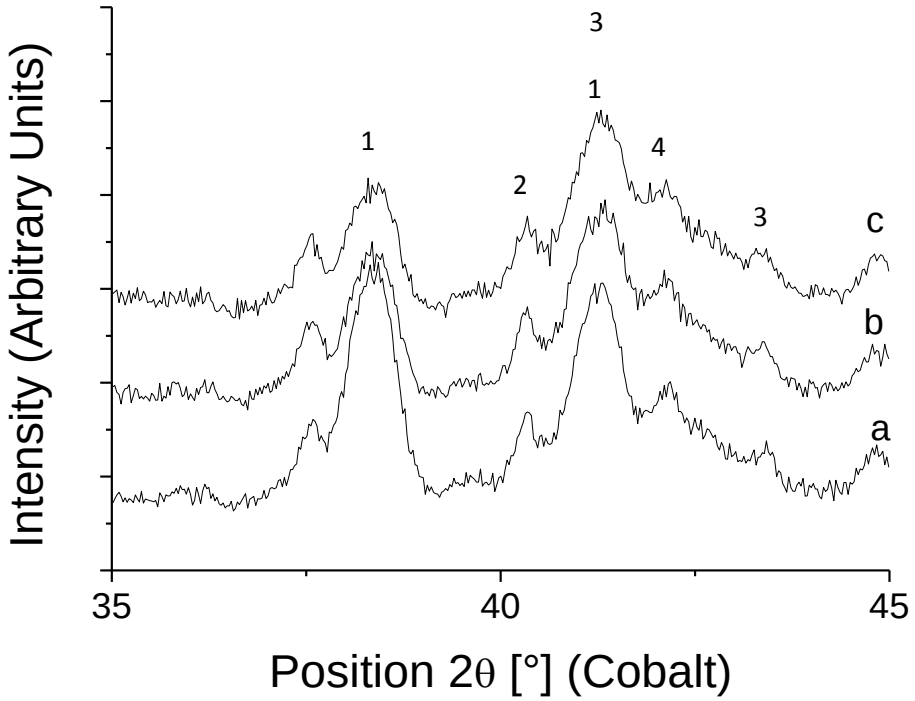

Figure 7.15 XRD spectra showing intensity of iron oxide peaks after a) 20 minutes b) 30 minutes and c) 45 minutes exposed to air at 470 °C 1) Fe_2O_3 haematite 2) Fe_3C cementite 3) Fe_3O_4 magnetite 4) SiO_2 trace silica contaminant

TEM micrographs and EDX analysis clearly show the effects of oxidation of the CNT on the monolith (Figure 7.16). Exposed nanoparticles can be observed on the surface of the CNT, at the tips of the now opened nanotubes, and inside the nanotube core. EDX analysis confirms that the iron nanoparticles on the surface of the CNT have been partially oxidised. The iron nanoparticle at the nanotube tip is less oxidised, suggesting that the iron still enclosed in the nanotube has not been oxidised. Iron detected inside the nanotubes shows the presence of minimal amounts of oxygen, suggesting it is either metallic iron, or iron carbide. The oxygen detected is very low intensity, and may be a false signal, but could also be due to oxygen functionality on the support surface.

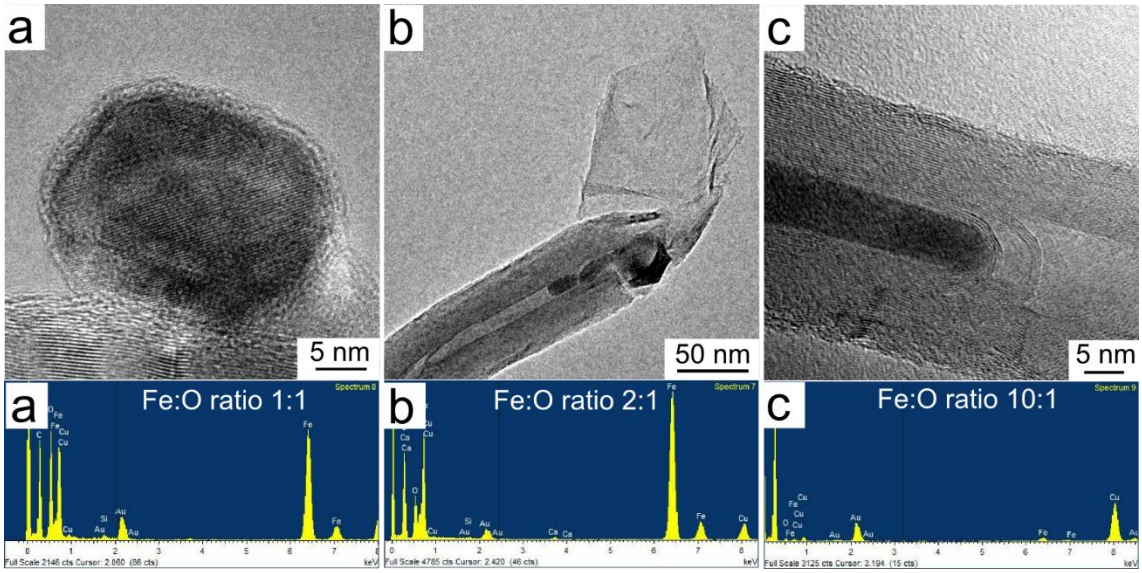

Figure 7.16 TEM micrographs of CNT taken from the monolith surface showing a) exposed nanoparticles on the surface of the nanotube b) exposed nanoparticle at the end of the nanotube c) nanoparticles still enclosed by the nanotube

Hydrogenation causes another change in the iron species detected. Haematite is very quickly converted into an iron metal peak, and a variety of reduced iron oxides, the major peaks belonging to wursite and magnetite (Figure 7.17). The magnetite peak (which can be considered to be a mixture of wursite and haematite $FeO.Fe_2O_3$) intensity decreases slightly, but then remains relatively constant, with a slight decrease over the reaction time, as the haematite is converted into wursite. The intensity of the iron metal and wursite peaks increases slightly with time as the magnetite peak decreases. The rapid conversion of haematite to iron metal and wursite indicates that hydrogenating the catalyst for longer periods would seem to have little effect on the resulting catalyst, with perhaps the only effect being the reduction of the remaining magnetite to iron metal. As magnetite is a known reverse water gas shift catalyst this may affect the resulting catalyst behaviour negatively. The XRD results reported here seem to be in conflict with data previously obtained via *in-situ* XPS, for the powdered catalyst. [276] There upon reduction the major species observed was Fe_3O_4, with little iron metal or carbide detected. The XRD results suggest that iron metal is also widely present, the lack of detection of iron metal via XPS would suggest that the metallic iron formed is for the most part confined within the tubes, and hence is not detected by XPS which is a surface sensitive technique.

Previous authors have observed that encapsulated nanoparticles can have very different reduction environments, compared to those supported on the outside of the CNT. [145] They

found that iron nanoparticles confined within the CNT could be reduced relatively easily at temperatures where nanoparticles on the surface of the nanotube remained as iron oxide. [57] This could provide an explanation for the discrepancy between the two techniques.

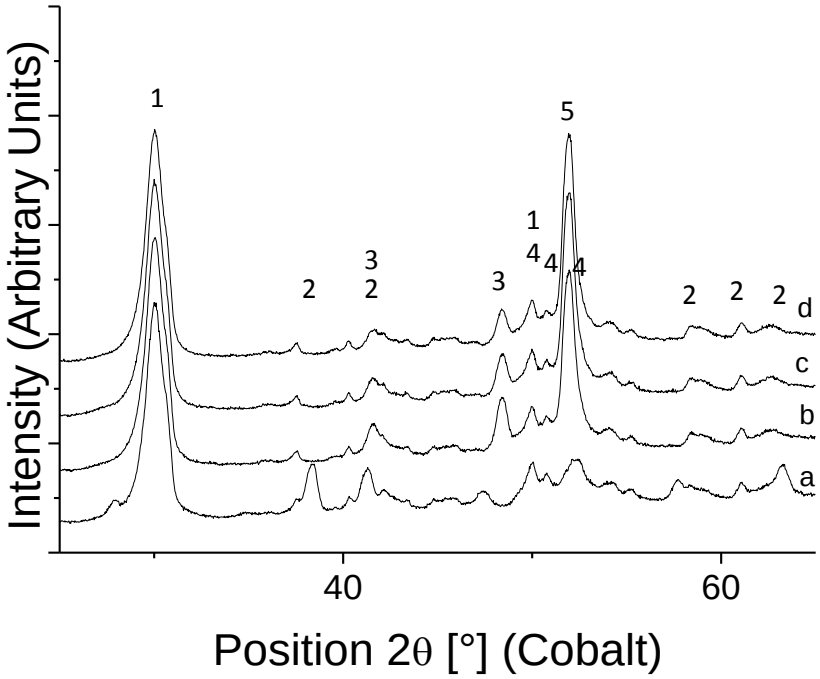

Figure 7.17 XRD spectra of Fe/CNT powder after a) 45 minutes oxidation in air at 470 b) 30 minutes c) 60 minutes and d) 90 minutes 1) CNT 2) Fe_2O_3 3) Fe_3O_4 magnetite/wursite 4) Fe_3C cementite 5) Fe(0) iron metal

Introduction of CO_2 and H_2 into the reaction chamber again causes a rapid change in the iron phases (Figure 7.18). Exposure of the catalyst to the carbon dioxide and hydrogen atmosphere, rapidly leads to the formation of iron carbides. As has previously reported, when iron catalysts are exposed to syn-gas, the iron metal is rapidly converted into a carbide species. Determination of the carbide species from XRD can be problematic, due to very similar peak positions, but it appears to be a mixture of cementite (Fe_3C) and the Hagg carbide (Fe_5C_2), both species which are known to be active for the Fischer Tropsch synthesis step. [281,282] This process is equally rapid when CO_2 is substituted for CO. It is unclear whether the CO_2 is first converted into CO which reacts and forms the carbide species, or whether CO_2 itself can form carbide species. It is to be noted that after carburisation, no oxide species can be detected via XRD, unlike previous studies performing Fischer Tropsch synthesis, where iron oxide and iron carbides have been observed to co-exist. [57] This is surprising as the water gas shift reaction is traditionally thought to be catalysed by these oxide species, and not by the iron carbide. [283]

Previous studies on CNT for the FT process have also demonstrated surprising water gas shift activity, despite little iron oxide being detected.[215] This was thought to be due to the presence of amorphous iron oxide which was not picked up by XRD. As mentioned previously in-situ XPS demonstrated the presence of iron oxide on the surface of the catalyst after reduction, it is likely this iron oxide, undetected by XRD, which is active for the reverse water gas shift reaction.

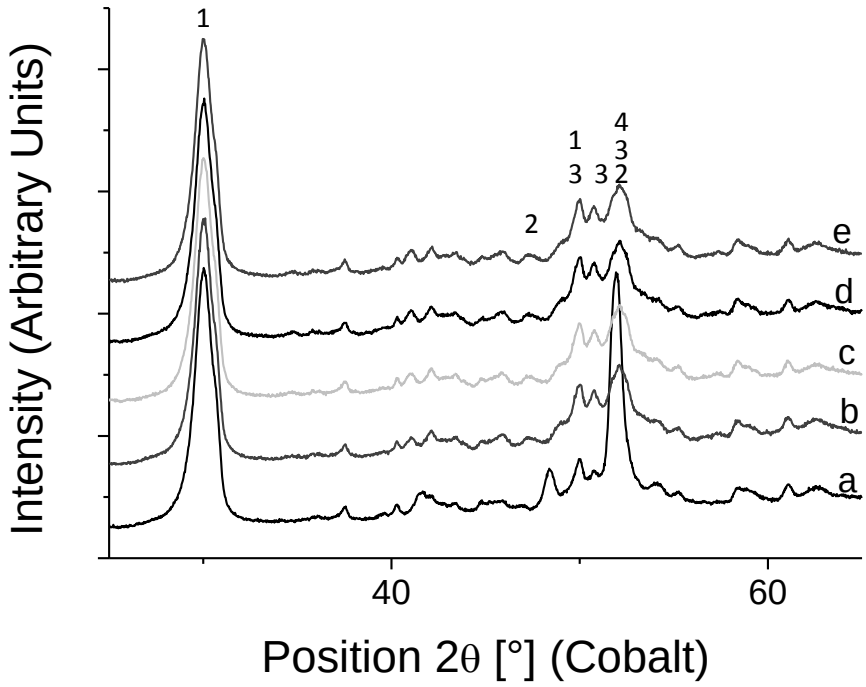

Figure 7.18 XRD spectra of Fe/CNT powder after a) hydrogenation for 2 hours b) reaction for 15 minutes c) reaction after 45 minutes d) reaction after 75 minutes e) reaction after 120 min 1) CNT 2) Fe_2C_5 Hagg carbide 3) Fe_3C cementite 4) Fe(0) iron metal

7.4 **Determining iron content and iron particle size**

As iron acts as the catalytic sites for the RWGS reaction and the FT process, determining the amount of accessible iron present in the catalyst is important in order to determine catalyst activity. In section 4.7 it was demonstrated that by combusting the CNT powder, and assuming the resulting residue was a mixture of Fe_3O_4 and Fe_2O_3, the iron content of the CNT powder catalyst can be estimated as being 21.9 and 22.7%. This does not however tell the full story, as some of this iron is enclosed and inaccessible to the passing gases, and therefore does not contribute to catalysis. In section 7.2, XPS studies detect approximately 1 atom % iron on the surface of the CNT, in many cases this could be considered to be the accessible iron content,

but the XRD and TEM studies completed in section 7.3 demonstrate that even iron metal enclosed within the CNT bore, and thus not detected by XPS, are oxidised and converted to iron oxide throughout the experimental process, and so must be considered as part of the active phase. XRD also demonstrates that some iron does not appear to be accessible to gases as it is not oxidised, remaining as cementite throughout the oxidation process, and so cannot be involved in catalysis. Thus, though the amount of iron present in the catalyst can be estimated, determining the extent of this iron's involvement in catalysis is non-trivial.

This problem is exacerbated when the case of the Fe@CNT supported on monolith is considered. In this case even estimating the total iron content is complicated, by the presence of the monolith powder amongst the ash, meaning iron content cannot be determined in the same manner. Since cordierite itself also contains small amounts of iron the exact amount of cordierite present (and its iron content) much also be known to accurately determine iron content. Typical techniques to determine iron content include atomic absorbance spectroscopy and ICP-EAI (though both these techniques are complicated by CNT's not being able to dissolve in many strong acids, so the catalyst must be combusted, then the oxide residues dissolved in a strong acid, before being analysed by the techniques). These techniques will still not be able to determine the amount of accessible iron.

Utilising techniques such as SEM-EDX, and XPS, an estimation of the surface iron can be obtained, but the large amount of iron present in the bore of the catalyst cannot be determined in this way. Perhaps the best method for determining iron content would be to perform a surface area analysis using a BET machine with a probe gas such as CO, known to absorb on iron metal. This technique was not available, but again encounters a number of issues associated with the very low surface area of the Fe@CNT/Monolith catalyst, with the resulting area of iron metal likely being below that which can be accurately determined by most ASAP machines.

Since the accessible iron content could not be accurately determined, catalysts are compared by activity per gram of catalyst, including support and iron metal. This allows comparison between other catalysts, and catalysts in the literature. Additionally, since the iron content of CNT deposited on the monolith cannot be accurately determined, it is assumed that the iron content of the CNT powder, and the CNT monolith is the same, as similar synthesis conditions would imply that this is likely the case.

Iron particle size cannot be easily determined, as the iron nanoparticles formed on the CNT have a variety of non-spherical structures, including cylinders inside the CNT bore, domes on the CNT surface, and spherical particles on the CNT ends. Traditional TEM images make it difficult to size the resulting nanoparticles, with high resolution microscopy necessary to distinguish nanoparticles in many cases. Low resolution particle counts do not show the existence of the large number of less than 10 nm size particles, which high resolution TEM shows to exist. Since high resolution TEM time was limited, not enough images were obtained in order to give statistically accurate particle size distributions.

7.5 Stability of CNT catalysts

A concern with the use of carbon catalysts must be that the support itself does not itself decompose and contribute to the products detected. The stability of the CNTs when exposed to a pure stream of hydrogen and CO_2 was tested.

The CNT were tested as produced, and after activation. During hydrogenation, in both cases very small amounts of methane (0.01%) were detected when placed in a gas stream of 8 sccm hydrogen, though the evolution of methane decreased over the 2 hours tested. The majority of this evolved hydrogen takes place during the hydrogenation step prior to reaction, and hence should not interfere with catalytic data. After hydrogenation the catalyst was placed under a stream of pure carbon dioxide (8 sccm), in both cases no alternative products were produced, with carbon dioxide being the only detected product.

Table 7.3 Hydrocarbons detected on treatment of as-prepared (MWCNT-AP) and after activation by oxidation (MWCNT-AO) with pure 8 sccm gas streams of H_2 and CO_2

Catalyst	Gas	Temperature	$HC_{detected}$ %
MWCNT-AP	Hydrogen	400	0.01
MWCNT-AO	Hydrogen	400	0.01
MWCNT-AP	Carbon Dioxide	400	Below detection limit
MWCNT-AO	Carbon Dioxide	400	Below detection limit

The stability of the CNT was also tested over a range of temperatures by heating them to high temperatures under the two gases, and observing decomposition at high temperatures, using a TGA (Figure 7.19). Apart from a reduction in mass under hydrogen at 340 °C (corresponding

to the reduction of iron oxide to iron (0)), the CNT remains stable at temperatures greater than the reaction temperature, with decomposition of the CNT beginning at over 500 °C under hydrogen, and with very little decomposition observed under CO_2, until over 600 °C.

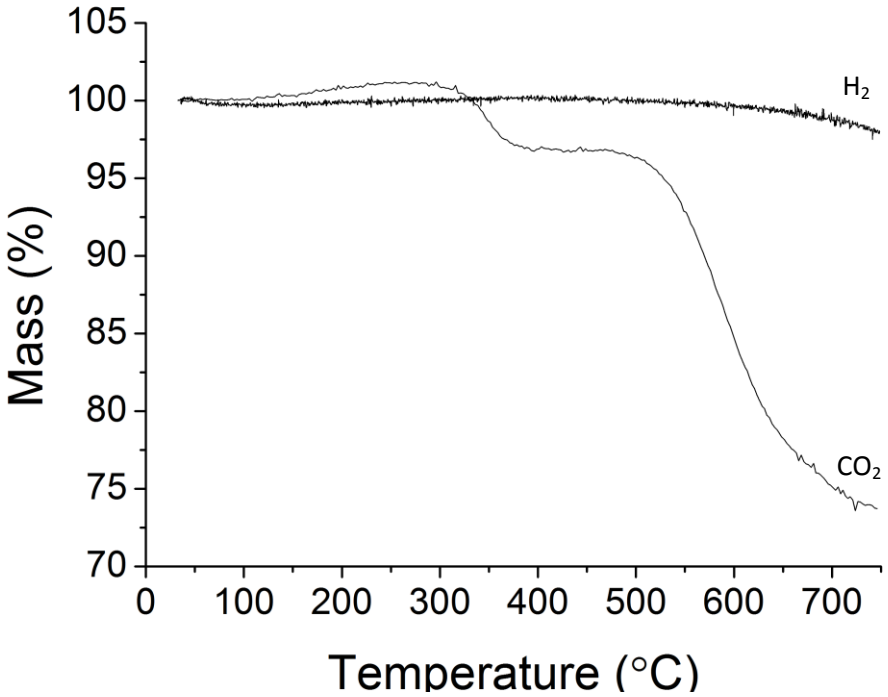

Figure 7.19 Hydrogen and CO_2 TGA

7.5.1 Catalyst Deactivation

The Fe@CNT monolith shows distinct de-activation over time with activity decreasing continuously over the 15 hours tested (Figure 7.20). As departmental safety regulations did not allow for the testing rig to be run unattended, the experiment was periodically stopped, and left running cold at atmospheric pressure under hydrogen overnight. The system was then restarted, pressurised and heated. Time on stream refers to the total time under reaction conditions. The change in performance over time is not insignificant, with approximately 30% of the total activity lost over the 15 hours on stream. In order to minimise the influence of deactivation on other parameter tests, all catalytic data is compared at comparable points in time, 240 minutes was used as standard.

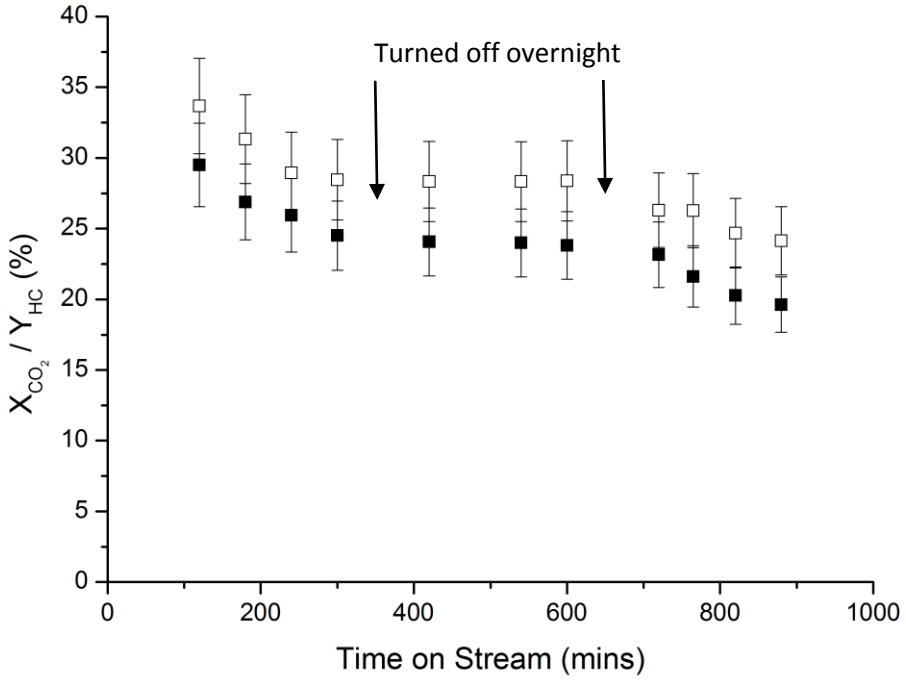

Figure 7.20 Effect of time on stream on CO_2 conversion, the reaction was performed at 370 °C over a 10 cm bed of Fe@CNT/monolith (synthesised at 790 °C for 60 minutes, approximately 0.15g of Fe@CNT, activated by 10 minutes oxidation), at 7.5 bar. Total flow rate was 8 sccm using a CO_2 to H_2 ratio of 1:3 (□) CO_2 conversion (■) Hydrocarbon yield

The origins of the deactivation mechanism observed here are not well understood. A number of deactivation mechanisms can occur in Fischer Tropsch synthesis including poisoning, sintering, phase changes or carbon deposition. [201] In the present case, it is unlikely that the catalyst is poisoned, as poisoning is usually the result of the presence of sulfur in most syn-gas feeds [201] and no sulfur will be present in this case.

Deactivation due to phase changes of the active species to less active species is possible, however observation of the catalyst via *in-situ* XRD shows no change over the two hours monitored. Since deactivation occurs continuously from the start of the reaction, it would be expected to see some change in the phase of the active species.

This leaves sintering or carbon deposition as the two most probable causes of deactivation, or more likely a mix of the two. Carbon deposition is difficult to determine on a carbon based catalyst, as the presence of the carbon catalyst masks deposited carbon from most detection methods. Deposition of amorphous carbon on the nanoparticle surface was not observed via

high resolution TEM. Re-oxidation and re-hydrogenation, or simply re-hydrogenation did not recover the catalytic activity.

After reaction TEM images showed the presence of agglomerations of large iron nanoparticles on the surface of the CNT (Figure 7.21), not observed for nanotubes as prepared, or after oxidation. It would appear that upon prolonged exposure to reaction conditions the nanoparticles on the surface of the tube can migrate forming nanoparticle clusters on the surface of the tube. This agglomeration may explain some of the catalyst deactivation.

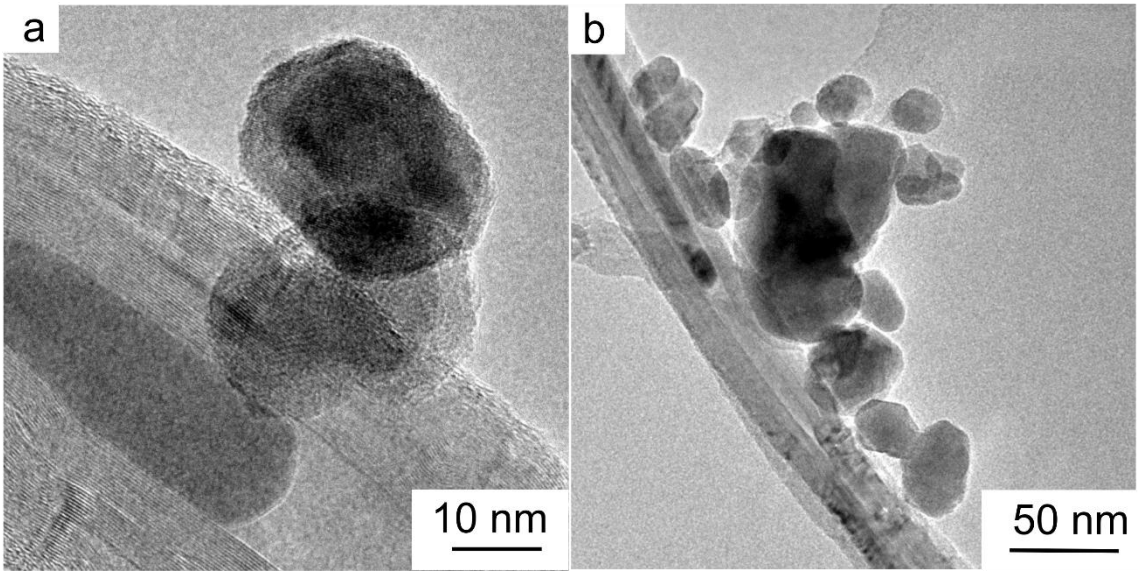

Figure 7.21 a) and b) agglomerations of iron nanoparticles observed by TEM after reaction

7.6 Effect of changing parameters on catalyst performance

7.6.1 Flow Rate

The flow-rate of the gas mixture can be seen to have a significant impact on the conversion of CO_2 over the Fe@CNT/Monolith catalyst. The overall conversion decreases with increasing flow-rate, progressing from conversions as high as 41.9% at the low overall flow-rate of 4 sccm (GHSV=1600 $cm^3\ g^{-1}\ h^{-1}$), to conversions as low as 13.4% at the higher overall flow-rate of 16 sccm (GHSV=6400 $cm^3\ g^{-1}\ h^{-1}$). The overall conversion, and the conversion to hydrocarbons both decrease linearly with increased flow rates. It can clearly be seen that the reaction has not reached thermodynamic equilibrium and changing the flow rate dramatically changes the apparent conversion.

Table 7.4 Effect of flowrate variation on CO_2 conversion, the reaction was performed at 370 °C over a 10 cm bed of Fe@CNT/monolith (synthesised at 790 °C for 60 minutes, approximately 0.15g of Fe@CNT), at 7.5 bar. Total flow rate was varied between 4 and 16 sccm (GHSV 1600-6400 $cm^3\ g_{CNT}^{-1}\ h^{-1}$) keeping a CO_2 to H_2 ratio of 1:3

GHSV $cm^3\ g_{CNT}^{-1}\ h^{-1}$	Alpha	Olefin Selectivity	X_{CO2} %	R_{obs} µmol $g^{-1}\ s^{-1}$	CO %	CH_4 %	C_2-C_4 %	$C5^+$ %
1600	0.47	0.09	41.89	1.95	15.86	45.33	35.16	3.66
3200	0.47	0.09	32.19	2.95	16.12	47.49	31.81	4.58
4800	0.44	0.06	21.30	2.97	41.32	35.55	21.37	1.77
6400	0.45	0.08	13.42	2.50	59.58	26.16	13.60	0.66

Reporting the observed rate of CO_2 conversion per gram of catalyst per second, gives a better idea of the true performance of the catalyst, and allows comparison between this work, and literature catalysts. This observed rate of reaction cannot be considered to be a true rate of reaction, as with larger values of conversion differences the change in the reactant mix may affect the rate of reaction. Additionally, a number of other factors could be masking the true rate of reaction, as the order of the reaction is not known. When comparing the observed reaction rates, no clear trends can be seen, suggesting that the flow rate has a negligible effect on the rate of reaction, and that there are no external mass transfer limitations. Residence time in the reactor can be seen to have no influence on the rate of reaction, varying from 1.38 minutes to 5.53 minutes.

Changing the flow rate significantly shifts the observed product distribution, with higher total flows shifting the product distribution towards CO. Anderson Schulz Flory (ASF) distributions, calculated for each flow rate showed very little change however, with calculated alpha values consistently being in the range 0.44 - 0.47. The faster flow rates shifting the product distribution would therefore seem to be due to insufficient time for carbon monoxide to react in the rate-limiting Fischer Tropsch reaction. Residence time within the reactor varies from 1.38 minutes at the highest flowrate, to 5.53 minutes at the lowest flowrate. Olefin selectivity remains roughly constant for different flowrates and is comparable to other un-doped catalysts. The observed rate of reaction (~3 µmol $g_{CNT}^{-1}\ s^{-1}$) is higher than any of the reported reaction rates for literature CNT catalysts (though many of these reactions take place at significantly lower temperature). A comparable Fe/Al_2O_3 catalyst at higher temperature (400 °C) and higher pressure (20 bar) used by Sai Prasad *et al.* reports activity of 0.83 µmol $g^{-1}\ s^{-1}$, and even heavy potassium doping does not increase activity beyond 1.23 µmol $g_{CNT}^{-1}\ s^{-1}$.

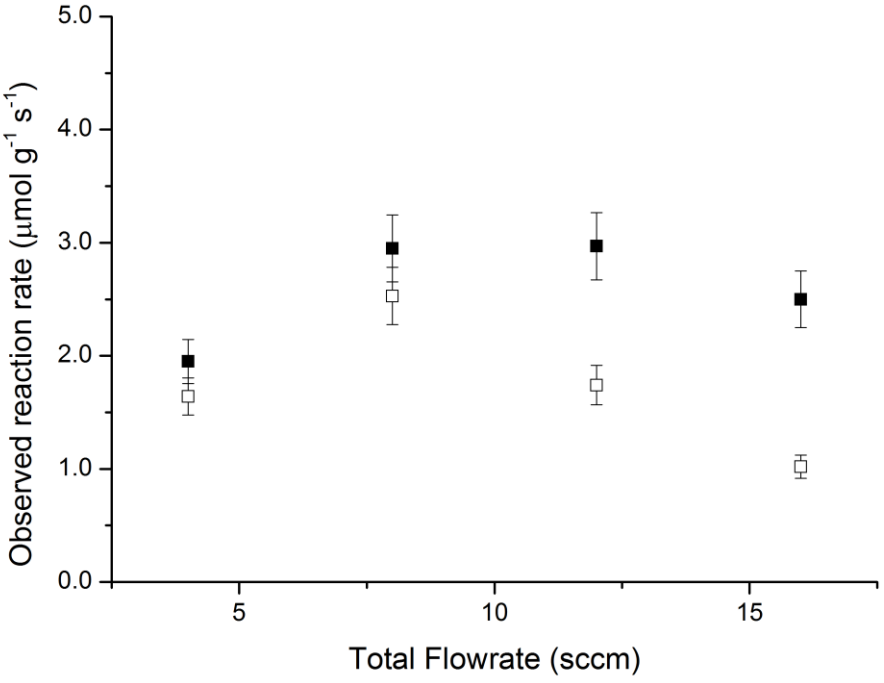

Figure 7.22 Effect of flowrate variation on CO_2 conversion, the reaction was performed at 370 °C over a 10 cm bed of Fe@CNT/monolith (synthesised at 790 °C for 60 minutes, approximately 0.15g of Fe@CNT), at 7.5 bar. Total flow rate was varied between 4 and 16 sccm (GHSV 1600-6400 $cm^3\ g_{CNT}^{-1}\ h^{-1}$) keeping a CO_2 to H_2 ratio of 1:3 (■) Rate of CO_2 consumption (□) Rate of hydrocarbon production

7.6.2 Temperature

The reaction temperature plays an important role in the activity of the catalyst. Figure 7.23 plots total conversion of CO_2 and the hydrocarbon yield against the inverse of the temperature. Two different regions can clearly be observed, at temperatures below 370 °C, the reaction temperature is clearly the rate controlling step, with the reaction being limited by the rate of reaction. As temperature increases the rate of reaction increases, showing significant changes in conversion. Above 370 °C the reaction rate no longer shows such significant increases, suggesting the rate determining step is no longer the rate of chemical reaction. As the previous test has indicated that the reaction is not limited by external mass transfer issues at 370 °C, the reaction must be limited by internal diffusion, or at 370 °C the reaction is just at the limit of the rate controlled region.

For the temperature controlled regions, an apparent activation energy for the reactions can be determined. The apparent activation energy for the conversion of CO_2 to CO is 34.9 kJ mol^{-1}, whilst the activation energy for the subsequent conversion to hydrocarbons is 82.8 kJ mol^{-1}.

Reported values for the activation energy of the reverse water gas shift reaction vary dramatically with values from 40 to 120 kJ mol^{-1} previously reported for a wide variety of catalysts. [284] [243] The observed rate of reaction here is remarkably low. The reported value for FT synthesis is within the range of those reported in the literature for iron catalysts (63-89 kJ mol^{-1}).[243]

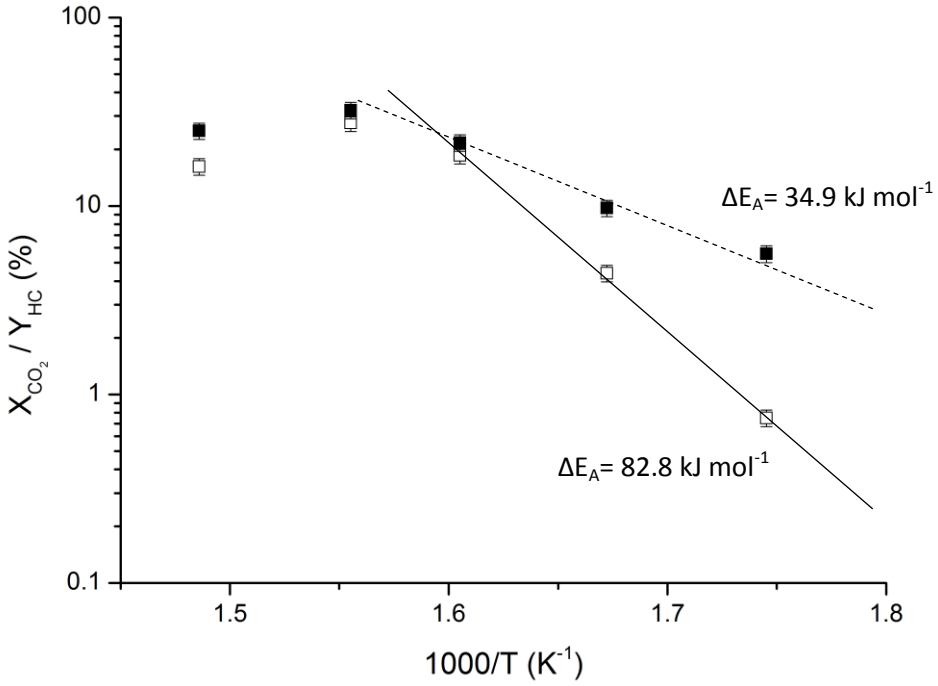

Figure 7.23 Effect of temperature variation on CO_2 conversion, the reaction was performed at 7.5 bar over a 10 cm bed of Fe@CNT/monolith (synthesised at 790 °C for 60 minutes, approximately 0.15g of Fe@CNT), temperature was varied from 300 to 400 °C. Total flow rate was 8 sccm using a CO_2 to H_2 ratio of 1:3 (■) Conversion of CO_2 (□) Hydrocarbon yield

The selectivity of the process varies with temperature, but alpha, remains constant over the majority of the temperature rise. At 400 °C however a significant drop in alpha is observed (Figure 7.24). This agrees with the results of Riedel *et al.*, who observed this behaviour using a $Fe/Al_2O_3/Cu/K$ catalyst.[243] They suggest that this drop in activity is most likely due to an increase in the rate of the Boudouard reaction (the disproportionation of CO to give graphite and CO_2).[243] At 400 °C the product distribution shifts, with much more carbon monoxide, and much less higher hydrocarbons produced, possibly due to increased coking. Olefin selectivity does not appear to shows any correlation to reaction temperature. Selectivity to hydrocarbons increases with temperature, with significantly higher selectivity to carbon

monoxide at low temperatures, presumably due to the slower FT reaction. The Robs of 0.52 µmol g^{-1} s^{-1} at 300 °C is higher than any of those reported by Sai Prasad *et al.*[237] at 300 °C and similar pressures (10 bar), with a variety of different dopants and supports, but slightly lower than that reported by Hu *et al.*,[247] with their unsupported FeMnK nanofibres at 260 °C and 13.7 bar, currently the highest activity reported for a catalyst in a fixed bed reactor. Dorner *et al.* using a CSTR reactor report slightly higher activities upwards of 1 µmol g^{-1} s^{-1}, but Drab *et al.*[249] have reported on how activities drop by an order of magnitude on switching from a CSTR to a fixed bed reactor. The activity of the CNT supported catalyst can be seen to be comparable or better than many catalysts in the literature in terms of activity. Olefin selectivity remains relatively poor when compared to literature catalysts, with selectivity remaining at 10% or below for viable reaction regions. A number of other authors have shown significant increases in activity and selectivity to olefins via the addition of dopants such as potassium and manganese, this may be an area to explore in the future.

Table 7.5 Effect of temperature variation on CO_2 conversion, the reaction was performed at 370 °C over a 10 cm bed of Fe@CNT/monolith (synthesised at 790 °C for 60 minutes, approximately 0.15g of Fe@CNT), at 7.5 bar. Total flow rate was 8 sccm (GHSV 3600 cm^3 g_{CNT}^{-1} h^{-1}) keeping a CO_2 to H_2 ratio of 1:3

Temperature °C	Alpha	Olefin Selectivity	X_{CO2} %	Robs µmol g^{-1} s^{-1}	CO %	CH_4 %	C_2-C_4 %	$C5^+$ %
300	0.43	0.10	5.58	0.52	86.57	9.18	4.2	0.0
325	0.43	0.04	9.76	0.93	54.82	26.95	17.0	1.2
350	0.47	0.08	21.66	2.01	14.67	48.94	32.7	4.3
370	0.47	0.08	32.19	2.95	16.12	47.49	31.8	4.6
400	0.28	0.19	25.01	2.33	35.88	44.20	19.6	0.3

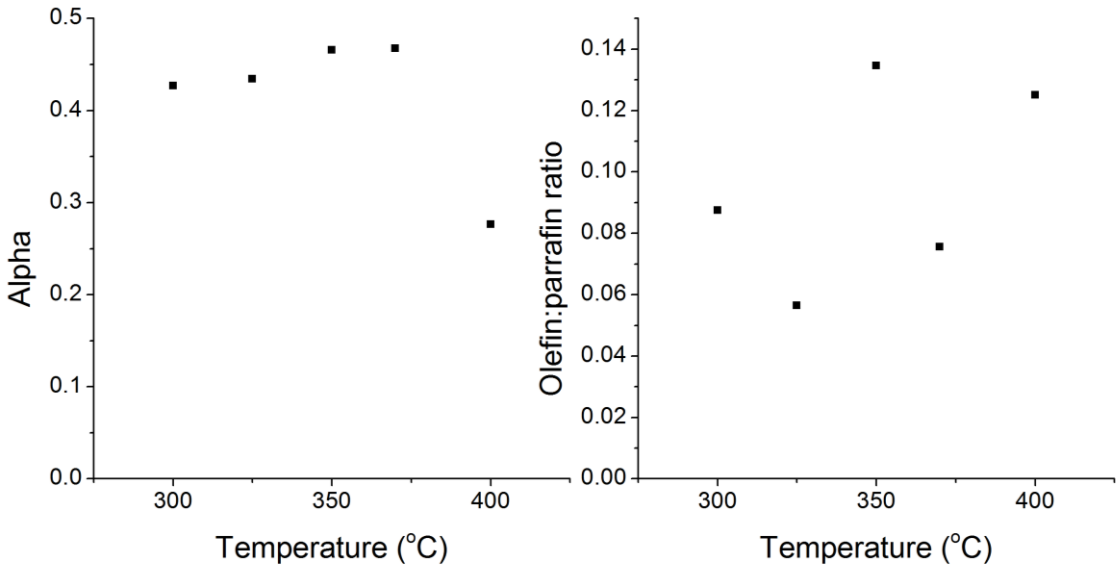

Figure 7.24 Variation in alpha (left) and olefin:parrafin ration (right) for (■) Fe@CNT monolith with increasing temperature

7.6.3 Synthesis Time and Temperature

In an attempt to probe whether mass transfer has a significant effect on catalytic activity the synthesis conditions were varied. This has been shown to significantly change the behaviour of the growth of the nanotube layer on the monolith surface (chapter 5). Varying the synthesis time of the process will change the mass of MWCNT grown, and the thickness of the CNT layer. The changing thickness of the CNT layer should have an effect if the reaction is mass transfer limited. Testing catalyst synthesised at various times, and comparing the observed rates of reaction shows very little dependence for rate of reaction against synthesis time (Figure 7.25). Growth for 60 minutes clearly gives the most active catalyst, whilst activity for other synthesis times is relatively low. Changing the synthesis temperature also changes the catalyst behaviour, with activity falling with increased synthesis temperature. Synthesis at 790 °C gives the highest conversion, whilst synthesis at 730 °C gives the highest activity. Conversion and activity both drop significantly for synthesis at 850 °C.

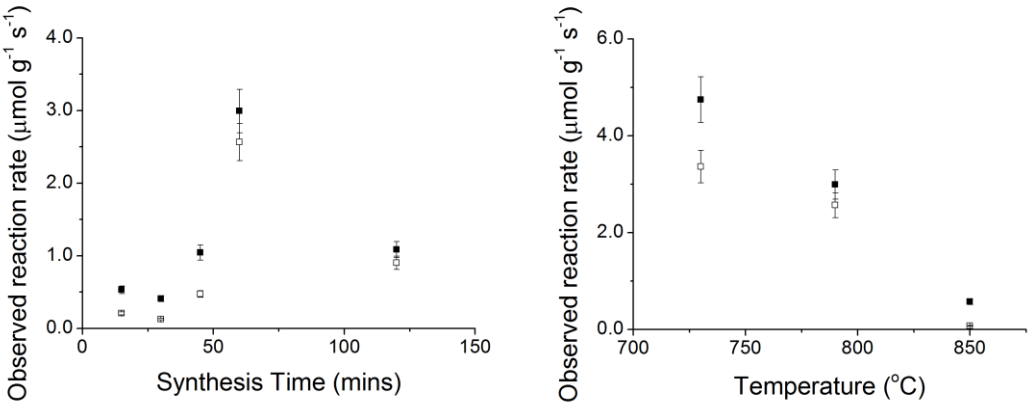

Figure 7.25 Activity of the Fe@CNT Monolith catalysts synthesised at different times at 790 °C (left) and at different temperatures for 60 minutes (right) testing was performed at 7.5 bar over a 10 cm bed of Fe@CNT/monolith (synthesised at 790 °C for 60 minutes, approximately 0.15g of Fe@CNT), at 370 °C. Total flow rate was 8 sccm using a CO_2 to H_2 ratio of 1:3 (■) rate of CO_2 consumption (□) rate of hydrocarbon production

Plotting activity of the catalyst against both the surface area of the catalyst and the thickness of the catalyst layer reveals little correlation between activity and these factors for the different synthesis conditions (Figure 7.26). This suggests that the effect of internal diffusion limitations is minimal (though it is possible the effects of diffusion limitations are being masked by other factors). Experiments indicate that both external diffusion (gas flow rate) and internal diffusion (thickness of the CNT layer), have little apparent effect on the resulting rate of reaction, suggesting that 370 °C must be at the edge of the mass transfer controlled region.

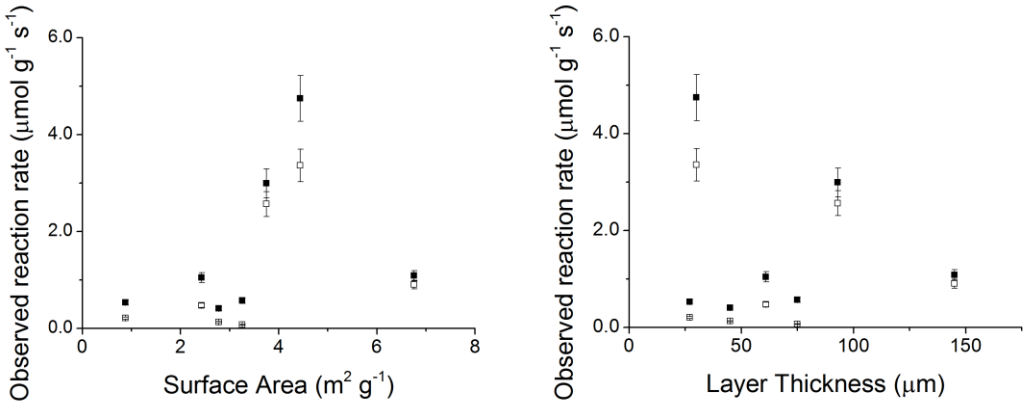

Figure 7.26 surface area (left) and layer thickness (right) plotted against activity, both showing no correlation (■) rate of CO_2 consumption (□) rate of hydrocarbon production

The apparently minimal effect of diffusion on the rate of reaction may be due to other factors which change when the synthesis conditions. Growth of CNT for longer or shorter times can change the thickness of the graphitic coating around the metal nanoparticles, and the size of the metal nanoparticles themselves. As the oxidation process has been optimised for monoliths grown for 60 minutes at 790 °C, catalysts synthesised outside of these conditions may oxidise differently. When synthesised over shorter time periods, or at different temperatures, the thinner graphitic layer can be quickly removed causing the CNT to decompose during activation. Equally a thicker graphitic layer can result in fewer nanoparticles being exposed, resulting in less activity. TEM micrographs of CNT synthesised at 850 °C, support this with TEM images showing the majority of nanoparticles still coated with a graphitic layer (Figure 7.27). These other effects may mask the impact of diffusion.

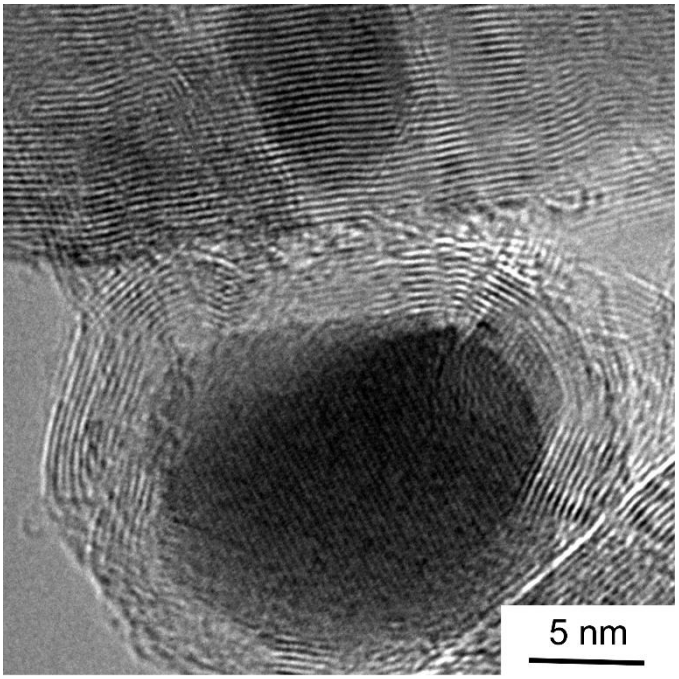

Figure 7.27 TEM micrograph of iron nanoparticle still coated with graphitic layer after oxidation of CNT synthesised at 850 °C for 60 min, the sample was oxidised at 470 °C for 10 minutes

7.7 Fe@CNT/Monolith compared to Fe@CNT/powder

Comparing the activity of the Fe@CNT/Monolith to the Fe@CNT/powder shows marked differences between the two catalysts. It is important to note that the two catalysts have very different amounts of active catalyst per unit volume. Reactions are typically performed in a 10 cm x 1.27 cm catalytic reactor which is filled with 0.4 g of the powder catalyst. However the monolithic catalyst in the same volume will only contain 0.11 g of CNT (or around 0.15 g of catalyst including iron). Despite this, at 7.5 bar both achieve similar conversions with different masses of catalyst (Figure 7.28). If the two catalysts are compared on a weight by weight basis, with 0.15 g of Fe@CNT powder dispersed amongst 0.25 g of un-activated CNT, the same weight of catalyst results in lower conversion for the powder catalyst. The two catalysts can achieve very similar conversions, despite different mass of catalyst. When similar mass of catalysts are used the conversion are different. The activity of the CNT powder catalyst remains roughly constant for different masses of catalyst, with an observed reaction rate of 1.02 µmol g_{CNT}^{-1} s^{-1} with 0.15 g of catalyst and 1.04 µmol g_{CNT}^{-1} s^{-1} at 0.4 g of catalyst, whilst the CNT monolith has almost triple the activity of the powder with 2.95 µmol g_{CNT}^{-1} s^{-1}.

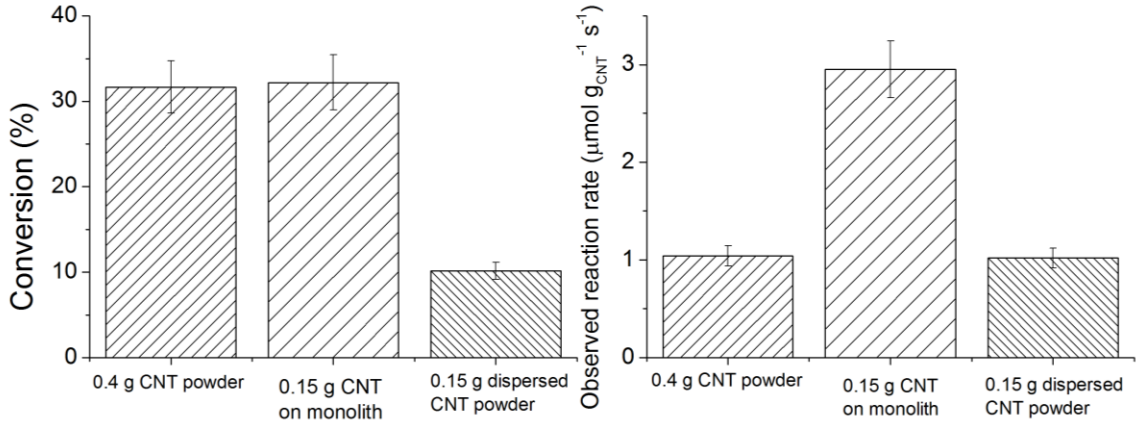

Figure 7.28 Comparison of MWCNT powder and monolith for equivalent mass and equivalent volume by conversion (left) and reaction rate(right). The reaction was performed at 370 °C over a 10 cm bed of Fe@CNT/monolith or CNT powder, when entire bed was not filled the activated powder was dispersed in active CNT powder (synthesised at 790 °C for 60 minutes activated by 10 minutes oxidation), at 7.5 bar. Total flow rate was 8 sccm using a CO_2 to H_2 ratio of 1:3

Table 7.6 Effect of pressure variation on CO_2 conversion, the reaction was performed at 370 °C over a 10 cm bed of Fe@CNT powder (synthesised at 790 °C for 60 minutes, approximately 0.4g of Fe@CNT), at varying pressures. Total flow rate was 8 sccm (GHSV 3600 cm^3 gCNT^{-1} h^{-1}) keeping a CO_2 to H_2 ratio of 1:3

Pressure (bar)	Alpha	Olefin Selectivity	X_{CO2} %	Robs µmol g^{-1} s^{-1}	CO %	CH_4 %	C_2-C_4 %	$C5^+$ %
1.0	0.38	0.27	15.8	0.54	44.8	29.1	24.6	1.4
5.0	0.54	0.09	27	0.92	26.8	30.8	34.7	7.8
7.5	0.53	0.09	30.4	1.04	11.5	38	42.4	8
10.0	0.35	0.03	36.1	1.24	33.6	35.7	28.4	2.4
15.0	0.49	0.03	47.6	1.62	54.4	22.2	21.5	2

Table 7.7 Effect of pressure variation on CO_2 conversion, the reaction was performed at 370 °C over a 10 cm bed of Fe@CNT/monolith (synthesised at 790 °C for 60 minutes, approximately 0.15g of Fe@CNT), at varying pressures. Total flow rate was 8 sccm (GHSV 3600 cm^3 $gCNT^{-1}$ h^{-1}) keeping a CO_2 to H_2 ratio of 1:3

Pressure (bar)	Alpha	Olefin Selectivity	X_{CO2} %	Robs µmol g^{-1} s^{-1}	CO %	CH_4 %	C_2-C_4 %	$C5^+$ %
1.0	0.19	0.09	4.6	0.42	96.9	2.8	0.3	0
2.5	0.30	0.03	9.0	0.84	46.6	38.6	14.8	0
5.0	0.35	0.03	18.5	1.71	64.6	26.2	9.1	0
7.5	0.47	0.04	32.2	2.95	16.1	47.5	31.8	4.6
10.0	0.44	0.06	32.0	3.09	17.5	48.7	30.6	3.2
12.5	0.52	0.04	34.6	3.18	14.4	45.5	35.3	4.7
15.0	0.44	0.02	29.6	2.75	21.7	49.1	26.8	2.4

The difference in the activity of the Fe@CNT/Monolith and the Fe@CNT powder can be seen as the pressure increases with both showing very different behaviour at different pressures. At atmospheric pressure the monolithic catalyst performs similarly to the powder catalyst, with activity of 0.42 µmol g_{CNT}^{-1} s^{-1} and 0.54 µmol g_{CNT}^{-1} s^{-1} respectively. The powder catalyst has a slightly higher observed rate of reaction, and conversion is higher as more catalyst is present. Activity of the two catalysts is relatively similar however, as would be expected as the active species, the CNT have been shown to be essentially the same in Chapter 4 and 5.

Increasing the pressure sees conversion and observed rate of reaction increasing, as would be expected as the formation of FT products is favoured by increased pressure due to Le Chatelier's principle. The increased pressure will increase the residence time of each mole of reactant in the reactor, but will concurrently increase the total moles present in the reactor, so rate of reaction should be unaffected. Experimental points between 3.75 and 15 bar, have residence times within the range of residence previously tested, with no effect on rate of reaction. Residence time may have an influence on reaction rate below this pressure. Increasing the pressure to 5 bar and beyond differences in the activity of the two catalysts starts to be observed, with the monolith catalyst increasingly outperforming the powder catalyst with increasing pressure until 7.5 bar, where the maximum difference in activity is observed with an activity of 2.95 µmol g_{CNT}^{-1} s^{-1} compared to 1.04 µmol g_{CNT}^{-1} s^{-1}.

From this point the two catalysts again behave differently, with conversion and activity appearing to plateau with increasing pressure for the monolithic catalyst, but with conversion and activity continuing to increase with pressure for the powder catalyst.

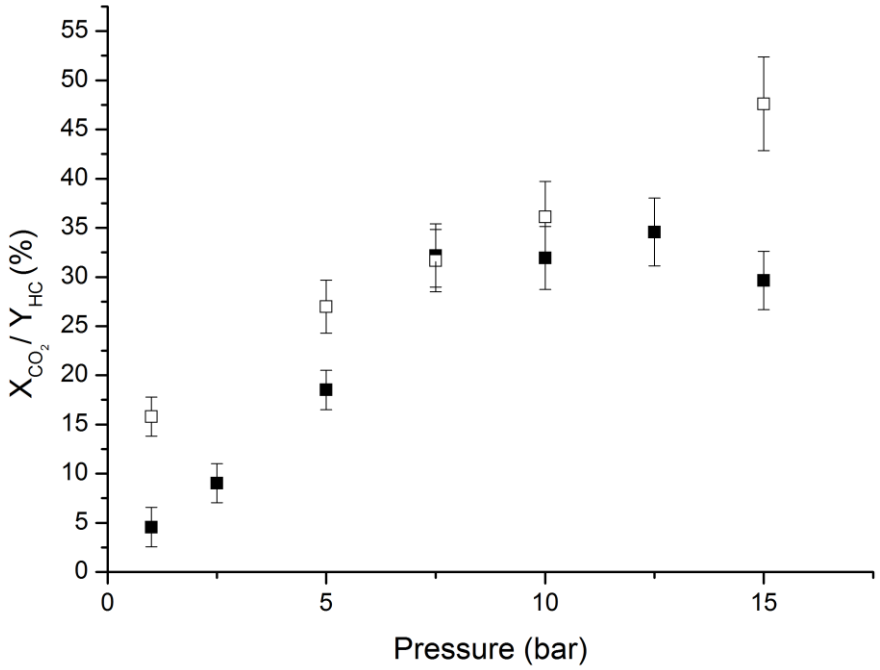

Figure 7.29 Effect of pressure variation on CO2 conversion, the reaction was performed at 370 °C over a 10 cm bed of (■) Fe@CNT/monolith (synthesised at 790 °C for 60 minutes, approximately 0.15 g of Fe@CNT, activated by 10 minutes oxidation at 470 °C) and (□) Fe@CNT powder (synthesised at 790 °C for 60 minutes, 0.4g, activated by 30 minutes oxidation at 570 °C), pressure was varied from 1 bar to 15 bar. Total flow rate was 8 sccm using a CO2 to H2 ratio of 1:3

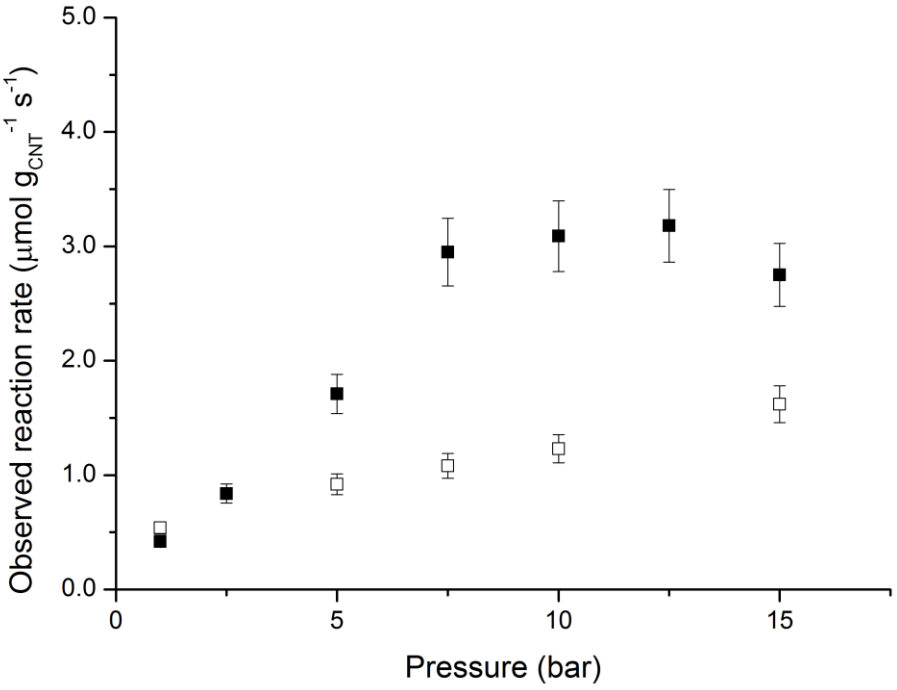

Figure 7.30 Effect of pressure variation on rate of CO_2 conversion, the reaction was performed at 370 °C over a 10 cm bed of (■) Fe@CNT/monolith (synthesised at 790 °C for 60 minutes, approximately 0.15 g of Fe@CNT, activated by 10 minutes oxidation at 470 °C) and (□) Fe@CNT powder (synthesised at 790 °C for 60 minutes, 0.4 g, activated by 30 minutes oxidation at 570 °C). Pressure was varied from 1 bar to 15 bar. Total flow rate was 8 sccm using a CO_2 to H_2 ratio of 1:3

The selectivity of the catalyst changes as the pressure is increased (Figure 7.31). With increased pressure alpha gradually increases before plateauing at around 0.5. Increased pressure is known to shift the Fischer Tropsch reaction towards higher weight products.[189] The olefin:paraffin ratio decreases with increased pressure as well, perhaps due to the increased hydrogenation activity of the catalyst at these higher pressures. The product distribution of the catalysts also varies with pressure. For the powder catalyst the best selectivity to C5+ hydrocarbons is at 7.5 bar, after which selectivity to C2-C4 and %+ hydrocarbons decreases, with increased selectivity to carbon monoxide. This may be due to saturation of the catalyst surface with carbon dioxide which can convert to carbon monoxide, increased saturation with carbon dioxide may prevent the subsequent FT reaction occurring. This effect is not observed for the monolithic catalyst, where the selectivity to carbon monoxide reaches a minimum at 12.5 bar, but remains roughly constant from 7.5 bar to 15 bar. Selectivity to hydrocarbons is lower for the monolithic catalyst at low pressures.

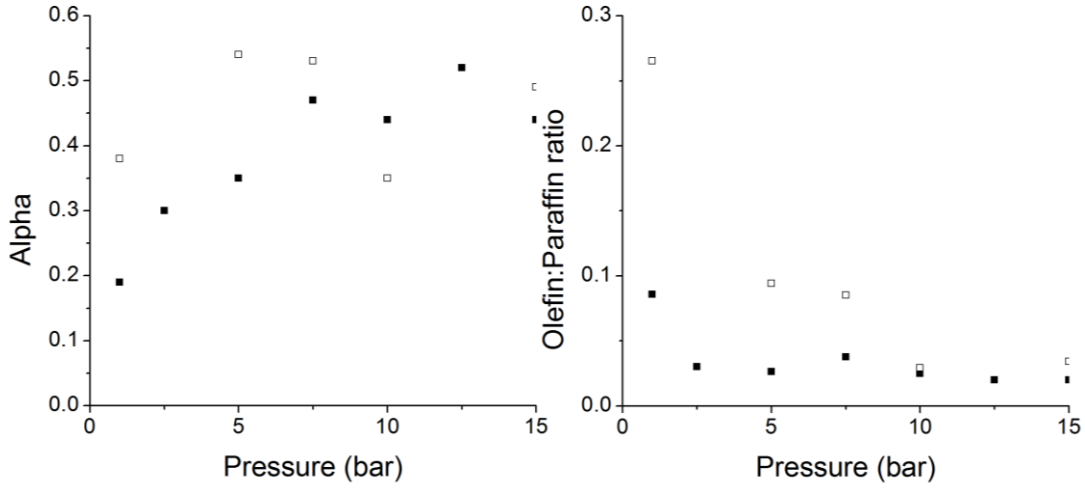

Figure 7.31 Variation in alpha (left) and olefin:paraffin ratio (right) for (□) Fe@CNT powder and (■) FE@CNT monolith with varying pressure

The significant differences between the two forms of catalyst are somewhat surprising. Since the two active species should be identical, it can only be assumed that the reason for the increased activity of the monolithic catalyst is due to its geometry. The structure of the monolith catalyst makes heat transfer, and diffusion of reactants and products in and out of the catalyst easier. Varying the flow rate, and the thickness of the CNT layer has not been observed to have any effect on catalytic activity suggesting no influence of mass transfer as a limitation, however varying the temperature of the catalyst it does seem that the reaction becomes mass transfer controlled at temperatures above 370 °C. The plateauing of activity reached at 7.5 bar suggests that the reaction rate is no longer the rate limiting step beyond this pressure, this maybe be due to switching into a mass transfer controlled region or changing reaction mechanism. Repeating the powder and monolith experiments at a lower temperature where the reaction is definitely not mass transfer limited may reveal conclusively whether there is any real difference in activity between the monolithic catalyst and the powder catalyst beyond possible mass transfer influences. These initial results suggest that there is a difference between the two catalysts behaviour.

7.8 Conclusions

In this chapter the MWCNT powders and the structured MWCNT/Monolith composites synthesised and characterised in Chapter 4 and Chapter 5 have been tested as supports for CO_2 conversion. MWCNT have not previously been tested as supports for CO_2 conversion, but

are here shown to be active supports for the conversion of CO_2 to hydrocarbons. The MWCNT supports gave higher activities than were obtained using an activated charcoal support of similar surface area.

A new technique was developed to allow the activation of the residual iron nanoparticles produced by the CVD synthesis process. Previous authors have remarked on the potential of these residual particles as catalysts, but aside from electrochemistry, few studies have utilised them as catalysts. This chapter shows that the iron nanoparticles formed are enclosed by a thin layer of graphitic carbon, preventing them from acting as catalysts. Removing this carbon layer by an oxidation treatment exposes the iron nanoparticles and activates them for catalysis. This method allows the production of a valuable iron/MWCNT catalyst directly from This activation must be carefully controlled, as oxidising the catalyst to much leads to decomposition of the MWCNT, rendering it less effective as a catalyst, whilst to little oxidation will not expose the iron nanoparticles, and so it will also be inactive. Surprisingly it was noted that repeated oxidation and hydrogenation of the stainless steel vessel could activate the stainless steel as a catalyst. Though unsurprising that iron metal can be a catalyst for CO_2 conversion, this has not previously been reported for temperatures below 450 °C.

Detailed characterisation of the catalyst revealed that the progression of the iron metal throughout the various stages of the process. The residual iron catalyst is initially present as metallic iron and iron carbide, enclosed within the bore of the MWCNT or on the surface of the nanotube enclosed by a graphitic layer. Upon oxidation a mixture of Fe_2O_3 and Fe_3O_4 are formed, with some metallic iron and iron carbide remaining, presumably enclosed in the bore of the catalyst and inaccessible to the reactant gases. After oxidation, hydrogenation quickly reduces most of the iron oxides into iron metal, with small traces of magnetite and wursite. XPS work has demonstrated that the iron species on the surface of the MWCNT after hydrogenation are iron oxide, suggesting that metallic iron mostly forms in the MWCNT bore due to increased reducibility of nanoparticles bound inside MWCNT. Upon exposure to carbon dioxide, the metallic iron is rapidly carburised forming a mixture of iron carbides, including cementite and the Hagg carbide which are believed to be active for Fischer Tropsch.

Varying the temperature of the reaction shows the reaction is rate controlled at lower temperatures (<370 °C), before becoming mass transfer controlled at higher temperatures. At temperatures above 400 °C conversion drops, probably due to the increased rate of the Boudouard reaction. There appears to be no correlation between activity and the layer thickness or the catalyst surface area, probably due to the activation process being optimised

for specific synthesis conditions. In fact activation of the CNTs synthesised at different reaction conditions results in a catalyst where the graphitic coating is not successfully removed from the iron nanoparticles.

Olefin selectivity is much lower than has previously been reported for iron catalysts in the Fischer Tropsch reaction. This could be due to several reasons including the necessity for a higher ratio of CO_2:H_2 compared to the CO:H_2 used in Fischer Tropsch, the reported hydrogen spill-over capability of CNT which allows them to act as highly effective hydrogenation catalysts, or the absence of the trace S and K reported to enhance activity in the previous work. The majority of studies which achieve high olefin ratios have been heavily doped, usually with Mn or K, or both to achieve these high olefin selectivities.

Testing the activated Fe/MWCNT catalysts produced on the monolith and those as a powder for CO_2 conversion demonstrated interesting behaviour. The two catalysts demonstrate similar activity per weight of CNT at atmospheric pressure, however increasing the pressure causes the activity of the MWCNT/monolith catalyst to increase dramatically up to 7.5 bar, whilst the activity of the MWCNT powder increases only relatively slowly, such that at 7.5 bar the MWCNT powder has around a third of the activity of the monolithic catalyst on a weight for weight basis. This improved activity is likely due to improved mass transfer of the gases into the CNT layer, especially at high pressure where the diffusivity can play an important role. This may be due to the thin layer of the aligned MWCNT on the monolith surface being more easily accessible than the powder catalyst.

The structured monolithic catalysts have been demonstrated to give improved activity over the powder catalysts for similar masses of catalyst. This improved behaviour coupled with the improved properties of structured CNT supports in comparison to a standard powder catalyst suggests that the use of monolithic CNT catalysts should be further explored. The activities obtained on the monolithic catalysts in a fixed bed system, are higher than the doped and undoped catalysts produced by Sai Prasad *et al.*[237], and only lower than those of Hu *et al.*[247] in a fixed bed system. Dorner *et al.*[244] report comparable or higher activities for a CSTR system. The higher activity than the doped catalysts reported is very promising, suggesting that doped CNT catalysts may be capable of reaching even higher activities.

8 Conclusions and Future Work

8.1 Conclusions

In this work a method has been developed allowing the controlled synthesis of aligned CNT forests on the surface of cordierite, a common industrially used catalytic support. A simple activation procedure has been developed allowing the residual iron nanoparticles from the CNT synthesis process to be used as catalysts for CO_2 conversion. The structured supports developed demonstrate improved activity per gram of catalyst compared to the equivalent powder catalyst for CO_2 conversion. Here the major conclusions of the work will be outlined, along with recommendations for future studies.

Synthesis of CNT

CNT synthesis has been performed by a number of different methods, and their suitability for production of CNT for use in catalysis was assessed. Injection based CVD was settled upon as the most appropriate method, as it reliably produced >200 mg of CNT with repeatable properties, unlike the floating catalyst CVD method previously used in the lab. It was noted that iron staining of quartz tubes could have a significant influence on CNT production, and a cleaning procedure using concentrated acids to regularly clean the reactor was instituted. It is recommended that quartz tubes used for CNT synthesis are cleaned regularly to prevent this iron build up. The synthesis method used is robust, and reliably produces MWCNT powders on silicon and quartz substrates. However CNT powders are noted to have a number of problems which would be a barrier to large scale catalysis, including high pressure drop and potential inhalation hazards, exacerbated by the CNTs low density which makes them difficult to handle. The development of structured CNTs as an alternative support was deemed necessary, and was investigated further.

Synthesis of CNT supported on cordierite monoliths

The production of structured CNT supports makes CNTs more viable as industrial catalysts. Previous work on the synthesis of CNT onto cordierite monoliths required the pre-treatment of the catalyst. [115,173] This work demonstrates the successful synthesis of CNT on a support without any pre-treatment, using an injection based CVD method. This also allows the production of aligned MWCNT layers which have not previously been observed on this sort of support.[261]

The resulting substrate has low pressure drop, is mechanically stable, and is easy to handle. The strong anchoring of the MWCNT to the cordierite reduces the risk of creating airborne MWCNT, reducing one of the chief hazards of MWCNT. The thickness of the resulting MWCNT layer can be controlled by varying the synthesis time and temperature. The surface areas of the resulting substrate are relatively low, only 4 m^2/g. While this is an improvement on cordierite, it still does not match the surface areas which have been reported previously. [115,173,181] This synthesis process has been shown to be scalable within the confines of the equipment used, with synthesis of MWCNT uniformly along a 9 cm long cordierite monolith. A conceptually similar CVD process has been demonstrated on up to 30 cm discs to date, suggesting that this technique could be scaled up further. [285]

CNT as catalysts for CO_2 conversion

Iron nanoparticles supported on carbon nanotubes have been demonstrated to be active for CO_2 conversion.[276] The CNT catalyst is more active than a similar catalyst made using activated carbon and iron impregnated on CNTs. A process to activate the residual iron nanoparticles has been further developed for use with monolithic catalysts.

The synthesis of CNT directly onto the surface of the cordierite monolith, and then activating the residual particles has dramatically shortened the process of making a structured catalyst, removing several of the previously necessary steps (Figure 8.1). Of the steps removed, washcoating of the catalyst is a difficult process to repeat uniformly, whilst removal or residual iron and impregnation of the catalyst require multiple washing and drying steps which are time consuming. The Fe@CNT monolith can conceivably be activated whilst cooling from the synthesis process, and is then ready for hydrogenation upon being transferred into the reaction vessel.

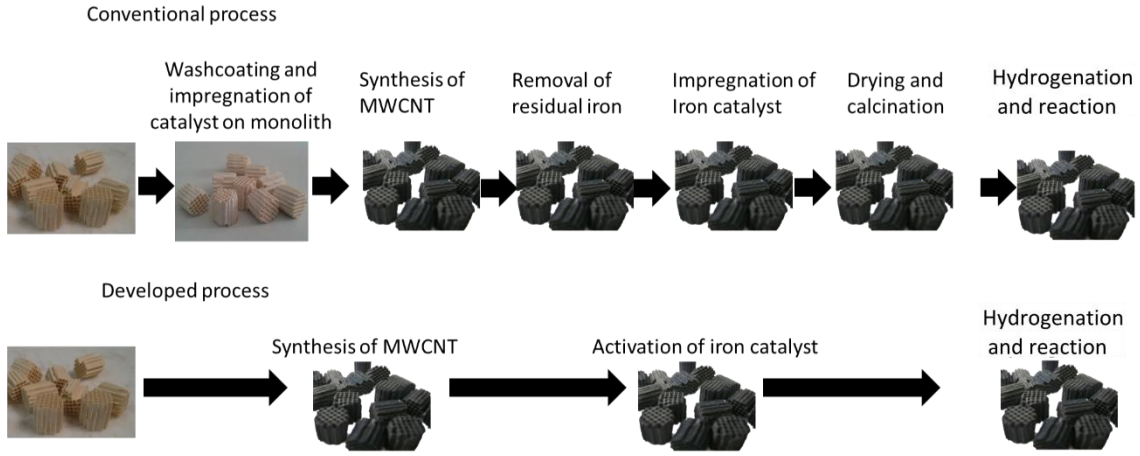

Figure 8.1 Comparison between conventional processes for the synthesis and preparation of a Fe/CNT/monolith composite, and the developed method

In-situ XRD analysis has identified that the active species present in the reaction is an iron carbide, similar to previous reports of iron carbide being the active species in Fischer Tropsch catalysis.[201] It is interesting to note that iron oxide was not detected under reaction conditions, via XRD, XPS analysis reveals the present of magnetite on the surface of the catalyst. [276] This suggests differences in reducibility between iron nanoparticles on the surface of the catalyst, and those in the core have created a two phase catalyst, iron magnetite on the nanotube surface (which is known to be active for the reverse water gas shift reaction) [201] and iron carbides in the core of the catalyst, known to be effective Fischer Tropsch catalysts. [282] Unfortunately it has also been observed that this catalyst is not stable over time, with the main cause of deactivation seeming to be the agglomeration or iron nanoparticles on the surface of the nanotube, suggesting that the iron nanoparticles are not tightly bound to the nanotube surface under reaction conditions.

Varying the flow rate, temperature and thickness of the CNT layer revealed somewhat conflicting results. Changing the flow rate and the thickness of the CNT showed no apparent change in the rate of reaction, suggesting that the reaction rate was limited by neither external nor internal diffusion. Changing the temperature however suggested that at around 370 °C the reaction switches from a reaction rate controlled region, to another region, presumably mass transfer controlled. It would seem that the catalyst may be operating on the limits of the region where the reaction rate is mass transfer limited. Operating at similar pressures to the literature, the catalyst activity was 0.42 µmol $gCNT^{-1}$ s^{-1}, similar or better than most comparable literature catalysts, even those which are heavily doped (Table 2.4). The only

catalyst which performed better in terms of activity was the FeMnK nanofiber catalyst produced by Hu *et al*,[247] which is very heavily doped. Doping the catalyst may allow higher activities to be achieved, and increase the selectivity towards olefins. The catalyst did not display the high selectivities to olefins reported for similar catalysts in the Fischer Tropsch reaction. [205] It would appear that doping the catalyst with potassium and sulfur and the low CO to hydrogen ratio is important for this high olefin selectivity.

The monolithic catalyst was demonstrated to be highly active, especially when at pressure, with activities of > 3 µmol $gCNT^{-1}$ s^{-1} achieved above 7.5 bar. At high pressures (over 7.5 bar) the 0.15 g of CNT on the monolith, gave similar conversions to 0.4 g of powder catalyst, but significantly better activity with more than twice the activity per gram of catalyst. At high pressure the activity of the monolithic catalyst plateaued, whilst the powder catalyst continued to rise, this suggests that the catalyst may enter a mass transfer limited region above 7.5 bar or the rate determining step changes to one not affected by pressure. Varying the temperature of the catalysts showed that at 370 °C and below the catalyst was rate limited by the temperature, suggesting that it is reaction limited, whilst at higher temperatures it was instead limited by another factor, probably mass transfer.

The method of combined synthesis and activation of the Fe@CNT catalyst significantly shortens the number of steps required to make a structured CNT catalyst that could be used in industry. Whilst this method is interesting, the catalyst in its current form cannot be recommended for scale up to an industrial level. The relative expense of CNT compared to traditional supports like Al_2O_3 and SiO_2, mean that for the catalyst to be economical it must be stable over a long period and achieve comparable selectivity. Doping the catalyst and modifying the synthesis route may be able to achieve this, as will be discussed in future work. The work outlined in this thesis has however shown that CNT could feasibly be scaled up to a support more suited to industrial reactions, and future work may show this catalyst has applications in other areas.

8.2 Future Work

In this section potential future investigations highlighted by this work are outlined, with suggestions for fruitful avenues of exploration.

Synthesis of CNT

The synthesis of MWCNT has successfully been performed using the injection CVD method. This process has been successfully optimised for the production of CNT, containing residual

iron nanoparticles which can be used for catalysis. This process can produce MWCNT with a range of diameters and a range of particle sizes. Improved control over the nanoparticle sizes and nanotube diameters could be a promising area of research. In particular the synthesis of controlled size nanoparticles would allow the exploration of particle size effects on catalysis, whilst control of the nanotube diameters would allow the investigation of diffusion and confinement effects on the catalytic reactions.

The reaction has currently been optimised using ferrocene and toluene as catalyst and carbon precursor respectively. The reaction also utilises argon as an inert gas. To increase the sustainability of the reaction, it might be thought preferable to replace the use of argon with another inert gas such as nitrogen, [286]and replace the carbon source with a non-fossil fuel based source, such as camphor. [67] Previous studies have shown the successful use of nitrogen as an inert, and camphor oil has been demonstrated to give an even higher growth rate than toluene. Life cycle assessment performed on the synthesis process has shown however that the majority of the impacts associated with CNT synthesis come from electricity and infrastructure costs, rather than the materials used. [287] As such the biggest impact on minimisation of energy costs could be achieved by lowering synthesis temperatures.

Synthesis of CNT supported on cordierite monoliths

The synthesis of MWCNT directly onto cordierite monoliths in one step has been achieved, producing well aligned layers of CNT. The surface area of the resulting substrates is however lower than would be desired at only 4 m^2/g. Future work should concentrate on producing substrates with a higher surface area, as these would be more interesting as catalyst supports, synthesis at lower temperature and for longer times seems to increase the surface area, a more thorough study of the effects of temperature and time on nanotube growth may prove enlightening.

CNT as catalysts for CO_2 conversion

In this study Fe@CNT monolith catalysts have been successfully synthesised, however a number of issues remain to be addressed before the catalyst can be considered to be industrially viable. The as-prepared catalyst utilises the residual iron catalyst as a CO_2 conversion catalyst, however a number of studies have shown that doping the iron catalyst with other metals can change the catalyst behaviour to give higher selectivity to olefins or improved selectivity to higher hydrocarbons. Typical dopants that have been used in the past are manganese and potassium for improved selectivity to olefins,[237] and cobalt for improved

selectivity to higher hydrocarbons.[288] Introducing well known alternative CVD catalyst precursors for CNT synthesis such as nickelocene and cobaltocene could allow the synthesis of mixed metal catalysts which could also be used for catalysis. Manganese[289] and potassium [290] have also been reported as catalysts for CNT growth. Mixing small amounts of CVD pre-cursors for these metals with ferrocene could allow the creation of more complex catalysts which are intimately bound with effective dopants. Care must be taken with this as the introduction of different metallic species will change the behaviour of the growth catalyst, which will require the synthesis conditions to be re-optimised.

One issue that needs to be addressed is repeating the results obtained at pressure at a lower temperature. Evidence for whether the reaction is mass transfer controlled is inconclusive, but the plateauing of activity would suggest that a mass transfer controlled region is entered. Repeating the reaction at lower temperatures (i.e. 300 °C), would allow determination of the rate of reaction for the process without the possible interference of mass transfer limitations, and to determine whether any difference in inherent activity between the monolith and powder catalyst exists.

A major issue to be addressed before this catalyst can be considered as a viable catalyst is the deactivation of the catalyst over time, the major problem appears to be the agglomeration of the catalyst nanoparticles. One way to avoid this decomposition could be to only partially remove the graphitic layer fixing the surface nanoparticles in place, with only partial remove the remaining carbon would help hold the nanoparticle in place, but at the cost of reduced activity of the catalyst. This would require further characterisation (HR-TEM, in-situ XPS) of the nanoparticles after different oxidation times, in order to observe the decomposition of the carbon layer, to determine if the decomposition would allow some of the graphitic layer to remain as an anchor. If the iron particles are not sufficiently well anchored the catalyst will not be able to act as a viable catalyst, as a long catalyst life time is vital for a large scale process like CO_2 conversion.

The Fe@CNT supports synthesised in this work have been used as catalysts for the hydrogenation of CO_2, however Fe@CNT catalysts, and similar catalyst produced by the same method may have potential as catalysts for other reactions. Reactions potentially of interest include the Fischer Tropsch reaction on its own, uncoupled from the CO_2 hydrogenation, ammonia decomposition and ammonia synthesis, as well as reactions such as NOx decomposition, or any of the wide range of reactions which require a heterogeneous iron catalyst. The Fe/CNT catalysts may also be particularly useful in other hydrogenation

reactions, for example the hydrogenation of nitrobenzene is known to use carbon coated monoliths, [179] a worthwhile study would be the screening of hydrogenation reactions over this catalyst that currently use expensive metals such as platinum and palladium, to determine if the hydrogenation ability of the Fe/CNT catalyst is sufficient to replace these catalysts.

8.3 References

(1) Core Writing Team, P., R.K. and Reisinger, A. (Eds.); IPCC, G., Switzerland. pp 104, Ed. 2007.

(2) Arrhenius, S. *Philos. Mag.* **1896**, *41*, 237.

(3) Fourier, J. *Am. J. Sci.* **1837**, *32*, 1.

(4) Tyndall, J. *Philos. Mag.* **1863**, *4*, 200.

(5) Solomon, S., D. Qin, M. Manning, Z. Chen, M. Marquis, K.B. Averyt, M. Tignor H.L. Miller (eds.). **2007**, 996.

(6) Rohde, R.; http://www.globalwarmingart.com/.

(7) Tans, P.; Keeling, R. 2013.

(8) NOAA, National Climatic Data Centre, **2013**

(9) International Energy Agency **2013**.

(10) European Comission, Renewable energy progress report, **2013**.

(11) CURC *CURC-EPRI Roadmap Coal Technology Roadmap*, **2012**.

(12) McKinsey; and; company. Carbon Capture and Storage: Assessing the economics. [Online Early Access]. Published Online: **2008**.

(13) Styring, P.; Jansen, D.; Coninck, H. d.; Reith, H.; Armstrong, K. **2011**.

(14) Choi, S.; Drese, J.; Jones, C. *ChemSusChem* **2009**, *2*, 796.

(15) Yang, H.; Xu, Z.; Fan, M.; Gupta, R.; Slimane, R. B.; Bland, A. E.; Wright, I. *J. Env. Sci.* **2008**, *20*, 14.

(16) D'Alessandro, D. M.; Smit, B.; Long, J. R. *Angew. Chem. Int. Ed.* **2010**, *49*, 6058.

(17) Lackner, K. S. *Science* **2003**, *300*, 1677.

(18) Nduagu, E.; Fagerlund, J.; Zevenhoven, R. *Energy Convers. Manage.* **2012**, *55*, 178.

(19) Aresta, M. In *Carbon Dioxide as Chemical Feedstock*; Wiley-VCH Verlag GmbH & Co. KGaA: **2010**, p 1.

(20) Catalytic Centre Aachen, **2013**

(21) Havran, V.; Duduković, M. P.; Lo, C. S. *Ind. Eng. Chem. Res.* **2011**, *50*, 7089.

(22) Boden, T. A., G. Marland, and R.J. Andres; Carbon Dioxide Information Analysis Center, Oak Ridge National Laboratory, U.S. Department of Energy, Oak Ridge, Tenn., U.S.A.: **2010**.

(23) Aresta, M.; Dibenedetto, A. In *Presentation at the ICCDU* 2013.

(24) Crabtree, G. W.; Dresselhaus, M. S.; Buchanan, M. V. *Physics Today* **2004**, *57*, 39.

(25) Dunn, S. *Int. J. Hydrogen Energy* **2002**, *27*, 235.

(26) Ni, M.; Leung, M. K. H.; Leung, D. Y. C.; Sumathy, K. ***RENEW. SUST. ENERG. REV.*** **2007**, *11*, 401.

(27) Mueller-Langer, F.; Tzimas, E.; Kaltschmitt, M.; Peteves, S. *Int. J. Hydrogen Energy* **2007**, *32*, 3797.

(28) Hammer, G.; Lübcke, T.; Kettner, R.; Pillarella, M. R.; Recknagel, H.; Commichau, A.; Neumann, H.-J.; Paczynska-Lahme, B. In *Ullmann's Encyclopedia of Industrial Chemistry*; Wiley-VCH Verlag GmbH & Co. KGaA: **2000**.

(29) Sabatier, P. **1912**.

(30) Park, J.-N.; McFarland, E. W. *J. Catal.* **2009**, *266*, 92.

(31) Brooks, K. P.; Hu, J.; Zhu, H.; Kee, R. J. *Chem. Eng. Sci.* **2007**, *62*, 1161.

(32) Perkas, N.; Amirian, G.; Zhong, Z. Y.; Teo, J.; Gofer, Y.; Gedanken, A. *Catal. Lett.* **2009**, *130*, 455.

(33) Wambach, J.; Baiker, A.; Wokaun, A. *Phys. Chem. Chem. Phys.* **1999**, *1*, 5071.

(34) Matsuo, T.; Kawaguchi, H. *J. Am. Chem. Soc.* **2006**, *128*, 12362.

(35) Riduan, S.; Zhang, Y. *Dalton Trans.* **2010**, *39*, 3347.

(36) Rankin, M. A.; Cummins, C. C. *J. Am. Chem. Soc.* **2010**, *132*, 10021.

(37) Stevens, P. The 'Shale Gas Revolution': Developments and Changes. *Chatham House Report* [Online Early Access]. Published Online: **2012**.

(38) Janke, C.; Farrauto, R. In *ICCDU* Washington, **2013**.

(39) Arakawa, H.; Aresta, M.; Armor, J. N.; Barteau, M. A.; Beckman, E. J.; Bell, A. T.; Bercaw, J. E.; Creutz, C.; Dinjus, E.; Dixon, D. A.; Domen, K.; DuBois, D. L.; Eckert, J.; Fujita, E.; Gibson, D. H.; Goddard, W. A.; Goodman, D. W.; Keller, J.; Kubas, G. J.; Kung, H. H.; Lyons, J. E.; Manzer, L. E.; Marks, T. J.; Morokuma, K.; Nicholas, K. M.; Periana, R.; Que, L.; Rostrup-Nielson, J.; Sachtler, W. M. H.; Schmidt, L. D.; Sen, A.; Somorjai, G. A.; Stair, P. C.; Stults, B. R.; Tumas, W. *Chem. Rev. (Washington, DC, U. S.)* **2001**, *101*, 953.

(40) Air Fuel Synthesis: **2013**.

(41) Blagoev, S. N. B. a. M. *Chemical Economics Handbook. SRI consulting* **2010**.

(42) Fornika, R.; Gorls, H.; Seemann, B.; Leitner, W. *Journal of the Chemical Society-Chemical Communications* **1995**, 1479.

(43) Gassner, F.; Leitner, W. *J. Chem. Soc., Chem. Commun.* **1993**, 1465.

(44) Hao, C.; Wang, S.; Li, M.; Kang, L.; Ma, X. *Catal. Today* **2011**, *160*, 184.

(45) Munshi, P.; Main, A. D.; Linehan, J. C.; Tai, C.-C.; Jessop, P. G. *J. Am. Chem. Soc.* **2002**, *124*, 7963.

(46) Tanaka, R.; Yamashita, M.; Nozaki, K. *J. Am. Chem. Soc.* **2009**, *131*, 14168.

(47) Federsel, C.; Boddien, A.; Jackstell, R.; Jennerjahn, R.; Dyson, P. J.; Scopelliti, R.; Laurenczy, G.; Beller, M. *Angew. Chem. Int. Ed.* **2010**, n/a.

(48) Farlow, M. W.; Adkins, H. *J. Am. Chem. Soc.* **1935**, *57*, 2222.

(49) Reuss, G.; Disteldorf, W.; Gamer, A. O.; Hilt, A. In *Ullmann's Encyclopedia of Industrial Chemistry*; Wiley-VCH Verlag GmbH & Co. KGaA: 2000.

(50) Lafyatis, D. S.; Creten, G.; Froment, G. F. *Applied Catalysis A: General* **1994**, *120*, 85.

(51) Lee, D. K.; Kim, D. S.; Kim, S. W. *Appl. Organomet. Chem.* **2001**, *15*, 148.

(52) Sakurai, H.; Ueda, A.; Kobayashi, T.; Haruta, M. *Chem. Commun. (Cambridge, U. K.)* **1997**, 271.

(53) Dorner, R. W.; Hardy, D. R.; Williams, F. W.; Davis, B. H.; Willauer, H. D. *Energy Fuels* **2009**, *23*, 4190.

(54) 2008.

(55) Serp, P.; Corrias, M.; Kalck, P. *Appl. Cat. A: General* **2003**, *253*, 337.

(56) De Jong, K. P.; Geus, J. W. *Cat. Rev.* **2000**, *42*, 481.

(57) Chen, W.; Fan, Z.; Pan, X.; Bao, X. *J. Am. Chem. Soc.* **2008**, *130*, 9414.

(58) Iijima, S. *Nature* **1991**, *354*, 56.

(59) Ionescu, M. I.; Liu, H.; Zhong, Y.; Zhang, Y.; Li, R.; Sun, X.; Kpetsu, J.-B.; Cote, C.; Jedrzejowsk, P.; Sarkissian, A.; Merel, P.; Laou, P.; Paradis, S.; Desilets, S. *ECS Trans.* **2009**, *25*, 737.

(60) Harris, P. J. F. *Carbon nanotubes and related structures : new materials for the twenty-first century*; Cambridge University Press: Cambridge, **2001**.

(61) Yang, W.; Ratinac, K. R.; Ringer, S. P.; Thordarson, P.; Gooding, J. J.; Braet, F. *Angew. Chem. Int. Ed.* **2010**, *49*, 2114.

(62) Chou, T.-W.; Gao, L.; Thostenson, E. T.; Zhang, Z.; Byun, J.-H. *Compos. Sci. . Technol.* **2010**, *70*, 1.

(63) Che, G.; Lakshmi, B. B.; Fisher, E. R.; Martin, C. R. *Nature* **1998**, *393*, 346.

(64) Maser, W. K.; Munoz, E.; Benito, A. M.; Martinez, M. T.; de la Fuente, G. F.; Maniette, Y.; Anglaret, E.; Sauvajol, J. L. *Chem. Phys. Lett.* **1998**, *292*, 587.

(65) Andrews, R.; Jacques, D.; Rao, A. M.; Derbyshire, F.; Qian, D.; Fan, X.; Dickey, E. C.; Chen, J. *Chem. Phys. Lett.* **1999**, *303*, 467.

(66) Pinault, M.; Mayne-L'Hermite, M.; Reynaud, C.; Pichot, V.; Launois, P.; Ballutaud, D. *Carbon* **2005**, *43*, 2968.

(67) Kumar, M.; Ando, Y. *J. Nanosci. Nanotechnol.* **2010**, *10*, 3739.
(68) De Volder, M. F. L.; Tawfick, S. H.; Baughman, R. H.; Hart, A. J. *Science* **2013**, *339*, 535.
(69) *Additives for Polymers* **2013**, *2013*, 8.
(70) *Additives for Polymers* **2012**, *2012*, 3.
(71) Huang, J.; Zhang, Q.; Zhao, M.; Wei, F. *Chin. Sci. Bull.* **2012**, *57*, 157.
(72) Eklund, P.; Ajayan, P.; Blackmon, R.; Hart, A. J.; Kong, J.; Pradhan, B.; Rao, A.; Rinzler, A. *International Assessment of Carbon Nanotube Manufacturing and Applications*, DTIC Document, **2007.**
(73) Melechko, A. V.; Merkulov, V. I.; McKnight, T. E.; Guillorn, M. A.; Klein, K. L.; Lowndes, D. H.; Simpson, M. L. *J. Appl. Phys.* **2005**, *97*.
(74) Dupuis, A. C. *Prog. Mater. Sci.* **2005**, *50*, 929.
(75) Oncel, C.; Yurum, Y. *Fuller Nanotub Carbon Nanostruct* **2006**, *14*, 17.
(76) Venegoni, D.; Serp, P.; Feurer, R.; Kihn, Y.; Vahlas, C.; Kalck, P. *Carbon* **2002**, *40*, 1799.
(77) Hernadi, K.; Fonseca, A.; Nagy, J. B.; Bernaerts, D.; Fudala, A.; Lucas, A. A. *Zeolites* **1996**, *17*, 416.
(78) Jourdain, V.; Bichara, C. *Carbon* **2013**, *58*, 2.
(79) Dupuis, A.-C. *Prog. Mater. Sci.* **2005**, *50*, 929.
(80) Cheng, H. M.; Li, F.; Su, G.; Pan, H. Y.; He, L. L.; Sun, X.; Dresselhaus, M. S. *Appl. Phys. Lett.* **1998**, *72*, 3282.
(81) Ci, L.; Rao, Z.; Zhou, Z.; Tang, D.; Yan, X.; Liang, Y.; Liu, D.; Yuan, H.; Zhou, W.; Wang, G.; Liu, W.; Xie, S. *Chem. Phys. Lett.* **2002**, *359*, 63.
(82) Lee, Y. T.; Kim, N. S.; Park, J.; Han, J. B.; Choi, Y. S.; Ryu, H.; Lee, H. J. *Chem. Phys. Lett.* **2003**, *372*, 853.
(83) Liu, H.; Zhang, Y.; Arato, D.; Li, R.; Mérel, P.; Sun, X. *Surf. Coat. Technol.* **2008**, *202*, 4114.
(84) Andrews, R.; Jacques, D.; Rao, A. M.; Derbyshire, F.; Qian, D.; Fan, X.; Dickey, E. C.; Chen, J. *Chem. Phys. Lett.* **1999**, *303*, 467.
(85) Mayne, M.; Grobert, N.; Terrones, M.; Kamalakaran, R.; Rühle, M.; Kroto, H. W.; Walton, D. R. M. *Chem. Phys. Lett.* **2001**, *338*, 101.
(86) Hou, H.; Schaper, A.; Weller, F.; Greiner, A. *Chem. Mater.* **2002**, *14*, 3990.
(87) Öncel, Ç.; Yürüm, Y. *Fuller Nanotub Carbon Nanostruct* **2006**, *14*, 17.
(88) Singh, C.; Shaffer, M. S.; Windle, A. H. *Carbon* **2003**, *41*, 359.
(89) Zhang, Z.; Wei, B.; Ramanath, G.; Ajayan, P. *Appl. Phys. Lett.* **2000**, *77*, 3764.
(90) McKee, G. S. B.; Deck, C. P.; Vecchio, K. S. *Carbon* **2009**, *47*, 2085.
(91) Kukovitsky, E. F.; L'Vov, S. G.; Sainov, N. A.; Shustov, V. A.; Chernozatonskii, L. A. *Chem. Phys. Lett.* **2002**, *355*, 497.
(92) Ding, F.; Rosen, A.; Bolton, K. *J.Chem. Phys.* **2004**, *121*, 2775.
(93) Yoshida, H.; Shimizu, T.; Uchiyama, T.; Kohno, H.; Homma, Y.; Takeda, S. *Nano Lett.* **2009**, *9*, 3810.
(94) Kuwana, K.; Saito, K. *Carbon* **2005**, *43*, 2088.
(95) Conroy, D.; Moisala, A.; Cardoso, S.; Windle, A.; Davidson, J. *Chem. Eng. Sci.* **2010**, *65*, 2965.
(96) Horváth, Z. E.; Kertész, K.; Pethő, L.; Koós, A. A.; Tapasztó, L.; Vértesy, Z.; Osváth, Z.; Darabont, A.; Nemes-Incze, P.; Sárközi, Z.; Biró, L. P. *Curr. App. Phys.* **2006**, *6*, 135.
(97) Mohlala, M. S.; Liu, X.-Y.; Coville, N. J. *J. Organomet. Chem.* **2006**, *691*, 4768.
(98) Mohlala, M. S.; Coville, N. J. *J. Organomet. Chem.* **2007**, *692*, 2965.
(99) Nyamori, V. O.; Nxumalo, E. N.; Coville, N. J. *J. Organomet. Chem.* **2009**, *694*, 2222.

(100) Singh, C.; Shaffer, M. S. P.; Koziol, K. K. K.; Kinloch, I. A.; Windle, A. H. *Chem. Phys. Lett.* **2003**, *372*, 860.

(101) Pattinson, S. W.; Prehn, K.; Kinloch, I. A.; Eder, D.; Koziol, K. K. K.; Schulte, K.; Windle, A. H. *RSC Advances* **2012**, *2*, 2909.

(102) Castro, C.; Pinault, M.; Coste-Leconte, S.; Porterat, D.; Bendiab, N.; Reynaud, C.; Mayne-L'Hermite, M. *Carbon* **2010**, *48*, 3807.

(103) Pinault, M.; Pichot, V.; Khodja, H.; Launois, P.; Reynaud, C.; Mayne-L'Hermite, M. *Nano Lett.* **2005**, *5*, 2394.

(104) Meysami, S. S.; Koós, A. A.; Dillon, F.; Grobert, N. *Carbon* **2013**, *58*, 159.

(105) Kumar, M.; Ando, Y. *Carbon* **2005**, *43*, 533.

(106) Azmina, M. S.; Suriani, A. B.; Falina, A. N.; Salina, M.; Rosly, J.; Rusop, M. *Preparation of Palm Oil Based Carbon Nanotubes at Various Ferrocene Concentration*

Nanomaterials - Synthesis and Characterization, **2011**; Vol. 364.

(107) Chatterjee, A. K.; Sharon, M.; Banerjee, R.; Neumann-Spallart, M. *Electrochim. Acta* **2003**, *48*, 3439.

(108) Kim, J. H.; Lee, K. H.; Burk, D.; Overzet, L. J.; Lee, G. S. *Carbon* **2010**, *48*, 4301.

(109) Dong, L. F.; Jiao, J.; Foxley, S.; Tuggle, D. W.; Mosher, C. L.; Grathoff, G. H. *J. Nanosci. Nanotechnol.* **2002**, *2*, 155.

(110) Hata, K.; Futaba, D. N.; Mizuno, K.; Namai, T.; Yumura, M.; Iijima, S. *Science* **2004**, *306*, 1362.

(111) Yang, X.; Yuan, L.; Peterson, V. K.; Yin, Y.; Minett, A. I.; Harris, A. T. *J. Phys. Chem. C* **2011**, *115*, 14093.

(112) Qian, H.; Bismarck, A.; Greenhalgh, E. S.; Shaffer, M. S. P. *Comp. Sci. Tech.* **2010**, *70*, 393.

(113) Pattinson, S. W.; Windle, A. H.; Koziol, K. K. K. *Mater. Lett.* **2013**, *93*, 404.

(114) Mi, W.; Lin, J. Y. S.; Li, Y.; Zhang, B. *Microporous Mesoporous Mater.* **2005**, *81*, 185.

(115) García-Bordejé, E.; Kvande, I.; Chen, D.; Rønning, M. *Carbon* **2007**, *45*, 1828.

(116) Jarrah, N.; van Ommen, J. G.; Lefferts, L. *Catal. Today* **2003**, *79-80*, 29.

(117) Jung, Y. J.; Wei; Vajtai, R.; Ajayan, P. M.; Homma, Y.; Prabhakaran, K.; Ogino, T. *Nano Lett.* **2003**, *3*, 561.

(118) Lu, J. Q. *J. Phys. Chem. C* **2008**, *112*, 10344.

(119) Xiang, R.; et al. *Nanotechnology* **2007**, *18*, 415703.

(120) Liu, H.; Zhang, Y.; Li, R.; Sun, X.; Désilets, S.; Abou-Rachid, H.; Jaidann, M.; Lussier, L.-S. *Carbon* **2010**, *48*, 1498.

(121) Meysami, S. S.; Dillon, F.; Koós, A. A.; Aslam, Z.; Grobert, N. *Carbon* **2013**, *58*, 151.

(122) Tessonnier, J.-P.; Su, D. S. *ChemSusChem* **2011**, *4*, 824.

(123) Helveg, S.; Lopez-Cartes, C.; Sehested, J.; Hansen, P. L.; Clausen, B. S.; Rostrup-Nielsen, J. R.; Abild-Pedersen, F.; Norskov, J. K. *Nature* **2004**, *427*, 426.

(124) Smalley, R. E.; Li, Y. B.; Moore, V. C.; Price, B. K.; Colorado, R.; Schmidt, H. K.; Hauge, R. H.; Barron, A. R.; Tour, J. M. *J. Am. Chem. Soc.* **2006**, *128*, 15824.

(125) Yoshida, H.; Takeda, S.; Uchiyama, T.; Kohno, H.; Homma, Y. *Nano Lett.* **2008**, *8*, 2082.

(126) Singh, C.; Shaffer, M. S. P.; Windle, A. H. *Carbon* **2003**, *41*, 359.

(127) Stadermann, M.; Sherlock, S. P.; In, J.-B.; Fornasiero, F.; Park, H. G.; Artyukhin, A. B.; Wang, Y.; De Yoreo, J. J.; Grigoropoulos, C. P.; Bakajin, O.; Chernov, A. A.; Noy, A. *Nano Lett.* **2009**, *9*, 738.

(128) Wang, X.; Feng, Y.; Unalan, H. E.; Zhong, G.; Li, P.; Yu, H.; Akinwande, A. I.; Milne, W. I. *Carbon* **2011**, *49*, 214.

(129) Kim, S. M.; Pint, C. L.; Amama, P. B.; Zakharov, D. N.; Hauge, R. H.; Maruyama, B.; Stach, E. A. *J. Phys. Chem. Lett.* **2010**, *1*, 918.

(130) Simate, G. S.; Iyuke, S. E.; Ndlovu, S.; Yah, C. S.; Walubita, L. F. *J. Nat. Gas Chem.* **2010**, *19*, 453.

(131) Xu, X.-j.; Huang, S.-m. *Mater. Lett.* **2007**, *61*, 4235.

(132) Hafner, J. H.; Bronikowski, M. J.; Azamian, B. R.; Nikolaev, P.; Rinzler, A. G.; Colbert, D. T.; Smith, K. A.; Smalley, R. E. *Chem. Phys. Lett.* **1998**, *296*, 195.

(133) Chu, W.; Ran, M.; Zhang, X.; Wang, N.; Wang, Y.; Xie, H.; Zhao, X. *J. Energ. Chem.* **2013**, *22*, 136.

(134) Ballesteros, B.; Tobias, G.; Shao, L.; Pellicer, E.; Nogués, J.; Mendoza, E.; Green, M. L. H. *Small* **2008**, *4*, 1501.

(135) Donaldson, K.; Murphy, F.; Duffin, R.; Poland, C. *Part. Fibr. Toxicol.* **2010**, *7*, 5.

(136) Liu, Y.; Zhao, Y.; Sun, B.; Chen, C. *Acc. Chem. Res.* **2012**, *46*, 702.

(137) Poland, C. A.; Duffin, R.; Kinloch, I.; Maynard, A.; Wallace, W. A. H.; Seaton, A.; Stone, V.; Brown, S.; MacNee, W.; Donaldson, K. *Nat Nano* **2008**, *3*, 423.

(138) Kostarelos, K. *Nat Biotech* **2008**, *26*, 774

(139) Ali-Boucetta, H.; Nunes, A.; Sainz, R.; Herrero, M. A.; Tian, B.; Prato, M.; Bianco, A.; Kostarelos, K. *Angew. Chem. Int. Ed.* **2013**, *52*, 2274.

(140) Castranova, V.; Schulte, P. A.; Zumwalde, R. D. *Acc. Chem. Res.* **2012**, *46*, 642.

(141) Bussy, C.; Paineau, E.; Cambedouzou, J.; Brun, N.; Mory, C.; Fayard, B.; Salome, M.; Pinault, M.; Huard, M.; Belade, E.; Armand, L.; Boczkowski, J.; Launois, P.; Lanone, S. *Part. Fibr. Toxicol.* **2013**, *10*, 24.

(142) Waldman, W. J.; Kristovich, R.; Knight, D. A.; Dutta, P. K. *Chem. Res. Toxicol.* **2007**, *20*, 1149.

(143) Taylor, A.; Lipert, K.; Krämer, K.; Hampel, S.; Füssel, S.; Meye, A.; Klingeler, R.; Ritschel, M.; Leonhardt, A.; Büchner, B.; Wirth, M. P. *J. Nanosci. Nanotechnol.* **2009**, *9*, 5709.

(144) Andriotis, A. N.; Menon, M.; Froudakis, G. E. *Appl. Phys. Lett.* **2000**, *76*, 3890.

(145) Pan, X.; Bao, X. *Chem. Commun. (Cambridge, U. K.)* **2008**, 6271.

(146) Mattia, D.; Korneva, G.; Sabur, A.; Friedman, G.; Gogotsi, Y. *Nanotechnology* **2007**, *18*, 155305.

(147) Ye, Y.; Geng, B. *Crit. Rev. Solid State Mater. Sci.* **2012**, *37*, 75.

(148) Pumera, M.; Miyahara, Y. *Nanoscale* **2009**, *1*, 260.

(149) Pumera, M. *Langmuir* **2007**, *23*, 6453.

(150) Van de Vyver, S.; Geboers, J.; Dusselier, M.; Schepers, H.; Vosch, T.; Zhang, L.; Van Tendeloo, G.; Jacobs, P. A.; Sels, B. F. *ChemSusChem* **2010**, *3*, 698.

(151) Van de Vyver, S.; Geboers, J.; Schutyser, W.; Dusselier, M.; Eloy, P.; Dornez, E.; Seo, J. W.; Courtin, C. M.; Gaigneaux, E. M.; Jacobs, P. A.; Sels, B. F. *ChemSusChem* **2012**, *5*, 1549.

(152) Bahome, M. C., University of the Witwatersrand, , **2007**.

(153) Zhang, J.; Comotti, M.; Schuth, F.; Schlogl, R.; Su, D. S. *Chem. Commun. (Cambridge, U. K.)* **2007**, 1916.

(154) Xue, B.; Chen, P.; Hong, Q.; Lin, J.; Tan, K. L. *J. Mater. Chem.* **2001**, *11*, 2378.

(155) Chen, P.; Wu, X.; Lin, J.; Tan, K. L. *The Journal of Physical Chemistry B* **1999**, *103*, 4559.

(156) Planeix, J. M.; Coustel, N.; Coq, B.; Brotons, V.; Kumbhar, P. S.; Dutartre, R.; Geneste, P.; Bernier, P.; Ajayan, P. M. *J. Am. Chem. Soc.* **1994**, *116*, 7935.

(157) Frehill, F.; Vos, J. G.; Benrezzak, S.; Koós, A. A.; Kónya, Z.; Rüther, M. G.; Blau, W. J.; Fonseca, A.; Nagy, J. B.; Biró, L. P.; Minett, A. I.; in het Panhuis, M. *J. Am. Chem. Soc.* **2002**, *124*, 13694.

(158) Giordano, R.; Serp, P.; Kalck, P.; Kihn, Y.; Schreiber, J.; Marhic, C.; Duvail, J. L. *Eur. J. Inorg. Chem.* **2003**, *2003*, 610.

(159) Wildgoose, G. G.; Banks, C. E.; Compton, R. G. *Small* **2006**, *2*, 182.

(160) Barnard, C. F. J.; Rouzaud, J.; Stevenson, S. H. *Org. Process Res. Dev.* **2005**, *9*, 164.

(161) Tavasoli, A.; Trépanier, M.; Malek Abbaslou, R. M.; Dalai, A. K.; Abatzoglou, N. *Fuel Process. Technol.* **2009**, *90*, 1486.

(162) Vieira, R.; Pham-Huu, C.; Keller, N.; Ledoux, M. J. *Chem. Commun. (Cambridge, U. K.)* **2002**, 954.

(163) Wang, Y.; Zhitomirsky, I. *Colloids and surfaces. A, Physicochemical and engineering aspects* **2010**, *369*, 211.

(164) Gao, R.; Tan, C. D.; Baker, R. T. K. *Catal. Today* **2001**, *65*, 19.

(165) Ma, J.; Moy, D.; Chishti, A.; Yang, J. *US patent 2009/0093360 A1* **2011**.

(166) Nijhuis, T. A.; Beers, A. E. W.; Vergunst, T.; Hoek, I.; Kapteijn, F.; Moulijn, J. A. *Cat. Revs.-Sci. Eng.* **2001**, *43*, 345.

(167) Tomašić, V.; Jović, F. *App. Catal. A: Gen* **2006**, *311*, 112.

(168) Nijhuis, T. A.; Kreutzer, M. T.; Romijn, A. C. J.; Kapteijn, F.; Moulijn, J. A. *Chem. Eng. Sci.* **2001**, *56*, 823.

(169) Lindholm, A.; Sjövall, H.; Olsson, L. *App. Catal. B: Env.* **2010**, *98*, 112.

(170) Clayton, R. D.; Harold, M. P.; Balakotaiah, V. *App. Catal. B: Env.* **2008**, *84*, 616.

(171) Liu, W.; Hu, J.; Wang, Y. *Catal. Today* **2009**, *140*, 142.

(172) Visconti, C. G.; Tronconi, E.; Lietti, L.; Groppi, G.; Forzatti, P.; Cristiani, C.; Zennaro, R.; Rossini, S. *App. Cat. A: Gen.l* **2009**, *370*, 93.

(173) Gong, B.; Wang, R.; Lin, B.; Xie, F.; Yu, X.; Wei, K. *Catal. Lett.* **2008**, *122*, 287.

(174) Zhao, Y.; Zhou, J.; Zhang, J.; Wang, S. *Catal. Lett.* **2009**, *131*, 597.

(175) Roh, H.-S.; Lee, D. K.; Koo, K. Y.; Jung, U. H.; Yoon, W. L. *Int. J. Hydrogen Energy* **2010**, *35*, 1613.

(176) Kolaczkowski, S. T.; Asli, U. A.; Davidson, M. G. *Catal. Today* **2009**, *147, Supplement*, S220.

(177) Leung, D.; Hayes, R. E.; Kolaczkowski, S. T. *Can. J. Chem. Eng.* **1996**, *74*, 94.

(178) García-Bordejé, E.; Kapteijn, F.; Moulijn, J. A. *Catal. Today* **2001**, *69*, 357.

(179) Rodriguez, P.; Simescu-Lazar, F.; Meille, V.; Bah, T.; Pallier, S.; Fournel, I. *App. Catal. A: Gen.* **2012**, *427–428*, 66.

(180) García-Bordejé, E.; Kvande, I.; Chen, D.; Rønning, M. *Adv. Mater. (Weinheim, Ger.)* **2006**, *18*, 1589.

(181) Jarrah, N. A.; van Ommen, J. G.; Lefferts, L. *J. Mater. Chem.* **2004**, *14*, 1590.

(182) Wang, J.; Wang, R.; Yu, X.; Lin, J.; Xie, F.; Wei, K. *J. Nat. Gas Chem.* **2006**, *15*, 211.

(183) Ulla, M. A.; Valera, A.; Ubieto, T.; Latorre, N.; Romeo, E.; Milt, V. G.; Monzón, A. *Catal. Today* **2008**, *133-135*, 7.

(184) Zhu, J.; Jia, Y.; Li, M.; Lu, M.; Zhu, J. *Ind. Eng. Chem. Res.* **2012**, *52*, 1224.

(185) Wang, Y.-l.; Wang, X.-j.; Zhan, L.; Qiao, W.-m.; Liang, X.-y.; Ling, L.-c. *New Carbon Mat.* **2012**, *27*, 153.

(186) Yu, X.; Lin, B.; Gong, B.; Lin, J.; Wang, R.; Wei, K. *Catal. Lett.* **2008**, *124*, 168.

(187) Ratnasamy, C.; Wagner, J. P. *Catal. Revs.* **2009**, *51*, 325.

(188) Kaiser, P.; Unde, R. B.; Kern, C.; Jess, A. *Chem. Ing. Tech.* **2013**, *85*, 489.

(189) Dry, M. E. *Catal. Today* **2002**, *71*, 227.

(190) Dorner, R. W.; Hardy, D. R.; Williams, F. W.; Willauer, H. D. *Energy Env.l Sci.* **2010**, *3*, 884.

(191) Claeys, M.; van Steen, E. In *Stud. Surf. Sci. Catal.*; André, S., Mark, D., Eds.; Elsevier: **2004**; Vol. Volume 152, p 601.

(192) Pichler, H.; Schulz, H. *Chem. Ing. Tech.* **1970**, *42*, 1162.

(193) Inderwildi, O. R.; King, D. A.; Jenkins, S. J. *Phys. Chem. Chem. Phys.* **2009**, *11*, 11110.

(194) van Santen, R.; Ciobica, I.; van Steen, E.; Ghouri, M. *Adv. Catal.* **2011**, *54*, 127.

(195) Maitlis, P. M.; Quyoum, R.; Long, H. C.; Turner, M. L. *App. Catal. A: Gen.l* **1999**, *186*, 363.

(196) Maitlis, P. M.; Long, H. C.; Quyoum, R.; Turner, M. L.; Wang, Z.-Q. *Chem. Commun. (Cambridge, U. K.)* **1996**, *0*, 1.

(197) H.H. Storch; N. Golumbic; Anderson, R. B. *The Fischer-Tropsch and Related Synthesis* John Wiley & Sons, New York **1951**.

(198) Kummer, J. T.; DeWitt, T. W.; Emmett, P. H. *J. Am. Chem. Soc.* **1948**, *70*, 3632.

(199) Brady, R. C.; Pettit, R. *J. Am. Chem. Soc.* **1980**, *102*, 6181.

(200) van Barneveld, W. A. A.; Ponec, V. *J. Catal.* **1984**, *88*, 382.

(201) de Smit, E.; Weckhuysen, B. M. *Chem. Soc. Rev.* **2008**, *37*, 2758.

(202) Lox, E. S.; Froment, G. F. *Ind. Eng. Chem. Res.* **1993**, *32*, 71.

(203) Riedel, T.; Schulz, H.; Schaub, G.; Jun, K.-W.; Hwang, J.-S.; Lee, K.-W. *Top. Catal.* **2003**, *26*, 41.

(204) Li, S.; Krishnamoorthy, S.; Li, A.; Meitzner, G. D.; Iglesia, E. *J. Catal.* **2002**, *206*, 202.

(205) Torres Galvis, H. M.; Bitter, J. H.; Khare, C. B.; Ruitenbeek, M.; Dugulan, A. I.; de Jong, K. P. *Science* **2012**, *335*, 835.

(206) Bezemer, G. L.; Bitter, J. H.; Kuipers, H. P. C. E.; Oosterbeek, H.; Holewijn, J. E.; Xu, X.; Kapteijn, F.; van Dillen, A. J.; de Jong, K. P. *J. Am. Chem. Soc.* **2006**, *128*, 3956.

(207) den Breejen, J. P.; Radstake, P. B.; Bezemer, G. L.; Bitter, J. H.; Frøseth, V.; Holmen, A.; Jong, K. P. d. *J. Am. Chem. Soc.* **2009**, *131*, 7197.

(208) Torres Galvis, H. M.; Bitter, J. H.; Davidian, T.; Ruitenbeek, M.; Dugulan, A. I.; de Jong, K. P. *J. Am. Chem. Soc.* **2012**, *134*, 16207.

(209) Jones, V. K.; Neubauer, L. R.; Bartholomew, C. H. *J. Phys. Chem.* **1986**, *90*, 4832.

(210) Jung, H. J.; Walker Jr, P. L.; Vannice, A. *J. Catal.* **1982**, *75*, 416.

(211) Venter, J.; Kaminsky, M.; Geoffroy, G. L.; Vannice, M. A. *J. Catal.* **1987**, *103*, 450.

(212) van Steen, E.; Prinsloo, F. F. *Catal. Today* **2002**, *71*, 327.

(213) Bahome, M. C.; Jewell, L. L.; Hildebrandt, D.; Glasser, D.; Coville, N. J. *App. Catal. A: Gen.l* **2005**, *287*, 60.

(214) Abbaslou, R. M. M.; Soltan, J.; Dalai, A. K. *App. Catal. A: Gen.* **2010**, *379*, 129.

(215) Schulte, H. J.; Graf, B.; Xia, W.; Muhler, M. *ChemCatChem* **2012**, *4*, 350.

(216) Motchelaho, A. M. M., 2011.

(217) Sun, B.; Xu, K.; Nguyen, L.; Qiao, M.; Tao, F. *ChemCatChem* **2012**, *4*, 1498.

(218) Chen, A. A.; Phillips, J.; Venter, J. J.; Vannice, M. A. *J. Catal.* **1989**, *118*, 443.

(219) Venter, J.; Kaminsky, M.; Geoffroy, G. L.; Vannice, M. A. In *Stud. Surf. Sci. Catal.*; B. Delmon, P. G. P. A. J., Poncelet, G., Eds.; Elsevier: 1987; Vol. Volume 31, p 479.

(220) Venter, J. J.; Chen, A. A.; Phillips, J.; Vannice, M. A. *J. Catal.* **1989**, *119*, 451.

(221) de Lecea, C. S.-M.; Linares-Solano, A.; Vannice, M. A. *Carbon* **1990**, *28*, 467.

(222) Venter, J. J.; Chen, A.; Vannice, M. A. *J. Catal.* **1989**, *117*, 170.

(223) Martin-Martinez, J. M.; Rodriguez-Reinoso, F.; Vannice, M. A. *App. Catal.* **1989**, *51*, 93.

(224) Kaminsky, M.; Yoon, K. J.; Geoffroy, G. L.; Vannice, M. A. *J. Catal.* **1985**, *91*, 338.

(225) Bahome, M. C.; Jewell, L. L.; Padayachy, K.; Hildebrandt, D.; Glasser, D.; Datye, A. K.; Coville, N. J. *App. Catal. A: Gen.* **2007**, *328*, 243.

(226) Torres Galvis, H. M.; Koeken, A. C. J.; Bitter, J. H.; Davidian, T.; Ruitenbeek, M.; Dugulan, A. I.; de Jong, K. P. *J. Catal.* **2013**, *303*, 22.

(227) Debouttiere, P.; Roiban, L.; Solhy, A.; Martinez, V.; Kihn, Y.; Castillejos, E. *Angew. Chem. Int. Ed.* **2009**, *48*, 2529.
(228) Pan, X.; Fan, Z.; Chen, W.; Ding, Y.; Luo, H.; Bao, X. *Nat. Mater.* **2007**, *6*, 507.
(229) Chen, W.; Pan, X.; Willinger, M.-G.; Su, D. S.; Bao, X. *J. Am. Chem. Soc.* **2006**, *128*, 3136.
(230) Lee, S. C.; Jang, J. H.; Lee, B. Y.; Kim, J. S.; Kang, M.; Lee, S. B.; Choi, M. J.; Choung, S. J. *J. Mol. Catal. A-Chem.* **2004**, *210*, 131.
(231) Machado, B. F.; Serp, P. *Catalysis Science & Technology* **2012**, *2*, 54.
(232) Sun, B.; Jiang, Z.; Fang, D.; Xu, K.; Pei, Y.; Yan, S.; Qiao, M.; Fan, K.; Zong, B. *ChemCatChem* **2013**, *5*, 714.
(233) Zhao, H.; Zhu, Q.; Gao, Y.; Zhai, P.; Ma, D. *App. Catal. A: Gen.* **2013**, *456*, 233.
(234) Wasmus, S.; Cattaneo, E.; Vielstich, W. *Electrochim. Acta* **1990**, *35*, 771.
(235) Dziembaj, R.; Makowski, W.; Papp, H. *J. Mol. Catal.* **1992**, *75*, 81.
(236) Park, Y.-K.; Park, K.-C.; Ihm, S.-K. *Catal. Today* **1998**, *44*, 165.
(237) Sai Prasad, P.; Bae, J.; Jun, K.-W.; Lee, K.-W. *Catal. Surv. Asia* **2008**, *12*, 170.
(238) Wang, W.; Wang, S.; Ma, X.; Gong, J. *Chem. Soc. Rev.* **2011**, *40*, 3703.
(239) Zhang, Q.; Zuo, Y.-Z.; Han, M.-H.; Wang, J.-F.; Jin, Y.; Wei, F. *Catal. Today* **2010**, *150*, 55.
(240) Huang, Y.; Meng, X.; Dang, Z.; Weng, S.; Zhang, C. *J. Chem. Soc., Chem. Commun.* **1995**, 1025.
(241) Xu, L.; Wang, Q.; Liang, D.; Wang, X.; Lin, L.; Cui, W.; Xu, Y. *App. Catal. A: Gen.* **1998**, *173*, 19.
(242) Choi, M. J.; Kim, J. S.; Kim, H. K.; Lee, S. B.; Kang, Y.; Lee, K. W. *Korean J. Chem. Eng.* **2001**, *18*, 646.
(243) Riedel, T.; Schaub, G.; Jun, K.-W.; Lee, K.-W. *Ind. Eng. Chem. Res.* **2001**, *40*, 1355.
(244) Dorner, R. W.; Hardy, D. R.; Williams, F. W.; Willauer, H. D. *App. Catal. A: Gen.* **2010**, *373*, 112.
(245) Dorner, R. W.; Hardy, D. R.; Williams, F. W.; Willauer, H. D. *Catal. Commun.* **2010**, *11*, 816.
(246) Dorner, R. W.; Hardy, D. R.; Williams, F. W.; Willauer, H. D. *Catal. Commun.* **2011**, *15*, 88.
(247) Hu, B.; Frueh, S.; Garces, H. F.; Zhang, L.; Aindow, M.; Brooks, C.; Kreidler, E.; Suib, S. L. *App. Catal. B: Env.* **2013**, *132–133*, 54.
(248) You, Z.; Deng, W.; Zhang, Q.; Wang, Y. *Chinese J. Catal.* **2013**, *34*, 956.
(249) Drab, D. In *ICCDU* Washington, **2013**.
(250) Velocys, Oxford Catalyst GTL update **2010**.
(251) Atkins, P. W.; De Paula, J. *Atkins' physical chemistry*; 8th ed.; Oxford University Press: Oxford, **2006**.
(252) Moxfyre 2009.
(253) Costa, S.; Borowiak Palen, E.; Kruszynska, M.; Bachmatiuk, A.; Kalenczuk, R. J. *Mat. Sci.* **2008**, *26*, 433.
(254) Belin, T.; Epron, F. *Materials Science and Engineering: B* **2005**, *119*, 105.
(255) Lehman, J. H.; Terrones, M.; Mansfield, E.; Hurst, K. E.; Meunier, V. *Carbon* **2011**, *49*, 2581.
(256) DiLeo, R. A.; Landi, B. J.; Raffaelle, R. P. *J. Appl. Phys.* **2007**, *101*, 064307.
(257) Institution, B. S. In *BS 4359-1, ISO 9277:1995* (**1996**).
(258) Wells, O. C. *Scanning electron microscopy*, **1974**.
(259) NIOSHH **2004**.
(260) O'Neill, M. *Internal Report*, **2010**.

(261) Minett, D. R.; P.O'Byrne, J.; Jones, M. D.; P. Ting, V.; Mays, T. J.; Mattia, D. *Carbon*.

(262) Ross, J.; Elsevier.

(263) Boger, T.; Heibel, A. K.; Sorensen, C. M. *Ind. Eng. Chem. Res.* **2004**, *43*, 4602.

(264) Laurent, C.; Flahaut, E.; Peigney, A. *Carbon* **2010**, *48*, 2994.

(265) www.cheaptubes.com **2013**.

(266) Lachman, I. M.; Lewis, R. M.; Office, U. S. P., Ed. **1975**.

(267) Motchelaho, M. A. M.; Xiong, H.; Moyo, M.; Jewell, L. L.; Coville, N. J. *J. Mol. Catal. A: Chem.* **2011**, *335*, 189.

(268) Xu, Y.-Q.; Peng, H.; Hauge, R. H.; Smalley, R. E. *Nano Lett.* **2004**, *5*, 163.

(269) Smith Jr, M. R.; Hedges, S. W.; LaCount, R.; Kern, D.; Shah, N.; Huffman, G. P.; Bockrath, B. *Carbon* **2003**, *41*, 1221.

(270) Zimmerman, J. L.; Bradley, R. K.; Huffman, C. B.; Hauge, R. H.; Margrave, J. L. *Chem. Mater.* **2000**, *12*, 1361.

(271) Sen, R.; Rickard, S. M.; Itkis, M. E.; Haddon, R. C. *Chem. Mater.* **2003**, *15*, 4273.

(272) Datsyuk, V.; Kalyva, M.; Papagelis, K.; Parthenios, J.; Tasis, D.; Siokou, A.; Kallitsis, I.; Galiotis, C. *Carbon* **2008**, *46*, 833.

(273) Tsang, S. C.; Chen, Y. K.; Harris, P. J. F.; Green, M. L. H. *Nature* **1994**, *372*, 159.

(274) Dementev, N.; Osswald, S.; Gogotsi, Y.; Borguet, E. *J. Mater. Chem.* **2009**, *19*, 7904.

(275) Osswald, S.; Havel, M.; Gogotsi, Y. *J. Raman Spectrosc.* **2007**, *38*, 728.

(276) O'Byrne, J. P.; Owen, R. E.; Minett, D. R.; Pascu, S. I.; Plucinski, P. K.; Jones, M. D.; Mattia, D. *Catal. Sci. Tech.* **2013**.

(277) Yamashita, T.; Hayes, P. *Appl. Surf. Sci.* **2008**, *254*, 2441.

(278) Smith, B. D.; White, R. R. *AIChE J.* **1956**, *2*, 46.

(279) Behr, M. J.; Gaulding, E. A.; Mkhoyan, K. A.; Aydil, E. S. *J. Appl. Phys.* **2010**, *108*, 053303.

(280) O'Byrne, J. P.; Owen, R. E.; Minett, D. R.; Pascu, S. I.; Plucinski, P. K.; Jones, M. D.; Mattia, D. *Catal. Sci. Tech.* **2013**, *3*, 1202.

(281) Shultz, J. F.; Hall, W. K.; Seligman, B.; Anderson, R. B. *J. Am. Chem. Soc.* **1955**, *77*, 213.

(282) Herranz, T.; Rojas, S.; Pérez-Alonso, F. J.; Ojeda, M.; Terreros, P.; Fierro, J. L. G. *J. Catal.* **2006**, *243*, 199.

(283) Pour, A. N.; Housaindokht, M. R.; Tayyari, S. F.; Zarkesh, J. *J. Nat. Gas Chem.* **2010**, *19*, 284.

(284) Smith, R.; Muruganandam, L.; Murthy, S. S. *ChemInform* **2010**, *41*.

(285) Boulanger, P.; Belkadi, L.; Descarpentries, J.; Porterat, D.; Hibert, E.; Brouzes, A.; Mille, M.; Patel, S.; Pinault, M.; Reynaud, C.; Mayne-L'Hermite, M.; Decamps, J. M. *J Phys.: Conf. Series* **2013**, *429*, 012050.

(286) Couteau, E.; Hernadi, K.; Seo, J. W.; Thiên-Nga, L.; Mikó, C.; Gaál, R.; Forró, L. *Chem. Phys. Lett.* **2003**, *378*, 9.

(287) Griffiths, O. G.; O'Byrne, J. P.; Torrente-Murciano, L.; Jones, M. D.; Mattia, D.; McManus, M. C. *J Cleaner Prod.* **2013**, *42*, 180.

(288) Ratchprapa, S. In *International Conference of Carbon Dioxide Utilisation* **2013**.

(289) Liu, B.; Ren, W.; Gao, L.; Li, S.; Liu, Q.; Jiang, C.; Cheng, H.-M. *The Journal of Physical Chemistry C* **2008**, *112*, 19231.

(290) Balogh, Z.; Halasi, G.; Korbély, B.; Hernadi, K. *App. Catal. A: Gen.* **2008**, *344*, 191.